

**Alma Mater Studiorum – Università di Bologna**

**DOTTORATO DI RICERCA IN**

**CHIMICA**

**Ciclo XXXIII**

**Settore Concorsuale: 03/C1**

**Settore Scientifico Disciplinare: CHIM/06**

**PEPTIDE-BASED LOW MOLECULAR WEIGHT GELATORS FOR THE  
PREPARATION OF SELF-ASSEMBLED MATERIALS**

**Presentata da: Demetra Giuri**

**Coordinatore Dottorato**

**Prof.ssa Domenica Tonelli**

**Supervisore**

**Prof.ssa Claudia Tomasini**

**Esame finale anno 2021**



*Alla mia famiglia.*



## ABSTRACT

Low molecular weight gelators (LMWGs) based on pseudo-peptides are here studied for the preparation of supramolecular materials. These compounds can self-assemble through non-covalent interactions such as hydrogen bonds and  $\pi$ - $\pi$  stacking, forming fibres and gels. A wide variety of materials can be prepared starting from these building blocks, which can be tuned and functionalised depending on the application.

In this work, derivatives of the three aromatic amino acids L-Phenylalanine, L-Tyrosine and L-DOPA (3,4-dihydroxyphenylalanine) were synthesised and tested as gelators for water or organic solvents. First, the optimal gelating conditions were studied for each compound, varying concentration, solvent and trigger. Then the materials were characterised in terms of mechanical properties and morphology. Water remediation from dye pollution was the first focus of this work. Organogels were studied as absorbent of dyes from contaminated water. Hydrogels functionalised with TiO<sub>2</sub> nanoparticles and graphene platelets were proposed as efficient materials for the photo-degradation of dyes. An efficient method for the incorporation of graphene inside hydrogels using the gelator itself as dispersant was proposed. In these materials a high storage modulus coexists with good self-healing and biocompatibility. The incorporation of a mineral phase inside the gel matrix was then investigated, leading to the preparation of composite organic/inorganic materials. In a first study, the growth of calcium carbonate crystals was achieved inside the hydrogel, which preserved its structure after crystal formation. Then the self-assembled fibres made of LMWGs were used for the first time instead of the polymeric ones as reinforcement inside calcium phosphate cements (CPCs) for bone regeneration. Gel-to-crystal transitions occurring with time in a metastable gel were also examined. The formation of organic crystals in gels can be achieved in multicomponent systems, in which a second gelator constitutes the independent gel network. Finally, some compounds unable to gelate were tested as underwater adhesives.



# Table of Contents

|   |           |
|---|-----------|
| <b>Chapter 1 .....</b>  | <b>1</b>  |
| <b>1. Introduction .....</b>                                  | <b>1</b>  |
| 1.1 Low molecular weight gelators .....                       | 1         |
| 1.2 Peptides and pseudo-peptides as LMWGs .....               | 4         |
| 1.2.1 Aromatic groups in LMWGs.....                           | 5         |
| 1.2.2 Peptide amphiphiles and bolaamphiphilic gelators .....  | 7         |
| 1.2.3 Oxazolidin-2-one containing gelators .....              | 8         |
| 1.3 Triggers.....   | 9         |
| 1.4 Gel characterisation: rheology .....                      | 13        |
| 1.4.1 Amplitude sweep.....                                    | 14        |
| 1.4.2 Frequency sweep .....                                   | 16        |
| 1.4.3 Thixotropy (step-strain) test .....                     | 17        |
| 1.4.4 Time sweep test.....                                    | 18        |
| 1.5 Aim of the thesis.....                                    | 19        |
| <b>Chapter 2 .....</b>  | <b>20</b> |
| <b>2. LMW gels for water decontamination .....</b>            | <b>20</b> |
| 2.1 Dye absorption into self-assembled gels .....             | 20        |
| 2.1.1 Hydrogels with graphene oxide for dye absorption .....  | 22        |
| 2.1.2 Lau-L-Dopa(Bn) <sub>2</sub> -D-Oxd-OBn organogels ..... | 22        |
| 2.1.3 Materials and Methods .....                             | 34        |

|                       |  |            |
|-----------------------|--|------------|
| 2.2                   | Light penetrating hydrogels for dyes photo-degradation .....           | 35         |
| 2.2.1                 | Hydrogels preparation and characterisation .....                       | 38         |
| 2.2.2                 | Photodegradation experiments .....                                     | 42         |
| 2.2.3                 | Materials and Methods .....  | 45         |
| <b>Chapter 3.....</b> |  | <b>47</b>  |
| <b>3.</b>             | <b>Graphene doped LMW gels for 3D cell growth .....</b>                | <b>47</b>  |
| 3.1                   | Mechanical properties of graphene doped LMWSHs .....                   | 49         |
| 3.2                   | Materials and Methods .....  | 57         |
| <b>Chapter 4.....</b> |  | <b>60</b>  |
| <b>4.</b>             | <b>LMWGs and mineral phase: formation of composite materials .....</b> | <b>60</b>  |
| 4.1                   | Biom mineralization: crystal growth in hydrogel matrices .....         | 60         |
| 4.1.1                 | Supramolecular hydrogels for growth of CaCO <sub>3</sub> crystals..... | 62         |
| 4.1.2                 | Reversibility of calcium uptake.....                                   | 68         |
| 4.1.3                 | Xerogel characterization .....   | 71         |
| 4.1.4                 | Materials and methods .....  | 80         |
| 4.2                   | Fibre-reinforced Calcium Phosphate Cements (FRCPCs) .....              | 83         |
| 4.2.1                 | Calcium Phosphate Cements as bone scaffolds .....                      | 83         |
| 4.2.2                 | Self-assembled LMWG for FRCPCs .....                                   | 87         |
| 4.2.3                 | Materials and Methods .....  | 102        |
| <b>Chapter 5.....</b> |  | <b>104</b> |
| <b>5.</b>             | <b>Gel-to-crystal transition in supramolecular gels .....</b>          | <b>104</b> |

|                         |   |            |
|-------------------------|---|------------|
| 5.1                     | Metastable gels .....   | 104        |
| 5.2                     | Multicomponent gels .....   | 115        |
| 5.2.1                   | Metastable multicomponent gel .....                                       | 117        |
| 5.2.2                   | Materials and Methods .....   | 123        |
| 5.2.3                   | Notes.....  | 125        |
| <b>Chapter 6.....</b>   |   | <b>126</b> |
| <b>6.</b>               | <b>From LMW gelators to LMW adhesives .....</b>                           | <b>126</b> |
| 6.1                     | Underwater adhesion: a mussel-inspired world.....                         | 126        |
| 6.1.1                   | Synthesis of Boc <sub>x</sub> -L-(DOPA) <sub>n</sub> -OMe adhesives ..... | 128        |
| 6.1.2                   | Characterisation of L-DOPA based adhesives .....                          | 130        |
| 6.1.3                   | Materials and Methods .....   | 141        |
| <b>Chapter 7.....</b>   |   | <b>144</b> |
| <b>7.</b>               | <b>Conclusions .....</b>  | <b>144</b> |
| <b>Chapter 8.....</b>   |   | <b>148</b> |
| <b>8.</b>               | <b>Experimental procedures .....</b>                                      | <b>148</b> |
| 8.1                     | Synthesis and characterisation.....                                       | 148        |
| <b>References .....</b> |   | <b>159</b> |

## Abbreviations

|            |   |
|------------|---|
| A          | Alanine   |
| ACN        | Acetonitrile  |
| AFM        | Atomic Force Microscope   |
| Arg        | Arginine  |
| ATR-IR     | Attenuated Total Reflection – Infrared  |
| Az         | Azelaic acid  |
| Bn         | Benzyl  |
| Boc        | <i>tert</i> -butyloxycarbonyl   |
| CB         | Conduction band   |
| Cbz        | Carboxybenzyl   |
| CPC        | Calcium phosphate cement  |
| DBU        | 1,8-Diazabicyclo[5.4.0]undec-7-ene  |
| DCM        | Dicloromethane  |
| DCPD       | Dicalcium phosphate dihydrate   |
| DIEA/DIPEA | N,N-Diisopropylethylamine   |
| DMAP       | Dimethylaminopyridine   |
| DMEM       | Dulbecco's modified Eagle medium  |
| DOPA       | 3,4-dihydroxyphenylalanine  |
| EDTA       | Ethylenediaminetetraacetate   |
| EDX        | Energy-dispersive X-ray spectroscopy  |
| F          | Phenylalanine   |
| Fmoc       | Fluorenylmethyloxycarbonyl  |
| FRCPC      | Fibre-reinforced calcium phosphate cement   |
| GdL        | Glucono- $\delta$ -lactone  |
| GO         | Graphene oxide  |
| HA         | Hydroxyapatite  |
| HATU       | 1-[Bis(dimethylamino)methylene]-1H-1,2,3-triazolo[4,5-b]pyridinium 3-oxid hexafluorophosphate |
| HBTU       | (2-(1H-benzotriazol-1-yl)-1,1,3,3-tetramethyluronium hexafluorophosphate                      |
| His        | Histidine   |
| HPLC       | High Performance Liquid Chromatography  |
| IBCF       | Isobutyl chloroformate  |
| L/P        | Liquid/Powder ratio   |
| Lau        | Lauric acid   |
| LMWGs      | Low-molecular-weight gelators   |
| LMWSHs     | Low-molecular-weight supramolecular hydrogels   |
| LVE        | Linear viscoelastic   |
| Me         | Methyl  |
| Mfp        | Mussel foot protein   |
| MS         | Mass Spectrometry   |
| Nap        | Naphtalene  |
| NIH-3T3    | Mouse embryonic fibroblast  |

|       |                                     |
|-------|-------------------------------------|
| NMM   | N-methylmorphiline                  |
| NMR   | Nuclear Magnetic Resonance          |
| NPs   | Nanoparticles                       |
| OCP   | Octacalcium phosphate               |
| Oxd   | 4-carboxy-5-methyl-oxazolidin-2-one |
| PAs   | Peptide amphiphiles                 |
| PBS   | Phosphate Buffered Saline           |
| PC    | Photo-catalysts                     |
| pGlu  | Pyroglutamic acid                   |
| Phe   | Phenylalanine                       |
| Pro   | Proline                             |
| RhB   | Rhodamine B                         |
| ROS   | Reactive oxygen species             |
| RT    | Room Temperature                    |
| SAFiN | Self-Assembled Fibrillary Network   |
| SANS  | Small Angle Neutron Scattering      |
| SAXS  | Small Angle X-Ray Scattering        |
| SEM   | Scanning Electron Microscope        |
| TBAB  | Tetrabutylammonium bromide          |
| TCP   | Tricalcium phosphate                |
| TEA   | Triethylamine                       |
| TEM   | Transmission Electron Microscopy    |
| TFA   | Trifluoroacetic acid                |
| THF   | Tetrahydrofuran                     |
| ThT   | Thioflavin T                        |
| Tyr   | Tyrosine                            |
| VB    | Valence band                        |



# Chapter 1

## 1. Introduction

### 1.1 Low molecular weight gelators

Low molecular weight gelators (LMWGs) are a fascinating class of compounds able to self-assemble into supramolecular structures, such as fibres and gels. They received great attention in the last two decades because of the possibility to tailor their structures, obtaining intriguing supramolecular architectures and materials suitable for several applications, including environmental remediation,<sup>1</sup> medicine,<sup>2</sup> biomineralization<sup>3</sup> and electronics.<sup>4</sup>

LMWGs are organic compounds with molecular weights lower than 1000 Daltons, able to self-assemble through non-covalent interactions such as hydrogen bonding,  $\pi$ - $\pi$  stacking (**Figure 1.1**), metal coordination, dipolar and van der Waals interactions, solvophobic forces (hydrophobic forces for hydrogels).<sup>5,6</sup> The dynamic nature of non-covalent interactions paves the way to the preparation of reversible materials, which distinguish these supramolecular gels from polymeric gels. This is an important property for several applications, mainly in the biomedical field.

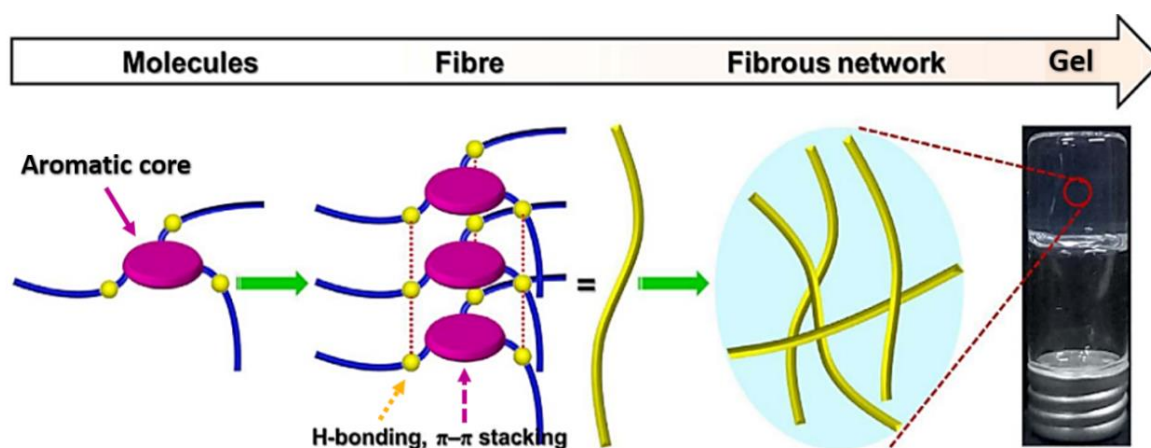


**Figure 1.1** Schematic representation of some of the interactions leading to the self-assembly of LMWGs.

Despite the limited range of non-covalent stabilising interactions, LMWGs molecules have access to a diverse and elaborate range of supramolecular structures which give rise to variable morphologies, presumably due to the large degrees of freedom available in three-dimensional packing motifs and subtle differences in the energies of intermolecular interactions.<sup>7</sup> Although these interactions are individually weak, their sum drives to the assembly, leading to the formation of materials that are permanent on analytical time scale and are considered “solid-like” in their rheological behaviour, even when more than 99% by weight of the material is liquid (the solvent).<sup>8</sup>

The formation of LMW gels (**Figure 1.2**) relies on a delicate balance between solubility and insolubility of the gelator in the solvent chosen. The gelation process usually starts when a trigger is added to the gelator solution and drives the gelator from a soluble to a partial-soluble state. The trigger may be a physical or chemical input such as temperature variation,<sup>9</sup> ultrasound sonication,<sup>10</sup> solvent switch,<sup>11</sup> salt addition<sup>12</sup> or a pH change.<sup>13</sup> The addition of the trigger causes the slow self-assembly of the gelator molecules in long structures, most commonly fibers (Self-Assembled Fibrillary Network, SAFiN), which entangle together at a certain concentration, forming a network able to trap the solvent.

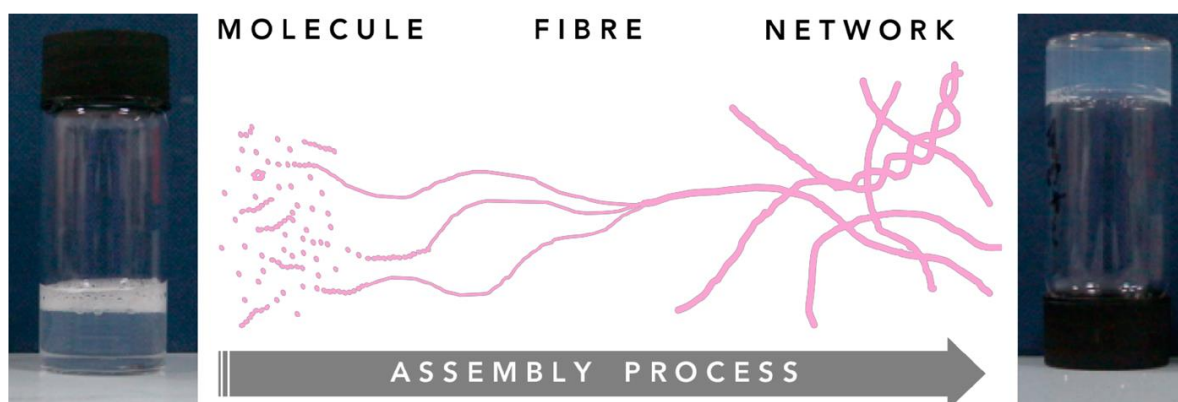


**Figure 1.2** Schematic assembly process of a gel across length scale. Reproduced from ref.<sup>14</sup>

The strength of the network prevents the flow of the solvent under gravity from the gel, even if the vial containing the gel is turned upside down, which is a usual and simple test to check whether a gel formed or not. Depending on the medium where the LMWG is dissolved, gels can be divided into hydrogels, if the solvent is water, or organogels, if an organic solvent is used.

The final properties of a gel are critically affected by the structure of the gelator molecule, as

well as the process by which gelation occurs. Every method implies a certain time and involves a specific kinetic for the formation of the fibres, of the entanglements and finally of the network (**Figure 1.3**). Even using the same trigger, gelation rates can vary, leading to materials with different bulk properties.<sup>15</sup> For this reason, it is very important to carefully control all the parameters of the process in order to prepare gels with reproducible properties, that is an essential feature when using gels in applications.

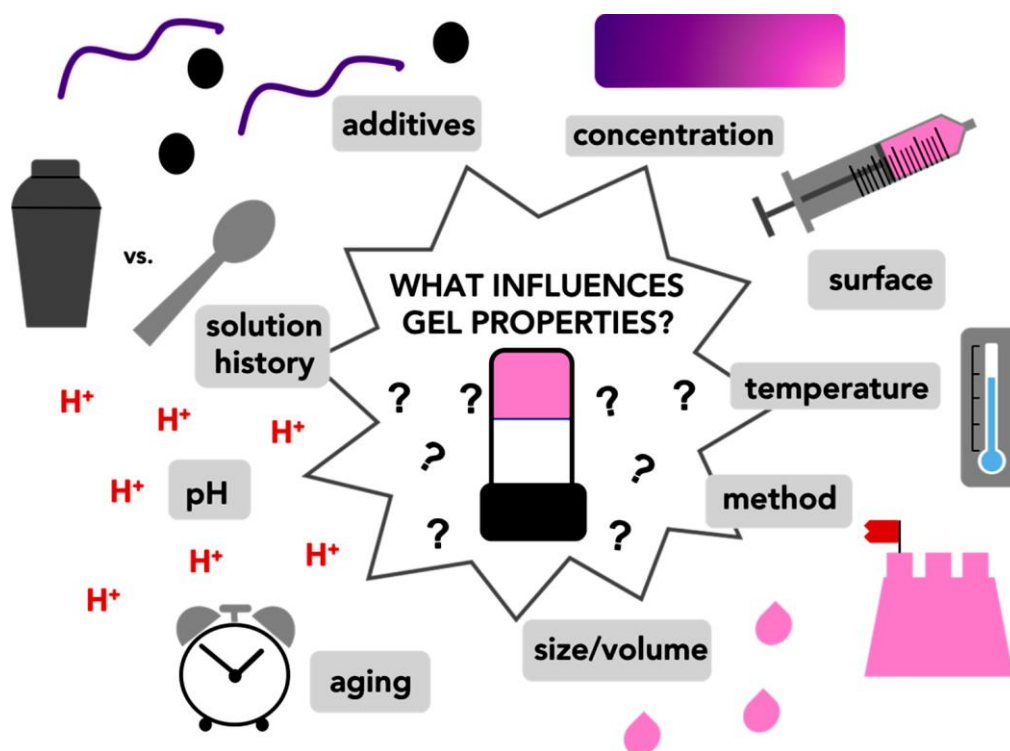


**Figure 1.3** Formulation parameters that may influence gel formation. Reproduced from ref.<sup>14</sup>

It is extremely difficult to predict whether a certain molecule will form a gel or not and understanding the rules behind the gelation process is still challenging. The formation of gels has been described as an empirical science, and the vast majority of gelator structures were discovered serendipitously.<sup>16</sup> Molecules with very similar structures can exhibit extremely different propensity to form gels.<sup>17–20</sup> In these last years, researchers devoted a significant effort to identifying potential gelator molecules only by screening large numbers of compounds and testing a wide range of solvents. Nevertheless, the tireless research in this field led to a remarkable improvement in the understanding of the general principles behind LMW gels formation and properties.

## 1.2 Peptides and pseudo-peptides as LMWGs

Peptides and peptide derivatives are particularly attractive building blocks for the construction of supramolecular materials. Nature itself is largely devoted to the expression of 20 amino acids. The expressed polypeptides and proteins undertake an impressive array of structural and functional roles, including molecular recognition, catalysis and energy storage. While many of these biological structures are too complex to provide scalable technological solutions, simplified versions of these systems may provide useful tools with properties and functions normally not associated with synthetic materials.<sup>21</sup>

Peptidomimetics are small protein-like molecules designed to mimic natural peptides. It is possible to design these molecules in order to obtain the same biological effects as their peptide role models with enhanced properties, such as higher proteolytic stability, increased bioavailability and, in some cases, improved selectivity or potency.<sup>22</sup>

Both peptides and peptidomimetics tend to form secondary structures, such as helices or sheets, which are stabilized by intramolecular or intermolecular N–H···O=C hydrogen bonds (**Figure 1.4**). Helices are stabilized by intramolecular hydrogen bonds, while sheets are usually stabilized by intermolecular hydrogen bonds, depending on the molecular structure and chain length. Self-organized oligomers that tend to form helices are usually bad candidates as LMWGs, in contrast, oligomers that have  $\beta$ -sheets as preferred secondary structure are good candidates to form fibres, and behave as gelators.<sup>23</sup>

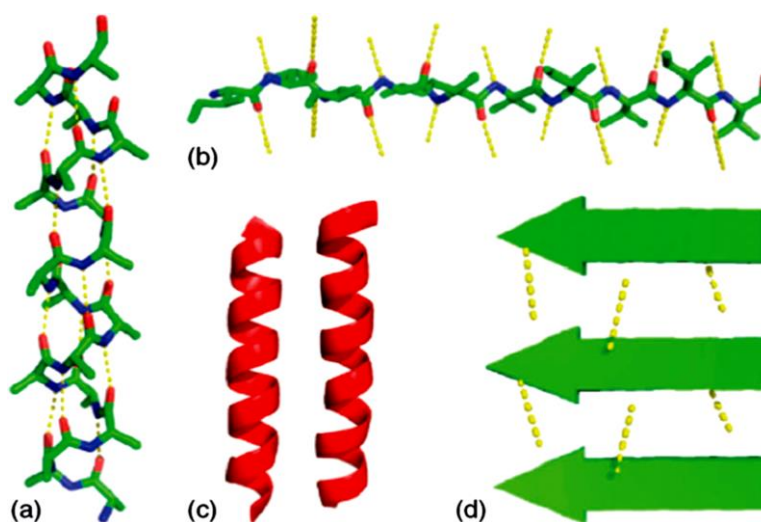


**Figure 1.4** (a) An  $\alpha$ -helix with the hydrogen-bonding pattern parallel to the helix axis; (b)  $\beta$ -strand with illustrative hydrogen bonds orthogonal to the direction of the chain; (c)  $\alpha$ -helices forming higher order

structures; (d)  $\beta$ -sheet assembly is stabilized by the formation of intermolecular hydrogen bonds. Adapted from ref.<sup>23</sup>

Peptide-based scaffolds are interesting candidates for hydrogelation and organogelation because they can self-assemble using various noncovalent interactions. Moreover, they can be manufactured easily and in large quantities, and modified both chemically and biologically. Some structural features have been identified as responsible for the formation of a good gelator: (i) it should contain a hydrophilic head, as a peptide bond; (ii) it should contain some hydrophobic moieties, usually aromatic rings or occasionally long aliphatic chains; (iii) it should be a chiral compound. In the following paragraphs these general features will be analysed in more details.

### 1.2.1 Aromatic groups in LMWGs

During the last two decades, a wide variety of dipeptide and tripeptide conjugates has been synthesised and tested as LMWGs. Efficient gelators appear to require the presence of an aromatic protecting group such as fluorenylmethoxycarbonyl (Fmoc),<sup>17,24</sup> naphthalene,<sup>18,25</sup> pyrene<sup>26</sup> or spiropyran<sup>27</sup> on the *N*-terminus of the dipeptide. For example, it was reported that Fmoc-Tyr-OH (Tyr=tyrosine) is an efficient hydrogelator, whereas Cbz-Tyr-OH (where Cbz is carboxybenzyl protecting group) and Boc-Tyr-OH (where Boc is a *tert*-butyloxycarbonyl protecting group) do not form fibrillar structures in water.<sup>28</sup> As a further example, a totally deprotected diphenylalanine, H-Phe-Phe-OH (Phe=Phenylalanine), can form vesicles or nanotubes in aqueous solution,<sup>29</sup> while Fmoc-Phe-Phe-OH can form extended fibrillar structures that associate to give hydrogels.<sup>30</sup> Reported studies of peptide gels suggest that the Fmoc groups assemble with  $\pi$ - $\pi$  stacking distances of  $<4$  Å,<sup>31,32</sup> supporting the idea that the presence of  $\pi$ - $\pi$  stacking is important to hydrogel formation.

Adams *et al.*<sup>33</sup> have carried out a comprehensive study on the gelation properties of a library of Fmoc protected dipeptides. In general, the ability of a dipeptide to form strong gels was found to be correlated to its hydrophobicity. Dipeptides with calculated hydrophobicities below  $\log P = 2.8$  ( $P$ =partition coefficient) formed weak and unstable gels, whereas when  $\log P$  was above 5.5 the dipeptides appeared to be too hydrophobic to form homogeneous gels.

At intermediate values of  $\log P$  (3.4–5.5), all the dipeptides assembled to give gels of similar strengths.

Another important study reported how the presence of aromatic amino acids in several dipeptide gelators can positively affect the gelation abilities of the compound.<sup>34</sup> The analysis was performed on 34 dipeptides and proved that those containing a phenylalanine as one of the constituent amino acids were much more likely to lead to a gelator compared to those having non-aromatic amino acids only. In the study, when neither amino acid in the dipeptide was a phenylalanine, there was a 55% chance that the molecule would form a gel. However, when either of the amino acids is phenylalanine, there is a 91% chance that the molecule will form a gel. The only dipeptides containing Phe which failed to form gels were those functionalised with an anthracene ring, which probably lacked flexibility for optimal packing for gelation. If those structures are not taken into account, then 100% of the molecules formed gels when either of the amino acids was phenylalanine. This is one of the reasons why the gelators studied in this Thesis are based on aromatic amino acids: phenylalanine, tyrosine and DOPA (3,4-dihydroxyphenylalanine).

In general, many studies in the last two decades have focused on phenylalanine containing dipeptides, functionalised with a range of protecting groups and leading to a variety of different materials.<sup>35–40</sup> Fewer examples have examined tyrosine based gelators,<sup>41–45</sup> but these are still a huge amount compared to studies focusing on DOPA gelators. The self-assembling of some DOPA-containing short peptides has been recently reported.<sup>44,46–49</sup>

L-DOPA is a chiral amino acid generated *via* biosynthesis from the amino acid L-tyrosine available from plants and mammals, including humans. L-DOPA is a psychoactive drug used in the clinical treatment of Parkinson's disease, because it can cross the blood–brain barrier and act as precursor to the neurotransmitters dopamine, norepinephrine (noradrenaline), and epinephrine (adrenaline).<sup>49</sup> DOPA is particularly interesting due to the multifunctional nature of the catechol moiety, which is capable of acting as an antioxidant, a radical trap, a metal chelator and an oxidizable reducing agent.<sup>50,51</sup> A deeper understanding of the self-assembly process of DOPA based compounds could lead to the preparation of a novel class of biocompatible materials with a wide range of useful properties. This is one of the reasons why derivatives and materials based on this amino acid are the major focus of this Thesis.

## 1.2.2 Peptide amphiphiles and bolaamphiphilic gelators

Another class of gelators that has been widely explored are peptide amphiphiles (PAs), consisting of a hydrophobic nonpeptidic tail covalently conjugated to a peptide sequence. These molecules consist of three segments (**Figure 1.5**): a hydrophobic sequence, commonly an alkyl tail, that drives aggregation through hydrophobic collapse; a  $\beta$ -sheet-forming peptide that promotes nanofibers formation; a peptide segment that contains ionizable side chains and often an amino acid sequence of interest for biological signalling.

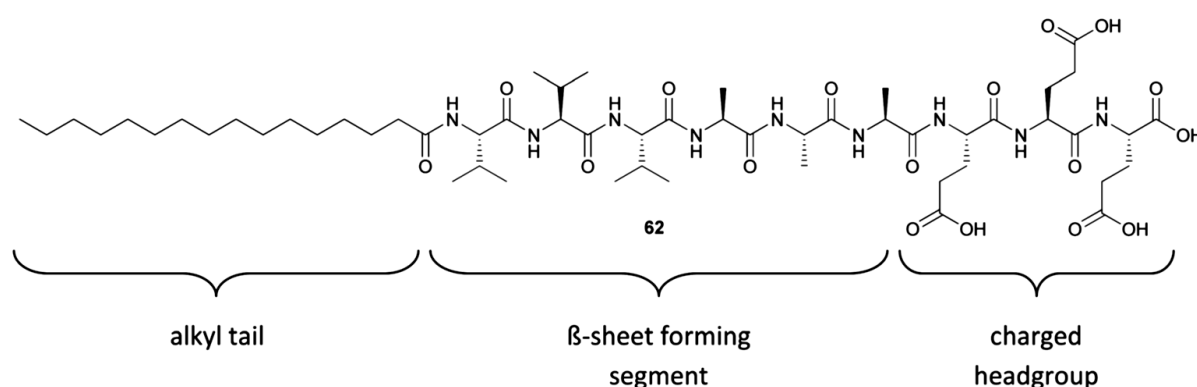


**Figure 1.5** Molecular structure of a peptide amphiphile.

A particular kind of amphiphilic peptides are bolaamphiphiles (two-headed amphiphiles), composed by a long hydrophobic alkyl chain acting as a spacer between two polar headgroups attached to its ends (**Figure 1.6**). They are named after the “bola”, which is a South American weapon made of two balls connected by a string. As with conventional amphiphiles, the chemical functionality of the headgroups and linking group can be varied to change the aggregation properties. Some groups have reported the design and synthesis of hydrogelators and/or organogelators having this skeleton for several applications.<sup>36,52–55</sup>

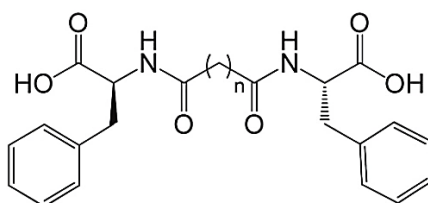


**Figure 1.6** Example structure of a bolaamphiphilic gelator.

### 1.2.3 Oxazolidin-2-one containing gelators

Tomasini *et al.* reported that 4-methyl-5-carboxy-oxazolidin-2-one moiety (denoted as Oxd from now on) could be successfully utilized in the formation of supramolecular materials. This molecule, that mimics a proline group, may form oligomers having stable secondary structures in solution, due to its ability to lock the peptide bond in the trans conformation.<sup>56–58</sup> This outcome does not take place in prolyl bonds which also adopt the cis conformation.<sup>59–61</sup> The imide bond of N-acyl oxazolidin-2-ones adopt rigid trans conformers due to the combination of Coulomb repulsion between carbonyl oxygen in the cis isomer and  $n \rightarrow \pi^*$  interactions in the trans isomer.<sup>62</sup> This property induces a local constraint in the pseudopeptide chain that may cause the formation of supramolecular materials, when it is combined with other factors, such as  $\pi$ -stacking interactions and intermolecular  $N-H \cdots O=C$  bonds. For example, the L-Phe-D-Oxd (L-Phe = L-phenylalanine) moiety (**Figure 1.7**) displays all these effects and may be considered a privileged scaffold for the formation of supramolecular materials.<sup>54</sup>

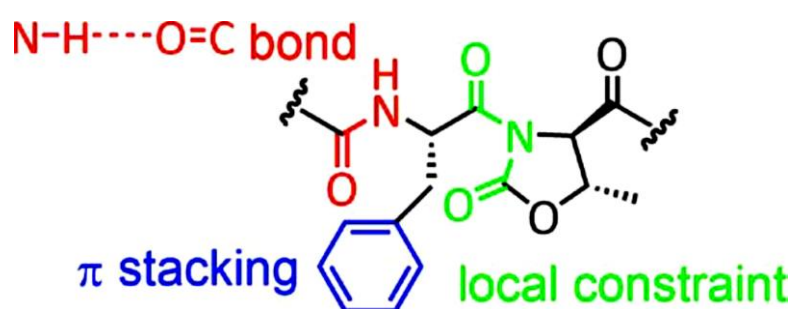


**Figure 1.7** Chemical structure of the L-Phe-D-Oxd moiety, a privileged structure for the formation of supramolecular materials. Adapted from ref.<sup>63</sup>

### 1.3 Triggers

As mentioned before, there are several types of triggers to start the gelation process, leading to gels with different final properties that can be suitable or not for a specific application. For example, a gel obtained with the solvent change method (which implies organic solvents) or with the pH change method (usually achieving a final pH around 3-4), cannot be used for cell culturing.

The gels presented in this work were obtained using four types of trigger: 1. pH change, 2. solvent switch, 3. sonication, 4. salt addition and 5. amino acid addition.

1. In addition to hydrophobic interactions, hydrogen bonding appears to be essential to the self-assembly process. Several publications<sup>33,64,65</sup> confirmed that dipeptides form gels when the carboxylic acid group is protonated.

Gelation may be initiated by changes in pH that cause protonation or deprotonation of gelator molecules. When molecules containing carboxylic acids are used, the gelator is dissolved in alkaline environment leading to a pH above its pKa, so that the formation of a carboxylate occurs. Then, when the trigger (an acid) is added to the solution and the pH drops below the pKa of the compound, the carboxylate is protonated again, decreasing the solubility of the LMWG and inducing the self-assembly process.<sup>33</sup>

At low pH, fibrils may form rapidly in a few seconds or even less, making the achievement of a homogeneous pH before the start of the gelation process a real challenge. For this reason, the acid used to lower the pH has a pivotal effect on the kinetics of formation of the network and thus on the final properties of the material.

A mineral acid, such as HCl, can be added to a high pH solution of gelator, causing a fast decrease in the pH. The quick drop in pH usually induces the formation of the gel at the surface, with a consequent gradual diffusion of the acid through the gel into the rest of the solution. This process may lead to irreproducible and even visibly inhomogeneous gels (**Figure 1.8**). A way to overcome this problem is to use lactones or anhydrides, which slowly hydrolyse in water forming an acid. Glucono- $\delta$ -lactone (GdL) is one of the most widespread precursor for such a pH change method of LMWGs, because it is readily dissolved in water and hydrolysed slowly to gluconic acid, providing a uniform distribution in the solution (**Figure 1.9**).<sup>64</sup> The hydrolysis process of the lactone is so slow (about 8 hours) that the solution can be mixed, to provide a homogeneously dispersed solution before

the pH change. The lactone hydrolysis generates the acid and allows a uniform and slow decrease in pH, which usually leads to the formation of homogenous and reproducible gels.

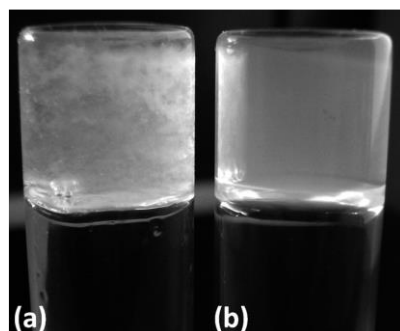


**Figure 1.8** Comparison between a gel prepared with Fmoc-leucine-glycine. (a) pH changed with HCl, (b) pH changed with GdL.

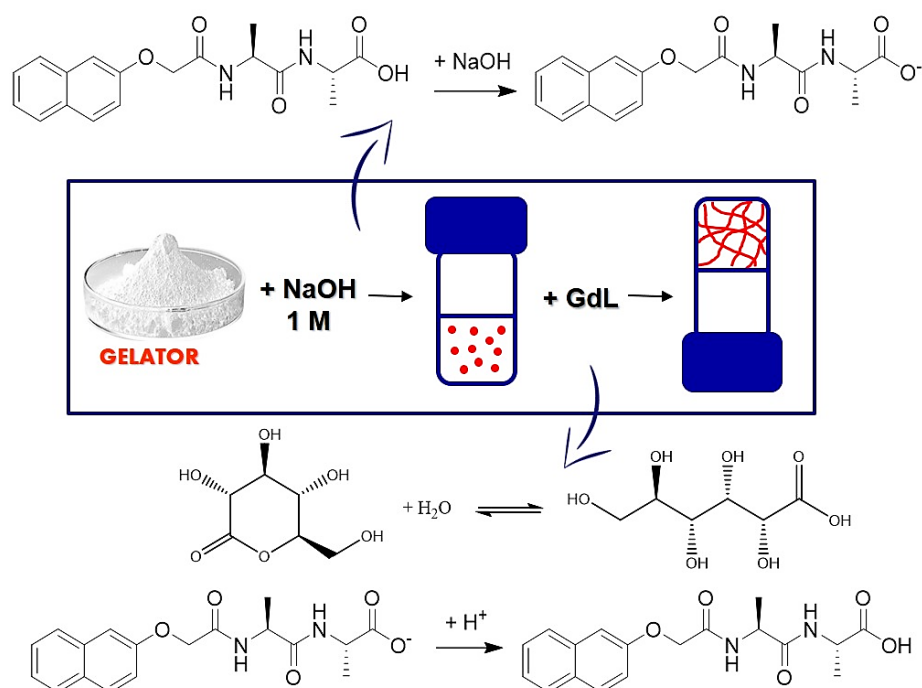


**Figure 1.9** Representation of the mechanism of gelation when GdL is used. The gelator represented will be discussed in Chapter 5.

2. The solvent change method relies on dissolution of the gelator in an organic solvent and subsequent addition of a miscible anti-solvent, which reduces the solubility of the compound and induces the gelation process. It is a useful tool for those LMWGs that do not dissolve in water, because they can be added to an organic solvent and water can be

added later as anti-solvent. The formation of the gel network is very fast with this method, usually taking place in a few minutes. The properties of the final material are mainly affected by the ratio between the two solvents.<sup>66,67</sup>

3. The first example of the influence of ultrasound sonication on organogelation was reported by Naota and co-workers for peptide-based palladium complexes.<sup>68</sup> Soon after, Reepmister's group reported the formation of organogels upon sonication of dipeptides.<sup>69</sup> In these works, the mechanism suggested involved conformational changes of the gelator induced by sonication, leading to the formation of self-assembled structures. They proposed that ultrasound waves were responsible for the cleavage of the intra-molecular interactions of the complexes ( $\pi$ -stacking and hydrogen bonds) enabling rapid and spontaneous aggregation through inter-molecular interactions in a "self-lock/interlock" switching. In this process, the formation of the gel and its final properties and morphology are highly affected by sonication time, temperature and solvent.
4. Another useful trigger is represented by metal-ions. The addition of divalent ions such as calcium, magnesium and zinc enhances the ionic strength of the interaction between fibres inducing cross-linking.<sup>70</sup> This process can occur when gelator molecules possess particular groups such as carboxylates, that can be bonded together by the metal-ions (**Figure 1.10**). It was reported that these interactions take place at high pH when the gelator molecules may organise in worm-like micelles, with buried hydrophobic cores and exposed carboxylate heads.<sup>12</sup>

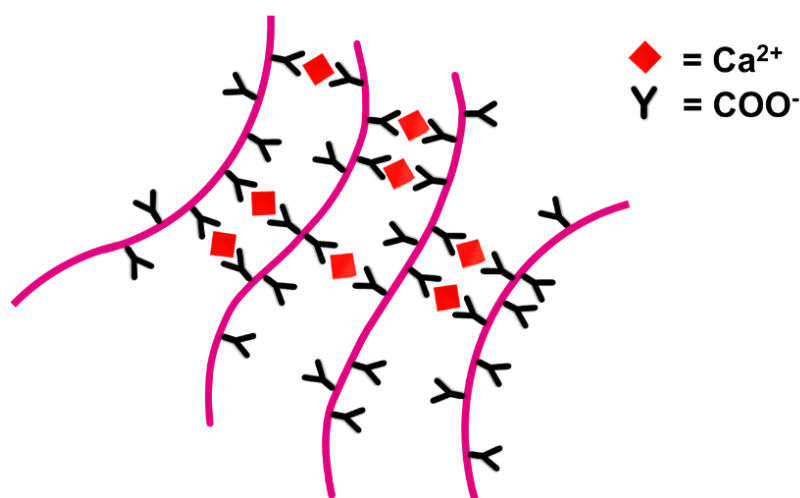


**Figure 1.10** Schematic representation of gelation triggered by Ca<sup>2+</sup> ions.

The three-dimensional network is presumably formed through the presence of salt bridges between the divalent cations and two negatively charged carboxylic groups belonging to neighbouring worm-like micelles. This process may be similar to what happens to biopolymers such as pectin and alginate in presence of calcium.<sup>71</sup> The use of metal ions for gelation trigger can have a pivotal role in trapping undesired cations pollutants and in biomedical applications, because gels can be formed over a wide range of pH including neutral conditions.<sup>45</sup>

5. Recently, Tomasini and co-workers reported an effective and inexpensive method to promote gelation in water using amino acids and bolaamphiphilic gelators.<sup>72</sup> Amino acids trigger the hydrogel formation by making non-covalent salt-bridge cross links between gelator molecules. The formation of strong networks was observed in particular with basic amino acids, such as Histidine (His) and Arginine (Arg). **Figure 1.11** shows the cross linking which is hypothesised to occur between gelator molecules and Arg. The basicity of Arg allows a better dissolution of the gelator. The electrostatic interactions between Arg and the gelator molecule helps to form a supramolecular chain, that mimics a polymer. This method allows the formation of hydrogels that can be used for biological application at a neutral or slightly basic final pH.

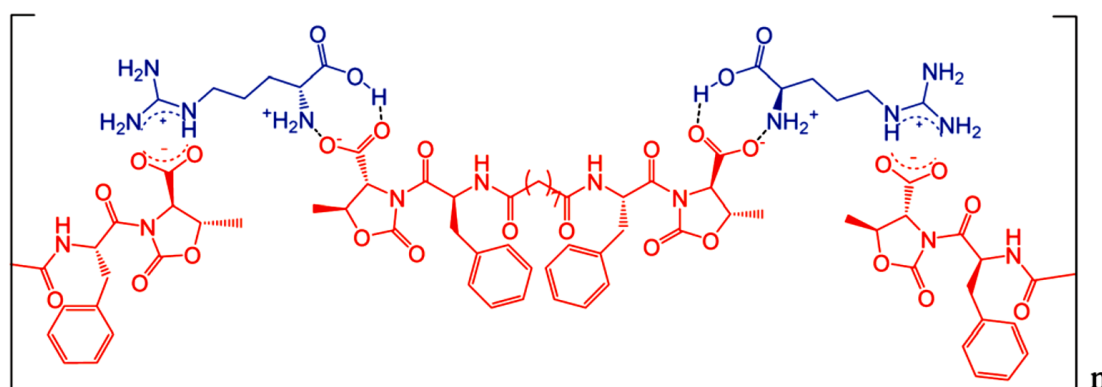


**Figure 1.11** Hypothetical interactions formed by a bolaamphiphilic gelator and Arg.

## 1.4 Gel characterisation: rheology

An essential tool for the characterisation of the mechanical properties of gels is rheology. Quite often the first diagnostic test for gelation is the so-called “tabletop” rheology. In one of these tests, the *tube inversion*, the vial or test-tube containing the sample is inverted upside-down and if the sample does not flow under its own weight it is considered a gel. However, this test is not sufficient to demonstrate the formation of gels, because some viscous liquids can be stable to inversion for a short time.<sup>73</sup>

The second tabletop rheological technique, the *falling sphere* or *dropping ball* test, consists in placing a small glass sphere on top of a sample which is heated in a test-tube. The melting temperature,  $T_{\text{gel}}$ , is detected when the sphere drops on the bottom of the gel, meaning that the network is broken. These two tests are very simple but may lead to inaccuracies, because they rely on visual observations. To deeper investigate the mechanical properties of gels, it is necessary to use a rheometer, which provides quantitative information on the gel network. However, it should be noted that rheological properties of different gels can only be compared if the gels have been prepared in the same ways and measured using the same measuring system. This sometimes makes interpreting the literature quite difficult.

Modern rheometers can be used to perform a complete analysis of the viscoelastic behaviour of gels. The two-plates model is used to define the rheological parameters needed for a scientific description of the flow behaviour of the material. Shear is applied to a sample sandwiched between the two plates. The lower stationary plate is mounted on a very rigid support, and the upper plate can be moved parallel to the lower plate (**Figure 1.12**).

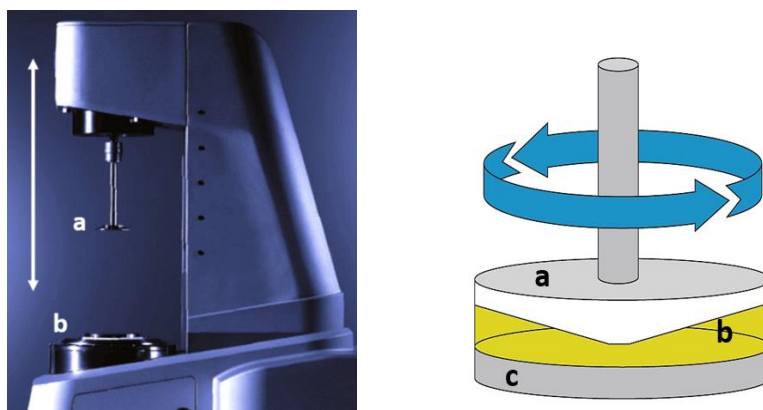


**Figure 1.12** *Left:* a generic rheometer. *Right:* representation of what happens when the shaft (a) moves down on the sample (b) and rotates, while the lower plate (c) is stationary.

### 1.4.1 Amplitude sweep

The two plates model is used to define the shear strain ( $\gamma$ ) using the parameters deflection path ( $s$ ) of the upper, movable plate, and distance ( $h$ ) between the plates. Shear strain  $\gamma$  is defined as deflection path  $s$  divided by shear gap width  $h$  (**Figure 1.13**). The unit for shear deformation is thus dimensionless, usually stated as a percentage.



**Figure 1.13** Two-plates model used to define the shear strain (left). Shear strain formula (right).

The first test usually performed with a rheometer on a gel is the Amplitude sweep, a strain sweep experiment where the deflection of the measuring system is increased stepwise from one measuring point to the next while keeping the angular frequency ( $\omega$ ) at a constant value (**Figure 1.14**).

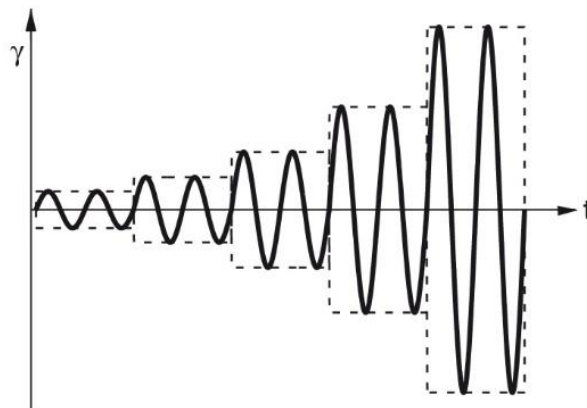


**Figure 1.14** Pre-set of an amplitude sweep experiment, with controlled strain ( $\gamma$ ) and five-steps increasing amplitude. Frequency is kept constant.

The outcome is generally presented as a diagram with shear stress or strain on the x axis and  $G'$  and  $G''$  on the y axis, with both axes on a logarithmic scale. Whereas  $G'$  (storage modulus) represents the elastic behaviour of a material and how solid-like it is,  $G''$  (loss modulus) represents the viscous portion and how liquid-like it is. Some important outcomes of this test are the values of  $G'$  and  $G''$  and the determination of the linear viscoelastic (LVE) region of the gel. In **Figure 1.15** the LVE is represented by the linear range on the left before  $\gamma_L$ , which is the linearity limit. LVE regions indicate the range in which the test can be carried out without breaking the network of the sample hence the strain needed to break it, thus providing indications on the strength of the gel.

In the LVE region,  $G'$  and  $G''$  are constant, showing a plateau value. After the linearity limit,  $G'$  starts decreasing, until the crossover point (or yield value  $\gamma_f$ ) is reached, where  $G''$  is larger than  $G'$ , meaning that the structure is destroyed and the material can flow (**Figure 1.15**).<sup>74</sup>

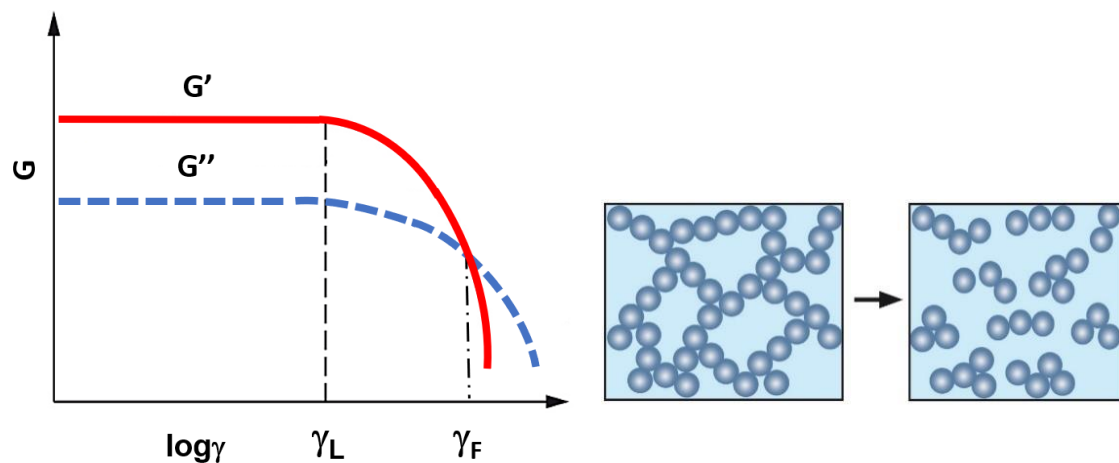


**Figure 1.15** *Left:* representation of an amplitude sweep test on a gel sample, with  $G' > G''$  before the crossover point. *Right:* after the yield point has been exceeded, the superstructure breaks down and the material may start to flow.

A true gel shows an LVE region where  $G'$  is about one order of magnitude higher than  $G''$  and the value of the loss factor  $G''/G'$  ( $\tan\delta$ ) is lower than 0.1.<sup>16</sup>

Amplitude sweep experiments are usually the first rheological characterisation, since all the other oscillatory tests require that the measure is performed at a strain or stress within the LVE region.

## 1.4.2 Frequency sweep

Frequency sweep experiments are generally the second important analysis performed on gels, describing the time-dependent behaviour of the material in a non-destructive deformation range. The angular frequency ( $\omega$ ) is increased stepwise from one measuring point to the next while keeping the deflection of the measuring system (shear strain) at a constant value (**Figure 1.16**). Hence, the only precondition is that the selected shear-strain amplitude is within the LVE region, determined through the Amplitude sweep test.

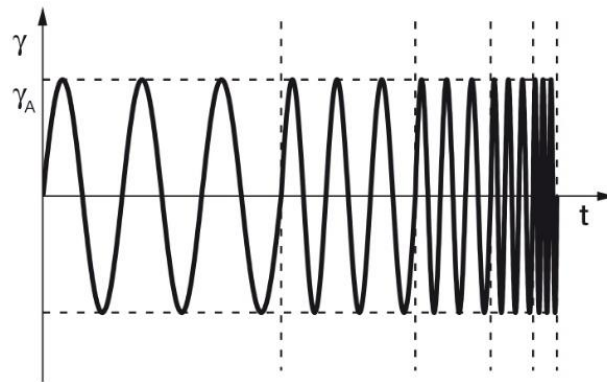


**Figure 1.16** Pre-set of a frequency sweep with controlled shear strain and a five-step variation in frequency. The strain amplitude  $\gamma_A$  is kept constant.

High frequencies are used to simulate fast motion on short timescales, whereas low frequencies simulate slow motion on long timescales or at rest. In practice, with a frequency sweep test it is possible to gather information on the behaviour and inner structure of the material, and to determine how stiff the gel is. The larger  $G'$  and  $G''$  are the stiffer the gel, as it has a more solid like properties. The results of frequency sweeps are usually presented in a diagram with the (angular) frequency plotted on the x-axis and storage modulus  $G'$  and loss modulus  $G''$  plotted on the y-axis, with both axes on a logarithmic scale (**Figure 1.17**).

A typical gel-like behaviour in these tests is observed when both  $G'$  and  $G''$  values are independent from frequency, since the relaxation time of the material is shorter than the frequency change.<sup>75</sup>

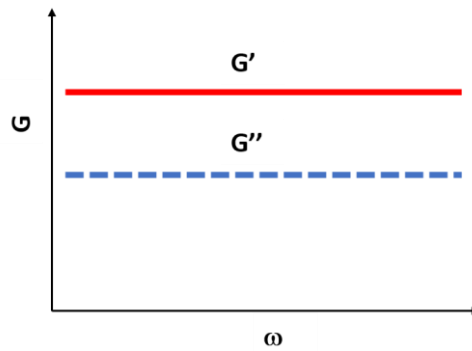


**Figure 1.17** Schematic representation of a frequency sweep test on a gel sample, with  $G' > G''$ , both independent from frequency changes.

### 1.4.3 Thixotropy (step-strain) test

Thixotropy or step-strain experiments can provide essential information on the thixotropic behaviour, which defines the material propensity to structural regeneration. The test is usually divided in intervals where different values of strain  $\gamma$  are applied.

The first interval, at a pre-set low shear rate (within the LVE region), simulates the material behaviour at rest ( $G' > G''$ ). In the second interval the sample is subjected to deformation characterised by an applied strain  $\gamma$  above the LVE region, which usually causes an inversion between  $G'$  and  $G''$  ( $G' < G''$ ), this meaning that the network has been broken. The third interval is the recovery step; the applied strain is again within the LVE region and should allow the reconstruction of the material network (**Figure 1.18**).

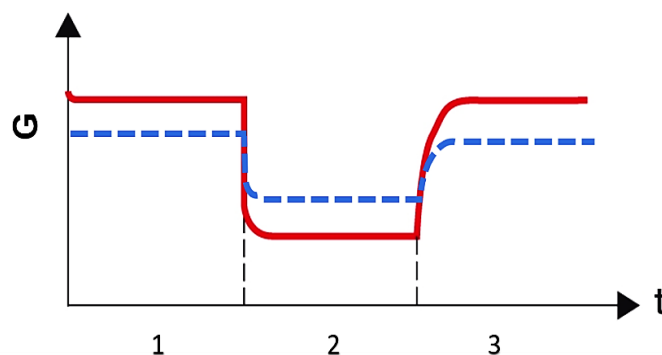


**Figure 1.18** Typical result of a thixotropy test with three intervals for a gel sample, depicted as a time-dependent  $G$  function.  $G'$  modulus is the red line and  $G''$  the blue line. (1) at the beginning, the sample

is at rest ( $G' > G''$ ), (2) structural breakdown is induced by high shear ( $G'' > G'$ ); (3) gel structural recovery at rest ( $G'$  exceeding  $G''$  again). The example shows a material with complete regeneration.

If a material can completely recover over time the mechanical properties of the initial state after the deformation step, it can be considered thixotropic. Interval 2 and 3 can be repeated several times to test the material ability to reconstruct the network after multiple breaks.

#### 1.4.4 Time sweep test

Time sweep tests can be a useful tool to determine gelation kinetics. These tests are generally performed under constant shear conditions either at a constant shear rate or at a constant shear stress and storage modulus and loss modulus are monitored over time. The measuring temperature is kept constant, thus providing for isothermal conditions. A small stress/strain is usually applied at small frequencies to minimise the disturbing effect of the experimental conditions towards the gelation process.<sup>76</sup>

In a typical gelation curve, the viscous behaviour dominates the initial part of the experiment ( $G'' > G'$ ), the elastic behaviour dominates the final part ( $G' > G''$ )<sup>77</sup> and the intersection point represents the starting of the gelation process (**Figure 1.19**).

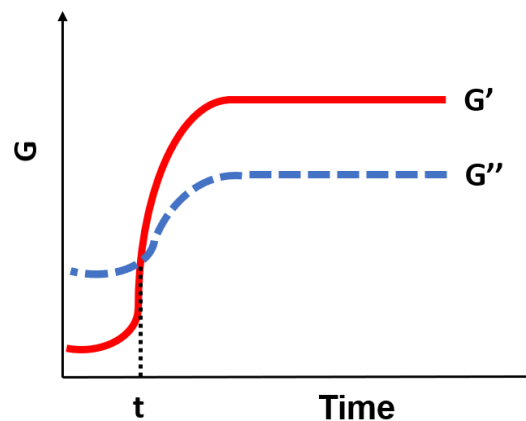


**Figure 1.19** Representation of a time sweep experiment of a gel. The intersection point where  $G'$  becomes higher than  $G''$  is marked as  $t$ .

## 1.5 Aim of the thesis

The overall aim of this Thesis is the preparation of supramolecular materials based on LMWGs. The first purpose is the synthesis of the gelators, performed through multistep procedures in solution and standard reactions of coupling, protection and deprotection. The gelators synthesised are based on pseudo-peptides and amino acids, sometimes coupled to long chain fatty acids. The attention is focused on derivatives of three aromatic amino acids, L-phenylalanine, L-tyrosine and L-DOPA, because the presence of aromatic groups introduces interactions favourable for the formation of supramolecular architectures.

After the purification and characterisation of the compounds, the conditions for the formation of supramolecular materials were investigated, varying the combination of gelator concentration, solvent and trigger. The formation of gels was first checked using the test tube inversion method. Then a full rheological characterisation was carried out, in order to determine the viscoelastic properties of each sample. The morphological analyses were performed to have a better understanding on the fibre network arrangement and dimensions. Starting from this first characterisation and from knowledge of the intrinsic features of the gel (functional groups on the molecule, final pH, solvent nature), the selected materials were functionalised for different applications.

Chapter 2 will describe organogels and hydrogels for water remediation (dye absorption and photodegradation). Chapter 3 will present a library of gels functionalised with graphene to improve the mechanical properties. In Chapter 4, composite materials will be prepared. The focus will be on the interactions between the organic phase (gels) and the inorganic mineral phase (crystals). Chapter 5 also describes gels which evolve from the gel to the crystal phase over time. These metastable materials undergo gel-to-crystal transitions with kinetics depending on trigger concentration. These gels will be also studied in combination with a gelator forming stable gels, for the preparation of multicomponent systems.

Finally, in Chapter 6, some molecules based on L-DOPA, which are unable to form gels, will be studied as underwater adhesives.

## Chapter 2

---

### 2. LMW gels for water decontamination

#### 2.1 Dye absorption into self-assembled gels

Water pollution is one of the most important unsolved contemporary problems affecting society. Massive industrialisation and world population growth have seriously affected water quality because of the release into the environment of several types of pollutants, such as pesticides, fertilizers, pharmaceuticals, dyes and heavy metals.<sup>78</sup> Dye pollution deriving from several types of industry (textile, paint, food, printing, plastics, rubbers, paper, cosmetics) is a concerning problem for aquatic environment. Most dyes are non-biodegradable and even at low concentrations have potential toxic effects, affecting aquatic life and the food chain. Many chemicals responsible for water contamination are organic pollutants, especially benzene derivatives and polycyclic aromatic hydrocarbons, as reported in the Contaminant Candidate List.

The adsorption of dissolved organic/inorganic pollutants from water onto solid materials has been widely investigated, due to simplicity, low-cost and ease of operation of this methodology. However, the limitations of this approach, such as lack of selectivity, generation of large amounts of toxic sludge and regeneration costs, underline the need to find more efficient materials and strategies.<sup>79,80</sup>

Supramolecular self-assembled gels based on LMWGs are colloidal soft matter systems, usually consisting of a nanostructured (or microstructured) solid-like network within a liquid-like medium. Being highly solvated yet having the rheological properties of solid-phase materials on analytical timescales, they can be potentially manipulated as solids, at the same time bringing their structures into intimate contact with environmental liquid phases in which the dye is dissolved. These materials possess high surface area and porosity and rapid internal diffusion kinetics, which potentially contribute to interactions with the solvated dye molecules. Moreover, these materials, relying on non-covalent interactions, are often reversible, an essential feature for recycling, reuse and eventually dye recovery. All these characteristics made

LMW gels a deeply investigated class of materials for the purification of water contaminated with dyes, but also with oil and solvent spills, heavy metals and toxic anions (**Figure 2.1**).<sup>81</sup>

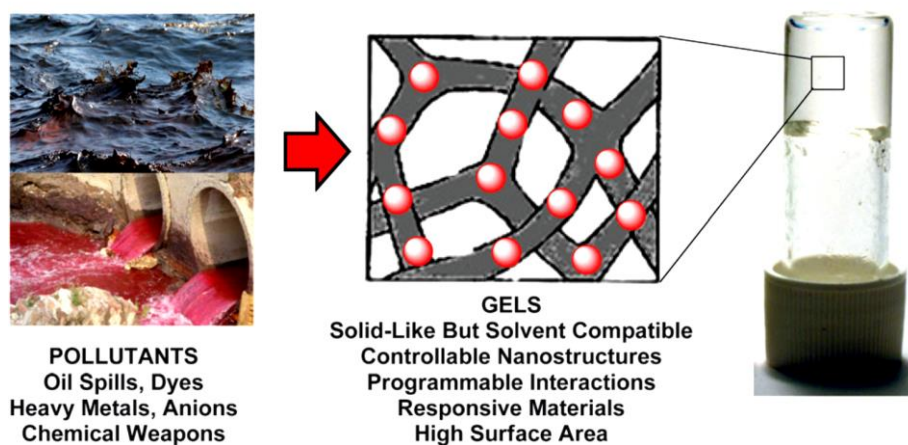


**Figure 2.1** Self-assembled gel for environmental remediation. Adapted from ref.<sup>81</sup>

A number of possible mechanisms has been proposed to be responsible for the absorption of dyes inside these supramolecular systems, such as intercalations into the self-assembled fibres or acid-base interactions,<sup>82,83</sup> hydrophobic<sup>84,85</sup> or ionic interactions, between cationic dyes and negatively charged gelators or viceversa.<sup>86</sup>

LMW gels have high potential in dye absorption and extraction, because their gelator structure may be readily tailored by insertion of particular functional groups to increase interactions and affinity with dye molecules and solvent to facilitate remediation of polluted water. Hydrogels, organogels and xerogels all have been reported for water remediation purposes. Hydrogels and xerogels are considered the most suitable for this application, because they prevent the introduction of potentially hazardous solvents.<sup>81</sup>

An optimised gel for water remediation should have (i) almost stoichiometric dye uptake, this meaning that almost every gelator molecule should participate in the interactions with the pollutant; (ii) fast absorption kinetics (in the scale of minutes); (iii) the possibility to be recycled and regenerated in a way that ideally grants not only its re-use but also the recovery of the dye in a form that allows a more appropriate disposal.<sup>81</sup>

Taking into account all these features, it is easy to understand the complexity of these materials and the further work that can be done to improve the performances of such systems.

### 2.1.1 Hydrogels with graphene oxide for dye absorption

In a previous work, Tomasini *et al.* showed that supramolecular hydrogels prepared from the dipeptide Fmoc-L-Phe-D-pGlu-OH (pGlu = pyroglutamic acid) and graphene oxide (GO) were able to trap dyes from water solutions with very high efficiency (**Figure 2.2**).<sup>87</sup> The absorption of aromatic dyes is favoured by several possible interactions between the pollutant and both GO and the gelator molecules, especially  $\pi$ - $\pi$  interactions between the aromatic rings, hydrogen bonds and electrostatic interactions with the hydrophilic groups. Even cation-anion interactions play a pivotal role in the absorption of dyes, since cationic methylene blue uptake was proven to be higher than the absorption of anionic eosin Y.

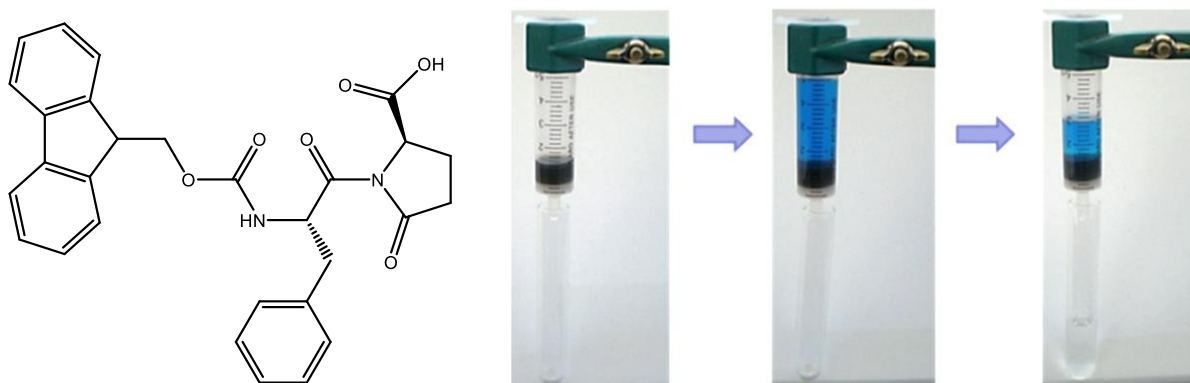


**Figure 2.2.** *Left.* Chemical structure of Fmoc-L-Phe-D-pGlu-OH. *Right.* Example of methylene blue solution in water flowing through a disposable plastic syringes loaded with GO-hydrogel: the recovered water is colourless. Adapted from ref.<sup>87</sup>

This gelator belongs to a group of foldamers containing the p-glutamic acid unit or the Oxd unit.<sup>88,89</sup> These two groups have been deeply investigated and largely used by Tomasini *et al.* and demonstrated to cause a local constraint in the pseudopeptide chain<sup>90-92</sup> favouring the formation of higher order structures such as fibres<sup>54,93,94</sup> and gels.<sup>55,70,95</sup> Taking into account the interesting results obtained with Fmoc-L-Phe-D-pGlu-OH hydrogels, it was decided to investigate the absorption of dyes inside organogelators.

### 2.1.2 Lau-L-Dopa(Bn)<sub>2</sub>-D-Oxd-OBn organogels

One of the main advantages of organogels obtained through ultrasound sonication is the fast formation of the network, within few minutes, in contrast to hydrogels prepared with the pH

change method which usually take several hours to gel.

During the last decades, Tomasini *et al.* synthesised a large family of LMWGs, especially dipeptides, focusing their attention on the role of the D-Oxd moiety compared to p-Glu or D-Pro (D-proline) moiety, on both the gelation process and the final properties of the materials.<sup>55,93,96</sup>

The first unit of these dipeptides is usually an aromatic amino acid, such as phenylalanine, tyrosine or Dopa usually protected on the N-terminus with a Fmoc group or long chain fatty acids (such as azelaic acid (Az)).<sup>3,36,45,97,98</sup>

After a deep investigation on phenylalanine derivatives, we decided to focus our attention on L-Dopa for forming materials, because the catechol aromatic ring allows functionalisation possibilities. Tomasini *et al.* started the synthesis and a first gelation study using this moiety in 2017,<sup>44</sup> comparing the properties of Fmoc-L-Dopa-D-Oxd-OH hydrogels with the corresponding L-Tyr and L-Phe derivatives (**Figure 2.3**).

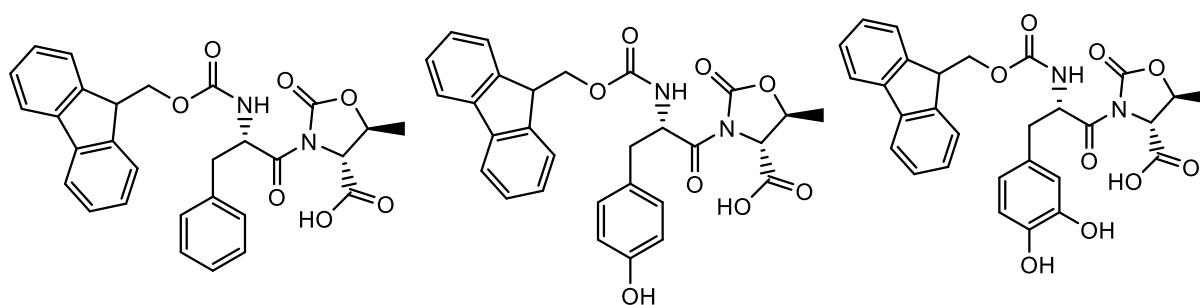


**Figure 2.3** Chemical structures of Fmoc-L-Phe-D-Oxd-OH, Fmoc-L-Tyr-D-Oxd-OH and Fmoc-L-Dopa-D-Oxd-OH (from left to right).

In this preliminary study, L-Dopa was used with the free catechol group to facilitate dissolution of the gelator in water for comparison with the other two moieties, but the resulting gels showed the poorest mechanical properties among all samples in terms of storage modulus  $G'$ .

We decided to synthesise a new gelator based on fully protected L-Dopa and D-Oxd moieties: the introduction of benzyl (Bn) protecting groups can provide additional  $\pi$ - $\pi$  stacking interactions between different gelator molecules. The Fmoc group on the N-terminus of the Dopa was replaced with lauric acid (Lau), a long chain fatty acid, which in general are suitable to form micelles, fibres and gels.<sup>99-101</sup> The final structure of the gelator for tests of organogels formation is Lau-L-Dopa(Bn)<sub>2</sub>-D-Oxd-OBn (**Figure 2.4**).

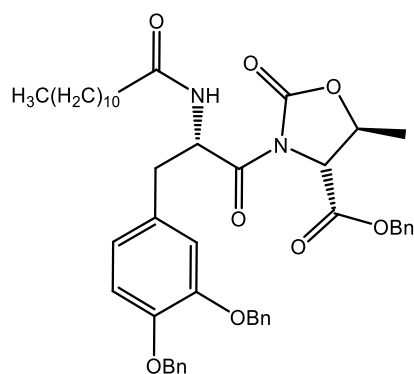
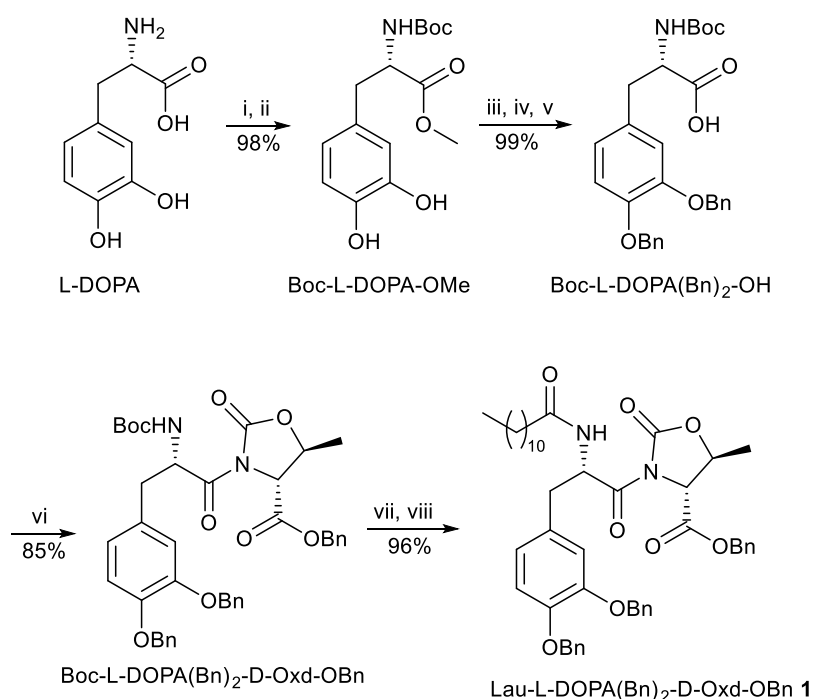


**Figure 2.4** Chemical structure of Lau-L-Dopa(Bn)<sub>2</sub>-D-Oxd-OBn.

Gelator Lau-L-Dopa(Bn)<sub>2</sub>-D-Oxd-OBn (**1**) was prepared by modification of the already reported procedure for the preparation of Fmoc-L-Dopa(Bn)<sub>2</sub>-D-Oxd-OBn,<sup>98</sup> starting from commercially available L-Dopa that was transformed into Boc-L-Dopa(Bn)<sub>2</sub>-OH<sup>102,103</sup> in four steps in a multigram scale with excellent yields. After coupling with the D-Oxd moiety, the Boc group was replaced with the lauric acid (**Scheme 2.1**).



**Scheme 2.1** Reagents and conditions for the synthesis of **1**: (i) SOCl<sub>2</sub> (excess), MeOH, 0 °C, 24 h; (ii) Boc<sub>2</sub>O (2 equiv.), NaHCO<sub>3</sub> (2 equiv.), THF/H<sub>2</sub>O, r.t., 18 h; (iii) BnBr (2.2 equiv.), K<sub>2</sub>CO<sub>3</sub> (2.2 equiv.), TBAB (0.2 equiv.), NaI (0.2 equiv.), acetone, reflux, 4 h; (iv) 1M NaOH, MeOH/THF, r.t., 18 h; (v) 1M HCl; (vi) D-Oxd-OBn (1 equiv.), HBTU (1.1 equiv.), DIEA (2 equiv.), ACN, r.t., 4 h; (vii) TFA (18 equiv.), CH<sub>2</sub>Cl<sub>2</sub>, r.t., 4 h; (viii) lauric acid (1 eq.), HBTU (1.1 eq.), DIEA (2.2 eq.), ACN, r.t. 3 h.

Gelator **1** was obtained pure as a white solid in 67% overall yield from L-Dopa.

The ability of **1** to form organogels was tested in several organic solvents and different conditions and then compared with Fmoc-L-Dopa(Bn)<sub>2</sub>-D-Oxd-OBn. Interestingly, the Fmoc analogue never formed organogels, in any solvent or condition. This comparison confirms the importance of lauric acid in the formation of supramolecular structures, probably due to the tendency of saturated long chain to stick together, producing micelles and fibres.<sup>104–106</sup> The final general procedure for the preparation of gels of **1** consisted in the dissolution of the gelator into an organic solvent (1.0% or 2.0% w/w concentration) followed by the sonication of the mixture for a time ranging between 15 and 30 minutes, to find out the best conditions to form the gels. With 1.0% w/w gelator concentration no gel was formed. After several attempts, the best operating condition includes 20 mg of gelator placed in a test tube with 1 mL of organic solvent (2.0% w/w concentration) and dissolved through sonication for 20 minutes. After this time the gels, already formed, are left to stand quiescently for 16 h. The formation of hydrogels with gelator **1** failed even after 30 minutes of sonication, because the molecule is not soluble in water. In **Figure 2.5** it is possible to see the gels obtained from different organic solvents.<sup>107</sup>



**Figure 2.5** Photographs of the organogels obtained using a 2% w/w concentration of gelator **1** in the following solvents (from left to right): toluene, ethyl acetate, acetonitrile, ethanol, methanol.

The formation of self-assembled LMW gels is the result of a well-balanced combination between gelator-solvent and gelator-gelator interactions. It is not easy to understand why a specific gelator can form gels only with a solvent among several, and why the properties of the same gelator in two similar solvents can be totally different. As reported in Chapter 1, the interactions involved in the formation of a self-assembled gel may be significant and have effects on the properties of final materials. It is well known that a polar gelator can only gel low polarity liquids because it will dissolve in polar liquids. Conversely, a non-polar gelator can only gel polar liquids. Therefore, when the number of carbon atoms of the gelator is increased,

as in this case with the introduction of the long alkyl chain of lauric acid, the gelator becomes hydrophobic and less polar, so it can gel more polar liquids.<sup>108</sup> However, the polarity by itself is not enough to explain the reason why a gel forms or not into a particular solvent. The solubility of the molecule in each solvent, which may not be strictly correlated to polarity, is probably another essential parameter influencing the formation and properties of these gels.<sup>109,110</sup>

To select the best gelator concentration, we performed a rheological analysis on three gels, each containing the gelator in 1.5%, 2.0% and 3.0% w/w concentrations, because with 1.0% w/w no gels were formed. The frequency sweep of ethanol organogels are reported as example of this study (**Figure 2.6**). From the comparison, the  $G'$  modulus deeply increases moving from 1.5% to the 2.0% w/w concentration; in contrast, no change in the frequency dependent behaviour is detected if the organogel concentration is further increased to 3.0% w/w. This is the reason why the 2.0% w/w gelator concentration was selected for further characterisations.

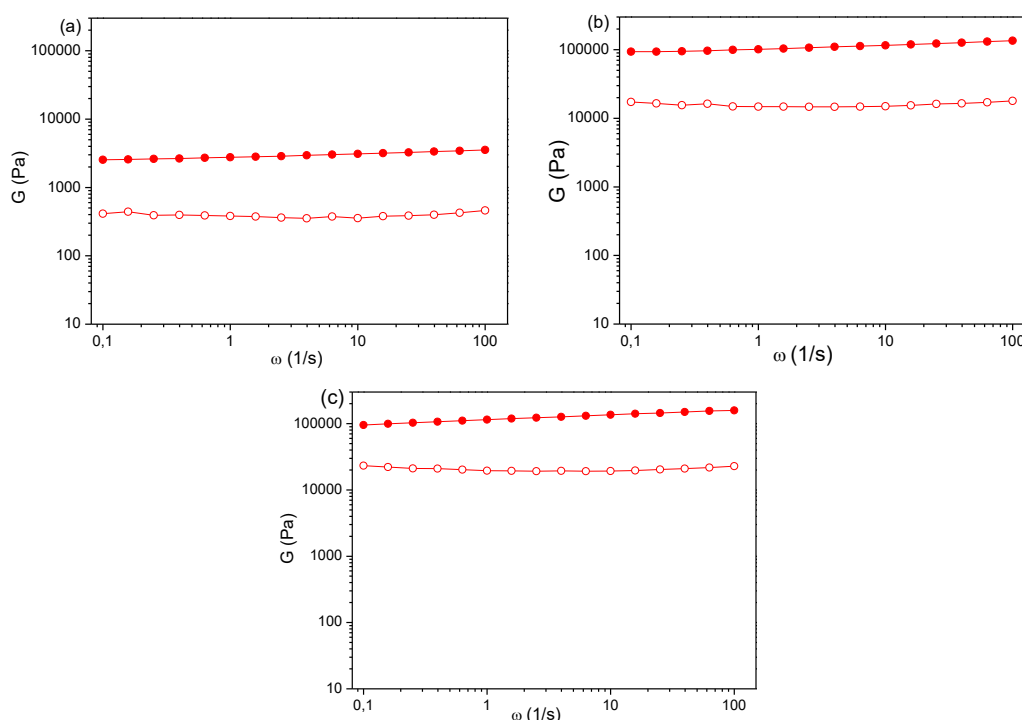


**Figure 2.6** Comparison of the Frequency Sweep experiments ( $\gamma = 0.04\%$ ,  $\omega = 1 \text{ s}^{-1}$ ) of Ethanol organogels: 1.5% concentration w/w (a), 2% concentration w/w (b) and 3% concentration w/w (c).

The properties of the gels obtained are listed in **Table 2.1** as a function of increasing polarity, from nonpolar toluene to polar methanol, using a scale where water is 100.<sup>111</sup> All measurements were repeated at least three times.

Usually the first test performed on a gel is the *dropping ball* test, to determine the melting temperature of the gel network ( $T_{gel}$ ) and have an idea of the stiffness of the material. Interestingly, for these organogels the  $T_{gel}$  was not strictly correlated to solvent boiling temperatures, meaning that the network type also has an influence. The melting points obtained with toluene, ethyl acetate and acetonitrile range between 40 and 50 °C. In contrast, a thermally stronger gel was obtained with the polar ethanol, while methanol produces a very weak organogel, probably due to a limited solubility of gelator **1** in the solvent.

**Table 2.1** Summary of the main characteristics of the organogels obtained using gelators **1** at 2% concentration in different solvents: gel melting point (m.p.) in comparison to solvent boiling point (b.p.),  $G'$  and  $G''$  from the frequency sweep tests ( $\omega = 1 \text{ s}^{-1}$  and  $\gamma = 0.04\%$ ). <sup>1</sup>Water is 100.

| Solvent       | Solvent polarity <sup>1</sup> | Solvent b.p. (°C) | Gel m.p. (°C) | $G'$ (KPa) | $G''$ (KPa) |
|---------------|-------------------------------|-------------------|---------------|------------|-------------|
| Toluene       | 9.9                           | 110.6             | 40-41         | 10         | 1.5         |
| Ethyl acetate | 23                            | 77                | 40-43         | 19         | 2.9         |
| Acetonitrile  | 46                            | 81.6              | 42-45         | 56         | 12.2        |
| Ethanol       | 65.4                          | 78.5              | 60-65         | 82         | 19          |
| Methanol      | 76.2                          | 64.6              | 25-28         | 2.3        | 0.3         |

After these preliminary tests, a wider rheological analysis was performed (amplitude sweep, frequency sweep and step-strain experiments), in order to characterise the viscoelastic behaviour of the five organogels. From the amplitude sweep analyses (**Figure 2.7**),  $\gamma = 0.04\%$  (within the LVE range for all these organogels) was chosen for the following frequency sweep tests. All analyses were performed at 23 °C.

Good rheological properties are usually associated with high  $T_{gel}$ .<sup>95</sup> For these samples the stiffness nicely correlates with the melting points temperatures (**Table 2.1**), confirming that ethanol provides the gel with the strongest network ( $G' = 82 \text{ KPa}$ ).

All the organogels tested are characterized by a “solid-like” behaviour, i.e. the storage modulus  $G'$  is approximately an order of magnitude higher than the loss component  $G''$ .

The complete rheological characterisation is reported in the following graphs: amplitude sweep (Figure 2.7), frequency sweep (Figure 2.8), step-strain experiments (Figure 2.9). The mechanical and rheological properties of the organogels demonstrated solvent-dependent properties.

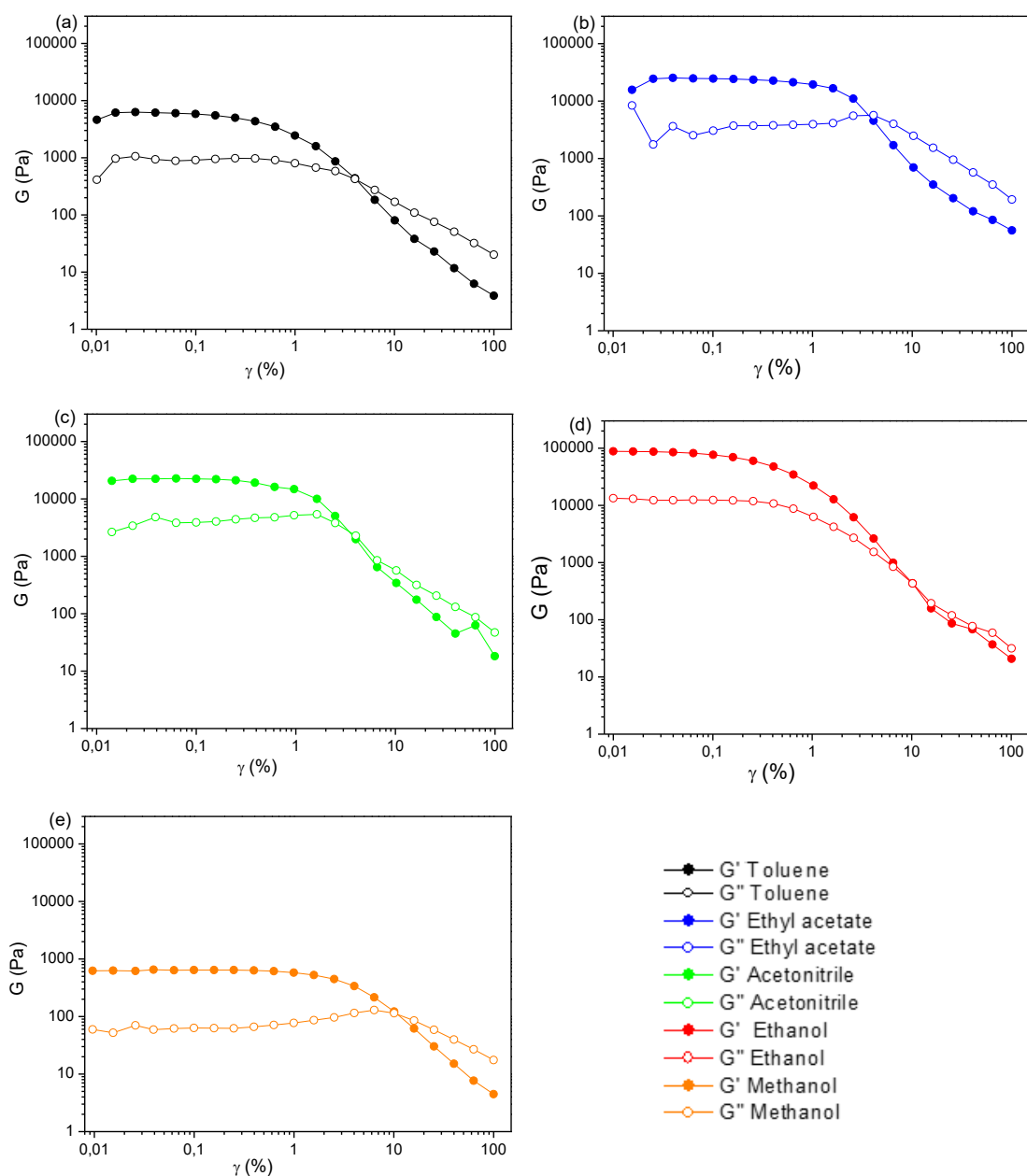


**Figure 2.7** Amplitude Sweep experiments of the organogels made with the 2% w/w concentration of gelator **1** in the solvents listed by increasing polarity: (a) toluene (black); (b) ethyl acetate (blue); (c) acetonitrile (green); (d) ethanol (red); (e) methanol (orange). The analyses were performed on the gels

about 20 hours after the gelation begun. (Storage modulus (solid circles) and loss modulus (empty circles)).

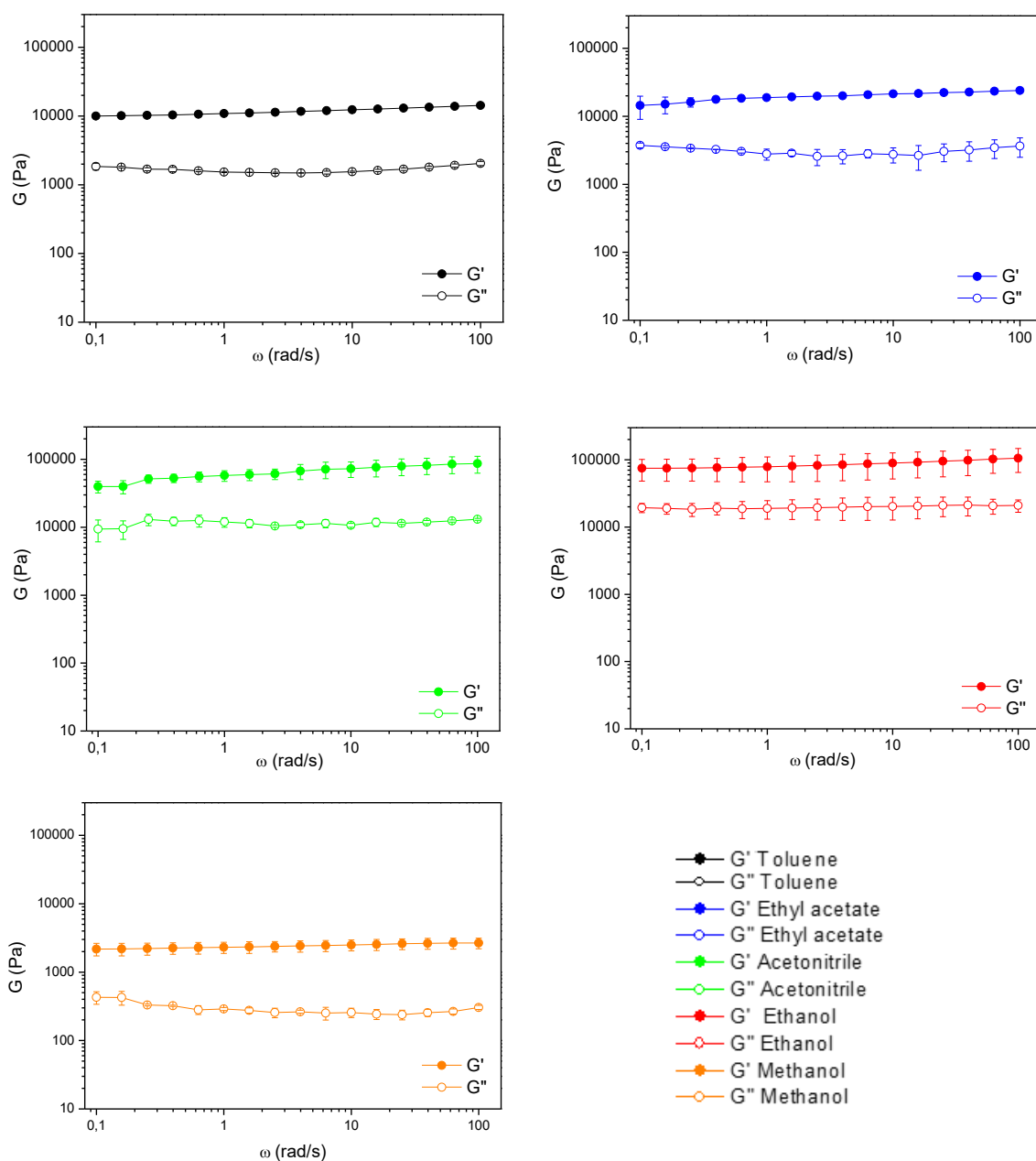


**Figure 2.8** Frequency sweep experiments performed on the organogels of **1**. The legend is the same of Amplitude Sweep experiments. The measures have been all repeated at least three times (the mean measurements and the standard deviation bars are shown in the graphs).

As reported in Chapter 1 (**1.4 Gel characterisation**), thixotropy<sup>112–115</sup> is a gel property related to the sol/gel equilibrium and describes the system ability to recover the gel status after a strong

stress that induces transformation into a solution. Moreover, self-healing property<sup>72,116–119</sup> may be defined as the ability to autonomously reconstruct the bonding interactions after damage.

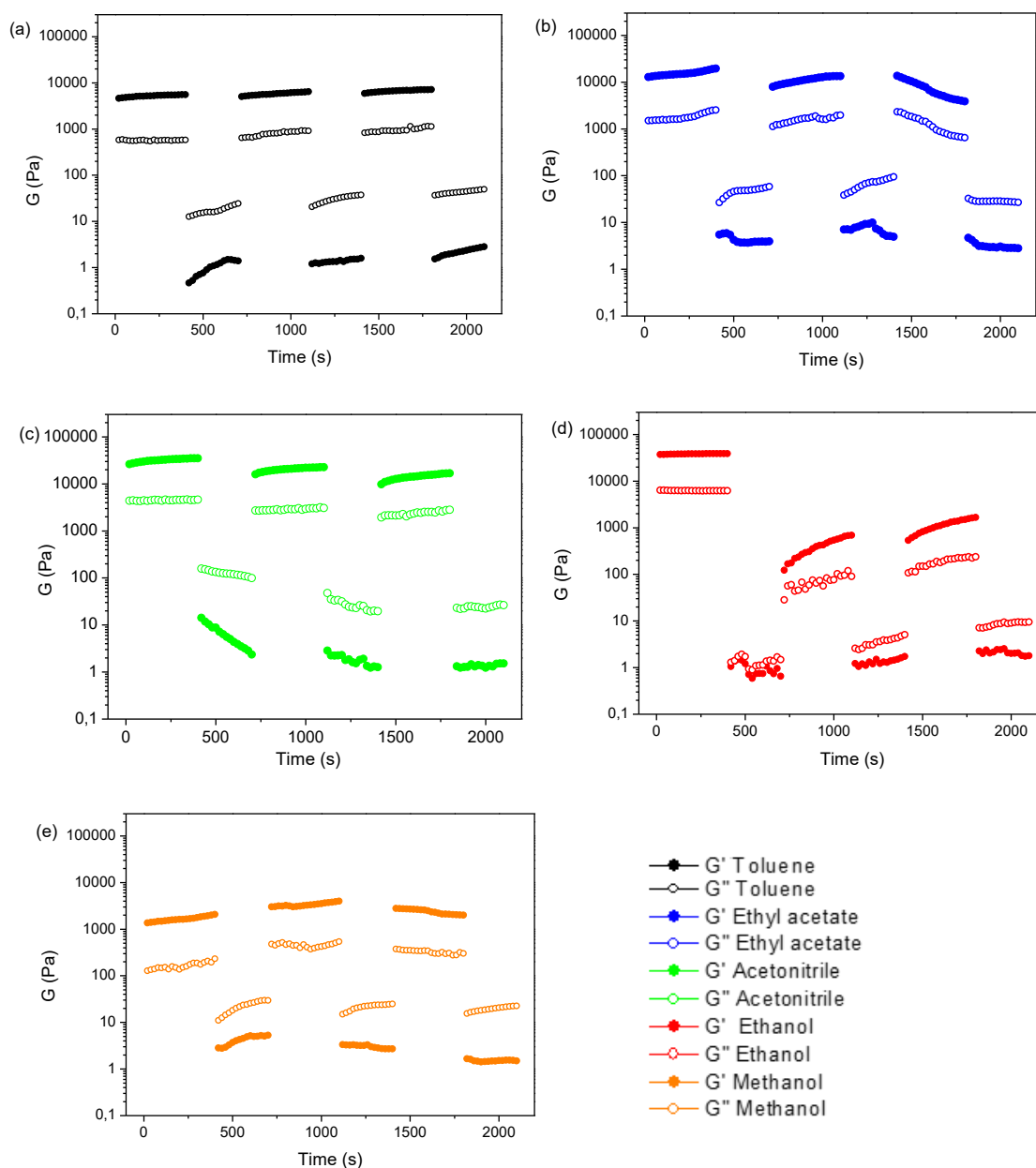


**Figure 2.9** Values of storage moduli  $G'$  (solid circles) and loss moduli  $G''$  (empty circles) recorded during step strain experiments performed on organogels in the solvent listed by increasing polarity: (a) toluene; (b) ethyl acetate; (c) acetonitrile; (d) ethanol; (e) methanol.

Three cycles of two steps were applied to the gels. During the first step, the sample was subjected to a strain value within the LVE region and was characterized by  $G'$  values greater than  $G''$  (gel-like behaviour). When the applied strain was increased above the crossover point

(second step), the sample behaviour switched from gel-like to sol-like, with  $G''$  values greater than  $G'$ . When the cycle is repeated (third interval of the graphs) the sample was left at fixed strain within the LVE range to check the recovery of the gel-like behaviour. Unfortunately, the ethanol organogel, which is the stiffer between all sample, has the poorest thixotropic properties, as its  $G'$  modulus is highly reduced when it recovers after the strain above the crossover point. The same inconvenient does not occur for the other organogels that promptly recover their properties, demonstrating thixotropic properties.

To have a preliminary test of the organogels ability to absorb pollutants,<sup>120,121</sup> we used Rhodamine B (RhB) as model molecule. RhB (**Figure 2.10**) is a model refractory organic dye pollutant containing four *N*-ethyl groups at either side of the xantheno ring, was chosen as the target pollutant, being an important representative of xantheno dye, widely used as a colorant in textiles and food stuffs, and also a well-known water tracer fluorescent.<sup>122</sup>

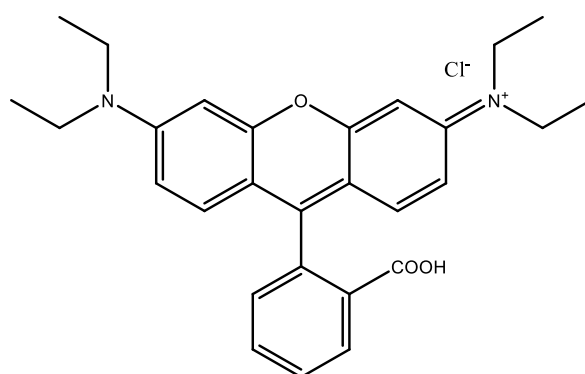


**Figure 2.10** Chemical structure of Rhodamine B.

Samples of the ethanol organogel were treated with 1 mL of an aqueous solution of RhB (2  $\mu$ M) for 24 hours (ratio gelator/RhB =  $12,9 \cdot 10^3$ ). The water solution did not mix with the gel and slowly lost its pink colour that moved to the gel (**Figure 2.11**). To quantify the amount of RhB absorbed inside the gel, the aqueous RhB solution on the top of the gel was transferred after 24 h treatment in disposable cuvettes with optical path length of 1.0 cm. Fluorescence spectra were collected with a Fluoromax-4 spectrofluorometer Horiba Jobin Yvon (emission spectra:  $\lambda_{exc} = 550$  nm;  $\lambda_{em}: 560-700$  nm). The emission spectrum of the water solution was measured after the treatment with the ethanol organogels and compared with a fresh sample of the aqueous solution of RhB. Under these experimental conditions, fluorescence intensity is proportional to the fluorophore concentration.<sup>123,124</sup>



**Figure 2.11** *Left.* Graphical representation of RhB absorption process inside the ethanol organogel. *Right.* Photograph of a fresh sample of the aqueous solution of RhB, of the same aqueous sample after treatment with the ethanol organogel, and of the organogel after 24 hours (from left to right).

After 24 hours of absorption, the spectrum intensity (and so RhB concentration in water) is reduced to the 23% of the original sample, thus confirming that the molecule is trapped into the organogels (**Figure 2.12**).

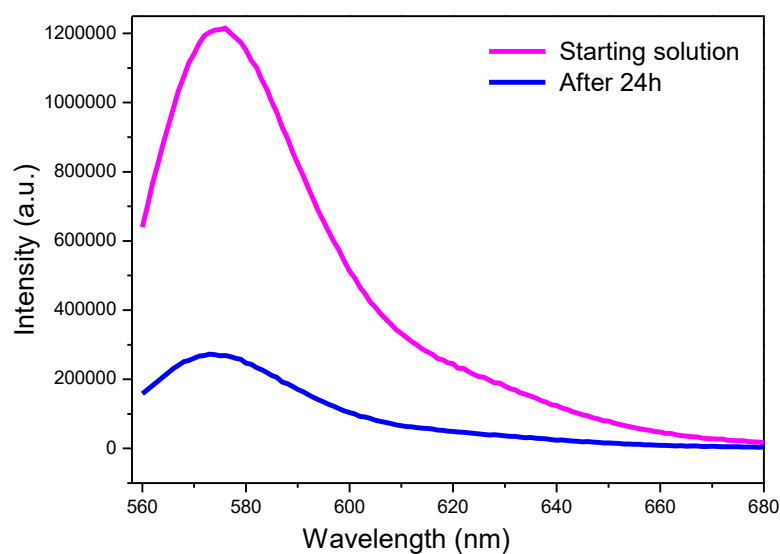


**Figure 2.12** Emission spectra of an aqueous solution of RhB (2.0  $\mu\text{M}$ ) (pink) and of the same solution after the treatment with the ethanol organogel for 24 hours (blue).

The analysis was also repeated after 48 hours and after 72 hours to check the absorption process over time, but no variation of the spectrum intensity of the sample was detected, meaning that the absorption ability reaches a plateau.

A drawback of organogels for environmental purposes is represented by the possible transfer of the organic solvent constituting the gel inside the water to remediate. Even though ethanol is not a hazardous solvent, the possible transfer of ethanol from the organogels to the aqueous solution was checked and quantified. After 24 h of contact between the aqueous RhB solution and the gel, the mols of water and ethanol were calculated using  $^1\text{H}$  NMR (Nuclear Magnetic Resonance) as a function of the corresponding peak intensities. Water/ethanol ratio was found to be 9.5:0.5, this meaning that a very small mixing of the two solvents occurs.<sup>107</sup> No variations were detected after 48 h and 72 h.

The decrease of the RhB amount from the aqueous solution was then confirmed to be only due to the absorption inside the gel and not to a hypothetical adsorption on the walls of the test tube during the 24 hours. The starting aqueous solution of RhB ( $2\ \mu\text{M}$ ) was placed inside one of the test tubes used for preparing the gels; after 24 h, the solution was transferred inside one of the fluorimeter disposable cuvette and the two spectra (starting solution and transferred solution) were compared (**Figure 2.13**). From the spectra it is possible to see that RhB is not lost during the experiment (transfer from test tube to cuvette, adsorption on the walls of the test tube).

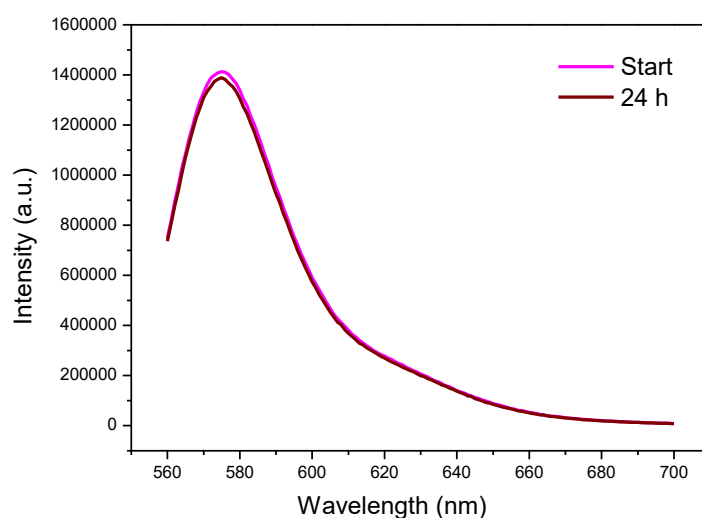


**Figure 2.13** Emission Spectra of the starting solution of RhB in water (pink) and of the solution transferred in the cuvette after 24 h inside the test tube (wine).

In conclusion, the new pseudopeptide Lau-L-Dopa(Bn)<sub>2</sub>-D-Oxd-OBn is able to form organogels in 2% w/w concentration. It can gel solvents of increasing polarity, as toluene, ethyl acetate, acetonitrile, ethanol and methanol. In contrast with Fmoc-L-Dopa(Bn)<sub>2</sub>-D-Oxd-OBn never formed organogel under any condition. This result suggests that the saturated long chain

of the lauric acid is crucial for the formation of the three-dimensional network. As the ethanol organogel proved to have the best rheological properties among all samples, it was treated with an aqueous solution of Rhodamine B, to have a preliminary test of its ability to adsorb pollutants from water. After 24 hours, the emission spectrum intensity of the Rhodamine B solution is reduced to the 23% of the original sample, thus confirming that the molecule is trapped into the organogel.

### 2.1.3 Materials and Methods

**Conditions for the Gel Formation** - All organogels were prepared in a concentration of 2% w/w under the following conditions. 20 mg of gelator (Lau-L-Dopa(Bn)<sub>2</sub>-D-Oxd-OBn) were placed in a test tube (8 mm of diameter) with 1 mL of organic solvent. The solution was stirred for 5 minutes and sonicated for 20 minutes in order to allow the complete dissolution of the sample and the formation of the organogel. All samples were allowed to stand quiescently for 16 hours before further characterization.

**Conditions for  $T_{gel}$  Determination** -  $T_{gel}$  was determined by placing a small glass ball (diameter: 5 mm, weight: 165 mg) inside the test tube (8 mm of diameter) containing the gel. When the gel is correctly formed, the ball is suspended on the top of it. The test tube is then gradually heated (2° C/min):  $T_{gel}$  is the temperature in which the ball penetrates inside the gel, because the network is dissolved. Some gel samples melt, producing a clear solution (and this was the behaviour of our organogels), while in other cases the gelator shrinks and the solvent is ejected, as syneresis occurs.

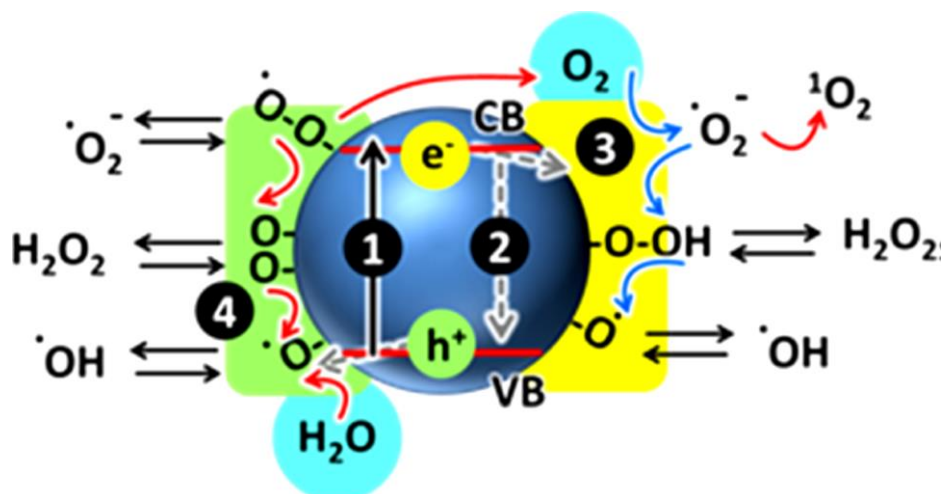
**Rheology** - Rheology experiments were carried out on an Anton Paar Rheometer MCR 102 using a parallel plate configuration (25 mm diameter). Experiments were performed at constant temperature of 23 °C controlled by the integrated Peltier system. All the analysis (amplitude sweep, frequency sweep and thixotropy) were performed with fixed gap value of 0.5 mm. The samples were prepared the day before the analysis and left overnight at controlled temperature of 20 °C to complete the gelation process. Oscillatory amplitude sweep experiments ( $\gamma$ : 0.01–100%) were carried out at fixed frequency of 10 rad·s<sup>-1</sup>, in order to determine the LVE range and the crossover point of the gels ( $G'' > G'$ ). Once established the LVE of each organogel, frequency sweep tests were performed ( $\omega$ : 0.1-100 rad·s<sup>-1</sup>) at constant strain within the LVE

region of each sample ( $\gamma = 0.04\%$ ). To verify the thixotropic properties of the samples, strain values within the crossover point region (for 400 s) and over the crossover point region (for 300 s) were consecutively applied to the organogels, for three cycles. The values of the applied strain were selected on the basis of the crossover point value obtained from amplitude sweep experiment (within the crossover point:  $\gamma = 0.04\%$ ,  $\omega = 10 \text{ s}^{-1}$ ; over the crossover point:  $\gamma = 100\%$ ,  $\omega = 10 \text{ s}^{-1}$ ).

## 2.2 Light penetrating hydrogels for dyes photo-degradation

An important achievement in the realisation of novel materials for water remediation is the possibility of trapping a pollutant inside the matrix, to remove it from the environment and degrade it into benign species.

In the last years, researchers have been focused on the design of novel photo-catalysts (PC) able to exploit solar light to convert pollutants into non-toxic derivatives. The use of photo-catalyst for the degradation of water pollutants is an eco-friendly approach, typically based on the use of a nanostructured PC, which is activated by solar light and uses the absorbed energy to produce reactive species starting from water and oxygen (Scheme 2.2).<sup>125</sup>



**Scheme 2.2** Reactive oxygen species generated in the photocatalytic reduction and oxidation steps of oxygen and water. Absorption of light (1) causes the transition of electrons to the conduction band and the formation of holes in the valence band. Part of the produced charges undergo recombination (2), whereas others migrate to the surface where trapped electrons (3) participate in the reductive steps (blue arrows) and trapped holes (4) in the oxidative processes.<sup>126</sup>

Most effective PCs are metal oxide semiconductors (such as ZnO, FeO<sub>3</sub>, WO<sub>3</sub>).<sup>127</sup> In particular, titanium dioxide nanoparticles (TiO<sub>2</sub>-NPs), in their anatase form, have been widely used for a range of applications, including self-cleaning,<sup>127</sup> surfaces sterilization,<sup>128</sup> air<sup>129</sup> and water<sup>130</sup> purification. Some of the main advantages of the use of TiO<sub>2</sub>-NPs are the excellent stability in water, large scale availability and low cost of production. TiO<sub>2</sub>-NPs also show low toxicity,<sup>131,132</sup> nevertheless recent concerns about the still partially unpredictable risks related to the impact of nanomaterials to the environment and human health suggested, as a defensive approach, to minimize their dispersion in the environment.<sup>133,134</sup> Hence, the fundamental challenge consists in the incorporation of TiO<sub>2</sub>-NPs in highly biocompatible and macroscopic matrixes that preserve the photocatalytic activity of the semiconductor NPs. These matrixes should present some fundamental features such as: a high-water content, since water plays an essential role in the photocatalytic process (see **Scheme 2.2**), a good permeability to small molecules (pollutants) and a good transparency to solar light.

We already spoke about the first two features in LMW hydrogels: they can be made up to 99.5% of water and we reported some examples of gels with high performances in dye absorption.<sup>87</sup> Regarding the transparency, Tomasini *et al.* recently reported the preparation of a highly transparent hydrogel (**Figure 2.14**) made with 0.5% w/w of Fmoc-L-Tyr-D-Oxd-OH (**2**) using the pH change method.<sup>135</sup> The transparency was quantified measuring the transmittance of the samples, that will be better discussed in the next section (**2.2.2 Photodegradation experiments**).

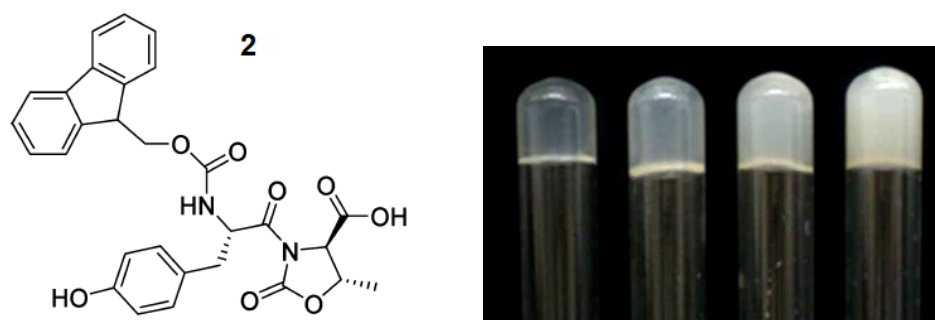


**Figure 2.14** Structure of gelator **2** and picture of the hydrogels prepared with different concentration (% w/w) of **2** in water (from left to right: 0.5, 1.0, 1.5 and 2.0).

In that work, the properties of this gel were compared with hydrogels formed with other dipeptide gelators (among them Fmoc-Phe-Phe)<sup>136,137</sup> and it resulted the most transparent among all. For this reason, we selected hydrogels of **2**, at 0.5% w/w concentration made through

the pH change method, as scaffold for the incorporation of the PC. As PC, we decided to compare TiO<sub>2</sub>-NPs with a preparation of TiO<sub>2</sub>-NPs in combination with graphene platelets, using once again as model pollutant compound Rhodamine B.

Upon UV irradiation. TiO<sub>2</sub>-NPs absorb in the UV part of the solar spectrum ( $\lambda < 380\text{nm}$ )<sup>138</sup> which is the band gap between the conduction band (CB) and the valence band (VB),<sup>132</sup> with  $\Delta E \approx 3.25\text{ eV}$  (**Scheme 2.2**). The integration of graphene in the photocatalytic TiO<sub>2</sub> platform was investigated, because carbon nanomaterials,<sup>139</sup> such as nanotubes,<sup>140</sup> carbon dots,<sup>141</sup> graphene oxide,<sup>142</sup> reduced graphene oxide,<sup>143</sup> have been reported to increase the photocatalytic performances of TiO<sub>2</sub>-NPs.

In contrast to other systems, in which TiO<sub>2</sub>-NPs<sup>144,145</sup> can be activated by exposure of the surface to sunlight (e.g. TiO<sub>2</sub> photocatalyst embedded in cementitious materials)<sup>127,146–148</sup> in our photocatalytic hydrogels light must penetrate into the matrix.

To achieve this outcome, a new real-time fluorescence-based method was developed, and used to investigate the photocatalytic activity inside the hydrogels. An original feature of this approach is that the photocatalyst irradiation and the target degradation detection can be performed simultaneously in a standard fluorimeter, as shown in **Figure 2.15**.

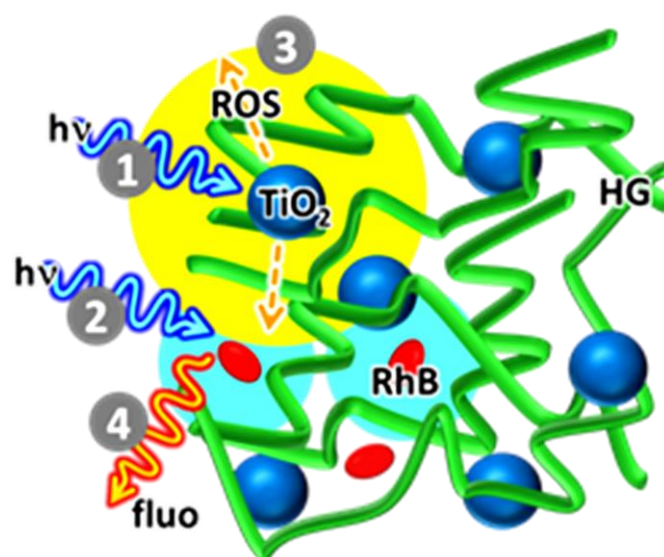
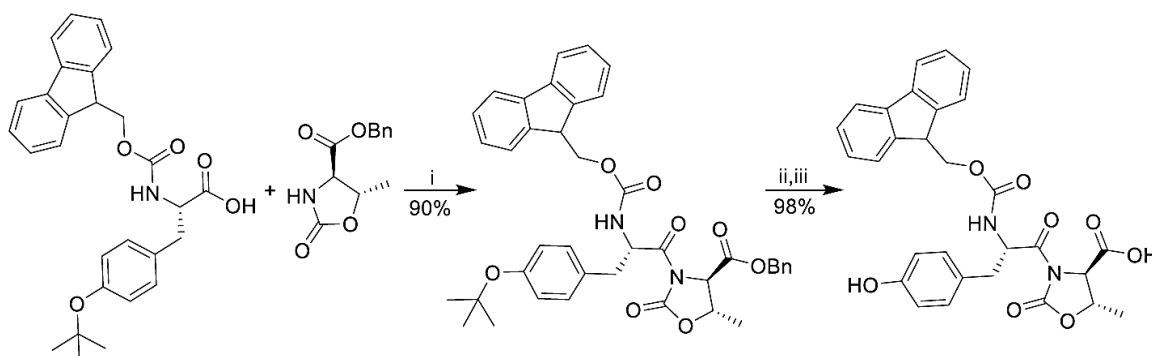


**Figure 2.15** Schematic representation of the TiO<sub>2</sub>-NPs incorporated in the hydrogel fibers formed by precursor **2** and of the photocatalytic process. UV photons (340 nm) are used for exciting both the photocatalysts NPs (1) and the target molecules RhB (2). Photogenerated reactive oxygen species (ROS) diffuse in the water solution (3) containing RhB causing its degradation which can be detected by fluorescence (4).

## 2.2.1 Hydrogels preparation and characterisation

Compound **2** was synthesised using an already reported procedure (Scheme 2.3).<sup>135</sup>



**Scheme 2.3** Reagents and conditions for the synthesis of gelator **2**: (i) HATU (1.1 equiv.), DIEA (2.5 equiv.), dry CH<sub>3</sub>CN, r.t., 2h; (ii) TFA (18 equiv.), dry DCM, r.t., 4h; (iii) H<sub>2</sub> (1atm), Pd/C (10% w/w), MeOH, r.t., 4h; (iv) HBTU (1.1 equiv.), DBU (2.2 equiv.), dry CH<sub>3</sub>CN, r.t., 2h.

After the purification and characterisation of compound **2**, three different samples of hydrogels (H) were prepared using the pH-change method: i) hydrogel **2H** contains only the gelator Fmoc-L-Tyr-D-Oxd-OH in 0.5% (w/w) concentration and GdL, the trigger; ii) hydrogel **2H-T** contains the gelator in 0.5% concentration, TiO<sub>2</sub>-NPs (0.2 mg/mL) and GdL; iii) **2H-TG** is prepared following the same procedure used for **2H-T**, but replacing TiO<sub>2</sub>-NPs with TiO<sub>2</sub>-NPs/graphene.<sup>87</sup> Considering that the solutions containing TiO<sub>2</sub> have a pH  $\approx$  1, we adopted the following procedure, to avoid the formation of non-homogeneous hydrogels: the gelator (0.5 % w/w) was placed in a test tube, then Milli-Q® water (1 mL) and aqueous 1 M NaOH (12  $\mu$ L) were added and the mixture stirred and sonicated in turn for about 10 minutes, until sample dissolution; 2.4 mg of GdL were added to all the samples under stirring; when the solution reached pH  $\approx$  6, we added the solution containing TiO<sub>2</sub> (for samples **2H-T**) and TiO<sub>2</sub>-graphene (for samples **2HT-G**) under stirring, followed by a rapid transfer into: cuvette (500  $\mu$ L) for photodegradation tests, vials (500  $\mu$ L) for the SEM (Scanning Electron Microscope) analysis or plate (700  $\mu$ L) for rheology analysis.

Before testing the photocatalytic activity of these matrices, the effect of TiO<sub>2</sub>-NPs or TiO<sub>2</sub>-NPs/graphene on the mechanical and morphological properties of the hydrogels was investigated. Rheological analyses have been performed to evaluate the viscoelastic properties of hydrogels **2H**, **2H-T** and **2H-TG** in terms of storage and loss moduli ( $G'$  and  $G''$

respectively). Although the hydrogels are characterized by a “solid-like” behaviour, i.e. the storage modulus is approximately an order of magnitude higher than the loss component (**Figure 2.16**), these hydrogels do not show very high  $G'$  values, due to the very low concentration of the gelator, required for obtaining good transparency. The results also pointed out that although the introduction of  $\text{TiO}_2$ -NPs or  $\text{TiO}_2$ -NPs/graphene does not inhibit the formation of the gels, it partially affects the mechanical properties of both hydrogels, for which in both cases  $G'$  decreased. This effect is more evident for hydrogel **2H-TG**. Nevertheless, frequency sweep analysis (**Figure 2.17**) pointed out that for all the obtained hydrogels both  $G'$  and  $G''$  were almost independent from the frequency in the range from 0.1 to 100  $\text{rad}\cdot\text{s}^{-1}$  (always with  $G' > G''$ ) confirming the “solid-like” rheological behaviour for the hydrogels and hence the stability of the hydrogel structure required for the photocatalytic application.

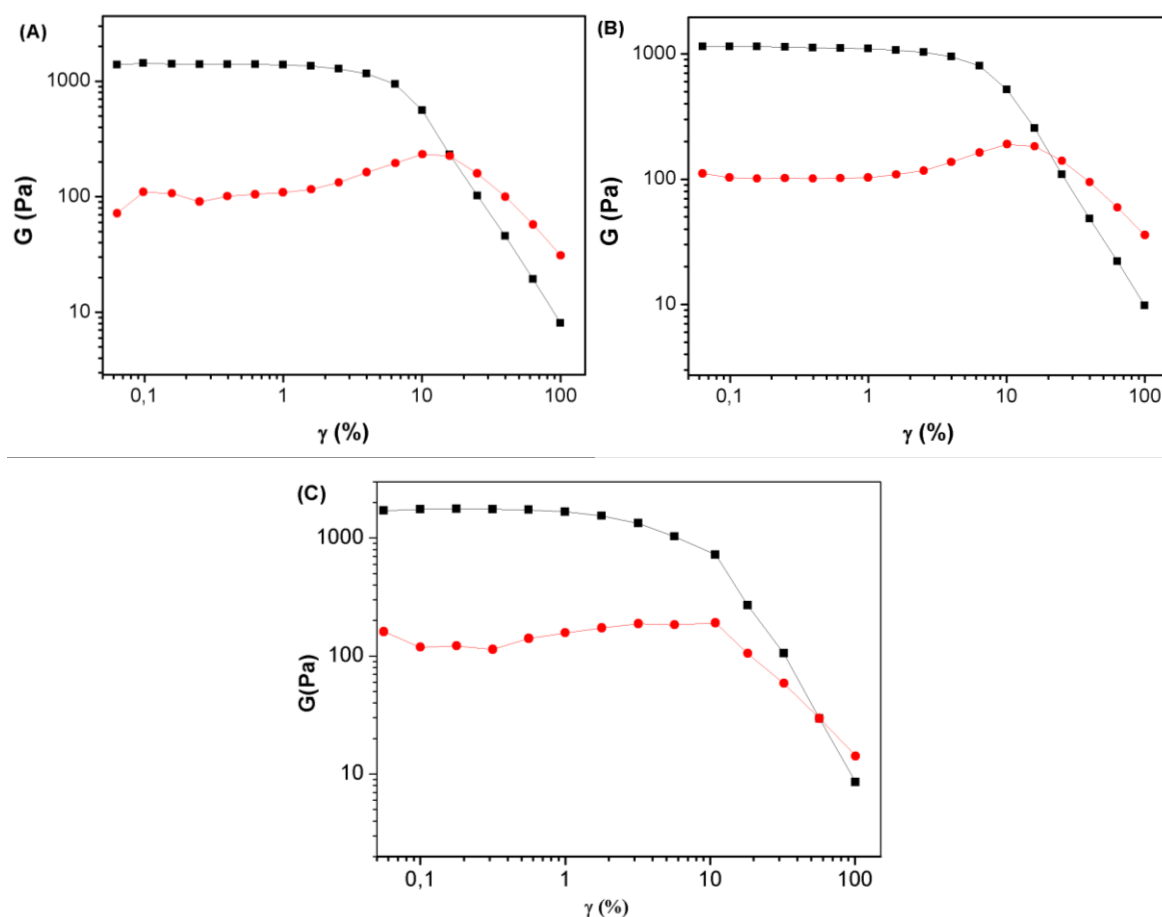


**Figure 2.16** Strain dependence of storage modulus (black square) and loss modulus (red circles) for: (A) hydrogel **2H**, (B) hydrogel **2H-T** and (C) hydrogel **2H-TG**. The analyses were performed on the gel about 20 hours after the gelation began.

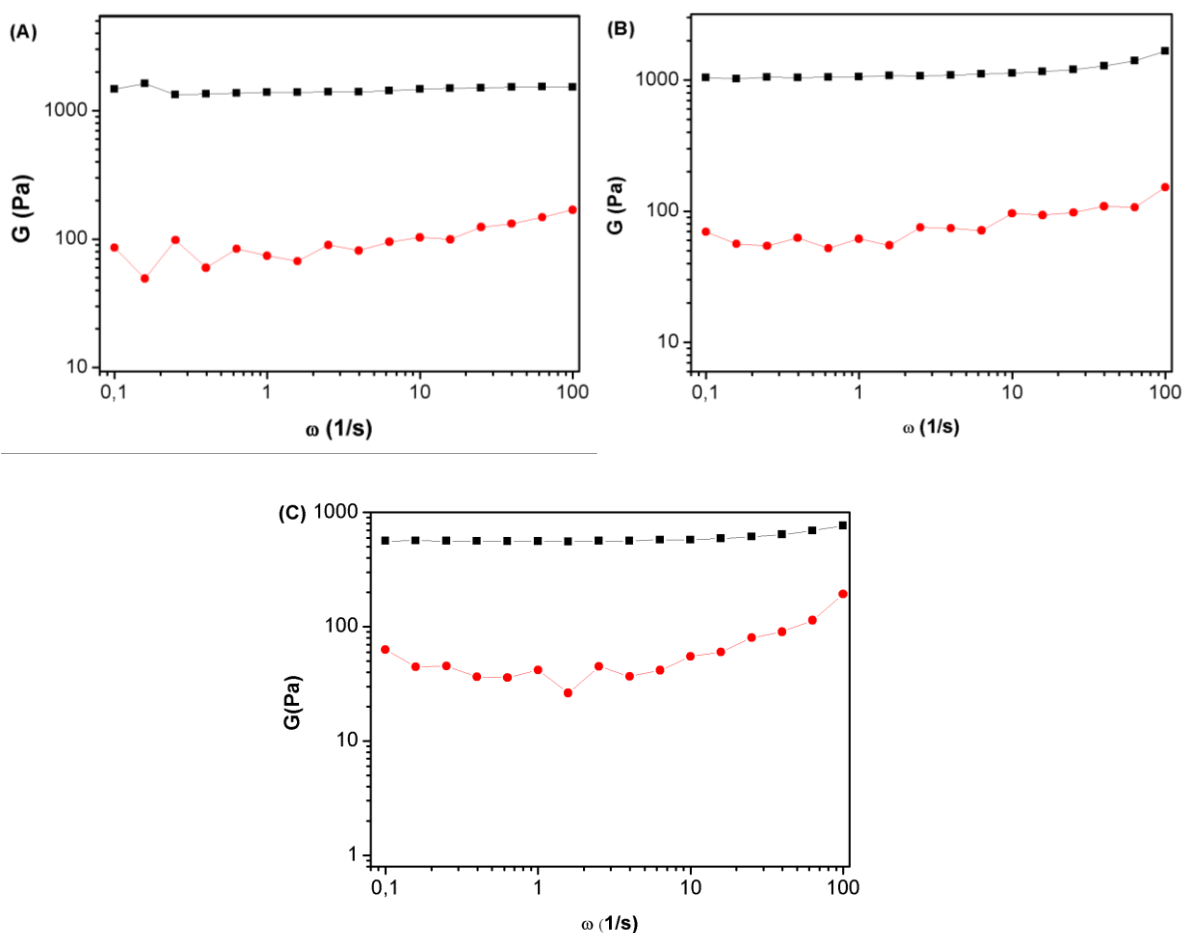


**Figure 2.17** Frequency dependence of storage modulus (square) and loss modulus (circles) for: (A) hydrogel **2H**, (B) hydrogel **2H-T** and (C) hydrogel **2H-TG**. The analyses were performed on the gel about 20 hours after the gelation begun.

**Table 2.2** Storage moduli ( $G'$ ) and loss moduli ( $G''$ ) of hydrogels **2H**, **2H-T** and **2H-TG** from frequency sweep ( $\omega = 0.5$  1/s).

| Hydrogel     | $G'$ (Pa) | $G''$ (Pa) |
|--------------|-----------|------------|
| <b>2H</b>    | 1370      | 90         |
| <b>2H-T</b>  | 1055      | 63         |
| <b>2H-TG</b> | 556       | 46         |

Step strain experiments were performed to check the thixotropic behaviour of **2H**, **2H-T** and **2H-TG** at the molecular level. Strain values within and above the LVE region were

consecutively applied to hydrogels (**Figure 2.18**), that lose their “solid-like” behaviour ( $G' < G''$ ) when the strain is applied above their LVE region and go back to a “solid-like” state ( $G' > G''$ ) if the strain is applied within the LVE region of hydrogels. The three hydrogels show a thixotropic behaviour, even though hydrogel **2H** shows a lower  $G'$  modulus every time the network is broken (strain above the LVE), this means that it is able to reconstruct the network but it is less stiff than the starting gel. Also with this analysis, we confirmed that graphene-doped hydrogels **2H-TG** show the lowest values of  $G'$  and  $G''$ .

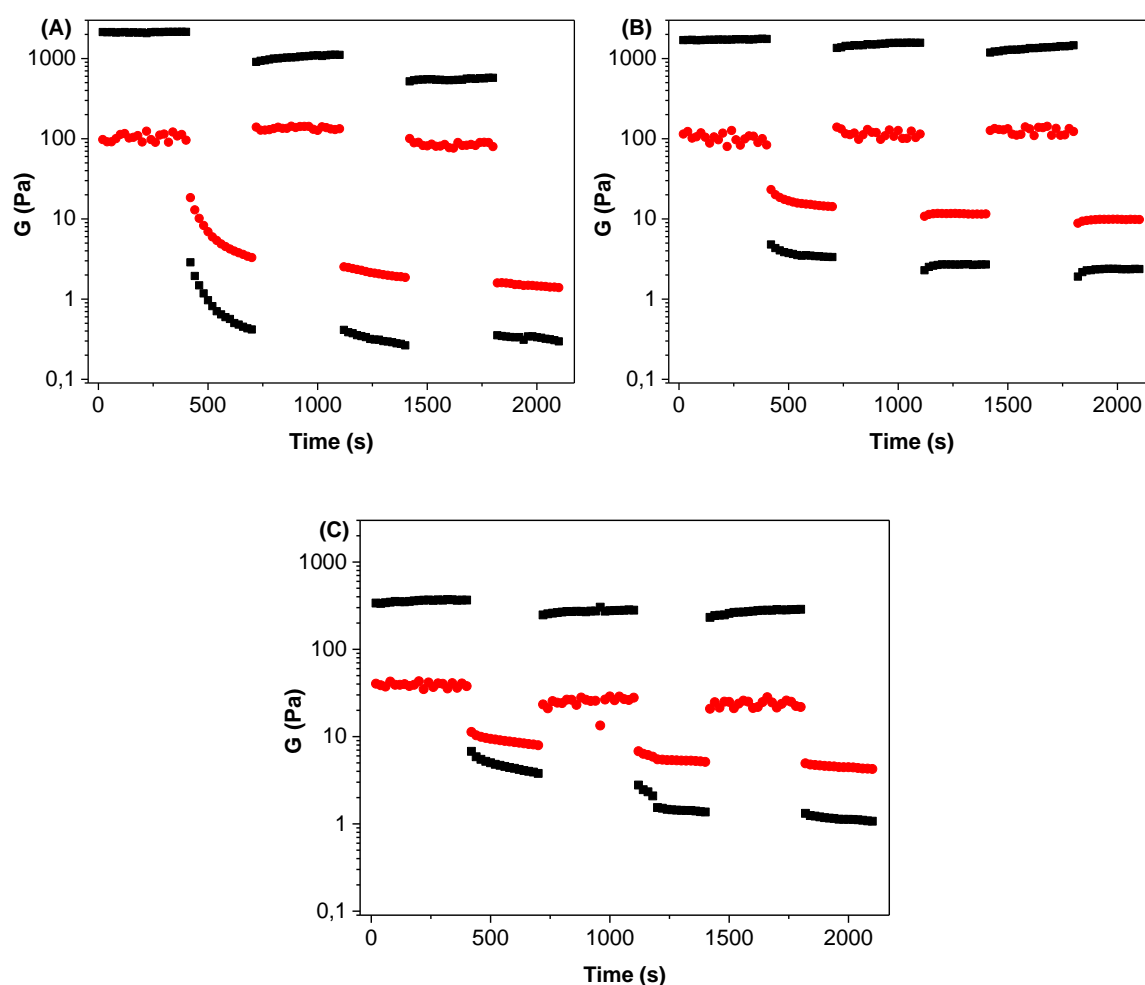


**Figure 2.18** Values of storage moduli  $G'$  (black) and loss moduli  $G''$  (red) recorded during a step strain experiment performed on (A) hydrogel **2H**, (B) hydrogel **2H-T** and (C) hydrogel **2H-TG**.

To have more information about the morphology of samples **2H**, **2H-T** and **2H-TG** we performed the SEM analysis on the freeze-dried samples. These aerogels show different morphologies, but they are all characterized by complex patterns with a rough orientation

(Figure 2.19). Moreover, in aerogel **2H-TG** we can notice the presence of some small aggregates (some of them even about 10  $\mu\text{m}$ ), responsible for the formation of a less homogeneous hydrogel, which can be one of the reason why the mechanical properties of the sample were the lowest from the rheological experiments.

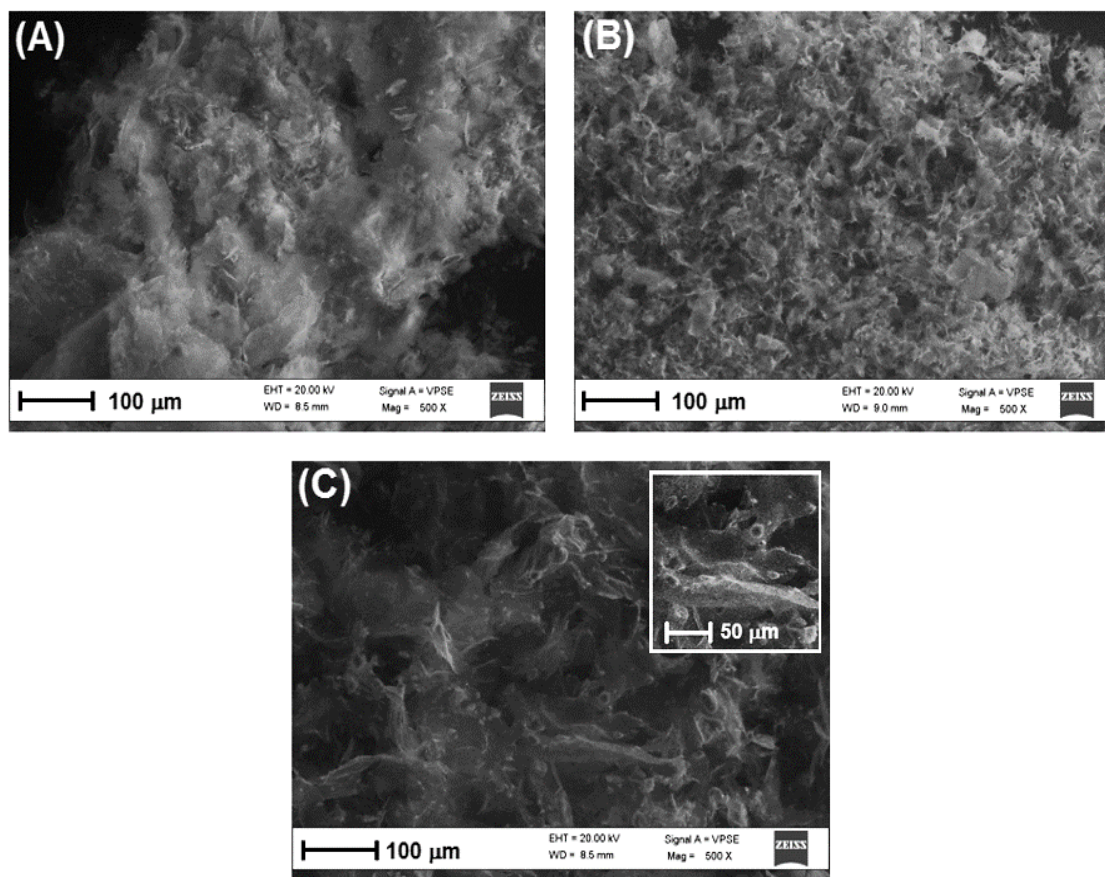


**Figure 2.19** (A) SEM image of a sample of aerogel obtained by freeze drying a sample of hydrogel **2H**. (B) SEM image of a sample of aerogel obtained by freeze drying a sample of hydrogel **2H-T**. (C) SEM image of a sample of aerogel obtained by freeze drying a sample of hydrogel **2H-TG** prepared with Fmoc-L-Tyr-D-Oxd-OH 0.5% concentration. In the inset: a magnification view of aerogel **2H-TG** fragment.

## 2.2.2 Photodegradation experiments

The experimental approach for the investigation of the photodegradation of a model pollutant such as RhB inside the gel is based on fluorescence detection. As a main difference with respect to other methods based on fluorescence, here the same excitation beam and the same excitation wavelength are used for both photoactivating the photo-catalyst ( $\text{TiO}_2$ ) and exciting the target

fluorophore RhB (**Figure 2.15**). As a main advantage this approach allows the continuous and real-time detection of the target dye concentration during the process using a conventional fluorimeter equipped with a 150 W Xenon lamp as an excitation source.

The absorption spectra of hydrogel **2H**, of TiO<sub>2</sub>-NPs (0.2 mg/ml) and RhB (1.0 μM) were analysed in a cuvette with 0.5 cm optical path to select a suitable irradiation wavelength (**Figure 2.20**). The spectra demonstrate that it is possible to excite simultaneously the TiO<sub>2</sub>-NPs and RhB upon irradiation in the UV spectral region when they are incorporated in the hydrogel (as sketched in **Figure 2.15**).

In fact, as foreseen, the hydrogel presents an edge of absorption around 310 nm, due to the characteristic absorption spectra of the Fmoc chromophore<sup>136</sup> that is present in the gelator structure<sup>132,149,150</sup> as protecting group of the Tyrosine N-terminus. The hydrogel transmittance is  $T > 60\%$  for wavelength  $\lambda > 320$  nm, hence the photocatalyst TiO<sub>2</sub>-NPs incorporated in the hydrogel can be efficiently excited at  $340 \pm 10$  nm using the fluorimeter excitation beam as an irradiation source (spectral profile shown in **Figure 2.20**).

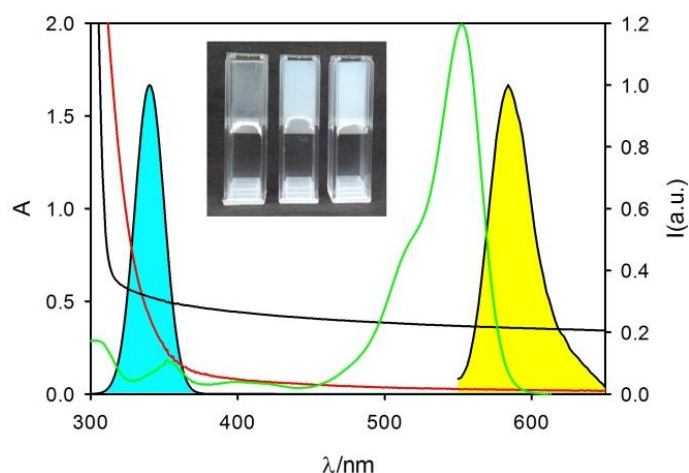


**Figure 2.20** Absorption spectrum of the hydrogel **2H** (black line) of the TiO<sub>2</sub> NPs (0.2 mg/ml, red line) and of RhB (x20, 1 μM, green line). Fluorescence spectrum of RhB (filled yellow) and spectrum of the irradiation source (filled cyan). Inset: photographs of samples of hydrogels **2H**, **2H-T**, **2H-TG** (from left to right respectively) prepared with gelator Fmoc-L-Tyr-D-Oxd-OH in 0.5% concentration.

Additionally, under the excitation conditions, RhB absorbs a minor fraction of the excitation light and the photo-degradation of this dye can be followed by its diagnostic fluorescence signal during the photocatalytic experiments. To investigate the TiO<sub>2</sub> photo-catalytic activity in the hydrogel, we prepared three samples similar to those previously described (**2H**, **2H-T** and **2H-**

**TG**), all containing a small concentration (1.0  $\mu\text{M}$ ) of RhB. For clarity, these sample will be referred to as **2HR**, **2HR-T** and **2HR-TG**. Hydrogel rheological properties were not affected by the presence of small concentrations of RhB (1.0  $\mu\text{M}$ ).

A conventional fluorometer with a L configuration was used to perform the simultaneous excitation and perpendicular detection of the fluorescence emission. Fluorescence signal of RhB was detected in real-time (5 sec integration) at  $\lambda_{\text{em}} = 585 \text{ nm}$  in the hydrogels containing the dye **2HR**, **2HR-T** and **2HR-TG** upon continuous irradiation at single wavelength light  $\lambda_{\text{exc}} = 340 \pm 10 \text{ nm}$ , and it was plotted as a function of irradiation time.

RhB undergoes a strong decrease in emission during the first hour of irradiation in case of hydrogel **2HR-T** and **2HR-TG**. In contrast, in the reference hydrogel **2HR**, which does not contain any photo-catalyst, the fluorescence signal decreases only by about 20% during the first 10 minutes (600 seconds), then it reaches a plateau.<sup>151,152</sup> Hence, as the fluorescence intensity is proportional to the fluorophore concentration in these experimental conditions,<sup>123,124</sup> we can gather that, after 60 minutes of irradiation, RhB concentration in the reference sample **2HR** is still 80% of the initial one, whereas the dye is completely degraded in sample **2HR-T** containing  $\text{TiO}_2$  and a residual 25% survived in **2HR-TG** (Figure 2.21).

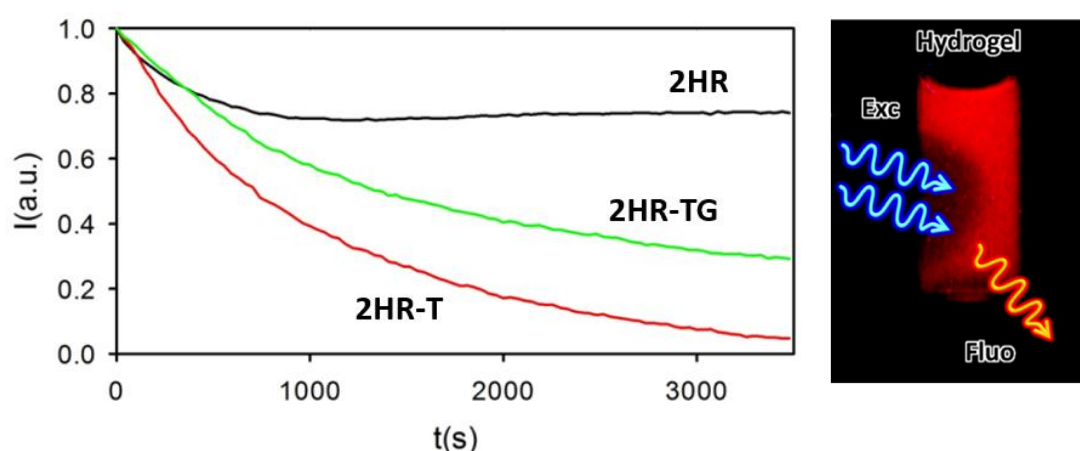


**Figure 2.21** *Left*. Fluorescence intensity at 585 nm of RhB as a function of irradiation time ( $\lambda_{\text{exc}} = 340 \text{ nm}$ ) in sample **2HR**, **2HR-T** and **2HR-TG**. *Right*. Fluorescence photograph of the sample **2HR-T** after 30 min irradiation.

These results clearly demonstrate that: i)  $\text{TiO}_2$ -NPs efficiently photo-decompose RhB, but ii) the introduction of graphene in hydrogel **2HR-TG** leads to a photoactivity decrease of  $\text{TiO}_2$ -NPs, in contrast to observations in other matrixes.<sup>153</sup>

In conclusion, TiO<sub>2</sub>-NPs (also in combination with graphene platelets) can be incorporated into biocompatible hydrogels, with high water content and good transparency to solar light. The degradation of a model pollutant molecule can occur inside the matrix with good efficiency upon irradiation.

Light penetrates inside the hydrogel. Photodegradation occurs in the bulk of the material. This important result was achieved by optimizing the composition and the production methodology of the hydrogel, especially avoiding sedimentation and segregation of the TiO<sub>2</sub>-NPs. Interestingly, the pollutant molecules are not absorbed either on the hydrogel fibres or on the TiO<sub>2</sub>-NPs, but rather solubilized in the hydrogel water channels. This result is very important in view of the development of photocatalytic water-permeable materials for continuous decontamination of water in fluxing systems.

### 2.2.3 Materials and Methods

**Synthesis of TiO<sub>2</sub>-NPs** – TiO<sub>2</sub> nanoparticles were synthesized in water solution by means of Pluronic® F127 (Plur) non-ionic surfactants following an industrial patented protocol.<sup>154</sup>

**Synthesis of TiO<sub>2</sub>-NPs/graphene** – A 15 mL aqueous dispersion was prepared with 9.4 mL of Plur-TiO<sub>2</sub> 15 mg/mL with 15 mg of natural graphite flakes was sonicated in an ultrasound bath for 6 hours, stirring for almost 1 minute each 30 minutes. Then, the dispersion was divided in two aliquots of 7,5 mL and it was centrifuged for 5 minutes at 9500 RPM. Then, the 65% of the supernatant was collected for the analysis. A 0.1% Graphene doping was expected to be obtained following the procedure reported in Ref.<sup>155</sup>

**Hydrogel Preparation** - A portion of Fmoc-L-Tyr-D-Oxd-OH (5 mg) was placed in a test tube (diameter: 8 mm), then Milli-Q® water (0.97 mL) and a 1M aqueous NaOH (1.3 equiv.) were added and the mixture was stirred until sample dissolution. Finally, we added 1.4 eq. of glucono-δ-lactone, and the mixture was left to sit for 16 hours at room temperature.

**Aerogel Preparation** - Hydrogels were freeze dried using a BENCHTOP Freeze Dry System LABCONCO 7740030 with the following procedure: the hydrogel was prepared into an Eppendorf test tube at room temperature. After 16 hours, the samples were placed in liquid nitrogen for 10 minutes, then freeze-dried for 24 hours *in vacuo* (0.2 mBar) at -50 °C.

**Morphological Analysis** - Scanning electron micrographs of the samples were recorded using a Zeiss EP EVO 50 field emission gun scanning electron microscope. Conditions: EHT=20 KeV - Variable Pressure (VP): 100 Pa - Images in secondary electrons (SE).

**UV- Vis absorption spectra** - UV-Vis absorption spectra (range 200-800 nm) were collected by using an optical path of 0.5 cm cuvette at 25 with a Cary300 UV-Vis double beam spectrophotometer, having an empty cuvette as a reference.

**Rheology** - Rheology experiments were carried out on an Anton Paar Rheometer MCR 102 using a parallel plate configuration (25 mm diameter). Experiments were performed at constant temperature of 23 °C controlled by the integrated Peltier system and a Julabo AWC100 cooling system. To keep the sample hydrated, a solvent trap was used (H-PTD200). Amplitude and frequency sweep analysis were performed with a fixed gap value of 0.5 mm on hydrogel samples prepared directly on the upper plate of the rheometer once the gelation reaction was completed. The samples were prepared the day before the analysis and left overnight at controlled temperature of 20 °C to complete the gelation process. Oscillatory amplitude sweep experiments ( $\gamma$ : 0.01–100%) were carried out to determine the LVE range at fixed frequency of 1 rad·s<sup>-1</sup>. Once established the LVE of each hydrogel, frequency sweep tests were performed ( $\omega$ : 0.1-100 rad/s) at constant strain within the LVE region of each sample. Thixotropic experiments were conducted on hydrogels **2H**, **2H-T** and **2H-TG** by applying consecutive deformation and recovery steps. The deformation step was performed by applying to the gels a constant strain above the LVE region of each sample for a period of 7 minutes. The recovery step was performed by keeping the sample at constant strain within the LVE region for 7 minutes. The cycles were performed multiple times at fixed frequency of 1 rad/s.

**Emission and excitation** - Spectra were collected with an Edinburgh FLS920 fluorimeter equipped with a photomultiplier Hamamatsu R928P, and the samples were analysed in disposable cuvettes with optical path length of 0.5 cm. Emission:  $\lambda_{exc} = 530$  nm;  $\lambda_{em}$ : 540-700 nm. Excitation:  $\lambda_{exc} = 330-600$  nm,  $\lambda_{em} = 620$  nm.

## Chapter 3

---

### 3. Graphene doped LMW gels for 3D cell growth

Hydrogels have been extensively explored as promising biomaterials for tissue engineering and drug delivery.<sup>156–159</sup> With tuneable mechanical and bioactive properties, hydrogels offer potential for biocompatibility and environmental responsiveness to mimic natural extracellular matrices.<sup>160–163</sup>

Low molecular weight supramolecular hydrogels (LMWSHs)<sup>164–166</sup> have some special properties that differentiate them from the traditional polymeric hydrogels offering advantages for certain applications, such as thixotropy, self-healing propensity and thermoreversibility. Peptide-based hydrogels<sup>15,39,40,167,168</sup> are appealing for biomedical applications, because they have high biocompatibility and good biodegradability. To overcome drawbacks of many peptide-based supramolecular hydrogels, such as low mechanical stability and high erosion rates in vivo<sup>169</sup> the class of pseudopeptide gelators described in this work provides potential for intrinsic proteolytic stability.

A recent strategy for improving the functionality of supramolecular hydrogels is the incorporation of nanofillers.<sup>170–175</sup> The specific properties of the fillers may modify the performance of the hydrogel or add functionality (i.e. hydrogel reinforcement, self-healing).<sup>126,176–178</sup> Nanocarbons are ideal nanofillers due to their peculiar chemical-physical properties, that have demonstrated great potential in nanomedicine and nanotechnology.<sup>179–182</sup> Electrical conductivity, mechanical strength, and high surface area, all make graphene an interesting filler for tissue engineering and regenerative medicine.<sup>183–186</sup> The generally poor mechanical stability of hydrogels limits their use as functional materials for many biomedical applications. On the contrary, graphene is the strongest material known (more than 200 times stronger than steel). The presence of graphene even at very low loadings inside a hydrogel can provide significant reinforcement to the final material.

In Chapter 2, inorganic filler in the form of titanium nanoparticles, in the presence or absence of graphene platelets, was added to a hydrogel matrix for the photodegradation of a model

pollutant. However, the addition of these fillers, especially the mix of titanium and graphene, caused a decrease of the mechanical properties of the final material, due to the formation of aggregates.

Recently, the incorporation of graphene-based nanofillers in hydrogels has been reported to tailor the properties of these versatile materials.<sup>187–192</sup> A crucial step for the inclusion of graphene in supramolecular hydrogels is the achievement of a stable dispersion before the addition of the trigger. Various polymers, surfactants and biomolecules have been used to facilitate the dispersion of carbon nanomaterials<sup>193–196</sup> in solution. For example, Pluronic<sup>®</sup> F127 was added to the gelator to stabilise the NPs solution.<sup>126</sup> However, these dispersants usually alter the gelation process or hamper the molecular self-assembly.

A promising strategy uses the supramolecular gel medium to disperse the graphene. The aromatic moieties contained in the gelator molecules can interact with the graphene delocalized  $\pi$  surface by  $\pi$ - $\pi$  stacking interactions to disperse the graphene in the supramolecular matrix and incorporate graphene sheets into the gel system, thus generating a hybrid system. The supramolecular gel, in turn, provides fibrillar network structures that may accommodate the dispersed graphene sheets.<sup>197</sup>

Supramolecular hydrogels were prepared using the pseudopeptide to act as both gelator and graphene dispersant. For this study, the already reported<sup>45,72</sup> bolaamphiphilic pseudopeptide  $\text{H}_2\text{C}[(\text{CH}_2)_3\text{CO-L-Phe-D-Oxd-OH}]_2$  (**3**) was chosen.

This robust gelator possesses two L-Phe-D-Oxd dipeptide units linked by an azelaic acid unit. The aromatic moieties of the L-Phe residue can interact with graphene favouring dispersion. (**Figure 3.1**).<sup>54</sup>

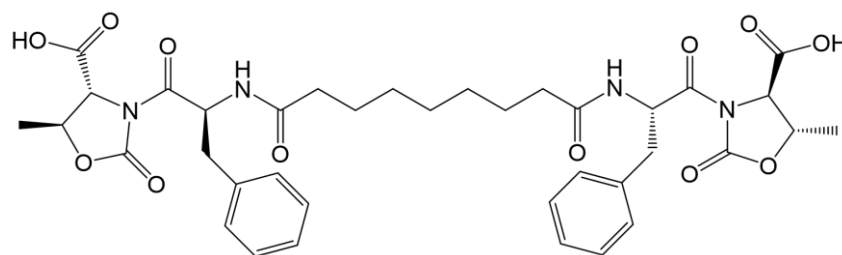


**Figure 3.1** Chemical structure of gelator **3**,  $\text{H}_2\text{C}[(\text{CH}_2)_3\text{CO-L-Phe-D-Oxd-OH}]_2$ .

A small library of graphene doped supramolecular hydrogels was prepared using two different triggers (pH variation and arginine addition) and the hydrogel mechanical properties were tested

and compared. Cell viability was studied to examine the safety and biocompatibility of graphene filler.<sup>198</sup>

### 3.1 Mechanical properties of graphene doped LMWSHs

A set of 16 hydrogels was prepared using solutions of gelator **3** and increasing amounts of graphene in Milli-Q® water (see **Table 3.1** for details) by adding either 2.2 equivalents of GdL (samples denoted as **3G**) or 1 equivalent of arginine (samples denoted as **3A**) to promote hydrogel formation. Samples prepared with GdL and 1% gelator concentration were named **3G1-3G4** and with 2% w/w concentration **3G5-3G8**; the same for Arg, **3A1-3A4** (1% w/w) and **3A5-3A8** (2% w/w).

**Table 3.1** Hydrogels properties as a function of gelator concentration (w/w), graphene concentration (mg/mL) and trigger.

| Entry      | Trigger | Gelator <b>3</b> | Graphene (mg/mL) | pH | $T_{gel}^a$ | Photo   |
|------------|---------|------------------|------------------|----|-------------|---|
| <b>3G1</b> | GdL     | 1%               | 0                | 4  | 70-77       |  |
| <b>3G2</b> | GdL     | 1%               | 0.5              | 4  | 79-81       |  |
| <b>3G3</b> | GdL     | 1%               | 1                | 4  | 77-79       |  |
| <b>3G4</b> | GdL     | 1%               | 5                | 4  | 80-89       |  |
| <b>3G5</b> | GdL     | 2%               | 0                | 4  | 98-100      |  |
| <b>3G6</b> | GdL     | 2%               | 0.5              | 4  | 94-99       |  |

|            |     |    |     |     |        |   |
|------------|-----|----|-----|-----|--------|---|
| <b>3G7</b> | GdL | 2% | 1   | 3.5 | 98-100 |    |
| <b>3G8</b> | GdL | 2% | 5   | 3.5 | 80-87  |    |
| <b>3A1</b> | Arg | 1% | 0   | 7   | 73-79  |    |
| <b>3A2</b> | Arg | 1% | 0.5 | 7   | 78-96  |    |
| <b>3A3</b> | Arg | 1% | 1   | 7.5 | 85-91  |    |
| <b>3A4</b> | Arg | 1% | 5   | 7.5 | 91-100 |    |
| <b>3A5</b> | Arg | 2% | 0   | 7   | 90-100 |   |
| <b>3A6</b> | Arg | 2% | 0.5 | 8   | 86-100 |  |
| <b>3A7</b> | Arg | 2% | 1   | 8   | 92-100 |  |
| <b>3A8</b> | Arg | 2% | 5   | 8   | 95-100 |  |

---

<sup>a</sup> Hydrogels are thermoreversible.

The use of GdL has been extensively reported to promote gel formation.<sup>64,199,200</sup> The choice of arginine as trigger was inspired by a previous work of Tomasini and co-workers,<sup>72</sup> as discussed in Chapter 1. Several amino acids had been tested as triggers for the gelation process of LMWGs, and arginine proved the best, giving strong, self-healing and thermoreversible hydrogels.

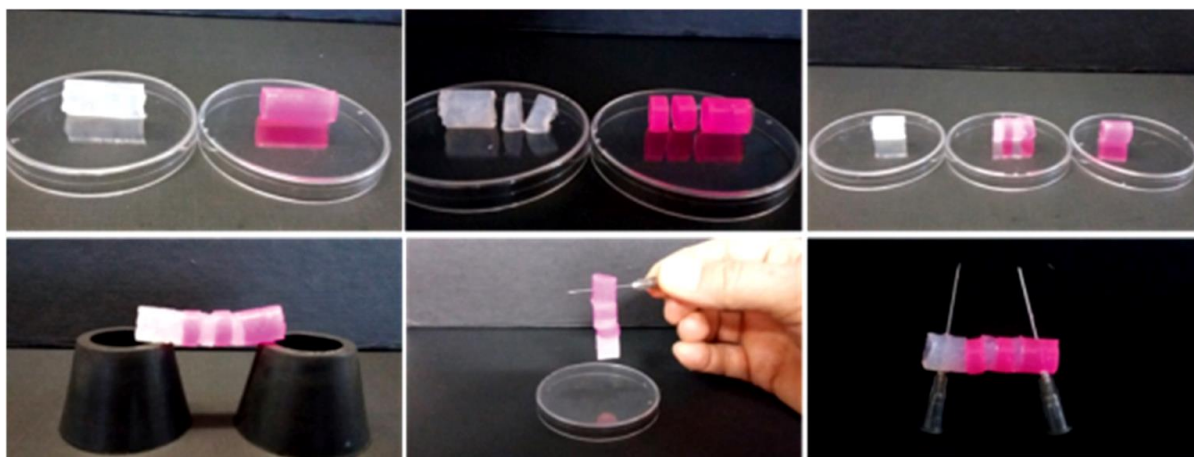


**Figure 3.2** The self-healing ability of gelator **3** reported in a previous work of Tomasini *et al.* when arginine is used as a trigger for the gelation process. Two gels were prepared (one marked with Rhodamine B) and cut into three blocks. When different gel blocks were placed in direct contact along the cut surface without any external stimuli, they recombined within 20 minutes.<sup>72</sup>

The 16 mixtures were stirred for 5-10 minutes, then left stand in the test tube overnight until gel formation. All samples are self-supporting and thermoreversible on heating, with  $T_{\text{gel}}$  increasing for hydrogels doped with increasing amounts of graphene (**Table 3.1**). Hydrogels **3G1-3G8** have a pH ranging between 3.5 and 4, due to the use of GdL as trigger, while hydrogels **3A1-3A8** reach a pH ranging between 7 and 8, due to the addition of arginine. The viscoelastic behaviour of the samples was analysed through rheological analyses. All hydrogels are characterized by a solid-like behaviour, with storage modulus approximately an order of magnitude higher than the loss component.  $G'$  always increases as the graphene concentration increases (**Figure 3.3**).

The reinforcement effect of graphene is impressive especially for arginine containing hydrogels at 2% concentration (**3A5-3A8**). Comparing the properties of hydrogels obtained at 1% and 2% w/w concentration, it can be gathered that hydrogels strength increases with the graphene concentration, in agreement with the results obtained from the  $T_{\text{gel}}$  analysis.

Taking into consideration the mechanical properties and the final pH of the 16 samples, the most promising hydrogels for applications as biocompatible materials are hydrogels **3A5-3A8** that couple an exceptional mechanical strength with a final pH ranging between 7 and 8, that is compatible with cellular environment.

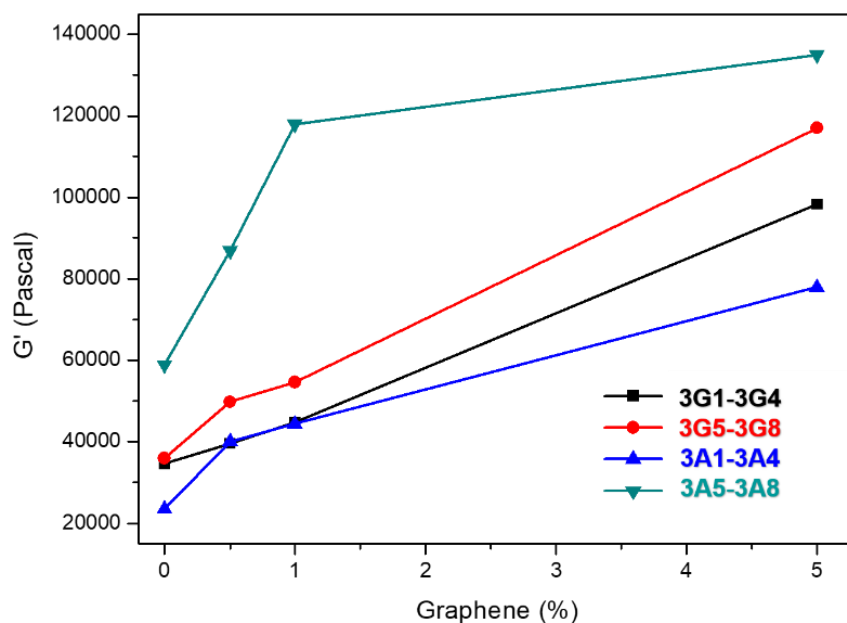


**Figure 3.3** Diagram of the  $G'$  values obtained from the frequency sweep analyses of hydrogels **3G1-3G8** and **3A1-3A8**, as a function of trigger, gelator concentration and graphene concentration. Each point represents one sample with graphene doping indicated on the x axis.

All the hydrogels were further analysed, but a particular attention was paid to the properties of hydrogels **3A5-3A8**. These four samples are characterized by a great capability to recover the gel-like behaviour as they all recover the “solid-like” state when the strain level goes back within the LVE region (**Figure 3.4** and **Figure 3.5**). Thus, they confirm at the molecular level their thixotropic properties, although a slight decrease in the storage modulus was observed.

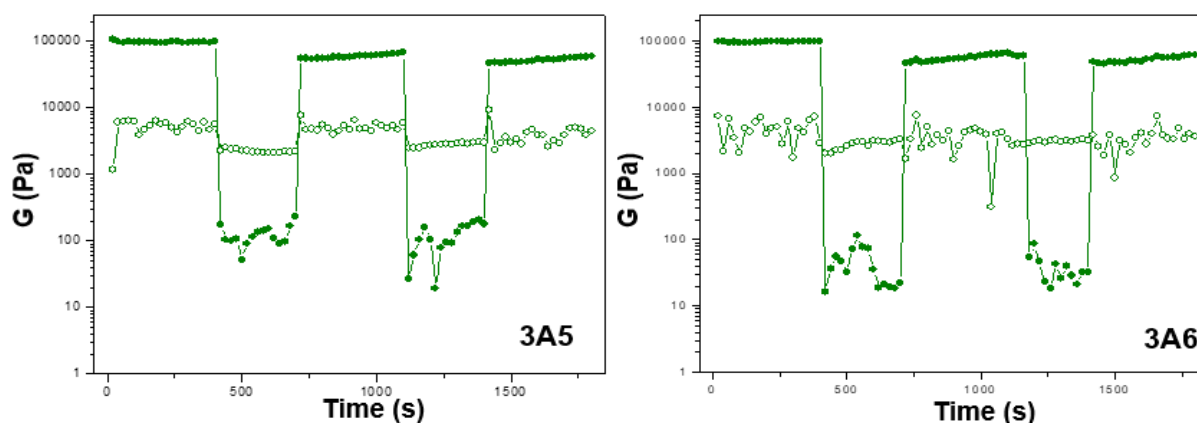


**Figure 3.4** Values of storage moduli (solid circles) and loss moduli (empty circles) during a step strain experiment performed on hydrogels **3A5-3A6**.

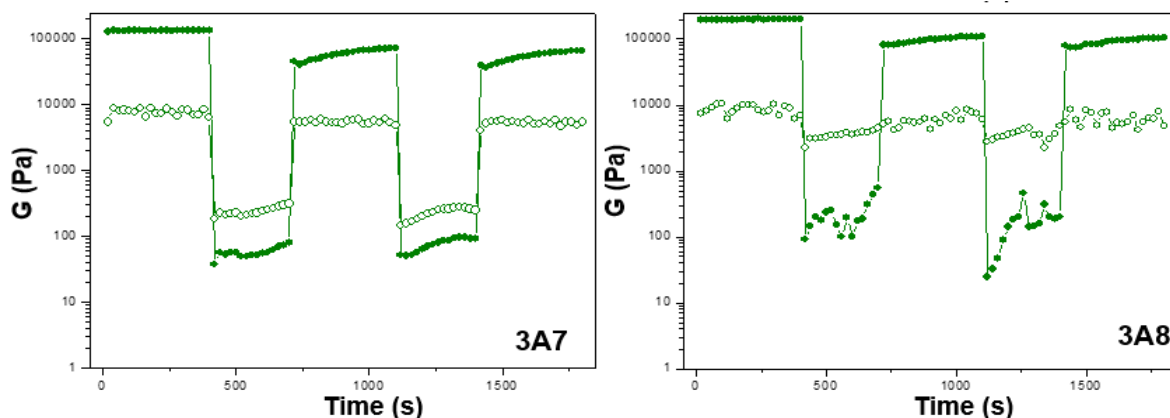


**Figure 3.5** Values of storage moduli (solid circles) and loss moduli (empty circles) during a step strain experiment performed on hydrogels **3A7-3A8**.

Hydrogels made with GdL (**3G1-3G8**) also show the capability to recover the gel-like behaviour after the application of a strain above their LVE region.<sup>198</sup>

The morphological analysis of the corresponding aerogels, obtained by freeze-drying of the samples, was performed with SEM (**Figure 3.6**). In any case, the comparison of the morphology between aerogels containing graphene and the corresponding aerogels without graphene do not suggest significant differences due to graphene.

| Trigger   | % Graphene |         |         |         |
|-----------|------------|---------|---------|---------|
|           | 0          | 0.5     | 1       | 5       |
| GdL<br>1% | 3G1<br>    | 3G2<br> | 3G3<br> | 3G4<br> |
|           | 3G5<br>    | 3G6<br> | 3G7<br> | 3G8<br> |
|           |            |         |         |         |
|           |            |         |         |         |

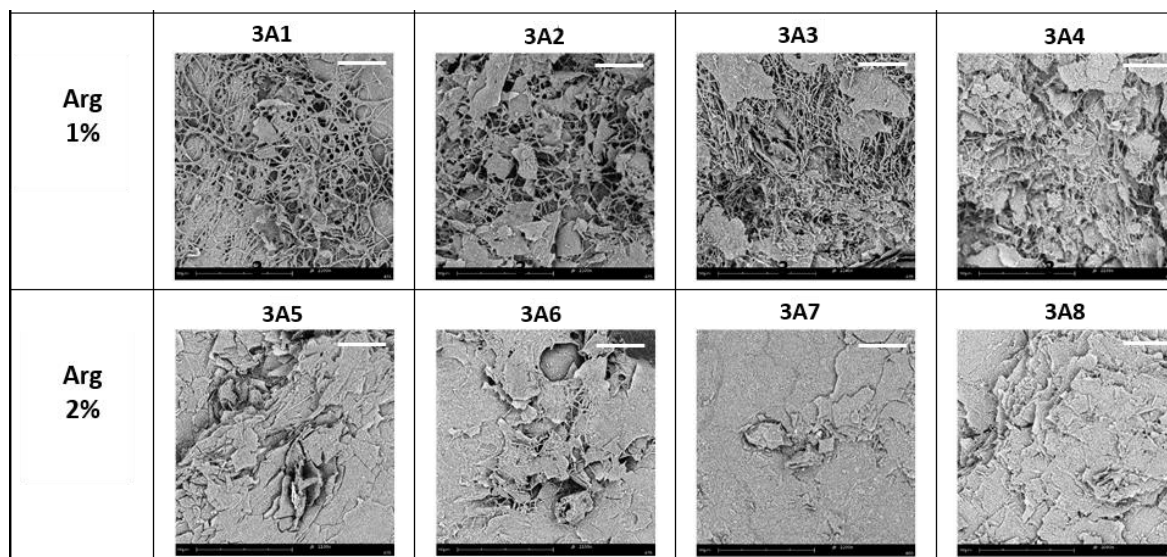


**Figure 3.6** SEM images of aerogels obtained by freeze drying hydrogels samples **3G1-3G8** and **3A1-3A8**. Scale bar (in white) represents 25  $\mu\text{m}$ .

Aerogels **3G1-3G8** and **3A5-3A8** show a morphology characterized by the formation of locally oriented long strips that cross on the large scale forming a network, while aerogels **3A1-3A4** are characterized by dense fibrous networks. The differences in morphology are likely related to the gelator concentration and the trigger nature.

This outcome is further confirmed by the analysis of the aerogels ATR-IR (Attenuated total reflection - Infrared) spectra, which provide information on the supramolecular interactions involved in the formation of the hydrogels. The spectra were compared of hydrogels prepared with different graphene concentrations and the same concentrations of gelator and trigger. In all of the spectra similar bands were observed, indicating that graphene did not alter significantly the supramolecular interactions in the network.

Aerogels **3G1-3G8** (trigger = GdL) exhibited reproducible IR spectra (**Figure 3.7**). All contained a band at  $3330\text{ cm}^{-1}$  characteristic of hydrogen bonded NH bonds ( $\text{N-H}\cdots\text{O}=\text{C}$  hydrogen bonds), together with another strong stretching band at  $1710\text{-}1720\text{ cm}^{-1}$ , typical of hydrogen bonded CO bonds, and a weaker band between  $1550$  and  $1600\text{ cm}^{-1}$  that may be attributed to the amide band II. Aerogels **3A1-3A8** (trigger = arginine) show a different pattern (**Figure 3.8**), in which a strong band I prevails at about  $1630\text{-}1650\text{ cm}^{-1}$  but no band II is visible, and the typical band of hydrogen bonded NH bonds is quite weak, due to the presence of arginine, and centred at  $3300\text{-}3330\text{ cm}^{-1}$ .

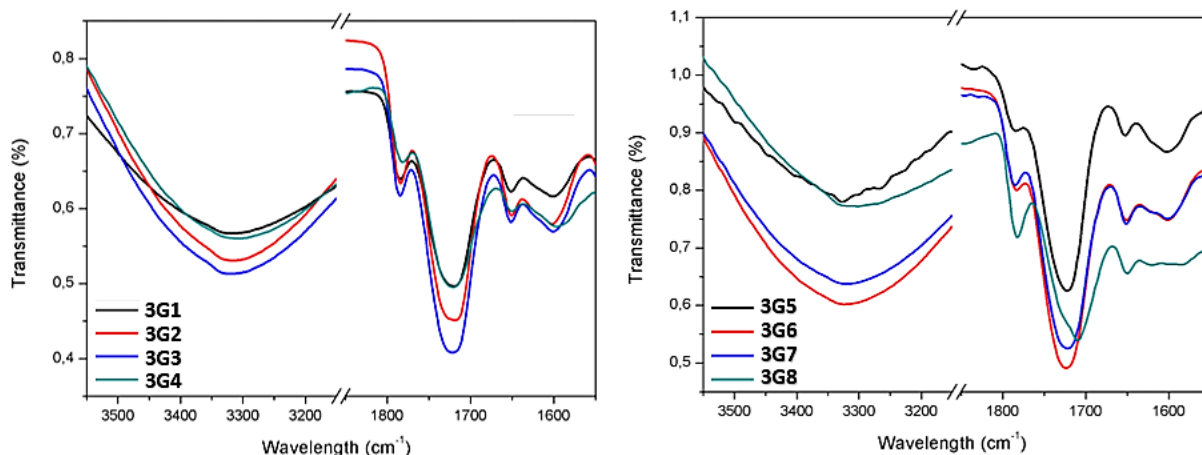


**Figure 3.7** Selected regions of ATR-IR spectra for aerogels **3G1-3G8**.

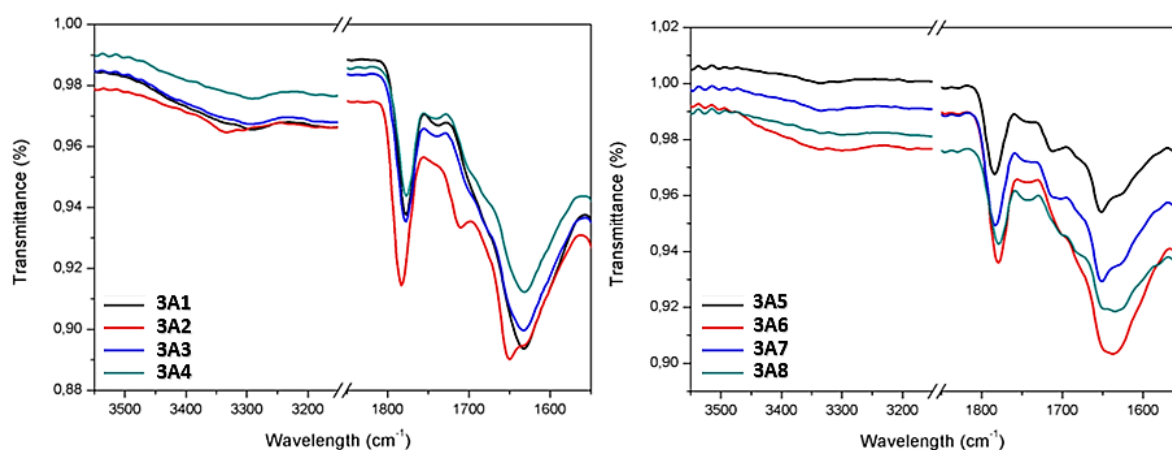


**Figure 3.8** Selected regions of ATR-IR spectra for aerogels **3A1-3A8**.

NIH-3T3 (mouse embryonic fibroblast) cells were used to evaluate the cell response to the presence of hydrogels **3A5-3A8**. The four hydrogels were prepared using cellular medium instead of Milli-Q® water, to assess the hydrogels biocompatibility. The use of cellular medium slowed down the gelation time from 16 hours to 2 days. **Figure 3.9** illustrates cell proliferation on hydrogel **3A5-3A8** in cellular medium after a culture period of 24h and 48h.

Cell adhesion is strongly influenced by graphene doping. Hydrogel **3A6** (graphene content = 0.5%) shows a good biocompatibility, while at higher graphene concentrations (hydrogels **3A7** and **3A8**) a significant toxic effect on fibroblasts is observed. However, after 48 hours, cells continue to proliferate both in hydrogel **3A5** (without graphene) and in hydrogel **3A6-3A8**,

insensitive to the graphene doping concentration, this meaning that the scaffold supports cell growth.

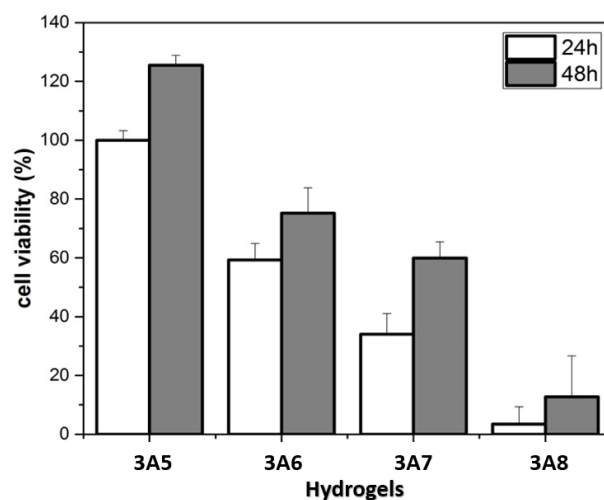


**Figure 3.9** Cell viability of NIH-3T3 on hydrogels **3A5-3A8** in cellular medium. Data represent the mean  $\pm$  standard deviation.

Supramolecular hydrogels doped with graphene may represent a promising building block for the development of smart materials for biomolecules and tissue engineering purposes. The degradation of the gel does not modify the toxicity of graphene. Cell viability was measured even after the destruction of the matrix and the results, **Figure 3.10**, showed that cell viability is similar to that obtained by the graphene embedded in the gel.

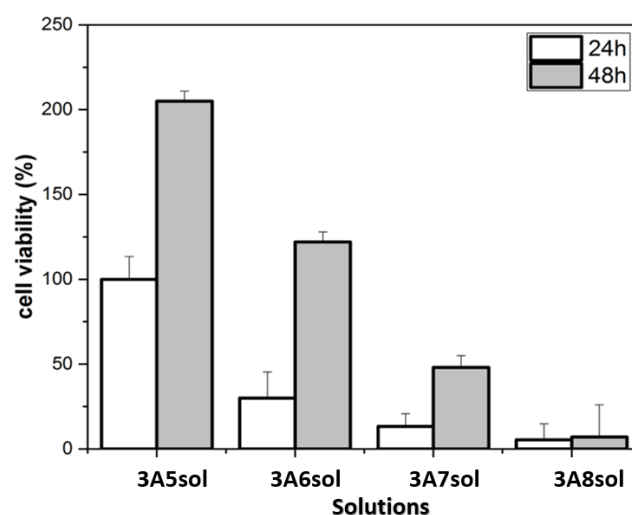


**Figure 3.10** Cell viability of NIH-3T3 in cellular medium solutions. From left to right: **3A5sol** (cellular medium added with 2% gelator), **3A6sol** (cellular medium added with graphene (0.5 mg)), **3A7sol**

(cellular medium added with graphene (1 mg)), **3A8sol** (cellular medium added with graphene (5 mg)). Data represent the mean  $\pm$  standard deviation.

In conclusion, strong supramolecular hydrogels were prepared using two triggers (GdL and Arg) and introducing increasing amounts of graphene in the gelling mixture. The G' modulus of these materials increases with the graphene amount; they are stable, thermoreversible and elastic. The concentration of gelator, the degree of graphene doping and the nature of the trigger are crucial to get hydrogels with the desired properties, such a high storage modulus and good self-healing properties. The hydrogels prepared are able to recover their modulus during thixotropy experiments. The biocompatibility of the most promising hydrogels **3A5-3A8** was tested by assessment of the bioavailability of mouse embryonic fibroblast (NIH-3T3) cells in the hydrogels in which pure water was replaced with complete serum medium. Cell adhesion on the hydrogel is strongly influenced by graphene doping. The hydrogel scaffold support cell growth at all the concentration of graphene doping.

The rheological properties and the biocompatibility of these graphene-hybrid hydrogels may be easily tuned selecting i) the degree of the graphene doping and ii) the nature of the gelator in the gelling mixture.

## 3.2 Materials and Methods

**Preparation of the Graphene Dispersions** – Three dispersion of Milli-Q® water (20 mL each) containing edge-functionalized graphene, MG24, (10 mg, 20 mg and 100 mg respectively) were prepared and vigorously stirred for about 20 minutes with a magnetic stirrer. Graphene sample MG 24, produced by 24 hours ball milling in the presence of CO<sub>2</sub> according to ref.<sup>201</sup>, was kindly provided by the University of Fribourg. Characterization of the graphene sheets (elemental analysis, surface area and size of the sheets) are reported in ref.<sup>201</sup>

**Hydrogel Preparation using the pH Variation Method** - A portion of gelator **3** (5 mg for hydrogels **3G1-3G4**; 10 mg for hydrogels **3G5-3G8**) was placed in a test tube (diameter: 8 mm), then Milli-Q® water (0.5 mL) or a graphene solution (see **Table 3.1** for details) was added, followed by a 1M aqueous NaOH (2.1 equiv.) and the mixture was stirred until sample dissolution. Finally, we added 2.2 eq. of glucono- $\delta$ -lactone. After a rapid mixing to allow the

GdL complete dissolution, the sample stood quiescently until complete gel formation which usually occurred after 16 hours.

**Hydrogel Preparation by Addition of Arginine** - A portion of gelator **3** (5 mg for hydrogels **3A1-3A4**; 10 mg for hydrogels **3A5-3A8**) was placed in a test tube (diameter: 8 mm), then arginine (1 equiv.) was added. 0.5 mL of Milli-Q® water or a graphene solution (see **Table 3.1** for details) was added to the test tube under stirring. After 1 minute, the magnetic stirrer was removed and the tube stood quiescently until complete gel formation which usually occurred after 16 hours.

**Conditions for  $T_{gel}$  Determination** -  $T_{gel}$  was determined by heating some test tubes (diameter: 8 mm) containing a glass ball (diameter: 5 mm, weight: 165 mg) on the top of the gel. After the gel is formed, the ball was suspended atop. The  $T_{gel}$  is the temperatures in which the ball starts to penetrate inside the gel. Some hydrogel samples melt, producing a clear solution, while in other cases the gelator shrinks and water is ejected, as syneresis occurs.

**Aerogels Preparation** - Samples of the hydrogels were freeze dried using a BENCHTOP Freeze Dry System LABCONCO 7740030 with the following procedure: the hydrogel was prepared in an Eppendorf test tube at room temperature. After 16 hours, the samples were placed in liquid nitrogen for 10 minutes, then freeze-dried for 24 hours in vacuo (0.2 mBar) at -50 °C.

## AEROGELS CHARACTERIZATION

**Morphological Analysis** - Scanning electron micrographs of the samples were recorded using a Hitachi 6400 field emission gun scanning electron microscope operating at 15 kV.

**Rheology** - Rheology experiments were carried out on an Anton Paar Rheometer MCR 102 using a parallel plate configuration (25 mm diameter). Experiments were performed at constant temperature of 23 °C controlled by the integrated Peltier system and a Julabo AWC100 cooling system. Oscillatory amplitude sweep experiments ( $\gamma$ : 0.01–100%) were carried out to determine the LVE range at a fixed frequency of 1 rad s<sup>-1</sup>. Once the LVE of each hydrogel was established, frequency sweep tests were performed ( $\omega$ : 0.1–100 rad s<sup>-1</sup>) at a constant strain within the LVE region of each sample ( $\gamma = 0.04\%$ ). Step strain experiments were performed on hydrogels to

analyse the thixotropic behaviour of the material. The sample was subjected to consecutive deformation and recovery steps. The recovery step was performed by keeping the sample at a constant strain  $\gamma = 0.04\%$ , i.e. within the LVE region, for a period of 400 s. The deformation step was performed by applying to the gel a constant strain  $\gamma = 100\%$ , i.e. above the LVE region of the sample for a period of 300 s. The cycles were performed 3 times at a fixed frequency  $\omega = 10 \text{ rad s}^{-1}$ .

**IR** - High quality infrared spectra (64 scans) were obtained with an ATR-FT-IR Bruker Alpha System spectrometer (64 scans).

**Cell culture** - Mouse embryonic fibroblast (NIH-3T3) cells were cultured under standard conditions in Dulbecco's modified Eagle medium (DMEM) ( $4.5 \text{ g L}^{-1}$  glucose), supplemented with 10% (v/v) Fetal Bovinum Serum, 2 mM L-glutamine, 0.1 mM MEM Non-Essential Amino Acids (NEAA),  $100 \text{ U mL}^{-1}$  penicillin and  $100 \text{ U mL}^{-1}$  streptomycin in a humidified incubator set at  $37^\circ \text{C}$  with 5%  $\text{CO}_2$ . For cell culture, the samples were sterilized with ultraviolet (UV) radiation for 20 min before use. The gels were incubated for 30 min at  $37^\circ$  with 5%  $\text{CO}_2$  with complete medium. Cells were seeded on gel in 24-well plates at a density of  $10^5$  cells per mL.

**Cell viability** - Cell viability was determined by resazurin reduction assay; the reagent is an oxidized form of the redox indicator that is blue in colour and non-fluorescent. When incubated with viable cells, the reagent is reduced and it changes its colour from blue to red becoming fluorescent. Briefly, cells were seeded on gels with complete medium. After incubation times, the resazurin reagent was added directly to the culture medium with 10% volume of medium contained in each sample and incubated for 4 h at  $37^\circ \text{C}$  with 5%  $\text{CO}_2$ . Subsequently, aliquots from each sample were transferred to a 96 multiwell plate for fluorescence measurement at  $\lambda_{\text{exc}}$  560 nm and  $\lambda_{\text{em}}$  590 nm (Thermo Scientific Varioskan Flash Multimode Reader). A negative control of only medium without cells was included to determine the background signal, as well as a positive control of 100% reduced resazurin reagent without cells.

## Chapter 4

---

### 4. LMWGs and mineral phase: formation of composite materials

#### 4.1 Biomineralization: crystal growth in hydrogel matrices

Biomineralization is the process by which organisms deposit in a controlled way mineral phases producing biominerals such as bones, teeth, mollusc shells.<sup>202–204</sup> One experimentally proven dogma of biomineralization is that the deposition of the mineral phase occurs in a highly viscous or gel environment.<sup>202,205</sup>

Biominerals have properties optimized for their specific function, but difficult to reproduce in laboratories. Recently, the possibility to exploit gels for the growth of crystals has been used as a model for biomineralization. A number of natural gel-like matrices (such as collagen, fibroin, amelogenin and  $\alpha$ -chitin)<sup>206</sup> have been identified in association with mineralisation processes in biological organisms.

Crystal growth in gels is a modification of crystal growth in solution and could be a useful tool for controlling purity, morphology and other properties of single crystals.

Gel matrices composed of synthetic and natural molecular gelators, are usually well hydrated, porous and fibrous networks, which provide structural frameworks for the mineral phase to grow, as well as chemical functionalities for nucleation of crystal growth.<sup>207,208</sup>

One of the unique aspects of gels is the high porosity of the three-dimensional network. Each cavity represents a compartment of solution in which the solute is confined, influencing crystal nucleation, growth and morphology. Physically, gel networks determine diffusion rates, local concentrations and supersaturation of solutes.

A wide variety of materials can be dissolved, suspended or trapped into the gel structure at the end of the gel formation (as already reported in Chapter 2 and 3) such as graphene,<sup>168,171,209,210</sup> cells,<sup>211–213</sup> catalysts,<sup>214,215</sup> and ions for crystal growth. After hydrogel formation, several processes may take place in the confined space of the gel, producing results that are significantly different from what is usually observed in solution.

Gel networks offer other advantages to support crystal growth including prevention of sedimentation and elimination of Brownian motion, laminar flow and convective currents,

making diffusion the dominant mass transport mechanism available to solutes. Such parameters lead generally to large and high-quality crystals. The organic matrix constituted by gel fibres can be intimately associated with the inorganic mineral phase and even incorporated inside of it, producing composite inorganic/organic materials with unique properties and morphologies.<sup>216–218</sup>

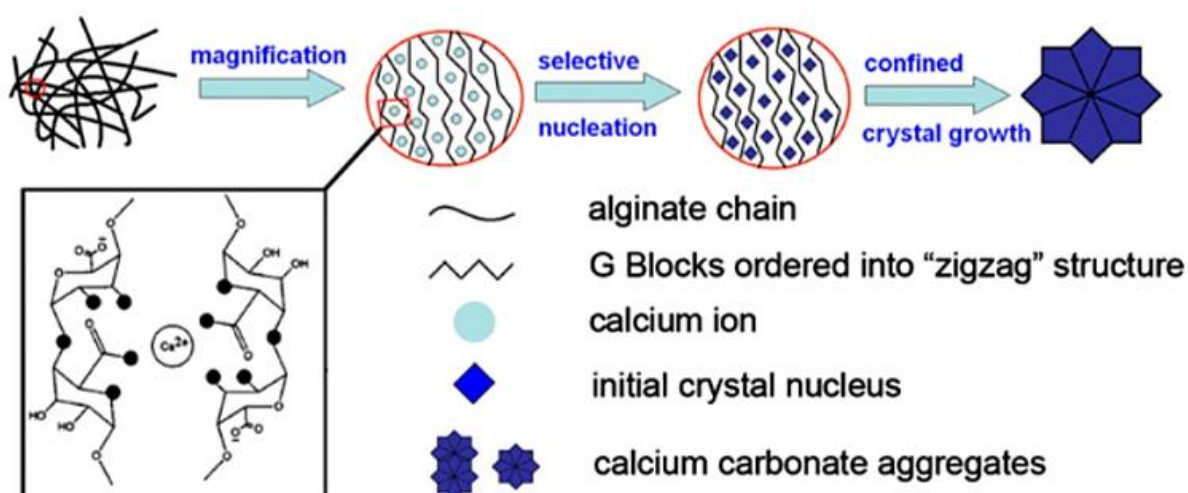


**Figure 4.1** Schematic illustration of the growth of calcite aggregates obtained from alginate gels. (G blocks are the  $\alpha$ -L-galuronic acid residues of alginate). Adapted from ref.<sup>219</sup>

Examples of hydrogels in biological, as well as synthetic, bio-inspired systems are discussed in Asenath-Smith et al.<sup>206</sup> They show the physical and chemical effects of a broad range of hydrogel matrices and their role in directing polymorph selectivity and morphological control in the calcium carbonate system. In these studies, the function of the gel has been to physically control the diffusion process of precipitating ions by chemical interactions between functional groups of gelator molecules and the growing crystals of the mineral.

Calcium carbonate has been one of the most studied minerals, alone and in combination with gels (**Figure 4.2**), because it is widespread among living organisms and represents a relatively simple chemical system to investigate *in vitro*.<sup>220,221</sup> It exists as one of three polymorphs (calcite, aragonite and vaterite), as well as amorphous forms. In a recent work, a gel that formed in the presence of calcium ions was used as a source of calcium ions for calcification.

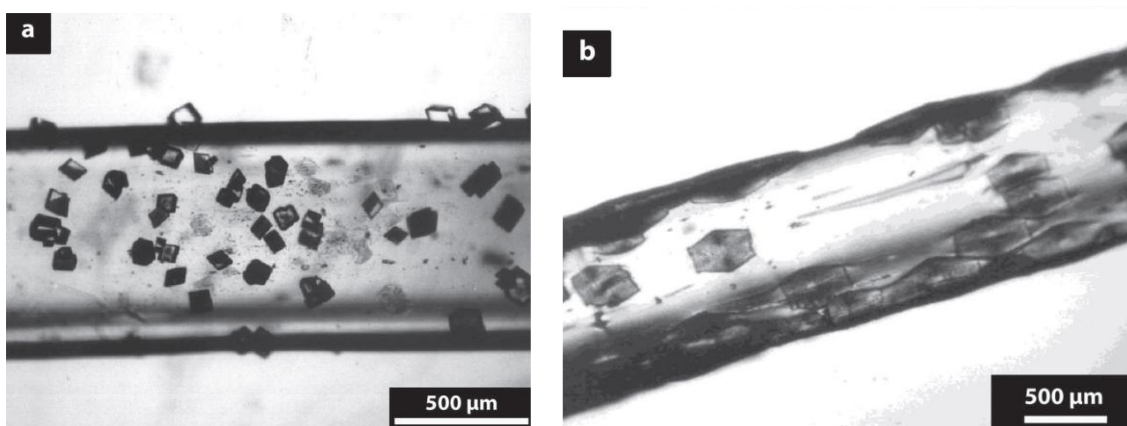


**Figure 4.2** Optical images of calcium carbonate crystallization in uniaxially deformed (200% elongation) gelatin films: a) Rhombohedral calcite crystals formed on film without entrapped poly-L-Aspartate. b) Aragonite aggregates formed inside the film with entrapped poly-L-Aspartate.<sup>221</sup>

However, the gel structure was lost during the calcification process.<sup>222</sup> Examples of hydrogels that i) form a framework in the presence of calcium ions, ii) provide the calcium ions for crystallization and iii) preserve the framework structure are absent in the literature, as far as we know. Such a system can have great relevance in biomineralization, because in many organisms the mineralization process takes place in a gelling environment rich of calcium ions, in which the diffusion of carbonate ions occurs.<sup>202,223</sup>

#### 4.1.1 Supramolecular hydrogels for growth of $\text{CaCO}_3$ crystals

Supramolecular gels, as already discussed, may be constituted of a liquid phase (water or organic solvents) in which a wide variety of materials are dissolved, suspended or trapped into the gel structure at the end of the gel formation. After hydrogel formation, several processes may take place in the confined space of the gel, producing results that are significantly different from those observed in solution.

A recent study reported the growth of calcium carbonate crystals inside a supramolecular gel based on a bis-urea gelator system with carboxylic acid functionalities.<sup>224</sup> Gels of this type, having  $\text{Ca}^{2+}$  binding domains on the fibres (carboxylate groups), can potentially nucleate the growth of a mineral or strongly and specifically interact with growing crystal faces, thus altering the morphology of the crystals in a controlled way.<sup>225</sup> Gelator molecules participated in the

crystallization of calcite, altering the physical properties, nucleation and growth processes of the crystals.

In this context, we decided to investigate the formation of calcium carbonate crystals inside a gel matrix made with one of our gelators containing carboxylic acid functionalities. In our continuous effort to find new gelators able to form stable hydrogels, useful for different applications, we found a LMWG based on a single amino acid, L-DOPA, that was able to gelate under several conditions. Gelator **4** Boc-L-DOPA(Bn)<sub>2</sub>-OH (**Figure 4.3**) may benefit from the additional presence of two benzyl esters in the chemical structure, that improve gelation efficiency through additional  $\pi$ - $\pi$  stacking interactions.

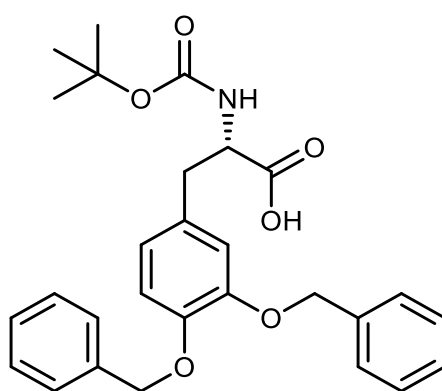


**Figure 4.3** Chemical structure of gelator **4**, Boc-L-DOPA(Bn)<sub>2</sub>-OH.

Unprotected and commercially available L-DOPA was transformed into gelator **4** with four synthetic steps, as previously reported (see Chapter 2). The effective preparation of this compound bears well for its applications in the formation of supramolecular materials. The preparation of the hydrogels followed a general procedure based on the dissolution of **4** in an alkaline aqueous solution (NaOH or Na<sub>2</sub>CO<sub>3</sub>), by stirring and sonication for about 15 minutes, followed by the addition of the trigger (GdL or CaCl<sub>2</sub>).<sup>226–228</sup>

Samples **4A** and **4B** both were prepared using NaOH as base for the dissolution, and different triggers (GdL and CaCl<sub>2</sub> respectively). For the preparation of samples **4C** and **4D**, NaOH was replaced by Na<sub>2</sub>CO<sub>3</sub> as a source of carbonate ions. The addition of CaCl<sub>2</sub> as trigger may induce the formation of CaCO<sub>3</sub> crystals. In this procedure, gelation takes place with the formation of CaCO<sub>3</sub> crystals.

Gelator **4** can form gels under these conditions with a concentration ranging between 0.5 and 2% w/w. After several attempts, we found that the optimal gelator concentration for this specific

study was 1% w/w. Gels were too weak using 0.5%. Gels formation was irreproducible and very fast using 2%, creating mechanical problems in the hydrogel network and the crystals. Moreover, before choosing the optimal Na<sub>2</sub>CO<sub>3</sub> and CaCl<sub>2</sub> concentrations used for samples **4B**, **4C** and **4D** (**Table 4.1**), several concentrations were tested, which were too low to detect the calcite formation, or too high to allow the formation of a strong hydrogel.

**Table 4.1** Reagents, conditions and final pH for hydrogels formation using gelator **4** in 1% w/w concentration.

| Sample    | Gelator (mg) | Eq.NaOH (1 M) | Eq.Na <sub>2</sub> CO <sub>3</sub> (0.1 M) | Eq. GdL | Eq.CaCl <sub>2</sub> (0.1 M) | Final pH |
|-----------|--------------|---------------|--|---------|------------------------------|----------|
| <b>4A</b> | 10           | 1.3           | -  | 1.4     | -                            | 5.5      |
| <b>4B</b> | 10           | 1.3           | -  | -       | 1                            | 8        |
| <b>4C</b> | 10           | -             | 1  | -       | 1                            | 6        |
| <b>4D</b> | 10           | -             | 2.5  | -       | 5                            | 6.5      |

In all the cases, gel formation was fast after the addition of the trigger, even in the case of the GdL, which usually requires prolonged times to form the network.<sup>64</sup> All gels appeared homogeneous and opaque (**Figure 4.4**).

The final pH of these gels (see **Table 4.1**) was affected by the chemical processes occurring inside of them. When the environment was alkaline because of the addition of NaOH and CaCl<sub>2</sub> solution as trigger, the final pH was 8. Since the starting concentration of [OH<sup>-</sup>] was 1 M, this final value suggested that a relevant part of the OH<sup>-</sup> groups were involved in the salification of the gelator. When Na<sub>2</sub>CO<sub>3</sub> was used instead of NaOH, the drop of pH was higher (samples **4C** and **4D** of **Table 4.1**), probably because Na<sub>2</sub>CO<sub>3</sub> was consumed by the salification process of the gelator molecules and by the formation of CaCO<sub>3</sub>.

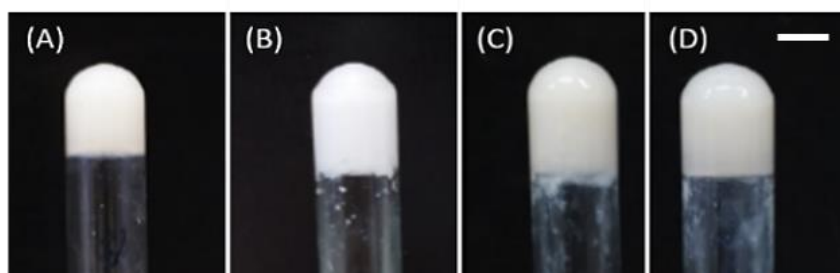


**Figure 4.4** Photographs of the hydrogels prepared using gelator **4** in 1% w/w concentration. From the left: sample **4A**, **4B**, **4C** and **4D**. Scale bar: 5 mm.

The viscoelastic behaviour of the hydrogels in terms of storage ( $G'$ ) and loss ( $G''$ ) moduli was analysed through standard rheological experiments. The first analysis performed was an Amplitude Sweep to evaluate the LVE range, with a constant frequency  $\omega = 1 \text{ rad s}^{-1}$  (**Figure 4.5**).

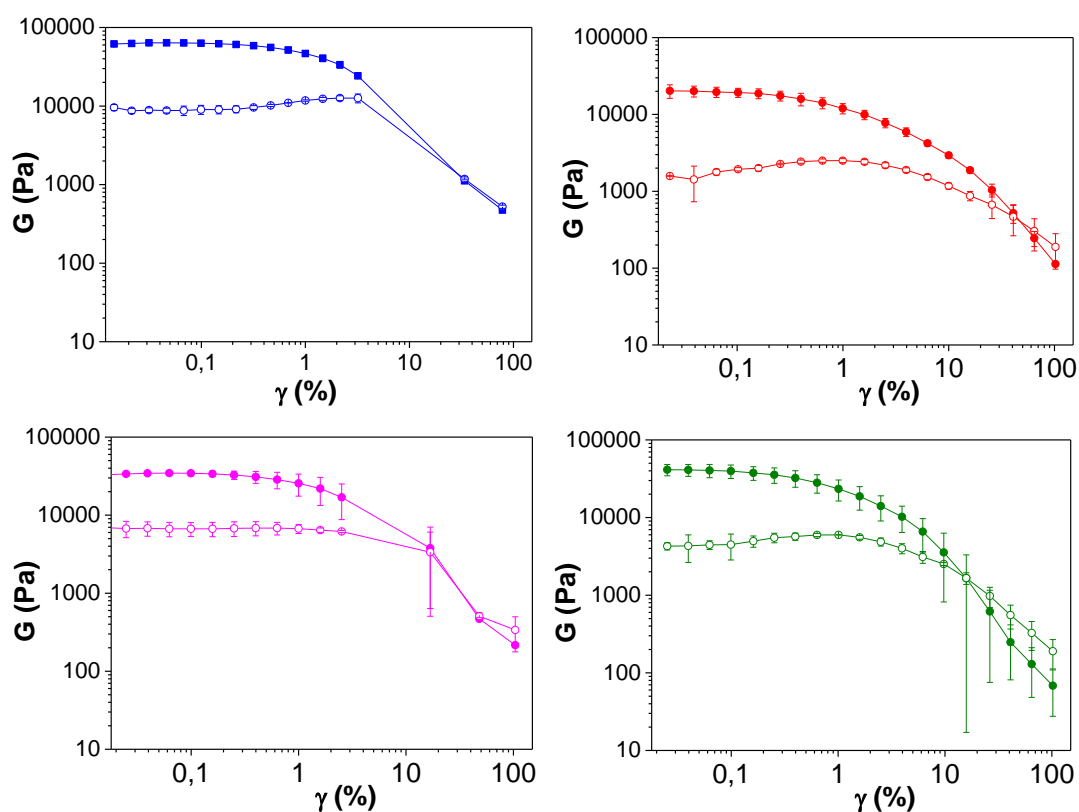


**Figure 4.5** Amplitude sweep experiments of the hydrogels **4A** (blue), **4B** (red), **4C** (pink) and **4D** (green), made with 1% w/w concentration of gelator **4**. The analyses were performed on the gels about 20 hours after the gelation begun. Storage modulus: solid circles, loss modulus: empty circles. The analyses were repeated three times for each sample.

All the hydrogels prepared are characterized by  $G'$  approximately an order of magnitude higher than  $G''$  (except samples **D** which are highly calcified), indicating their solid-like behaviour.<sup>199,229</sup> Frequency sweep experiments (**Figure 4.6**) were performed applying a constant shear strain within the LVE region of each sample ( $\gamma = 0.04\%$ ). For all hydrogels, both the  $G'$  and  $G''$  were almost independent from frequency in the range from 0.1 to 100  $\text{rad s}^{-1}$ , with  $G'$  always greater than  $G''$ .

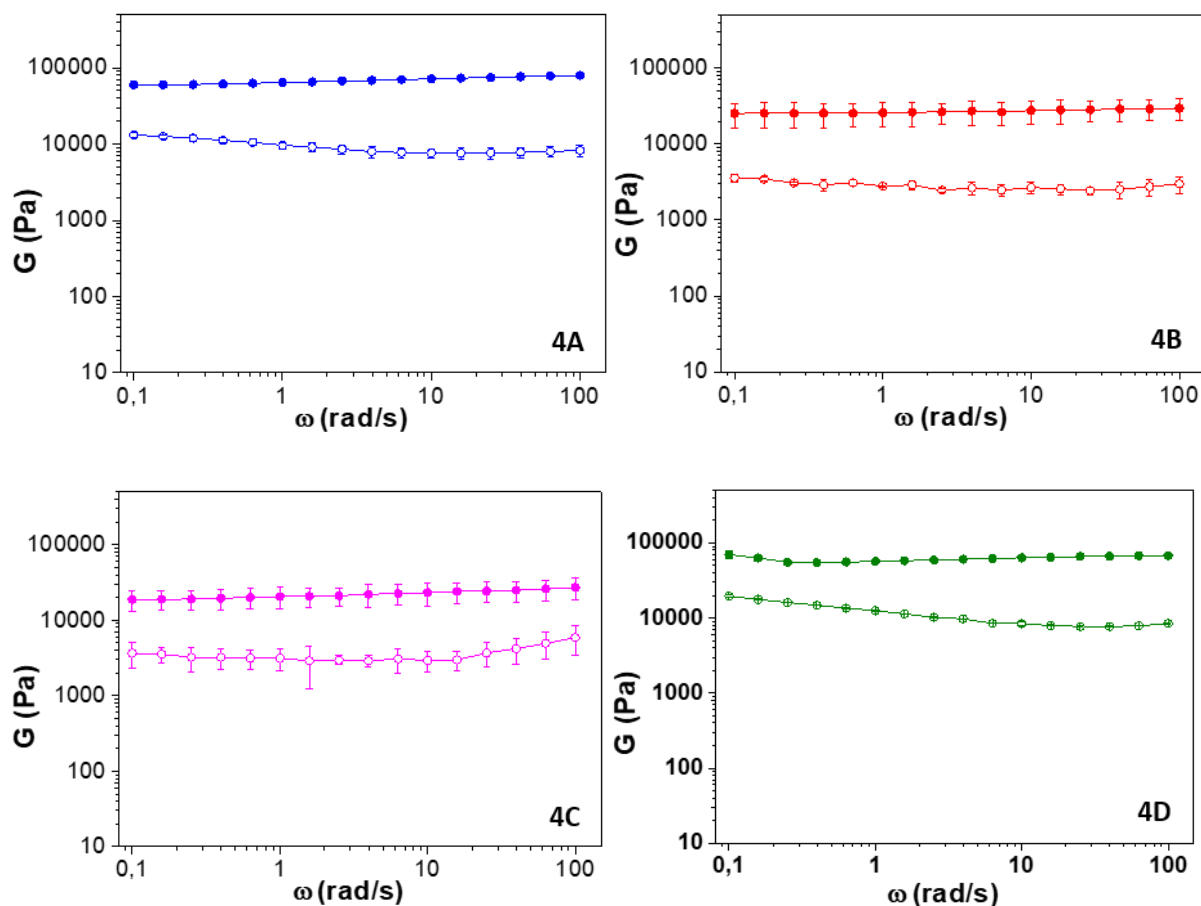


**Figure 4.6** Frequency sweep experiments (constant  $\gamma = 0.04\%$ ) performed on 1% w/w hydrogels. The analyses were performed in triplicate on the hydrogels about 20 hours after the beginning of gelation.

A comparison of the rheological properties of the four samples, taken from the frequency sweep experiment, is summarised in **Table 4.2**.

**Table 4.2** Values of  $G'$  and  $G''$  (mean moduli and standard deviation) from frequency sweep experiments ( $\gamma = 0.04\%$ ,  $\omega = 1$  rad/s).

| Sample | $G'$ (KPa)   | $G''$ (KPa)  |
|--------|--------------|--------------|
| 4A     | 64.181±2.761 | 9.648±0.884  |
| 4B     | 25.800±9.051 | 2.790±0.042  |
| 4C     | 20.650±6.435 | 3.140±0.990  |
| 4D     | 56.738±0.735 | 12.507±0.111 |

Finally, the system's ability to recover the gel status after a strong stress was checked. All samples were subjected to a strain value within the LVE region (characterized by  $G'$  values greater than  $G''$ ), followed by a stress that induces transformation into solution (thixotropy). These two steps were applied to the respective hydrogels for multiple cycles (**Figure 4.7**).

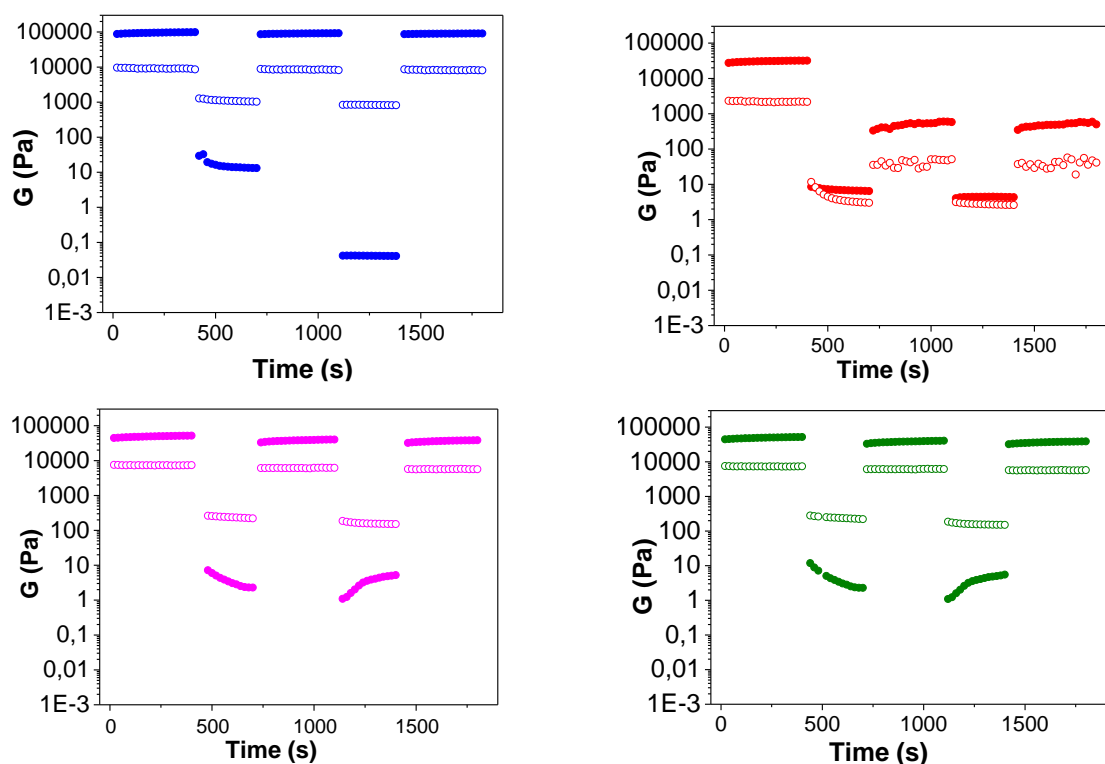


**Figure 4.7** Values of storage moduli  $G'$  (solid circles) and loss moduli  $G''$  (empty circles) recorded during step strain experiments performed on the hydrogel samples **4A** (blue), **4B** (red), **4C** (pink) and **4D** (green).

When the applied strain was increased above the crossover point, the sample behaviour switched from gel-like to sol-like, with  $G''$  values greater than  $G'$ . Then the samples rested at fixed strain within the LVE range and the recovery of the gel-like status was checked. Samples **4A**, **4C** and **4D** showed good thixotropic behaviour, as they promptly recovered their properties after each cycle. In contrast, hydrogel **4B** recovered a gel-like status after the first cycle, although the  $G'$  value was significantly reduced (from 21000 Pa to 400 Pa). After the second cycle, the hydrogel recovered again a gel-like behaviour with a  $G'$  value of about 400 Pa.

### 4.1.2 Reversibility of calcium uptake

The role of  $\text{Ca}^{2+}$  ions in hydrogel formation and the reversibility of calcium release (from the gel to the environment) and uptake (inside the gel from the environment) were then investigated. To perform this study, samples of hydrogel **4B** were immersed after gelation in a 0.05 M disodium ethylenediaminetetraacetate ( $\text{Na}_2\text{EDTA}$ ) dihydrate solution under gentle stirring for 5 hours (**4B-E**). The aim was to replace  $\text{Ca}^{2+}$  with  $\text{H}^+$  inside the gel network and to check possible changes in the gel properties. Then, sample **4B-E** was re-suspended in a  $\text{CaCl}_2$  solution for 5 hours (**4B-Ca**) to check the reversibility of calcium uptake. This study is represented in **Figure 4.8**.

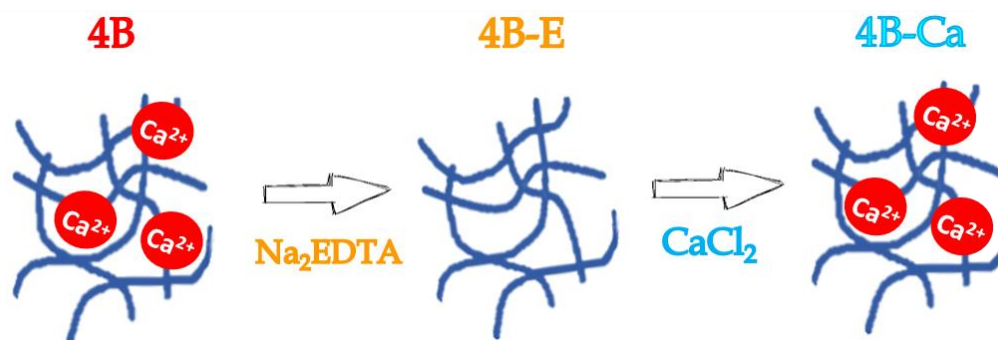


**Figure 4.8** Representation of calcium uptake from the gel network using  $\text{Na}_2\text{EDTA}$  and subsequent calcium addition to the network using  $\text{CaCl}_2$ .

The first treatment successfully removed  $\text{Ca}^{2+}$  from the hydrogel, as verified by the Energy-dispersive X-ray spectroscopy (EDX) spectrum of a fragment of the dry sample (xerogel) of **4B-E** (later named as **4B-EX**) in which no signal for calcium was observed (**Figure 4.9**). The following addition of calcium showed the presence of about 1 atom% content of calcium in the corresponding dry samples (later named as **4B-CaX**).

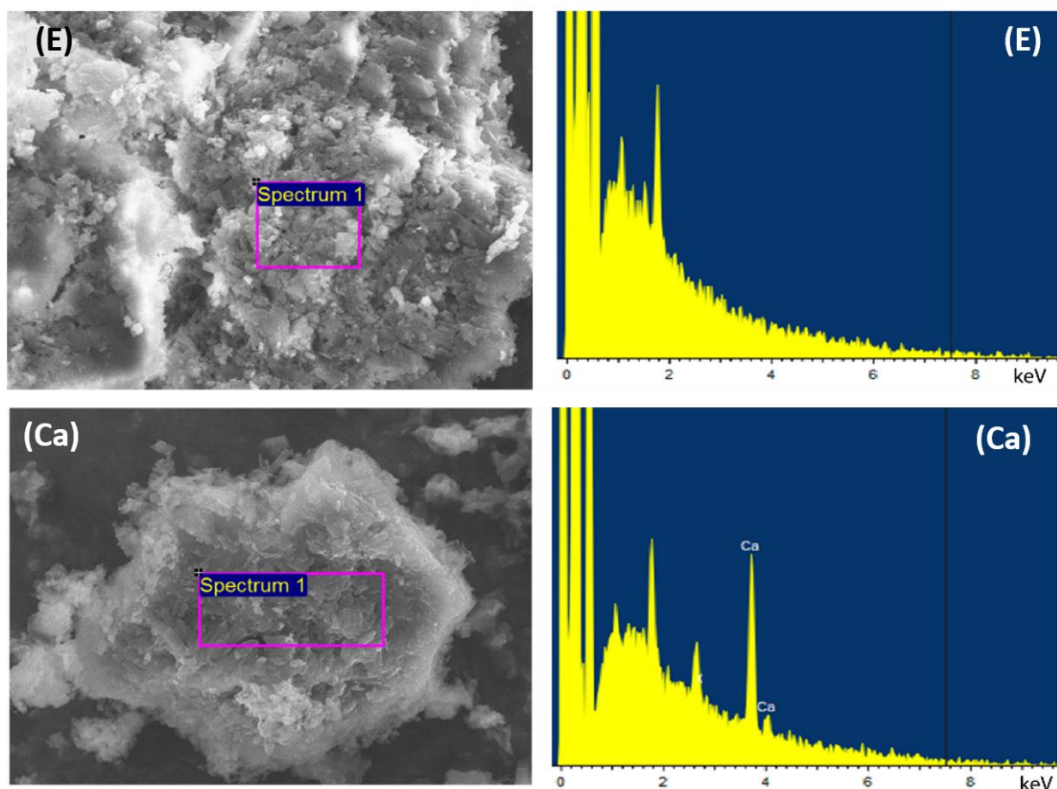


**Figure 4.9** EDX spectrum of the xerogel of **4B-E** (top) and **4B-Ca** (bottom). The area of collection of the EDX spectrum is the one inside the purple coloured quadrilateral. Only the xerogel sample of **4B-Ca** shows the peaks due to the presence of Ca.

The mechanical properties of sample **4B-E** were analysed with the rheometer and compared with those of sample **4B** (**Figure 4.10**, **Figure 4.11** and **Figure 4.12**).

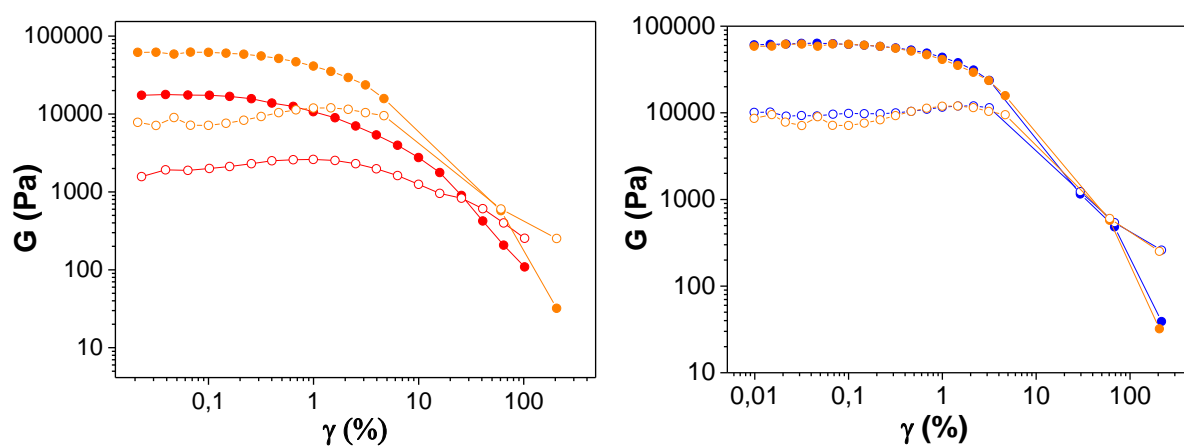


**Figure 4.10** Amplitude sweep experiments performed on the 1% w/w hydrogels. The results obtained for **4B-E** (orange) were compared with **4B** (on the left, red line) and **4A** (on the right, blue line). ( $G'$  modulus: solid circles,  $G''$  modulus: empty circles).

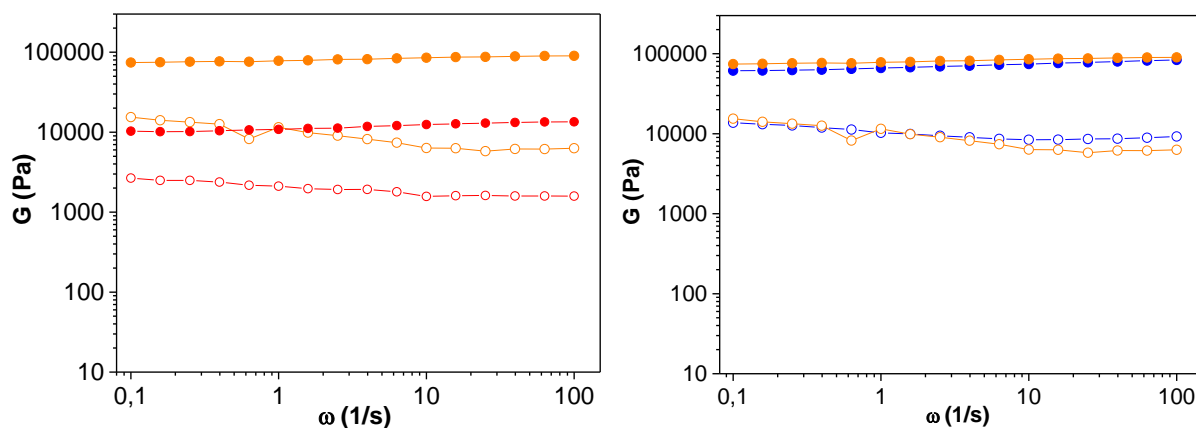


**Figure 4.11** Frequency sweep experiments (constant  $\gamma = 0.04\%$ ) performed on the 1 wt.% hydrogels. The results obtained for **4B-E** (orange) were compared with **4B** (red, left) and **4A** (blue, right). Storage moduli  $G'$  (solid circles) and loss moduli  $G''$  (empty circles).

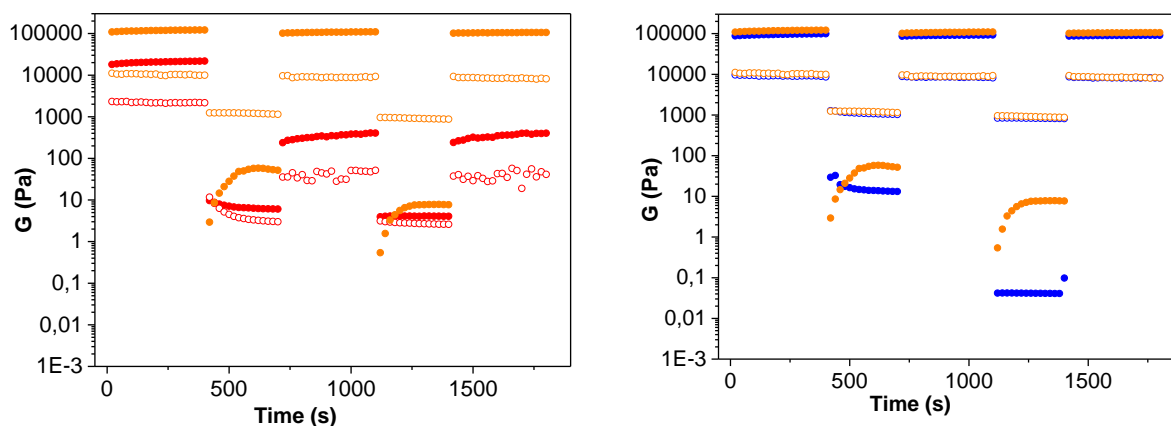


**Figure 4.12** Step strain experiments performed on the hydrogels. The results obtained for **4B-E** (orange) were compared with **4B** (red, left) and **4A** (blue, right). Storage moduli  $G'$  (solid circles) and loss moduli  $G''$  (empty circles).

Interestingly, hydrogels **4B-E** after the EDTA treatment are stiffer than sample **4B**, showing properties similar to those of sample **4A**, which does not include calcium in the network. When sample **4B-E** was re-suspended in a  $\text{CaCl}_2$  solution, no variation on its aspect neither on its mechanical properties were observed (**Figure 4.13**).

A possible reason for this behaviour can be found in the pH change during the treatment. After the removal of calcium with EDTA from hydrogel **4B** to form **4B-E**, the pH decreased from 8 to 4 and remained unchanged when sample **4B-E** was re-suspended in the calcium solution to form **4B-Ca**.

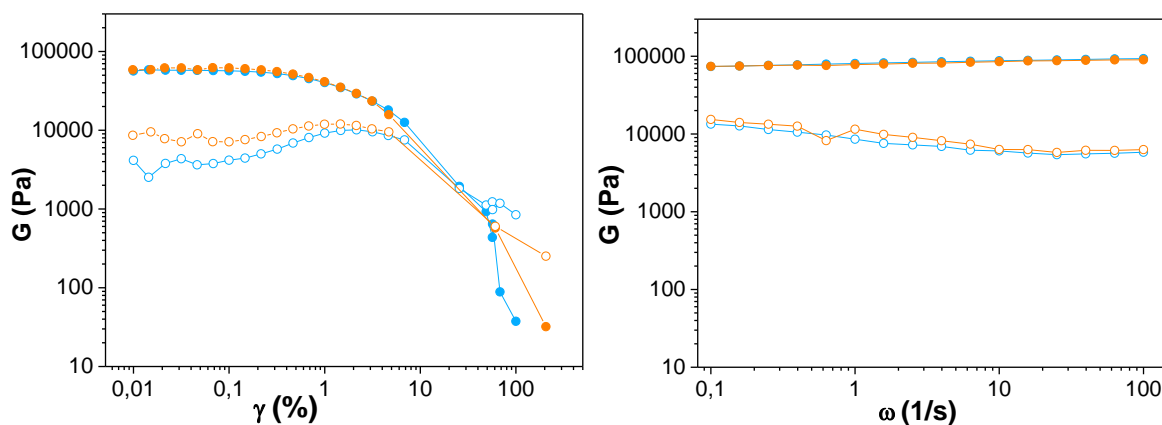


**Figure 4.13** Amplitude sweep experiments (left) and frequency sweep experiments (constant  $\gamma = 0.04\%$ , right) performed on the 1% w/w hydrogels. The results obtained for **4B-Ca** (light blue) were compared with **4B-E** (orange).

These outcomes suggest not only that it is possible to remove calcium from the hydrogel network, improving the mechanical properties of the material, but also that a modification in the organization of the supramolecular fibres occurs upon  $\text{Ca}^{2+}$  removal and this modification is not reversible by re-adding calcium ions.

### 4.1.3 Xerogel characterization

The drying process is usually a critical point for a gel, since the morphology of the network can change compared to the hydrated state producing artefacts, especially for aggregation processes that may take place.<sup>230,231</sup> To investigate hydrogels still containing the liquid phase some powerful techniques, such as cryo-TEM (Transmission Electron Microscopy), small angle X-ray scattering (SAXS) and small angle neutron scattering (SANS), are necessary but not always accessible. Nonetheless, it is often necessary to produce dried samples to have at least an idea of the morphology of the gel. Two types of dry gels can be produced depending on the drying method: xerogels are obtained when the gel is allowed to dry in air, while to produce aerogels the sample is first frozen and then freeze dried.

Xerogels were here produced to perform SEM and synchrotron XRD analyses. These tools were exploited to investigate the mineral phase formed and the interactions between fibres and crystals more than the morphology of the hydrogel itself. Taking into account the focus of these

analyses on the crystalline phase, it was also decided to wash the samples (using two methods) to remove part of the fibres and produce cleaner crystals.

With *procedure 1*, xerogels of samples **4A**, **4B**, **4C**, **4D**, **4B-E** and **4B-Ca** were obtained by solvent removal in oven. The dried samples were washed with ethanol to remove part of the fibrous network of the gel and have cleaner crystals for the following analyses, then they were dried again and named **4AX**, **4BX**, **4CX**, **4DX**, **4B-EX** and **4B-CaX** (X for xerogels). SEM images were collected for sample **4CX** and **4DX** before and after ethanol washing to make a comparison. The ethanol wash produces cleaner crystals, as reported in **Figure 4.14** (right) for sample **4CX**.

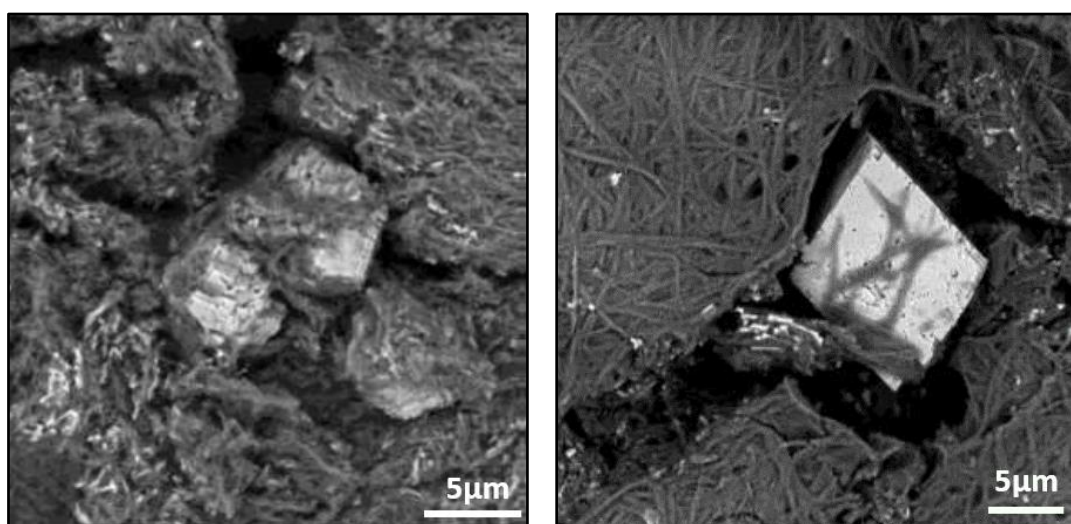


**Figure 4.14** SEM images of xerogel **4CX** before (*left*) and after (*right*) washing with ethanol.

For some samples of hydrogels **4C** and **4D** the xerogels were prepared with a modified procedure (*procedure 2*) based on washing with water and ethanol before solvent removal in oven, thus forming the modified xerogels **4CX#** and **4DX#**. This procedure was envisaged to remove unreacted ions and molecules and change the hydrogel chemical environment before drying. The SEM images of the samples **4AX**, **4BX**, **4CX** and **4DX** are reported in **Figure 4.15**.

Compared to sample **4AX**, in sample **4BX** the presence of calcium determines evident differences in the morphology and fibres organisation. In sample **4BX**, the fibrous structure is well visible: the fibres are separated one from the other and form a network in which they are strongly entangled, also thanks to the branching that appears in some fibres.

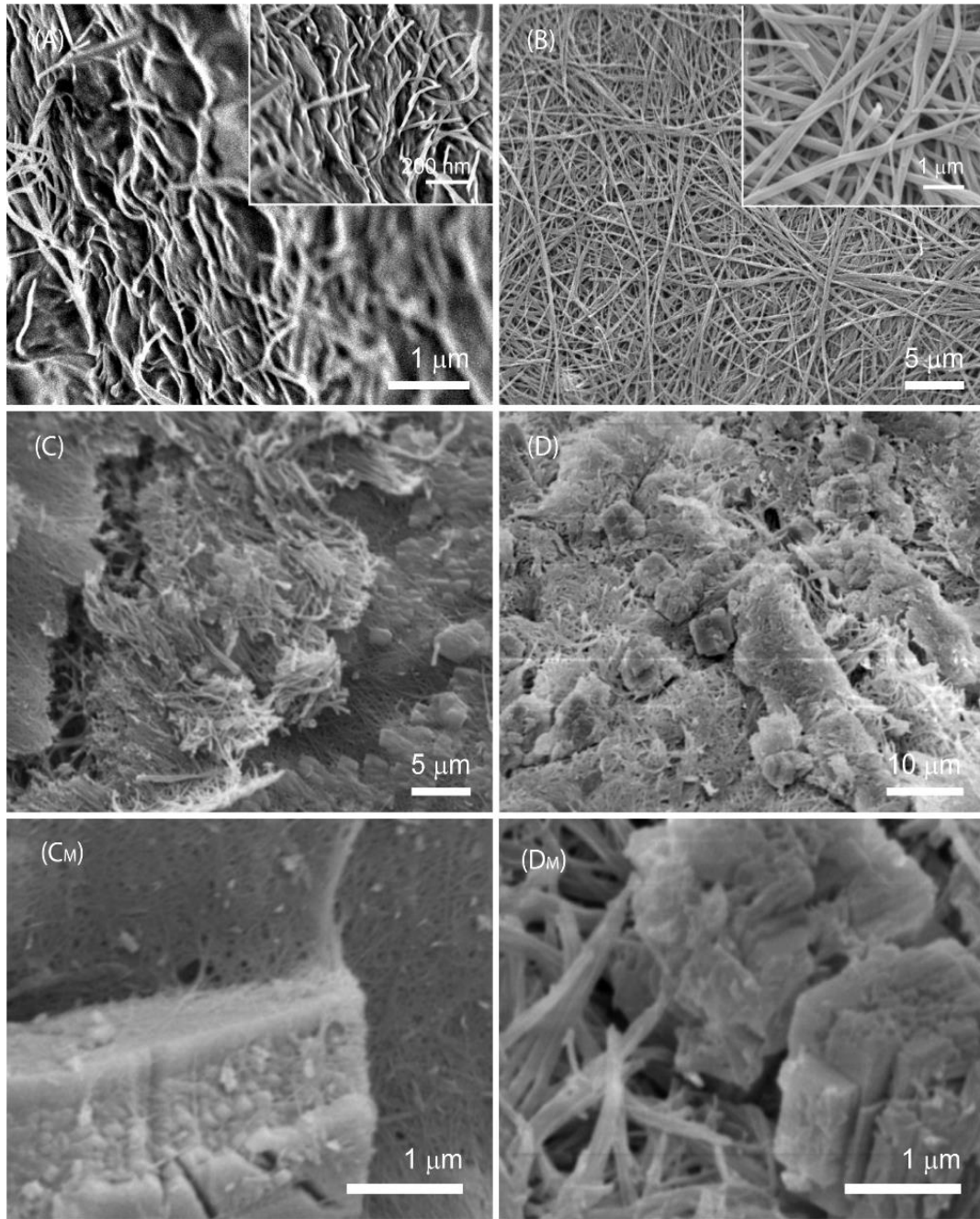


**Figure 4.15** SEM images of the xerogel samples **4AX** (A), **4BX** (B), **4CX** (C and magnification  $C_M$ ) and **4DX** (D and magnification  $D_M$ ). The insets in (A) and (B) illustrate a high magnification image for xero-1 and xero-2. The images ( $C_M$ ) and ( $D_M$ ) illustrate the composite nature of the calcite crystals from **4CX** and **4DX** that entrap gelator fibres. Each image is representative of the entire sample.

In sample **4AX**, on the contrary, the fibres, around 25 nm in diameter, are partially embedded in a compact matrix, that prevents an accurate determination of the average diameter.

In the two samples containing both calcium and carbonate ions, **4CX** and **4DX**, a fibrous

structure is present, with entrapped calcium carbonate crystals inside. Both composites show a high embedding of the crystals inside the fibrous network. The fibres entrap the crystals almost completely and even penetrate inside them, thus forming an organic-inorganic composite material (**Figure 4.15** C<sub>M</sub> and D<sub>M</sub> and **Figure 4.16** C and D).

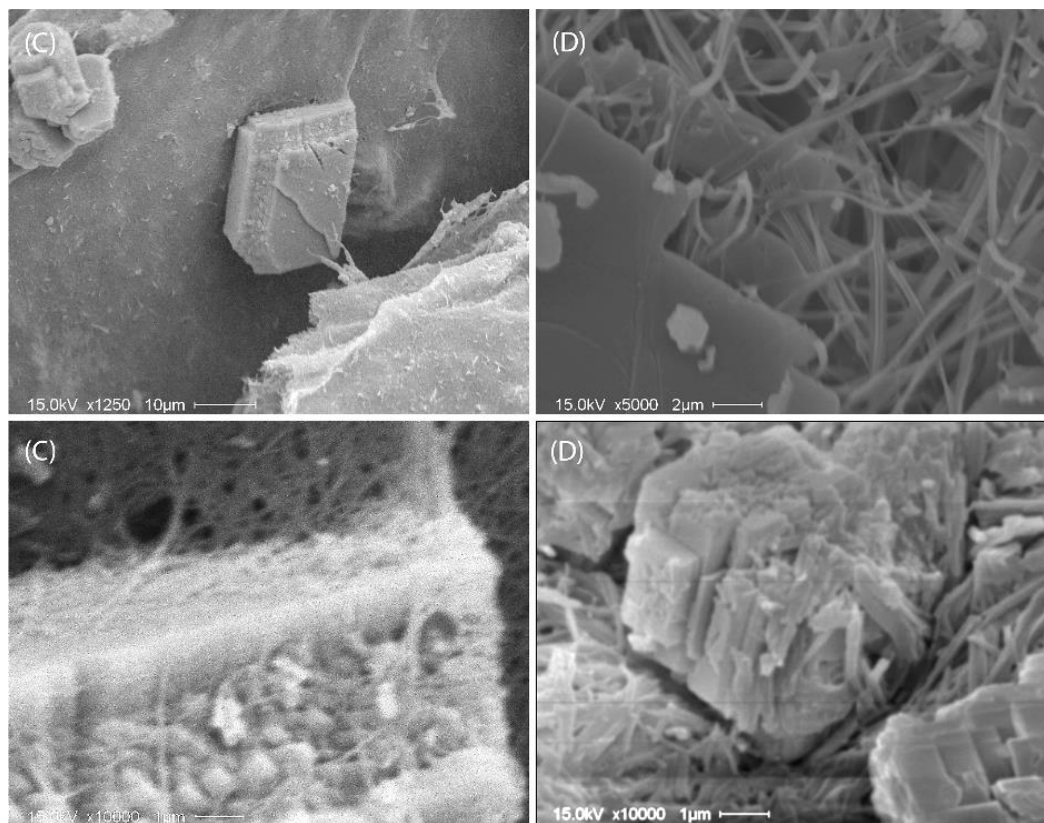


**Figure 4.16** SEM images of the xerogel samples **4CX** (C) and **4DX** (D).

The amount of crystals observed in sample **4CX** is lower than that in sample **4DX**, as expected since the concentrations of calcium and carbonate ions were lower in the starting chemical system of hydrogel **4C**.

For what concerns the study on the reversibility of calcium uptake, the SEM images of the xerogels after the EDTA treatment (**4B-EX**) and after the re-addition of calcium (**4B-CaX**) are reported in **Figure 4.17**. It is possible to notice that sample **4B-EX** has the same fibre organization observed in sample **4BX**, an entanglement of separated and well-defined fibres, with almost constant diameters. Sample **4B-CaX** is heterogeneous, composed by fibres, similar to those observed in sample **4BX**, and less defined segments, similar to those observed in sample **4CX** and **4DX**.

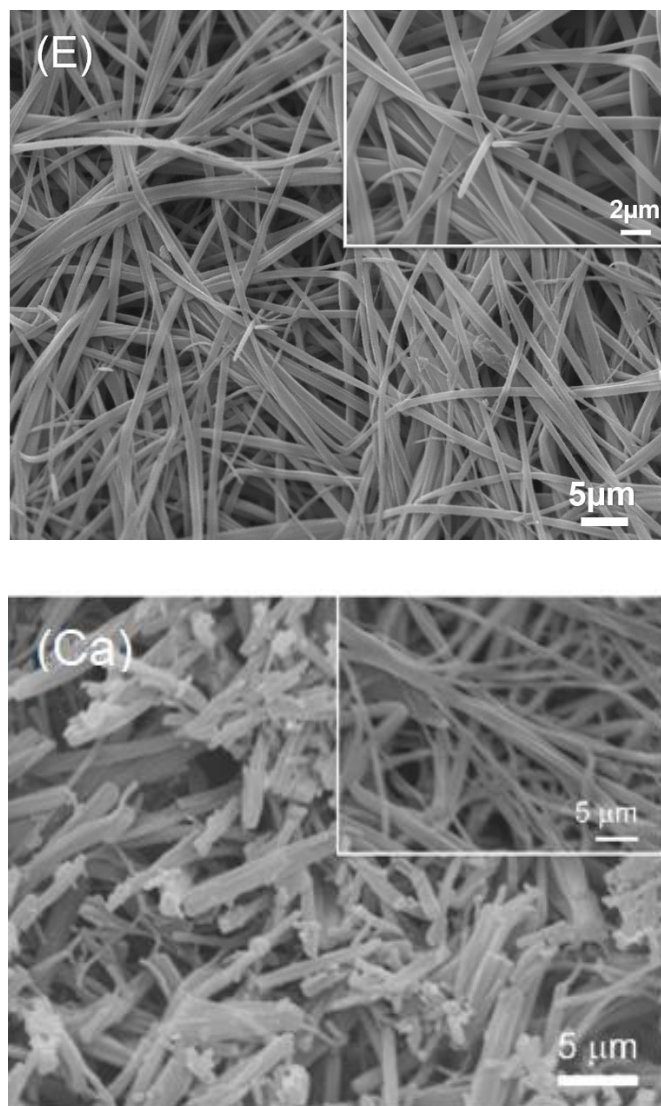


**Figure 4.17** SEM images of the xerogel samples **4B-EX** (E) and **4B-CaX** (Ca).

The fibres diameter distribution was analysed through a box plot, taking the diameters from the SEM images of samples **4BX**, **4B-EX** and **4B-CaX** ( $n \geq 50$ ).<sup>232</sup> The box plots are shown in **Figure 4.18** and reveal a different diameter distribution for the fibres obtained in different conditions. It is possible to notice that when calcium ions are involved in the formation of the hydrogels, fibres are thin. Unlike, when the calcium ions are removed from the hydrogel fibres by the interaction with EDTA, an aggregation process occurs, which is preserved in the xerogel.

The structure of the xerogels was then investigated by synchrotron X-ray diffraction. The corresponding X-ray powder diffraction patterns, obtained by integration of the intensities along the  $2\theta$  angle, are reported in **Figure 4.19**.

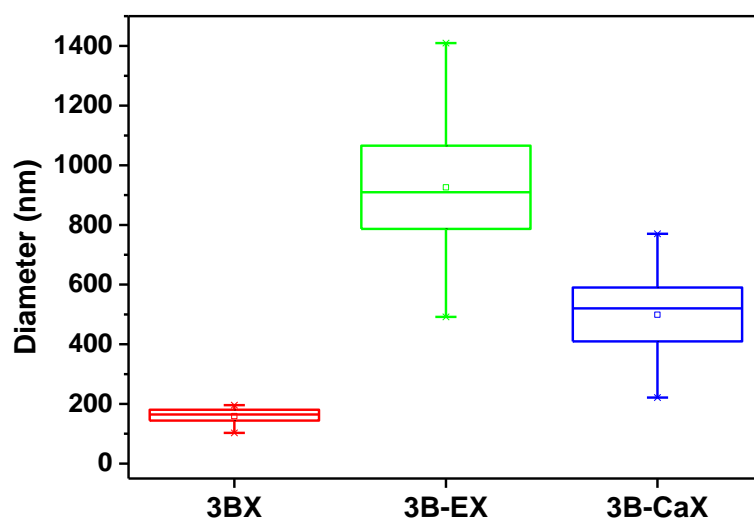


**Figure 4.18** Box plot showing the distribution of the fibres diameters measured in the xerogel obtained from the samples **4BX**, **4B-EX** and **4B-CaX**.

These data show that all xerogel samples were crystalline and with different structures, according to their synthesis, or their post-synthesis treatment. The xerogels of the four starting samples **4AX**, **4BX**, **4CX** and **4DX**, show intense low angle diffraction peaks at 2.99 nm and 1.74 nm; in addition, intense diffraction peaks at 0.51 nm, 0.46 nm and 0.34 nm are also observed (**Figure 4.19**). The relative intensity of these peaks is different among the samples and this observation can be due to the preferential orientation effect. Other diffraction peaks were also observed at 1.46 nm, 0.99 nm, 0.92 nm, 0.67 and 0.61 nm that were common among the samples containing calcium (**4BX**, **4CX** and **4DX**). Sample **4AX**, the only one formed in presence of GdL without calcium, shows diffraction peaks at 1.34 nm and 0.83 nm, which are absent in the other samples, suggesting that in the presence of GdL the Boc-L-Dopa(Bn)<sub>2</sub>-OH assembly occurs with a diverse packing. The calcified xerogel, **4CX** and **4DX**, show additional diffraction peaks at about 0.38 nm, 0.301 nm and 0.228 that correspond to diffraction peaks of calcite.<sup>233</sup> No diffraction peaks that could be associate to other anhydrous or hydrated calcium carbonate polymorphs were observed. The diffraction patterns did not show any intense background signal that could suggest the presence of relevant amounts of amorphous calcium carbonate. The relative intensity of the diffraction peaks of calcite with respect to those of the fibres was higher in samples **4DX** than in samples **4CX**, indicating a higher concentration (not

quantified) of calcite in agreement with the higher concentration of  $\text{Ca}^{2+}$  and  $\text{CO}_3^{2-}$  in the starting hydrogel chemical system, as already observed from the SEM images.

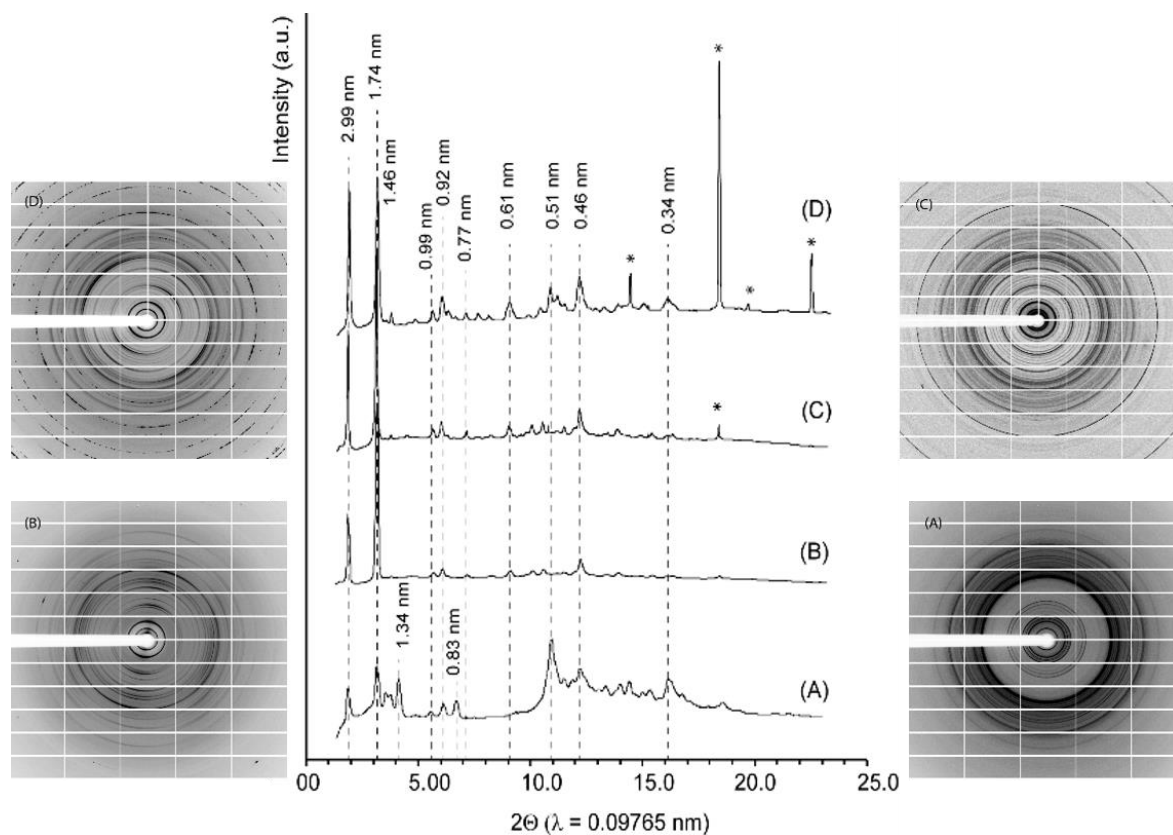


**Figure 4.19** (left and right side) Synchrotron X-ray fibre diffraction image of the samples **4AX** (A), **4BX** (B), **4CX** (C) and **4DX** (D). (centre) Corresponding powder diffraction profiles obtained by integration of the intensities along the  $2\Theta$  angle. The main diffraction peaks from the xerogel structure are indicated with their associated periodicities. The diffraction peaks of calcite are marked by an asterisk.

Different structures were observed in samples **4B-EX** and **4B-CaX** (Figure 4.20), obtained by EDTA decalcification of the sample **4B** and subsequent incubation in a  $\text{CaCl}_2$ , respectively. Their diffraction patterns showed several diffraction peaks having the same periodicities, but different relative intensities. Most of these diffraction peaks were at different periodicities from those observed in the samples **4AX**, obtained in the absence of  $\text{Ca}^{2+}$ , and **4BX**, formed in presence of  $\text{Ca}^{2+}$ , with the exception for diffraction peaks at 0.51 nm, 0.46 nm. In **4B-EX** and **4B-CaX** low angle diffraction peaks were at 2.51 nm and a 1.26 nm. In the same samples other intense peaks were observed at 0.94 nm, 0.87 nm and 0.37 nm, while in the sample **4BX** most of these peaks were very weak.

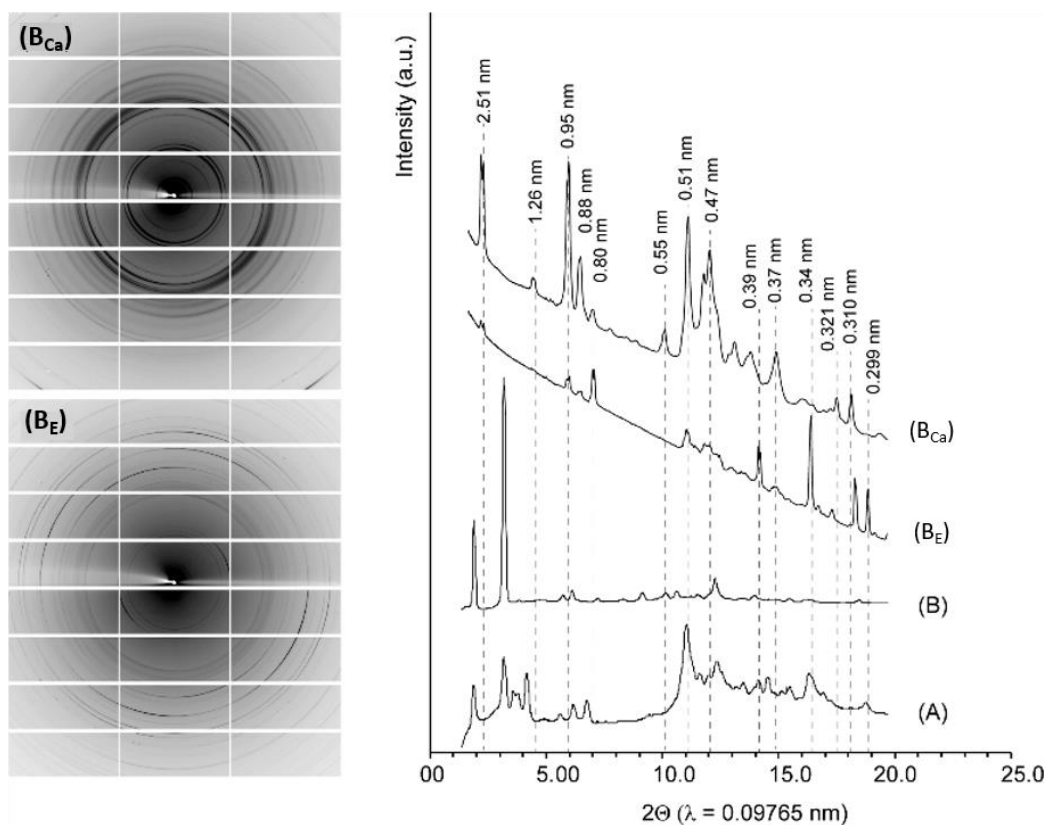


**Figure 4.20** (*left*) Synchrotron X-ray fibre diffraction image of the samples **4B-EX** ( $B_E$ ) and **4B-CaX** ( $B_{Ca}$ ). (*right*) Corresponding X-ray powder diffraction profiles obtained by integration of the intensities along the  $2\Theta$  angle. The main diffraction peaks from the xerogel structure are indicated with their associated periodicities. The X-ray powder diffraction profiles from the samples **4AX** (A) and **4BX** (B) are reported for comparison.

Xerogels **4CX#** and **4DX#**, prepared with *procedure 2*, show a different organization of the fibres and the presence of fibres bundles (**Figure 4.21**).

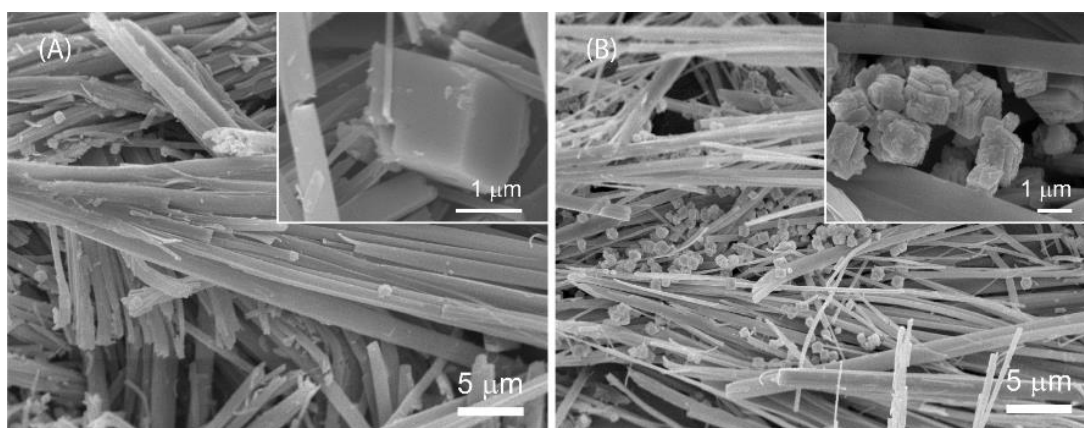


**Figure 4.21** SEM images of the xerogel samples **4CX#** (A) and **4DX#** (B).

Even in these samples the amount of crystals of calcium carbonate formed in sample **4DX#** is clearly higher than that of sample **4CX#** and related to the ion concentrations of the starting solutions.

In conclusion, SAFiN hydrogels that can be exploited as a bio-inspired matrix for calcification were prepared using a simple and robust process. They formed through electrostatic and  $\pi$ - $\pi$  stacking interactions of Boc-L-DOPA(Bn)<sub>2</sub>-OH molecules in aqueous solutions. The four kinds of hydrogels were prepared by varying the trigger (GdL or CaCl<sub>2</sub>) and the base. They were solid-like with mechanical, compositional and structural properties depending on choice of the trigger. When Na<sub>2</sub>CO<sub>3</sub> was used to alkalinize and CaCl<sub>2</sub> as trigger, calcite crystals formed within the conserved solid-like hydrogel, generating a composite material. When Ca<sup>2+</sup> was replaced with H<sup>+</sup> the SAFiN hydrogel assumed the same properties of the one formed using GdL as trigger. This suggested that once assembled the hydrogel molecular chains relied more on the  $\pi$ - $\pi$  stacking interactions than on the source of the electrostatic ones.

The calcified hydrogels produced xerogels that gave different X-ray fiber diffraction pattern and morphology if harshly washed before drying. It has been supposed the inter-fibril interactions were affected by the washing, which by removing unreacted molecules and free ions changed the chemical environment. Of course, these considerations are derived by observations on xerogels and could be not representative of the fibre structures and interactions inside the hydrogels.

In all xerogels from calcified hydrogels, calcite crystals were observed to be entrapped in the fibre network and entrapping fibres within their structure, generating a composite material. This scenario is supposed to be a realistic prediction of the hydrogel, since calcite formed into the hydrogel. In addition, the amount of calcite crystals formed, which was qualitatively evaluated, increased with the concentrations of calcium and carbonate ions in the starting hydrogel chemical system. These final observations confirm the starting hypothesis that the fibrous structure of the hydrogel can be considered a bio-inspired matrix that has the capability to confine the space of mineralization, to act as a source of Ca<sup>2+</sup> and to preserve its structural organization once the mineral formation has occurred, as frequently occurs in biomineralization.

#### 4.1.4 Materials and methods

**Conditions for Gel Formation** - The control sample (**4A**) was prepared by adding Milli-Q® water (0.97 mL) and aqueous 1 M NaOH (1.3 equiv.) to a test tube (8 mm of diameter) containing 10 mg of the gelator, in order to produce a final concentration of the gelator of the 1% w/w. The mixture was stirred and sonicated in turn for about 30 minutes until the complete dissolution of the sample. Then glucono- $\delta$ -lactone (1.4 equiv.) was added to the mixture. After a rapid mixing and complete dissolution of GdL, the sample was allowed to stand quiescently until gel formation, which occurred over several hours.

Sample **4B** was prepared by adding Milli-Q® water (0.76 mL) and aqueous 1 M NaOH (1.3 equiv.) to a test tube (8 mm of diameter) containing 10 mg of the gelator to produce a final concentration of the gelator of the 1% w/w. The mixture was stirred and sonicated in turn for about 30 minutes, until the complete dissolution of the sample. Then a 0.1 M aqueous CaCl<sub>2</sub> solution (1 equiv.) was added to the mixture. After a rapid and complete dissolution of CaCl<sub>2</sub>, the sample was allowed to stand quiescently before further studies, even if the formation of gel occurs immediately.

Sample **4C** and **4D** were prepared following the same procedure as for sample **4B**, but, instead of NaOH, Na<sub>2</sub>CO<sub>3</sub> was used. In sample **4C** and **4D** 1 and 2.5 equiv. of Na<sub>2</sub>CO<sub>3</sub> and 1 and 5 equiv. of CaCl<sub>2</sub> were respectively employed (see Table 1).

**Rheology** - Rheological measurements were performed on an Anton Paar Rheometer MCR 102 using a parallel plate configuration (25 mm diameter). The experiments were performed at a constant temperature of 23 °C, controlled by the integrated Peltier system. All analyses were performed with a fixed gap value of 0.5 mm on the respective gel samples, prepared the day before the analysis and left overnight at a controlled temperature of 20 °C to complete the gelation process (around 20 hours). Oscillatory amplitude sweep experiments ( $\gamma$ : 0.01–100%) were carried out to determine the linear viscoelastic range at a fixed frequency of 1 rad s<sup>-1</sup>. Once the LVE of each hydrogel was established, frequency sweep tests were performed ( $\omega$ : 0.1–100 rad s<sup>-1</sup>) at a constant strain within the LVE region of each sample ( $\gamma = 0.04\%$ ). Step strain experiments were performed on hydrogels to analyse the thixotropic behaviour of the material. The sample was subjected to consecutive deformation and recovery steps. The recovery step was performed by keeping the sample at a constant strain  $\gamma = 0.04\%$ , i.e. within

the LVE region, for a period of 400 s. The deformation step was performed by applying to the gel a constant strain  $\gamma = 100\%$ , i.e. above the LVE region of the sample for a period of 300 s. The cycles were performed 3 times at a fixed frequency  $\omega = 10 \text{ rad s}^{-1}$ .

### **Samples Preparation for X-Ray Diffraction and Scanning Electron Microscopy analysis**

Two procedures were used for the preparation of the xerogels.

**Procedure 1.** Each hydrogel (1 mL) was oven-dried 3 hours at 100 °C until it became completely dry. Then the sample was washed twice with ethanol (2 x 2 mL). After the solvent addition, the test tube containing the sample was stirred with Vortex (1 min) and spin-dried (5 minutes - 5000 rpm), then the supernatant was removed. The solid residue was oven-dried at 100 °C for two hours.

**Procedure 2.** Each hydrogel (1 mL) was washed twice, with Milli-Q® water (2 mL) followed by ethanol (2 mL). In both cases, after solvent addition, the test tube containing the sample was stirred with Vortex (1 min) and spin-dried (5 minutes - 5000 rpm), then the supernatant was removed. The solid residue was oven-dried at 100 °C for two hours. These samples were named with an #.

**EDTA treatment** - After gelation, hydrogel **4B** (1 mL) was placed in a vial with 6 mL of a 0.05 M Na<sub>2</sub>EDTA solution and gently stirred for 5 h. Then, the solution was removed and the sample was used for rheological analyses (**4B-E**). Before SEM and XRD analysis, the samples were washed according to the procedure reported above.

**EDTA-CaCl<sub>2</sub> treatment** - After gelation, hydrogel **4B** (1 mL) was placed in a vial with 6 mL of a 0.05 M Na<sub>2</sub>EDTA solution and gently stirred for 5 h. Then, the solution was replaced with 6 mL of a 0.1 M CaCl<sub>2</sub> solution. The solution was removed after 5 h and the sample was used for rheological analyses (**4B-Ca**). Before SEM and XRD analysis, the samples were washed according to the procedure reported above.

**Scanning Electron Microscopy** - For the SEM imaging the uncoated samples were observed with a Phenom G2 Pure using an energy of 3 kV. Gold coated (2 nm) samples were observed using a Hitachi SEM 6400 operating at 15 kV.

**X-ray fiber diffraction** - X-ray diffraction images were collected at XRD1 beamline, Elettra, Trieste, Italy and at the beamline ID23-1, ESRF, Grenoble, France. Each frame was collected

at the peak wavelength (0.9765 Å) using an exposure of 60 s. The XRD diagrams were analysed using Fit2D software.<sup>234</sup>

Number of experiments - All the experiments for the preparation of the hydrogel **4A**, **4B**, **4C**, **4D**, **4B-E** and **4B-Ca** were repeated at least three time. The preparation of the xerogels was performed using two experimental procedures that were also repeated at least three times for each sample. The rheological analyses were repeated three times. The scanning electron microscopy observations were performed on at the least three independent samples for each preparation. The diffractometric measurements were performed on one sample.

## 4.2 Fibre-reinforced Calcium Phosphate Cements (FRCPCs)

### 4.2.1 Calcium Phosphate Cements as bone scaffolds

Many synthetic biomaterials (e.g. metallic,<sup>235</sup> polymeric,<sup>236</sup> ceramic,<sup>237–239</sup> and cements,<sup>240,241</sup>) have been developed as bone substitute materials. Among them, an extensive research has been dedicated towards calcium phosphate cements (CPCs). Discovered in 1980s, CPCs are frequently used to repair bone defects because of their excellent biocompatibility, bioactivity, osteoconductivity, injectability and moldability.<sup>242,243</sup> CPCs are defined as a combination of one or more calcium phosphate powders which, upon mixing with a liquid phase (water or a solution containing calcium or phosphate), form a paste able to self-set and harden *in situ* in the bone defect site to form a scaffold.<sup>244</sup>

Bone is a complex material with a well-structured architecture. To obtain optimal bone integration and regeneration, the components and structure of bone repair materials are often functionalized using biomimicry. Inspired by the components of natural bones, in numerous studies organic and inorganic compounds have been used to obtain scaffolds and bone-repairing cements.<sup>245</sup> Bone cements are used as fillers in the treatment of metastatic bone disease, and as stabilizers in surgical procedures for the treatment of pain resulting from vertebral compression fractures, such as vertebroplasty (VP), balloon kyphoplasty, and vertebral body stenting.<sup>246</sup> Cements are, by definition, materials made up of one or more solid phases (powders) which when mixed with a liquid phase, give a mass of a modellable consistency, that hardens at room temperature.

Many cements are based on calcium phosphates (CPCs).<sup>247–249</sup> Tricalcium phosphate (TCP), also known as tribasic calcium phosphate, is a calcium salt with phosphoric acid. It has two different crystalline forms:  $\alpha$ -TCP and  $\beta$ -TCP, both used for the preparation of calcium phosphate cements.  $\beta$ -TCP is the allotropic phase, stable below 1180 °C, and has exactly the same chemical composition as  $\alpha$ -TCP, but a different crystallographic structure. The  $\beta$  form can be stabilized by some ionic impurities, such as magnesium ions. It is a bioabsorbable material but is not present in biological tissues. The different crystallographic structure makes  $\alpha$ -TCP less biodegradable than  $\beta$ -TCP.<sup>250</sup> Many of the most recent formulations are based on the use of  $\alpha$ -TCP ( $\alpha$ -Ca<sub>3</sub>(PO<sub>4</sub>)<sub>2</sub>) which, in aqueous solution and at physiological

pH, undergoes hydrolysis through a mechanism that involves the dissolution and subsequent precipitation of a more stable phase, similar to hydroxyapatite:



In this reaction scheme the main products are hydroxyapatite (HA) and phosphoric acid but the formation of other products, such as  $\text{CaHPO}_4 \cdot 2\text{H}_2\text{O}$  (dicalcium phosphate dihydrate - DCPD) or  $\text{Ca}_8\text{H}_2(\text{PO}_4)_6 \cdot 5\text{H}_2\text{O}$  (octacalcium phosphate - OCP), is also possible. Under physiological conditions of pH and temperature, these two products are transformed into HA, which is the most thermodynamically stable.<sup>251</sup> Actually, calcium deficient hydroxyapatite is mainly formed in a physiological environment. The non-stoichiometric phase of hydroxyapatite, the calcium deficient form, has chemical and structural properties similar to biological apatite. The hardening of cements occurs through the entanglement of the crystals formed by the reaction between  $\alpha\text{-Ca}_3(\text{PO}_4)_2$  and water.

The use of CPCs in orthopaedic surgery is limited due to their mechanical properties: calcium phosphates have relatively poor tensile and shear properties. The mechanical resistance of CPCs is lower than that of bone, teeth and bioceramics of sintered calcium orthophosphate. These properties limit the use of CPCs to areas not subjected to load or to areas subjected to pure compression load. Typical applications include the treatment of maxillofacial defects or deformities and cranial facial repair or augmentation of the spinal and tibial plateau.<sup>252-254</sup> An improvement in mechanical properties would significantly extend the applicability of calcium phosphate cements. This may be achieved by preparation of composite materials. The additives used to reinforce calcium phosphate-based cements are either polymers that penetrate the porous matrix or fibrous reinforcements. The mechanical strength of calcium phosphate composites with polymers can be improved. Biodegradable polymers lack however for the most part the stiffness, ductility and mechanical properties required for load bearing applications. Furthermore, the sterilization processes typically used (autoclave, ethylene oxide) can influence the properties of the polymer. Among all the approaches for the preparation of composite cements, the use of fibre reinforcements is one of the most successful. Cements exhibit typically brittle cracks and fracture without any prior plastic deformation. The mechanical behaviour of fibre-reinforced cements, on the other hand, is the result of the complex interaction between all the constituent components: the behaviour at macroscopic level depends on both the mechanical properties of the matrix and those of the reinforcement and on

the mechanical interaction between fibres and cement as well as complementary effects of additives or polymeric aggregates. In contrast to the brittle behaviour and fracturing which are characteristic of CPC cements alone, larger amounts of stress energy are absorbed before breakage of the fibre-reinforced counterparts (**Figure 4.22**). By subjecting *quasi-brittle* composites to critical loads, the matrix fractures but the fibre bridges dissipate energy, resulting in a delay of cements fracture.<sup>255</sup> In ductile composites, after elastic expansion, a loss of stiffness is observed but the composite can still absorb some load. Micro-cracks are formed, and their number and density increase with increasing tensile/bending load until reaching a saturation level.<sup>256</sup> Such multiple cracking can be macroscopically observed and is the key to composite ductility.

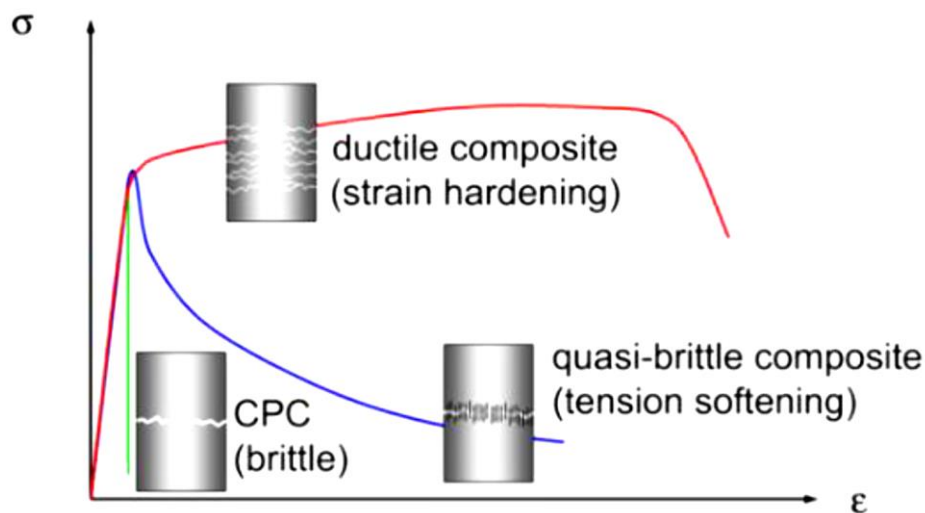


**Figure 4.22** Comparison between CPCs and FRCPCs in stress-strain curves.

Other factors related to the fibre, such as length, volume fraction, orientation and adhesion to the matrix, all may influence the final properties of the composite. The fusion of the fibres with the cement paste or precursor powder can be achieved by using different structures of the fibrous materials. The fibres can be introduced into the cements as short fibres or yarns (**Figure 4.23 a**) or as long fibres forming a random bundle (**b**). The random bundles can also be cut into small pieces and dispersed in the concrete matrix (**c**). If the fibres are intertwined to form a yarn, the latter can also be randomly cut and introduced into the cement (**a, b**), oriented (**e**), or it can be worked to form laminated textile structures (**d**).

It is possible to classify the CPC fibre composites reported in the literature into two groups: CPC composites with non-absorbable fibres, in which the fibres mechanically reinforce the

cement, and CPC composites with absorbable/biodegradable fibres, in which the fibres reinforce and create macro-porosity in the cement matrix after the degradation of the fibres, which allows tissue colonization by cells.<sup>257</sup>

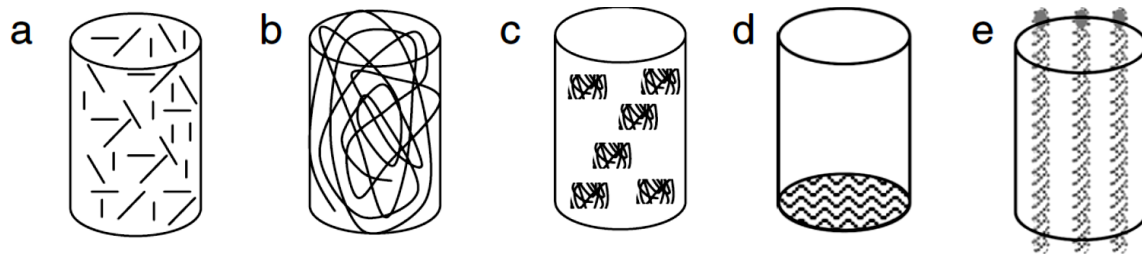


**Figure 4.23** Disposition of the fibres inside FRCPCs.<sup>257</sup>

A highly porous structure characterized by interconnected pores generally favours bone regeneration.<sup>257</sup> Mechanical properties of a material weaken as porosity increases, making the development of porous CPCs for bone tissue engineering challenging. The degradable polymers mainly used for this purpose are polyglycolic acid, polylactic acid (also as a copolymer with the previous one) and polycaprolactone.<sup>257</sup> In recent years, a fibre preparation technique (electrospinning) has allowed the preparation of ultra-fine polymeric fibres, from 100 nm to 5  $\mu\text{m}$ , which have excellent adhesion with the various elements of the matrix due to the large fraction of available surface. A composite reinforced with chitosan nanofibers was produced using the electrospinning technique.<sup>258</sup> Mechanical tests revealed that the tensile properties were significantly increased due to the introduction of nanofibers. It has therefore been hypothesized that the incorporation of ultrafine fibres into CPCs results in interconnected macropores and improves the toughness of the CPC.

The possibility of reinforcing bone cements based on calcium phosphates has already been explored in several works in the literature. However, the various fibre-CPC composites were obtained by inserting pre-formed fibres inside the cement matrix.

So far, no studies have been reported in the literature on the development of FRCPCs using fibres directly self-assembled inside bone cements. Nevertheless, the possibility to achieve a composite material reinforced with fibres growing directly inside the cement, would represent a unique opportunity to obtain a better cohesion between fibres and cement paste, thus improving the mechanical performances of the final material. The major challenge in the development of such innovative materials is the search for the right formulation of these

composites and the determination of the relationships between raw materials, process parameters and final properties, not to mention the effective feasibility of supramolecular fibres growth directly within the cements and during their setting.

If the self-assembled fibres are made of LMWGs, another important aspect to consider is the amount of liquid usually required for the formation of the networks. The general gelator/solvent ratio used to prepare LMWGs is below 50 mg/mL (5% w/w), and often even below 20 mg/mL (2% w/w). Such materials are mainly composed of a liquid phase. CPCs are mainly composed of the inorganic powder mix necessary for the formation of the cement. The liquid/powder (L/P) ratio, expressed in mL/g, can hugely vary depending on the starting cement powder, but is often comprised between 0.2 and 0.5, this meaning that for 1 g of inorganic powder mix the liquid (water) is only 0.2 or 0.5 mL. Until now, no studies have been reported in literature on the growth of self-assembling LMW fibres inside such a dense and compact inorganic matrix as that of bone cements.

#### **4.2.2 Self-assembled LMWG for FRCPCs**

In order to prepare bone cements containing self-assembled fibres, gelator **4** was chosen once again as LMWG, since it forms fibres in presence of calcium, which is compatible with bone scaffolds, and has a final pH close to the physiological one.

The general preparation of CPCs relies on i) mixing the starting material inorganic powders using an electric mortar (3M ESPE RotoMix) 2x20 s, ii) adding Milli-Q® water, iii) mixing the cement paste using the electric mortar (2x20 s) (**Figure 4.24**). The cement paste obtained is then compressed for 1 minute using an INSTRON 4465. After cutting the bottom edge of the cylindrical vial, the paste is extruded from it using a piston, and immersed for 7 days at 37°C in 0.1 M phosphate buffered saline (PBS) solution (pH 7.4) to simulate the physiological environment.

For the dissolution of gelator **4** in water, it is necessary to use alkaline water with a pH around 9-10, usually reached through the addition of NaOH 1M (see **4.1.4 Materials and Methods**). For this reason, in the general preparation of the cement paste, Milli-Q® water was replaced with an aqueous solution of NaOH 1M (1.3 eq. calculated with respect to gelator amount) in Milli-Q® water.



**Figure 4.24** General procedure for the preparation of CPCs.

The formation of fibres usually starts soon after the addition of the trigger ( $\text{CaCl}_2$ ). To obtain a homogeneous dispersion of the fibres inside the cement paste, several preparation methods were investigated. The inorganic powder mix for CPCs was kept constant in the different methods, and prepared using a literature procedure:<sup>259</sup> 25 mg of DCPD ( $\text{CaHPO}_4 \cdot 2\text{H}_2\text{O}$ ) were added to 475 mg of gelatine/ $\alpha$ -TCP (15% wt of gelatine with respect to the total amount), also prepared as previously reported.<sup>256</sup> This amount will be indicated as ‘starting material’ from now.

## 1. Method $\alpha$

In this first method, the trigger of the gelation,  $\text{CaCl}_2$ , as powder, is mixed to the starting material (which is also a powder mix) and the gelator dissolved in alkaline water is added later (**Figure 4.25**). For the preliminary test, a high amount of gelator (260  $\mu\text{L}$ , 5% w/w) was introduced inside the starting material together with 1 equivalent of  $\text{CaCl}_2$  to facilitate the formation of fibres in the compact powder matrix. The gels obtained with this method were named “**CaG5\_1\_260**” to indicate that the cement (C) was prepared with method  $\alpha$ , using gel (G) at 5% concentration (5) with 1 equivalent (1) of calcium trigger and 260  $\mu\text{L}$  of gelator aqueous solution (260).

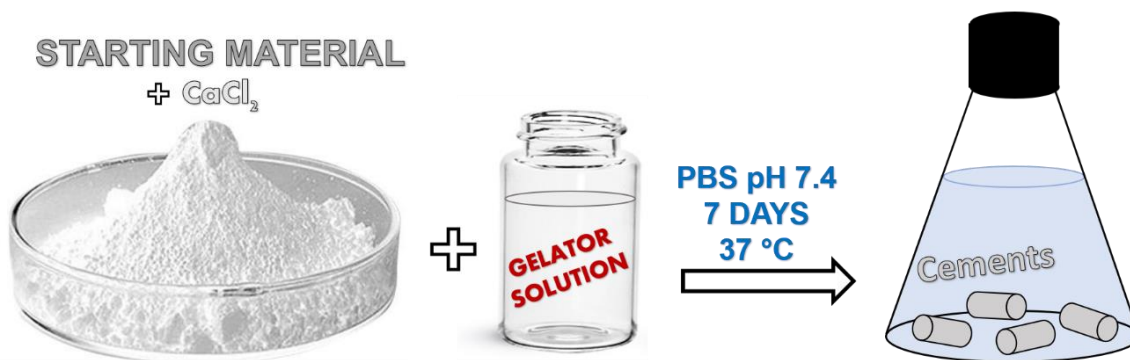


**Figure 4.25** Schematic representation of **Method a**.

The morphology of the cements obtained was analysed using SEM (**Figure 4.26**). The analyses highlighted the lack of fibres in all the cements prepared and the presence of small fragments of gel.

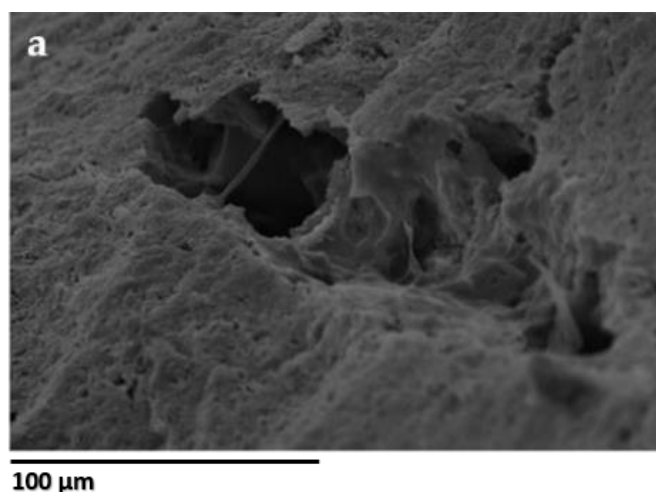


**Figure 4.26** SEM image of a) **CaG5\_1\_260**.

Thus, the preparation with 1 equivalent of CaCl<sub>2</sub> was replaced with two more preparations, one with 1.35 equivalents of CaCl<sub>2</sub> (**CaG5\_1.35\_260**) and the other with 1.6 equivalents of CaCl<sub>2</sub> (**CaG5\_1.6\_260**), following the same procedure previously described to obtain the cement paste. The SEM images (**Figure 4.27**) reveal again a compact structure with some fragments of gel. However, no fibres were observed even with higher equivalents of CaCl<sub>2</sub> and despite the use of highly concentrated gelator.

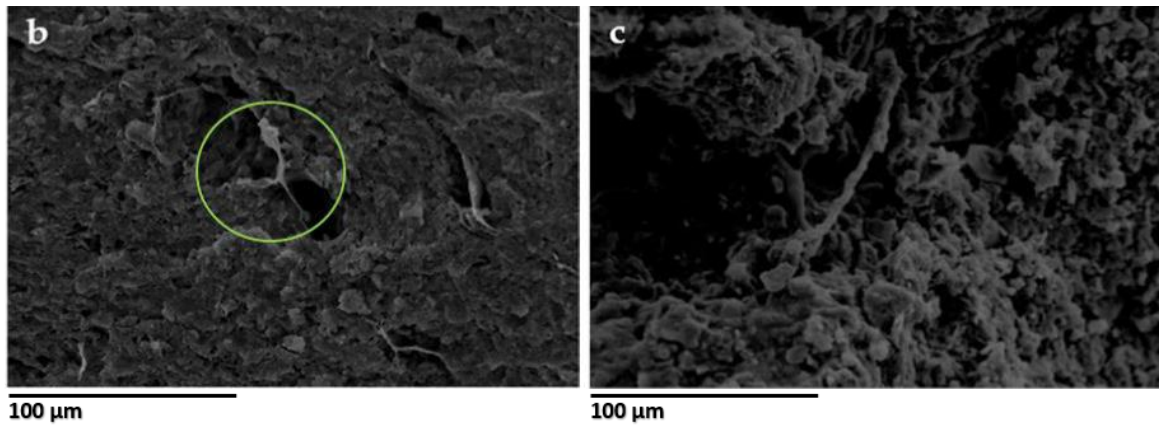


**Figure 4.27** SEM images of b)  $\text{CaG5}_{1.35\_260}$ ; c)  $\text{CaG5}_{1.6\_260}$ .

It was hypothesized that the gelator, even in such conditions, is unable to come into contact with the trigger dispersed in the gelatine-phosphate starting mixture, thus making the formation of the fibres difficult. For this reason, a further test was performed for the composition containing 1.35 equivalents of  $\text{CaCl}_2$ : the gelatine-phosphate starting mixture, the trigger and the gelator were carefully mixed in a mortar with pestle to favour both a better dispersion of  $\text{CaCl}_2$  inside the powders and the interaction between calcium and the gelator. From the SEM images shown in **Figure 4.28**, collected on the cements obtained with this procedure ( $\text{CaG5}_{1.35'\_260}$ ), it is possible to notice, in various points of the cement, the presence of fibres agglomerated in bundles, proving that fibre formation does not depend exclusively on the concentration of the gelator solution and the amount of trigger, but also on the way they are mixed.

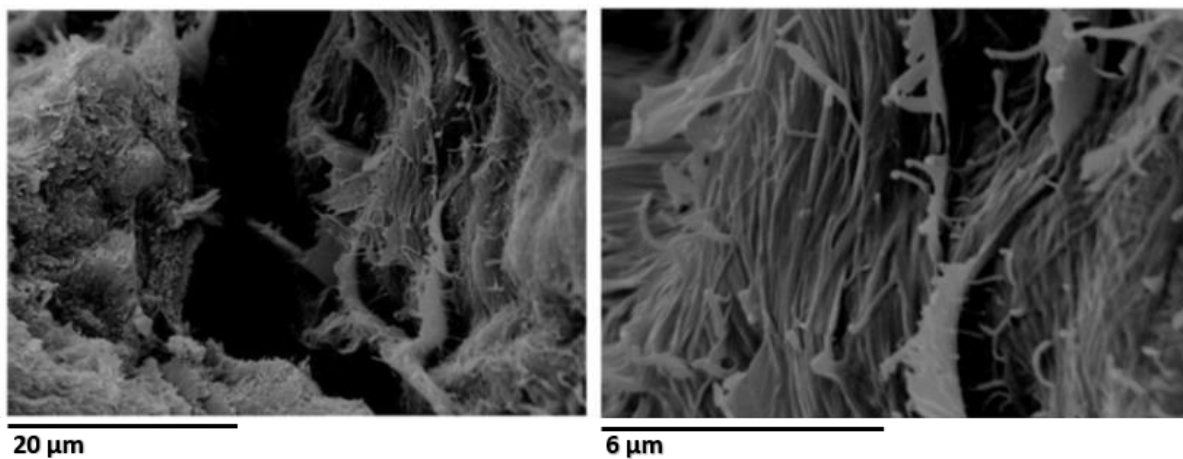


**Figure 4.28** SEM images of sample  $\text{CaG5}_{1.35'\_260}$  prepared in a mortar.

**Method  $\alpha$**  was considered unsuccessful for the reasons listed above and no further analyses were performed on the samples prepared. However, it was essential to understand that the formation of fibres highly depends on the mixing procedure, opening the way for the next preparation method.

## 2. Method $\beta$

In this second method ( $\beta$ ) the calcium trigger is added directly inside the gelator solution, mixed with the RotoMix, and soon after with the inorganic starting material (**Figure 4.29**) at time “0”. 1.35 equivalents of  $\text{CaCl}_2$  were first joined to the gelator solution and then the compound obtained was mixed with the starting material.



**Figure 4.29** Schematic representation of cements preparation with **Method  $\beta$** .

For this method, the 2% gelator solution was investigated (**C $\beta$ 0G2\_1.35\_260**) in addition to the 5% (**C $\beta$ 0G5\_1.35\_260**). Furthermore, since with a L/P ratio of 0.52 mL/g the cement paste was rather fluid, a smaller volume of gelator (200  $\mu\text{L}$ ) was also prepared (L/P = 0.40 mL/g) (**C $\beta$ 0G2\_1.35\_200** and **C $\beta$ 0G5\_1.35\_200**).

After 7 days immersed in PBS solution, all samples were cohesive and there was no dispersion of the powders in solution (**Figure 4.30**). The samples were then compared with reference samples, prepared using the same amount of starting material, water and calcium trigger, but without gelator. The reference samples for the preparation with 5% and 2% gelator were named **C5\_1.35\_260** and **C2\_1.35\_260** for the L/P ratio of 0.52 and **C5\_1.35\_200** and **C2\_1.35\_200** for the L/P of 0.40.



**Figure 4.30** Cements containing gel at 2% (a) and 5% (b) after 7 days immersed in PBS.

The mechanical properties of the composite cements were analysed through compression tests performed on cylindrical samples, using an INSTRON dynamometer equipped with a 5 KN load cell. Stress-strain curves were recorded using SERIES IX software for Windows. The compression tests on the cements were carried out after 7 days of immersion in PBS at 37 °C. Each test was repeated on four samples.

From the stress-strain curves the values of elastic modulus (E) and of the maximum stress ( $\sigma$ ) in compression were calculated. **Table 4.3** shows the comparisons between the reference cements and the cements containing fibres, with 5% gelator concentration.

**Table 4.3** Values of maximum stress ( $\sigma$ ) and elastic modulus (E) in compression tests for reference cements and fibre reinforced cements with 5% gelator.

| Sample                                 | $\sigma$ (MPa) | E (MPa)      |
|--|----------------|--------------|
| <b>C<math>\beta</math>0G5_1.35_260</b> | 15.4 $\pm$ 2.5 | 484 $\pm$ 82 |
| <b>C<math>\beta</math>0G5_1.35_200</b> | 9.7 $\pm$ 0.6  | 422 $\pm$ 73 |
| <b>C5_1.35_260</b>                     | 10.1 $\pm$ 0.1 | 468 $\pm$ 67 |
| <b>C5_1.35_200</b>                     | 11.6 $\pm$ 0.3 | 478 $\pm$ 40 |

The addition of 5% gel significantly affects the mechanical properties of the cements. From **Table 4.3** it is possible to notice that samples with 200  $\mu\text{L}$  of gel have lower mechanical properties not only compared to samples with 260  $\mu\text{L}$ , but also compared to reference cements. In addition, during the compression tests of the samples with 200  $\mu\text{L}$  of gel, the effect of axial compression results in a total crumbling of the material (**Figure 4.31 a**) while samples with a higher L/P ratio (0.52), after completing the compression test can be recovered as a single piece, even showing fractures in the form of cracks (**Figure 4.31 b**). This is the reason why the preparation containing 200  $\mu\text{L}$  were excluded from further characterisations.

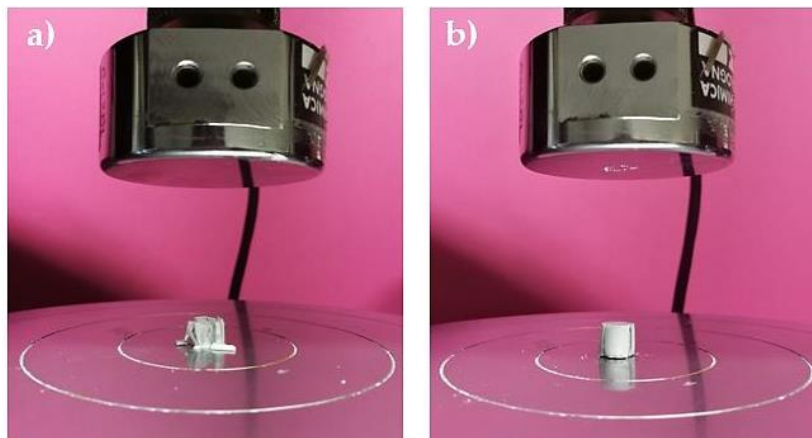


**Figure 4.31** Compression test on cement **C $\beta$ 0G5\_1.35\_200** (a) and **C $\beta$ 0G5\_1.35\_260** (b).

The morphological analysis of sample **C $\beta$ 0G5\_1.35\_260** highlighted the presence of highly porous matrices. The gelator fibres entirely cover the inner walls of the pores and, in some places, are grouped to form small bushes (**Figure 4.32**).

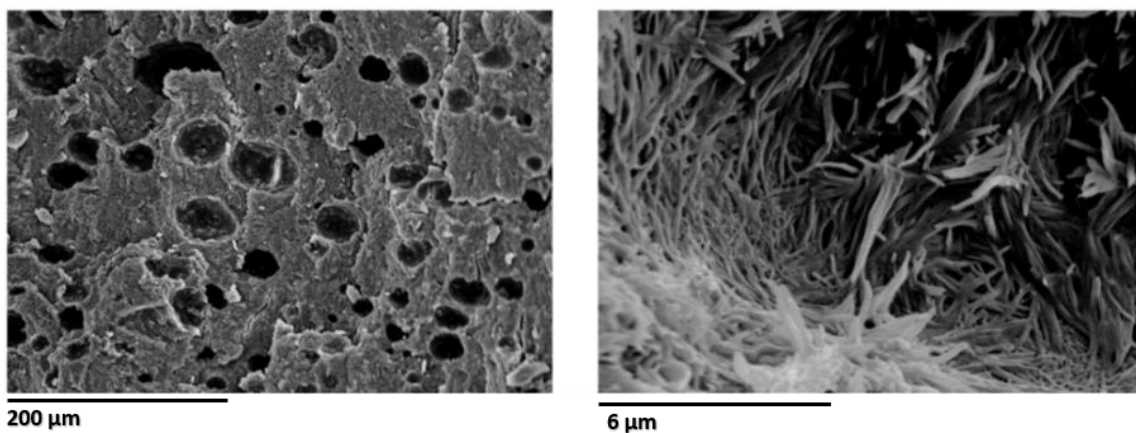


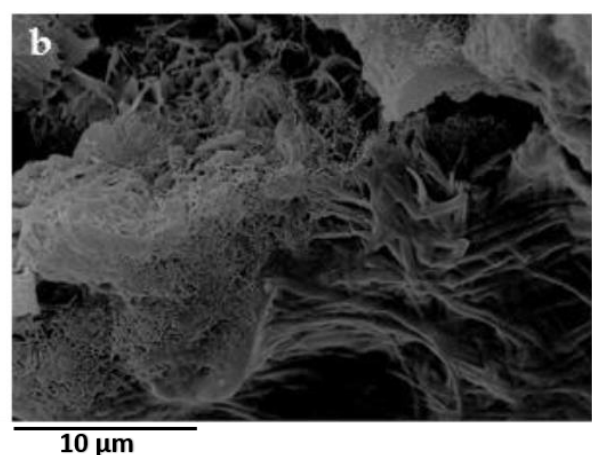
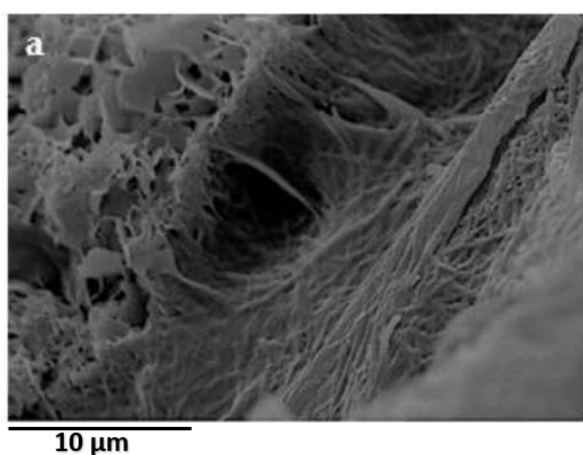
**Figure 4.32** SEM images of sample **C $\beta$ 0G5\_1.35\_260**.

With regard to cements containing 2% gelator concentration, from the compression tests (**Table 4.4**) they have very similar characteristics to the reference cements (**C2\_1.35\_260**), showing lower  $\sigma$  but higher E. It seems that the addition of 2% gel does not significantly affect the mechanical properties, in contrast to what happens for samples loaded with the 5%.

**Table 4.4** Values of maximum stress ( $\sigma$ ) and elastic modulus (E) in compression tests for reference cements and fibre reinforced cements with 2% gelator.

| Sample                                 | $\sigma$ (MPa)                | E (MPa)                       |
|--|-------------------------------|-------------------------------|
| <b>C<math>\beta</math>0G2_1.35_260</b> | <b>5.6<math>\pm</math>0.8</b> | <b>385<math>\pm</math>111</b> |
| C2_1.35_260                            | 6.2 $\pm$ 0.8                 | 184 $\pm$ 42                  |

The morphological analysis of the sample **C $\beta$ 0G2\_1.35\_260** highlighted the presence of numerous fibres, homogeneously distributed in various areas of the cement scaffold. It is also possible to notice a perfect compatibility and integration between the gelator fibres and the apatite phase. **Figure 4.33 a**, in particular, shows a good interface adhesion between the fibres and the apatite strips of the cement.



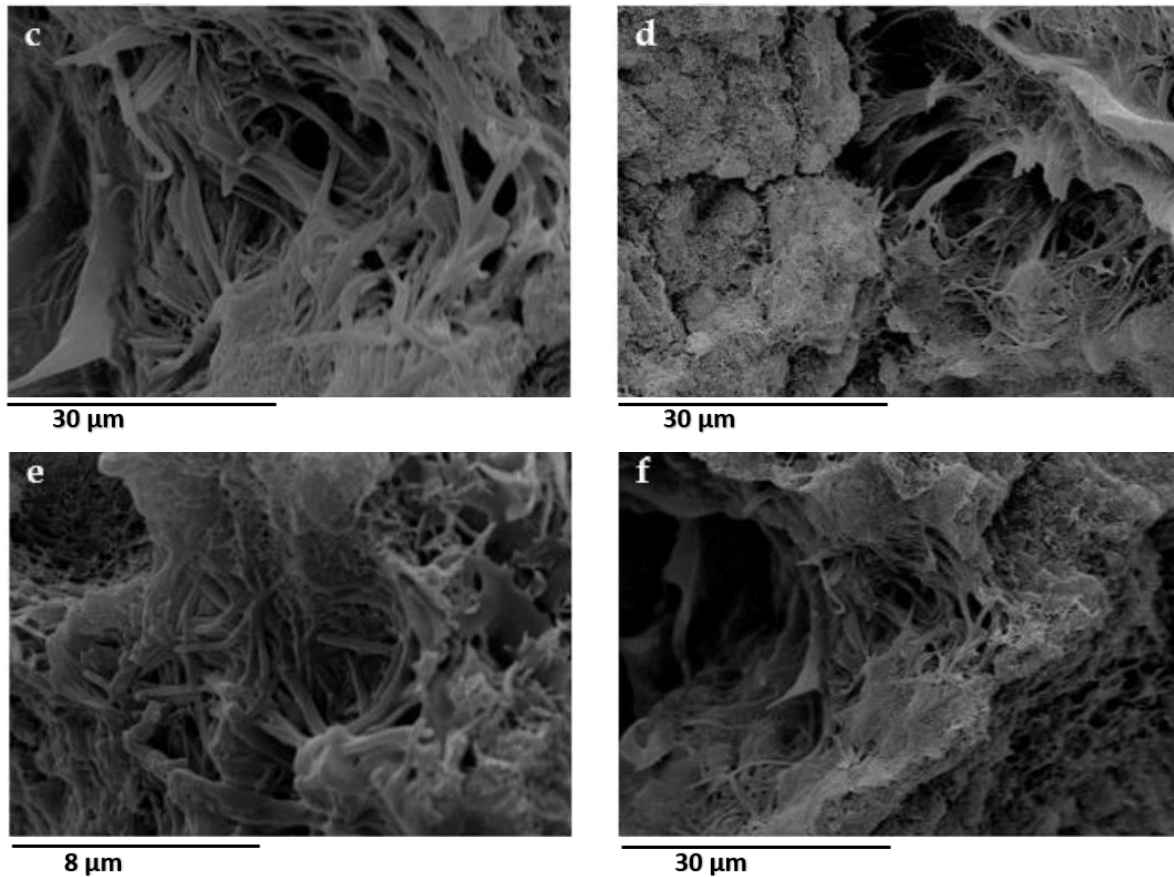


**Figure 4.33** SEM images of sample C $\beta$ 0G2\_1.35\_260.

The preparation of FRCPCs using **Method  $\beta$ 0** leads to cements containing fibres in all the samples. Depending on the composition, it is possible to obtain different morphologies. For samples loaded with 2% gelator, the SEM images reveal not only a better distribution of the fibres within the cements compared to samples with 5% gelator, but also a better interconnection of the fibres with the apatite phase. However, the addition of 5% gelator in the cements leads to an increase in the stress values for all the samples analysed, while for cements loaded with the 2% the mechanical properties are comparable with the reference cements.

### 3. Method $\beta$ 30

In order to obtain a greater number of fibres and improve their distribution within the cements, after mixing the gelator with the trigger, a waiting time of 30 minutes was introduced before the addition of the starting material. This waiting time could allow the interaction of the trigger

with the gelator and a first fibre assembling process in absence of the starting material, thus leading to higher mechanical properties of the final cement. **Method  $\beta$ 30** was therefore tested for the same compositions tested with **Method  $\beta$ 0**.

The gelator solution was treated with 1.35 equivalents of  $\text{CaCl}_2$ , then, after 30 minutes, the mixture obtained was mixed with the starting material (**Figure 4.34**). Gelator concentration of 2% and 5% and L/P ratios of 0.52 mL/g (260  $\mu\text{L}$ ) were respectively used to obtain the samples named **C $\beta$ 30G5\_1.35\_260** and **C $\beta$ 30G2\_1.35\_260**.



**Figure 4.34** Schematic representation of **Method  $\beta$ 30**.

The mechanical properties of the samples were analysed using compression tests. Samples made with 5% gelator concentration gave E values which were higher than those of the reference cements (**Table 4.5**), but lower  $\sigma$  values than those obtained with the  **$\beta$ 0 method**, probably due to precipitation of the highly concentrated 5% gel during the 30 minutes of setting period.

**Table 4.5** Comparison of the compression tests for reference cement,  **$\beta$ 0** and  **$\beta$ 30** with 5% gelator.

| Sample                                  | $\sigma$ (MPa) | E (MPa)       |
|---|----------------|---------------|
| C $\beta$ 0G5_1.35_260                  | 15.4 $\pm$ 2.5 | 484 $\pm$ 82  |
| <b>C<math>\beta</math>30G5_1.35_260</b> | 9.3 $\pm$ 1.1  | 570 $\pm$ 132 |
| C5_1.35_260                             | 10.1 $\pm$ 0.1 | 468 $\pm$ 67  |

From the SEM analysis, a non-reproducible behaviour was also observed for sample **C $\beta$ 30G5\_1.35\_260**, probably due to an excessive gelator concentration (5%). Random morphology and fibre arrangements were observed in samples **C $\beta$ 30G5\_1.35\_260**. For example (Figure 4.35), pores were observed with gel fragments containing visible fibres (images b, c) and pores entirely covered by dense carpets of fibres (images d, e). Samples **C $\beta$ 30G5\_1.35\_260** were excluded from further characterization because of such inconsistencies.

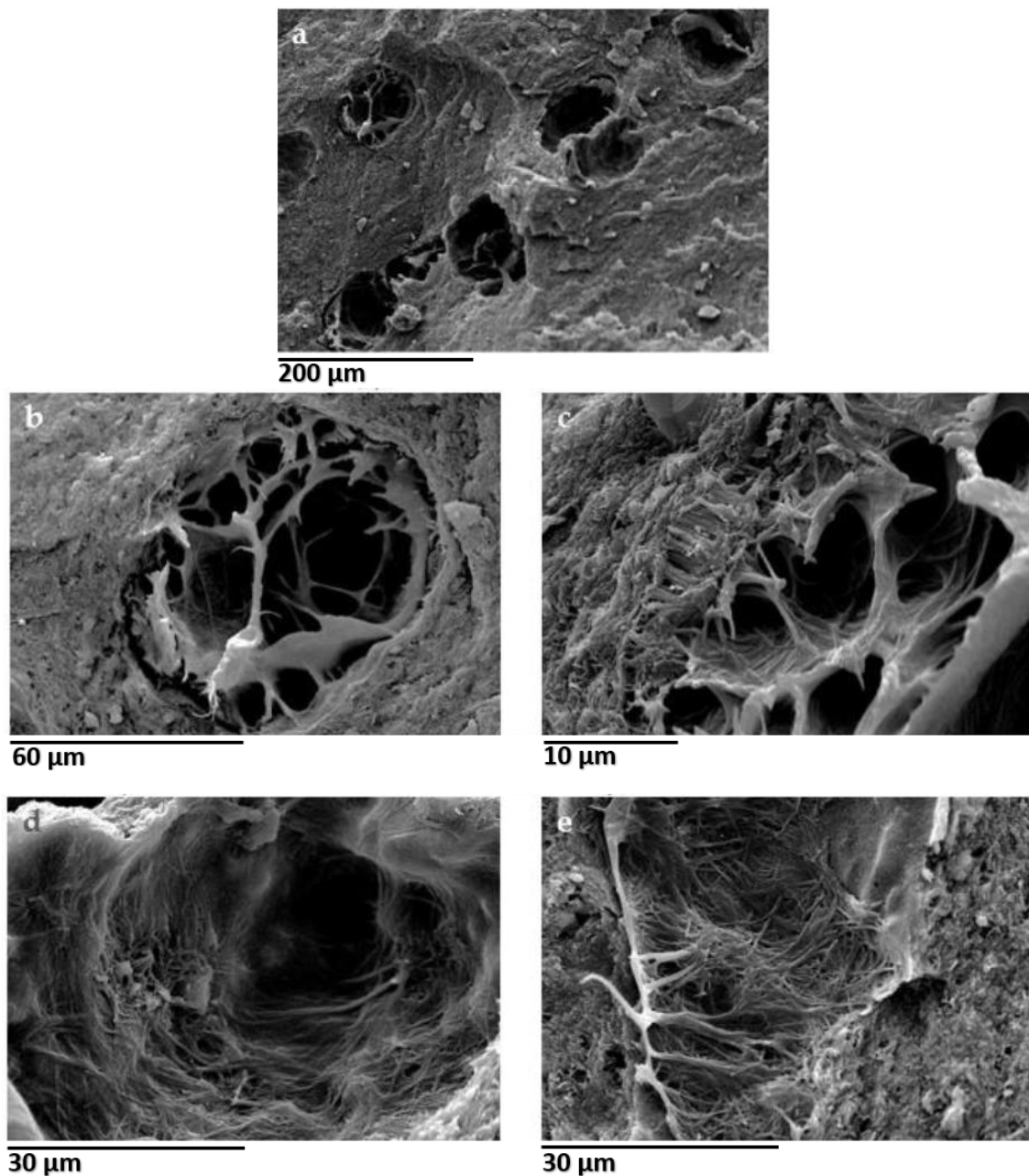


**Figure 4.35** SEM images of samples **C $\beta$ 30G5\_1.35\_260**.

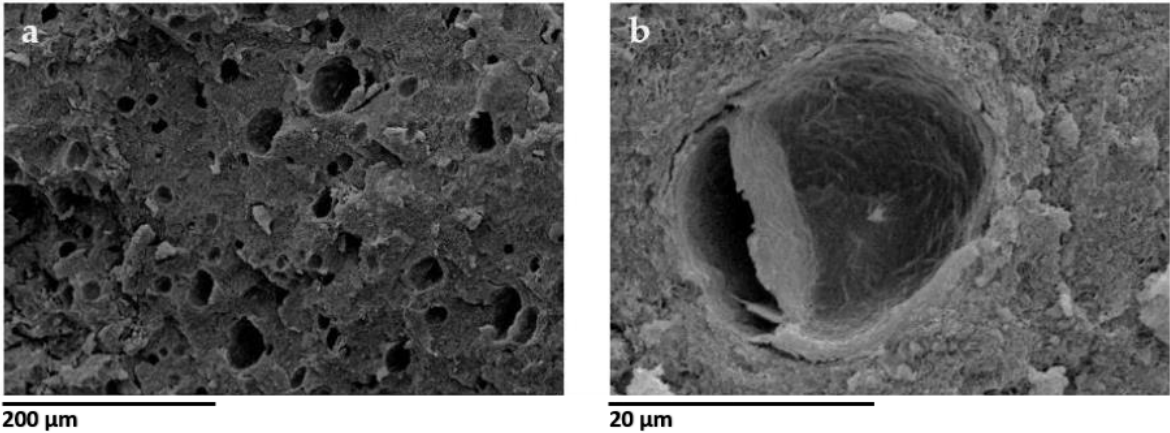
Compared to reference cements, better mechanical properties ( $\sigma$  and E values, **Table 4.6**) were obtained in cements which were prepared with 2% gel using **Method  $\beta$ 30**, likely due to fibre formation during the 30 minutes waiting time after the addition of the trigger to the gelator and before the robust mixing inside the RotoMix.

**Table 4.6** Comparison of the compression tests for reference cement,  $\beta$ 0 and  $\beta$ 30 with 2% gelator.

| Sample                  | $\sigma$ (MPa) | E (MPa)       |
|-------------------------|----------------|---------------|
| C $\beta$ 0G2_1.35_260  | 5.6 $\pm$ 0.8  | 385 $\pm$ 111 |
| C $\beta$ 30G5_1.35_260 | 9.2 $\pm$ 1.6  | 570 $\pm$ 132 |
| C2_1.35_260             | 6.2 $\pm$ 0.8  | 184 $\pm$ 642 |

The morphological analysis highlights how the fibres, not only cover the pores entirely, as seen for previous compositions, but are also present within the entire sample. Image c) of **Figure 4.36** shows a section of the cement with a surface rich in fibres and detail d) highlights their homogeneous distribution within the cement matrix.

After this deep investigation, the most promising samples were selected for further characterisations: C $\beta$ 0G2\_1.35\_260, C $\beta$ 30G2\_1.35\_260 and C $\beta$ 0G5\_1.35\_260.



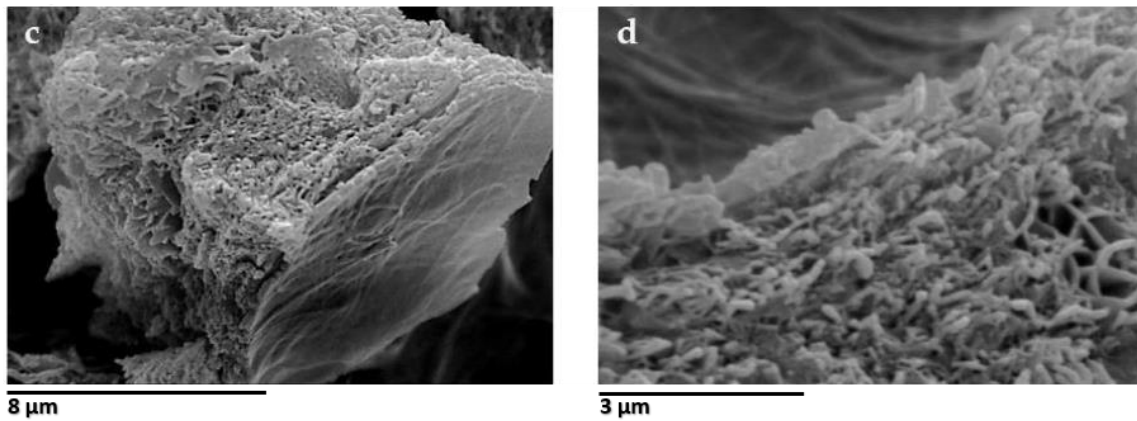


**Figure 4.36** SEM image of Cβ30G2\_1.35\_260.

Time sweep experiments (**Figure 4.37**) were then performed to investigate the behaviour of the different samples prepared with methods **β0** and **β30** during the first 30 minutes after the mixing between gelator solution (containing the calcium trigger) and the starting material. For the cement paste containing 5% gel,  $G'$  and  $G''$  values are higher using **method β0**, in agreement with the results obtained from the compression tests (sample Cβ30G5\_1.35\_260 was added for comparison).

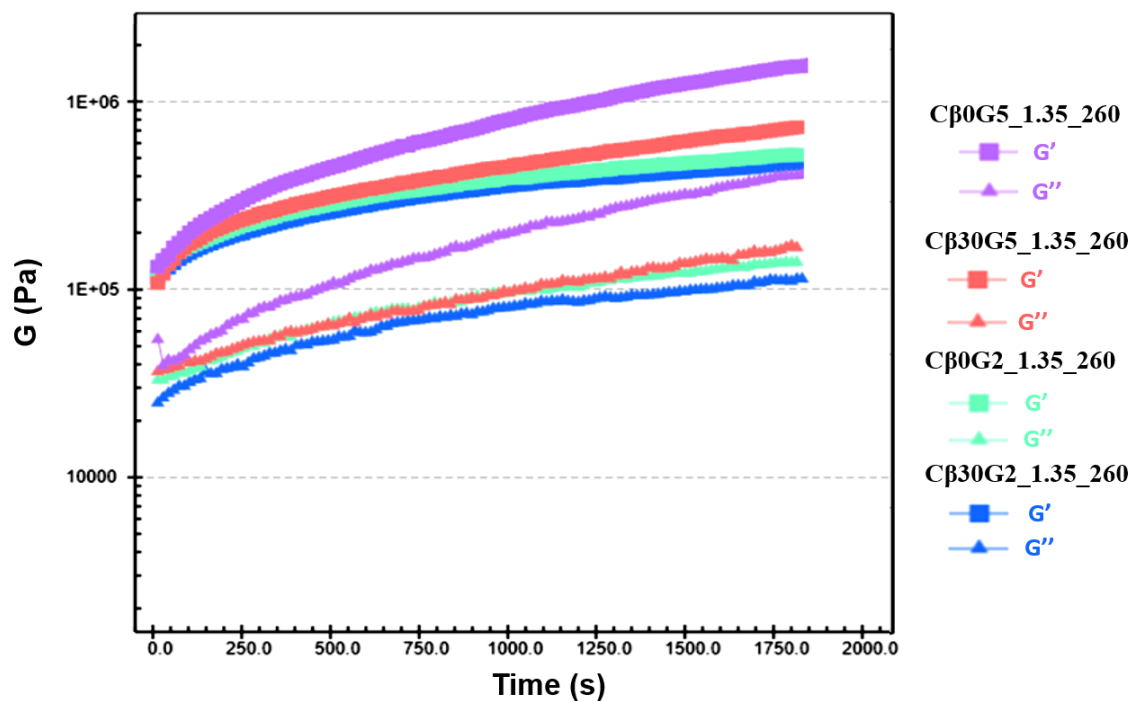


**Figure 4.37** Time sweep comparison for samples Cβ0G5\_1.35\_260 (violet), Cβ30G5\_1.35\_260 (pink), Cβ0G2\_1.35\_260 (green) and Cβ30G2\_1.35\_260 (blue).

For the cement paste containing 2% gelator concentration (**C $\beta$ 30G2\_1.35\_260** and **C $\beta$ 0G2\_1.35\_260**),  $G'$  and  $G''$  values are lower than those obtained for the 5% and are perfectly superimposable for the two different preparation methods,  **$\beta$ 0** and  **$\beta$ 30**. However, this analysis could not explain why after 7 days the mechanical properties of sample **C $\beta$ 30G2\_1.35\_260** are higher than those of sample **C $\beta$ 0G2\_1.35\_260**.

A further investigation of the mechanical properties of the three selected samples employed the three-point bending flexural test on an Instron 4465. This analysis provides useful information for composite materials reinforced with fibres, such as the modulus of elasticity in bending ( $E_f$ ) and flexural stress ( $\sigma_f$ ). The three-points bend test (**Figure 4.38**) is a common experiment in mechanics, used to measure the Young's modulus of a material in the shape of a beam. The beam, of length  $L$ , rests on two roller supports and is subject to a concentrated load  $F$  at its centre.

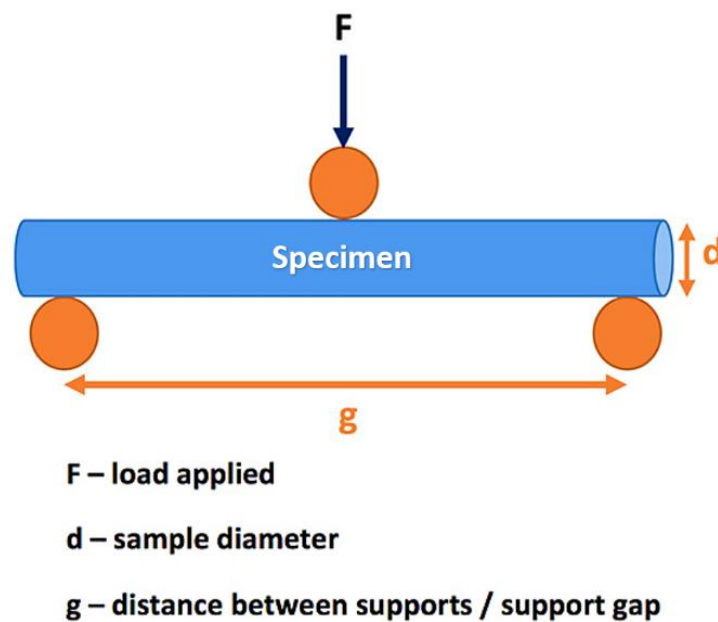


**Figure 4.38** Representation of the three points bending test.

For the FRCPCs analysed, the reinforcement effect of the gelator fibres is evident in all three samples. The surprising result is that for the 2% preparations the values obtained from the bending tests of the composite cements are much better than the results in compression, which were instead comparable with the values of the reference samples. This test also confirms the difference in **Method  $\beta$ 0** and  **$\beta$ 30**, proving that waiting 30 minutes after the addition of the trigger leads to improved properties for the sample with 2% gel.

**Table 4.7** Flexural strength values for the selected cement samples in comparison to the reference samples.

| Sample                                  | $\sigma_f$ (MPa)                |
|---|---------------------------------|
| <b>C<math>\beta</math>0G5_1.35_260</b>  | <b>6.63<math>\pm</math>1.15</b> |
| C $\beta$ 0G2_1.35_260                  | 8.48 $\pm$ 1.61                 |
| <b>C<math>\beta</math>30G2_1.35_260</b> | <b>9.06<math>\pm</math>4.1</b>  |
| C5_1.35_260                             | 3.81 $\pm$ 0.89                 |
| C2_1.35_260                             | 2.74 $\pm$ 1.13                 |

In conclusion, after several attempts, an efficient method for the preparation of fibre reinforced cements for bone regeneration was developed. Supramolecular fibres formed by LMWGs self-assembly were grown for the first time inside bone cements using calcium as trigger. Dense fibre matrices were observed in SEM images of cements which were made using a 2% gelator concentration and a 0.52 L/P ratio. The fibres were homogeneously dispersed in the matrix which gave better reinforcement than the reference cements without fibres. The reinforcement was particularly high when the LMWG solution was placed into contact with the trigger for 30 minutes before the addition of the cement paste. Improved cement quality was confirmed by compression and flexural tests.

The preparation of FRCPCs in combination with LMWGs opens up the possibility to produce a whole new class of bone cements. The fibre morphology in the inorganic matrix may be tuned using different gelator structure, concentration and volume.

Preliminary biocompatibility tests of the composite scaffolds on osteoblast cells are now taking place, as well as some further characterisations, including cytotoxicity, biodegradability and porosity, to validate these materials as scaffold for tissue engineering applications.

### 4.2.3 Materials and Methods

**Preparation of the reference cement paste.** DCPD and  $\alpha$ -TCP were synthesized following an already reported procedure.<sup>260</sup> Starting cement powders, made of gelatin and  $\alpha$ -TCP (15% wt of gelatin with respect to the total amount) were prepared as previously reported.<sup>261</sup> The gelatin/ $\alpha$ -TCP mix powder (475 mg) was treated with DCPD (25 mg), packed in a Teflon mold (6 × 12 mm). To simulate the composition of the samples containing the gelator, the same amounts of CaCl<sub>2</sub> (1, 1.35 or 1.6 equivalents) were added to the starting material, depending on the reference sample prepared. The powders were then mixed in an electric mortar (3 M ESPE RotoMix) two times for 20 s.

A liquid to powder ratio of 0.40 or 0.52 mL/g was used, with Milli-Q® water as liquid phase (the pH of which was adjusted to 9 using 1M NaOH to replicate that of the gelator solutions). After the addition of the liquid phase, cement powders were mixed in the electric mortar two times for 20 s to obtain a paste of workable consistency and compacted for 1 min inside the Teflon mold by using a 4465 Instron dynamometer set at 70 N. After being compacted for 10 minutes, cement samples were demolded and immersed in PB at 37 °C and pH 7.4 for up to 7 days.<sup>259</sup>

**Preparation of the gelator solution.** For the preparation of the solution with 2% w/w gelator concentration, 20 mg of Boc-L-DOPA(Bn)<sub>2</sub>-OH were dissolved using sonication in 1 mL of Milli-Q® water containing 1.2 equivalents of NaOH. The 5% solution was similarly prepared using 50 mg of the gelator in 1 mL of Milli-Q® water.

**Preparation of fibre-reinforced cement paste.** To prepare the samples of CPCs containing LMWG fibres, the gelator solutions (2% and 5% w/w gelator concentration) were used in place of Milli-Q® water as liquid phase, following the same procedure described for reference cements.

**Compression tests.** The mechanical compression tests were conducted on cylindrical samples using an INSTRON dynamometer, model 4465 equipped with a 5KN load cell, setting a compression speed equal to 1 mm/min. Stress-strain curves were recorded using SERIES IX software for Windows. The compression tests on the cements were carried out after 7 days of immersion in PB at 37 °C. Four samples were tested for each preparation. From the stress-strain

curves the values of elastic modulus (E) and of the maximum stress ( $\sigma$ ) in compression were calculated.

**Three-points bending test.** The flexural tests were conducted on the cement samples using an INSTRON dynamometer, model 4465 equipped with a 5KN load cell, setting a compression speed equal to 1 mm/min. The bars were loaded to failure and the maximum outer-fibre stress was calculated. Flexural stress was calculated as:

$$\sigma_f = \frac{3 \cdot F \cdot L}{2 \cdot b \cdot d^2}$$

F is the force at break, L the outer loading points, b and d are the width and the thickness of the specimen respectively. The tests were carried out after 7 days of immersion of the cements PBS at 37 °C. Four samples were tested for each preparation.

**Time sweep rheology.** The rheological analyses were carried out with an Anton Paar modular compact rheometer MCR102. Time sweep tests were carried out with a plate/plate configuration (diameter 25 mm) keeping a constant shear strain ( $\gamma = 0.03\%$ ) and a constant oscillation frequency (1Hz) and recording a point every 15 seconds for 30 minutes soon after the preparation of the cement paste.

**SEM analyses.** The morphological analysis of the fractured surfaces of the cements was carried out after the mechanical tests using a Cambridge Stereoscan 360 scanning electron microscope. To perform the SEM analysis, the samples were mounted on metal stubs, previously covered with carbon conductive tape, and coated with gold before observation (30 mA for 2.5 min).

### 5. Gel-to-crystal transition in supramolecular gels

#### 5.1 Metastable gels

Most supramolecular gels are stable with time, although the effects of gel aging are often not studied over time. Some gels show however clear aging effects. A few systems have exhibited gel-to-crystal transitions.<sup>262–264</sup> In these gel formations, crystals emerge over time at the expense of the network underpinning the gel which may fall apart (**Figure 5.1**).

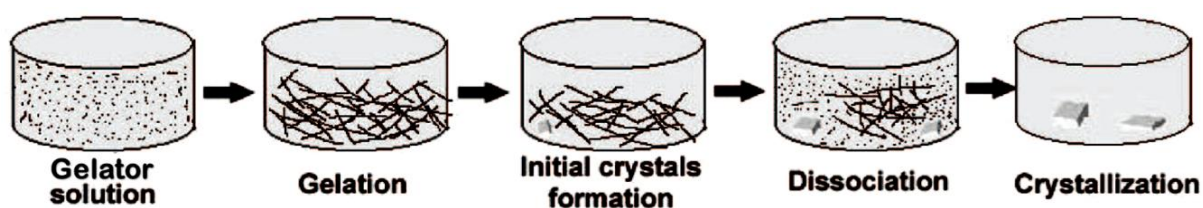


**Figure 5.1** Schematic representation of a metastable gel: after the addition of trigger, the gelator solution starts the self-assembly process; but over time, the network converts into crystals leading to gel dissociation.

As described in a previous work,<sup>19</sup> 2-naphthyloxyacetylalanyl-alanine (2NapAA, **5**, Nap=Naphthalene, A=Alanine, **Figure 5.2**) forms metastable gels when GdL is used as a trigger and a slow crystallization occurs over time from the gel phase. By careful control of the amount of GdL, crystals suitable for diffraction were grown from the gel phase, which is rare for LMWG.<sup>263,265–270</sup> Usually, crystal structures are determined from crystals which are grown from a solvent different from the gel in which they may be formed. The unusual behaviour exhibited by 2NapAA was investigated, with a particular attention on how this crystallisation can be controlled and used to prepare multicomponent gels with increased rigidity.

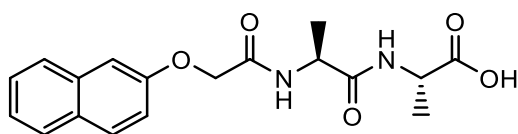


**Figure 5.2** Chemical structure of gelator **2NapAA (5)**.

Gelator **5** was synthesised following a literature procedure.<sup>271</sup> Stock solutions of gelator **5** in Milli-Q® water were adjusted to pH 10.5, using 1M NaOH, to increase the pH and allow the dissolution of the gelator. Gelation was then triggered by a slow reduction in pH from approximately 10.5 to around 3.5 induced by the hydrolysis of GdL.<sup>64</sup> It was observed that the rate of crystallisation increases using larger quantities of GdL, which resulted in a faster decrease in the pH of the system. Crystal formation required a minimum concentration of GdL of 6 mg/mL. With a concentration of GdL of 4 mg/mL, the formation of a stable gel was observed inside the vial, and it did not convert into crystal and solution for weeks.

Three concentrations of GdL were chosen for further characterizations of the 2NapAA gels on the basis of relative rates of gelation and crystallisation: 4 mg/mL (denoted **AA4**), 20 mg/mL (**AA20**) and 36 mg/mL (**AA36**). The samples prepared were followed over time by rheology, while monitoring the pH of the samples (**Figure 5.3**).

The slowest pH change occurred with the lowest amount of GdL (**AA4**). In this sample, the pH initially drops at a relatively quick rate before reaching the apparent pKa of the system (5.0).<sup>19,272</sup> At this point, the rate of decrease in the pH changes due to buffering of the system by the gelator. The final pH in this case is around 4.0.

From the time-sweep rheology, it can be seen that the storage modulus ( $G'$ ) and loss modulus ( $G''$ ) begin to increase when the apparent pKa is reached. Initially, both  $G'$  and  $G''$  are very similar before  $G'$  starts to dominate significantly over  $G''$  (gel formation). Before it starts to increase again, a decrease in  $G''$  can be observed.<sup>273</sup> This implies that there is a structural transition occurring in the solutions as the sample reaches the gel point where  $G'$  becomes greater than  $G''$ . The final gels are stiff ( $G'$  of around 100 kPa) and these gels are stable to further change for at least two weeks. For **AA20**,  $G'$  and  $G''$  both increase as the pH decreases, but at a pH of below 4.1,  $G'$  and  $G''$  decrease before becoming constant. This can be correlated with the onset of crystallisation, which causes the conversion of the gel network into solution containing crystals.

For **AA36**, this behaviour happens faster than for **AA20** as expected from the larger amount of GdL used, with the final values of  $G'$  and  $G''$  being lowest in this case.

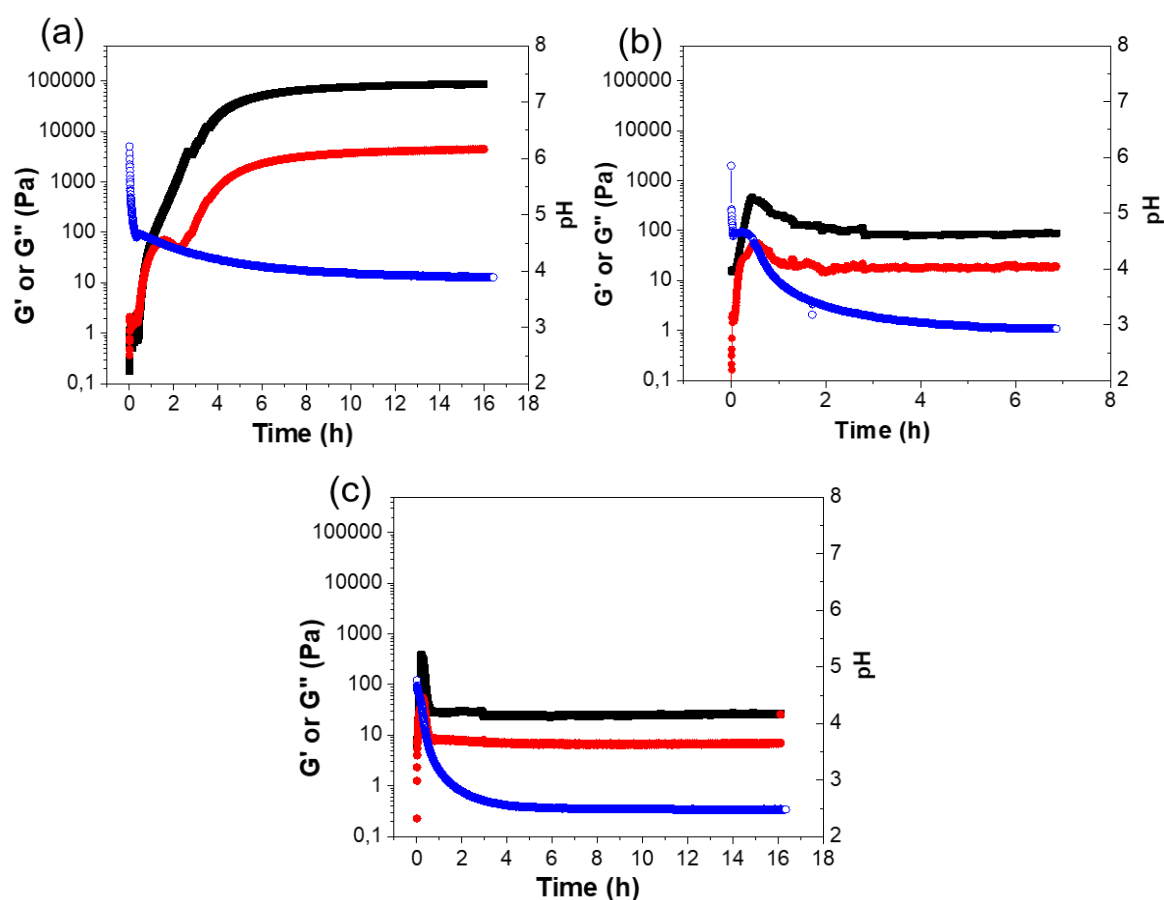
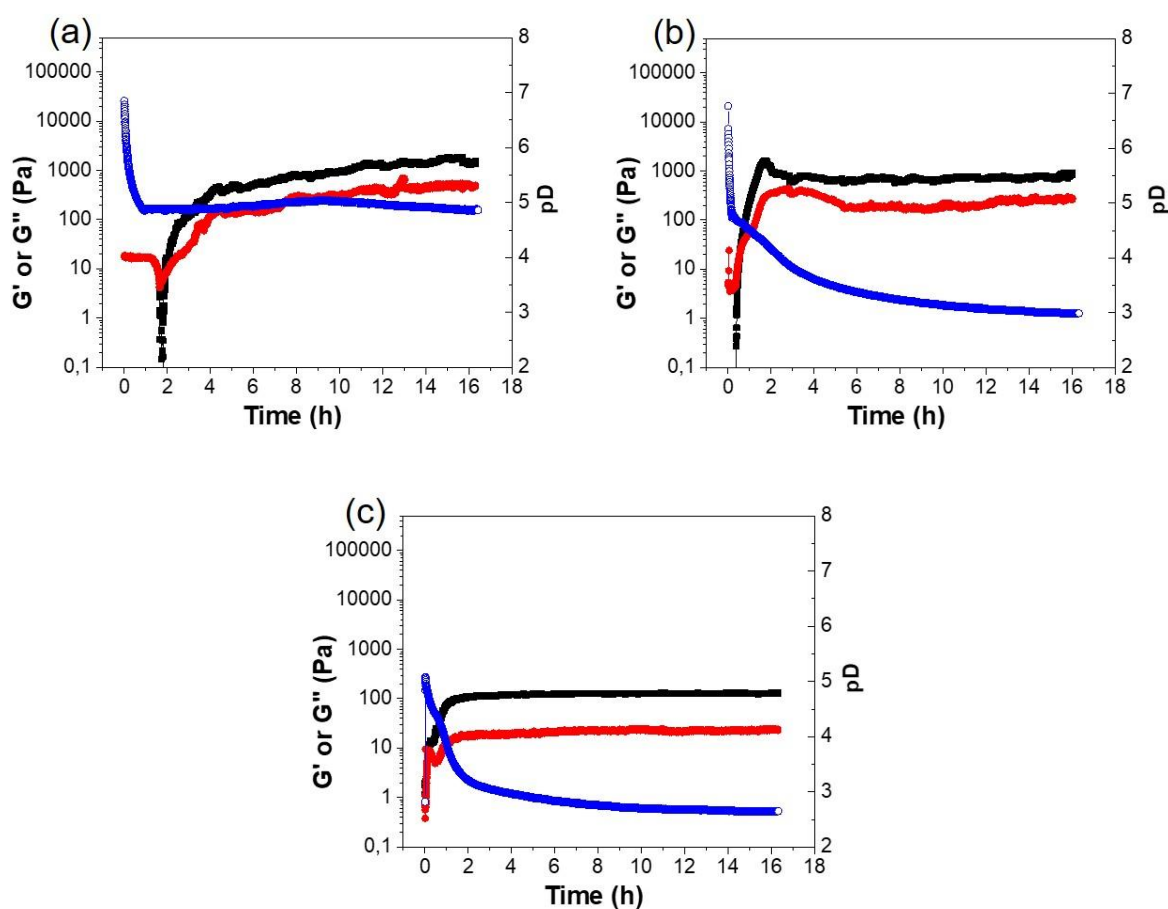


**Figure 5.3** Time sweep experiments of sample **AA4** (a), **AA20** (b) and **AA36** (c).  $G'$ : black line;  $G''$ : red line; pH: blue line.

For hydrogels, hydrophobicity and hydrogen bonding are dominant noncovalent interactions.<sup>274</sup> It is common to carry out a number of experimental techniques for the characterization of gels using  $D_2O$  instead of water: NMR experiments, infrared spectroscopy (to minimize the absorbance of water)<sup>275,276</sup>, small-angle neutron scattering (to allow contrast with the gelators).<sup>277,278</sup> In all cases, the often implicit assumption is that this change has no effect, but on changing from  $H_2O$  to  $D_2O$ , many properties change (density, viscosity, hydrogen bond strength).<sup>279</sup> The hydrophobic effect has also been reported to be more pronounced in  $D_2O$  than in  $H_2O$ .<sup>280</sup> Even the rate of hydrolysis of GdL has been reported to differ in  $H_2O$  and  $D_2O$ , which is considered the major reason of the different behaviour.<sup>281</sup> Recently, Adams *et al.* described how there can be differences in some cases when self-assembly and gelation are

performed in D<sub>2</sub>O compared to in H<sub>2</sub>O.<sup>282</sup>

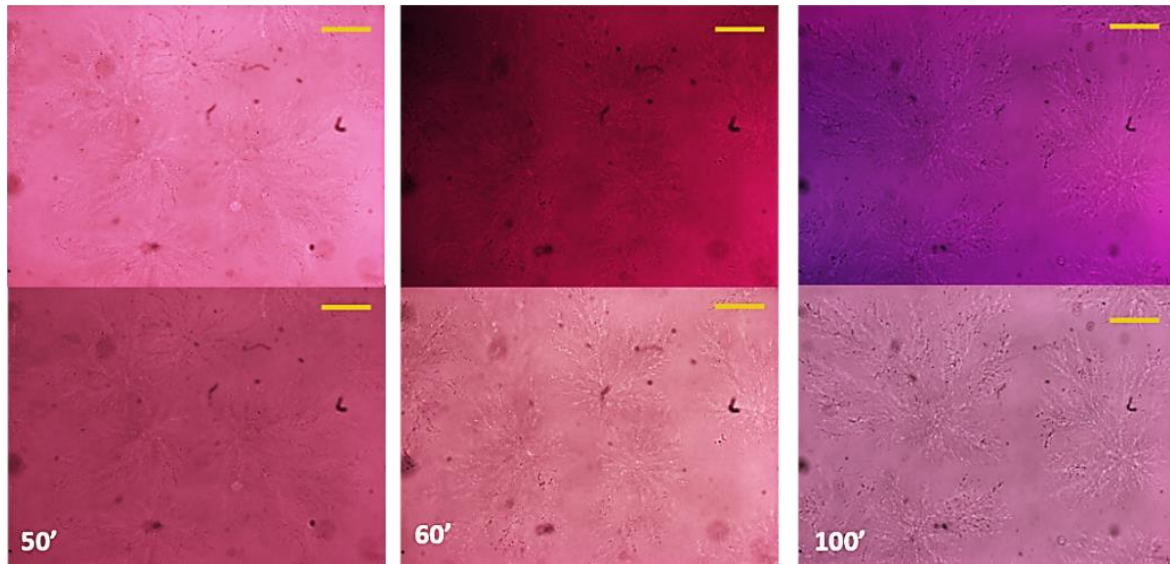
The three samples prepared in water were also made and studied in D<sub>2</sub>O (these samples have a “(D)” after the name for clarity). For 2NapAA, the system is more prone to crystallisation in D<sub>2</sub>O. Even with 4 mg/mL of GdL, crystallisation occurs and the rheological data with time show a very different profile in H<sub>2</sub>O and D<sub>2</sub>O (**Figure 5.3** (a) and **Figure 5.4** (a)). The relatively noisy data in some cases is due to crystallisation occurring during the experiment as described in the text.



**Figure 5.4** Time sweep experiments of sample AA4(D) (a), AA20(D) (b) and AA36(D) (c). G': black line; G'': red line; pD: blue line.

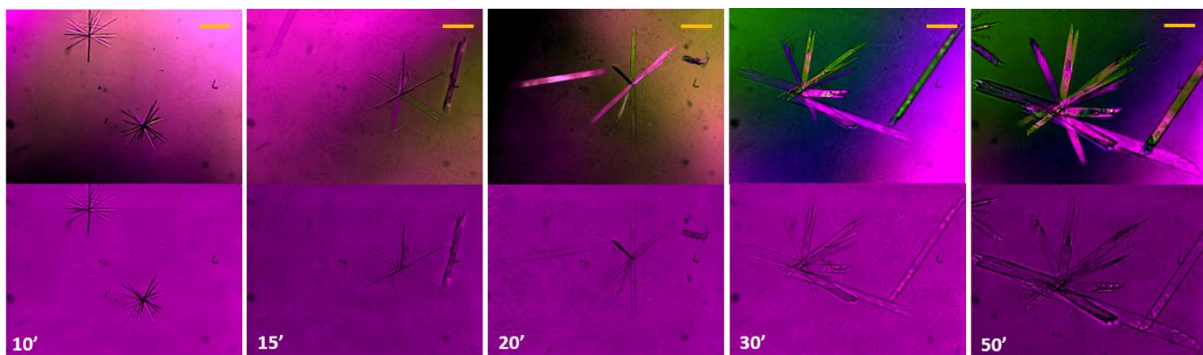
The evolution of these gels was followed over time using optical microscopy. The following optical microscope images show full time course data and corresponding polarised optical microscopy images; the colours are artefactual, due to differences in the initial white balance at time zero (all samples are transparent). Gelator solution (1 mL) was placed in a 35 mm plastic

cell culture dish soon after the addition of the trigger. Large spherulitic domains ( $\sim 0.7$  mm) can be found in sample **AA4** after 50 minutes (**Figure 5.5**). No sign of crystal formation was observed over several hours.



**Figure 5.5** Optical microscope images (polarised light on the top) of sample **AA4** over time. The scale bar represents 300  $\mu\text{m}$ .

For **AA20**, both spherulitic domains and crystals appear after 10 minutes after the addition of GdL. The spherulitic domains are smaller compared to those in sample **AA4** (see last image at 110 minutes in **Figure 5.6**) while the crystals reach about 1.4 mm radius in 1 hour. The formation of crystals over this time period correlates with the time sweep rheology. The kinetics of crystal formation for **AA36** is even faster: many small and thin crystals appear 2 minutes after the addition of the GdL, and then grow with time. The crystal dimensions grow with time, although they do not get as large as those reached in **AA20**; it is also less clear that spherulitic domains are formed.



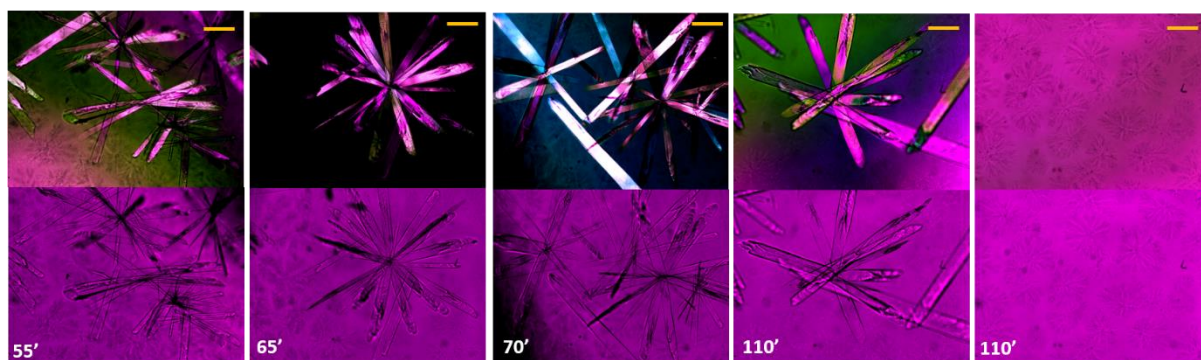


**Figure 5.6** Optical microscope images (polarised light on the top) of sample **AA20** over time. The scale bar represents 300  $\mu\text{m}$ .

Again, the rapid formation of crystals correlates with the time sweep rheology. Full time course data and corresponding polarised optical microscopy images are shown in **Figure 5.7**.

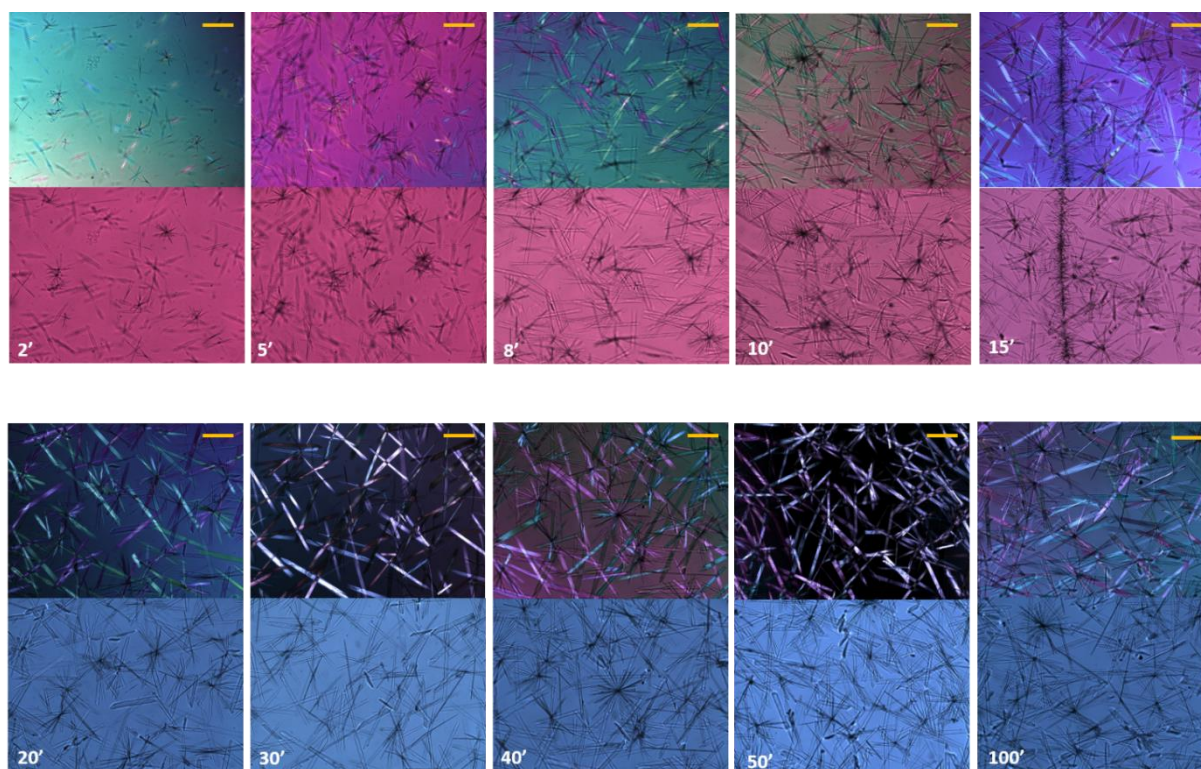


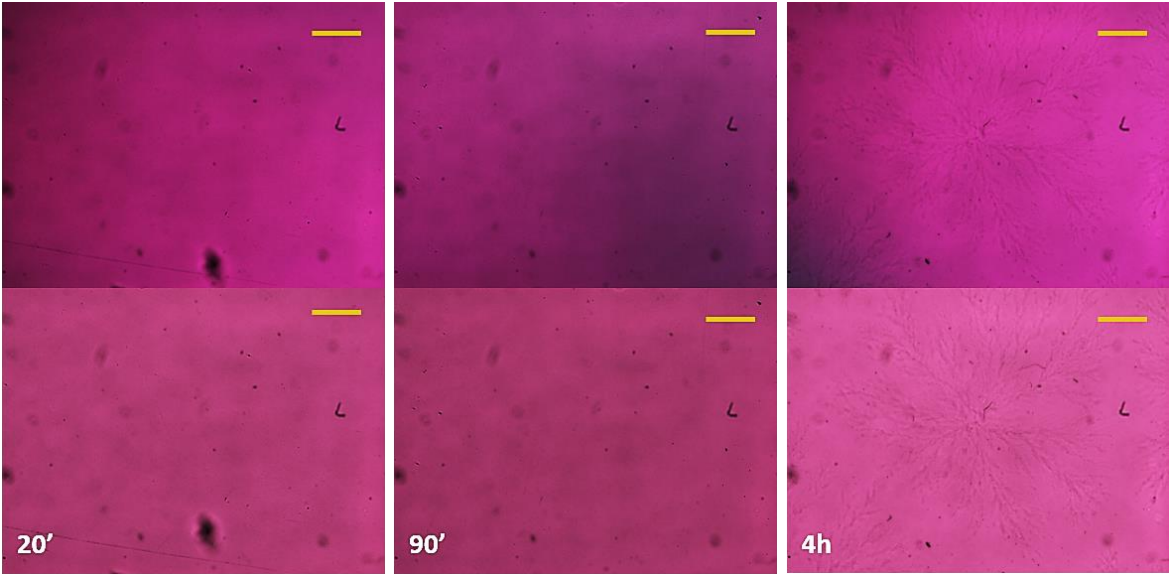
**Figure 5.7** Optical microscope images (polarised light on the top) of sample **AA36** over time. The scale bar represents 300  $\mu\text{m}$ .

Similar structures were formed in the systems in  $\text{D}_2\text{O}$ , although the growth of crystals seems slower with smaller crystals at early time. In sample **AA4(D)** no crystals are formed, as for the

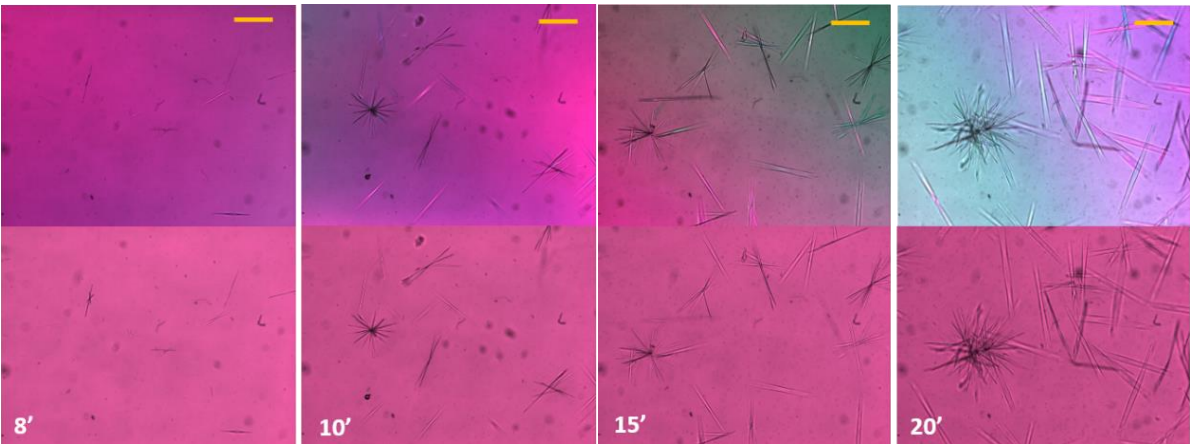
corresponding sample in water. Only big spherulitic domains can be seen at the optical microscope (**Figure 5.8**).

The crystals for both sample **AA20(D)** and **AA36(D)** are thinner and longer (**Figure 5.9** and **Figure 5.10**) as compared to those of **AA20**, which are larger and more regular in shape, and of **AA36**, which are shorter.

Despite these differences, from the optical microscope images the crystals seem to have the same underlying structure.



**Figure 5.8** Optical microscope images (polarised light on the top) of sample **AA4(D)** over time. The scale bar represents 300  $\mu\text{m}$ .



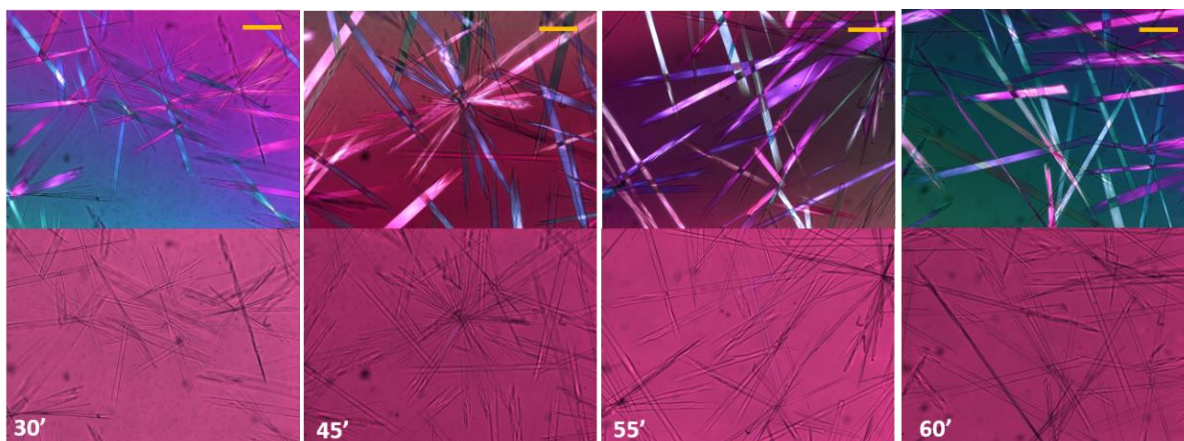


**Figure 5.9** Optical microscope images (polarised light on the top) of sample **AA20(D)** over time. The scale bar represents 300  $\mu\text{m}$ .

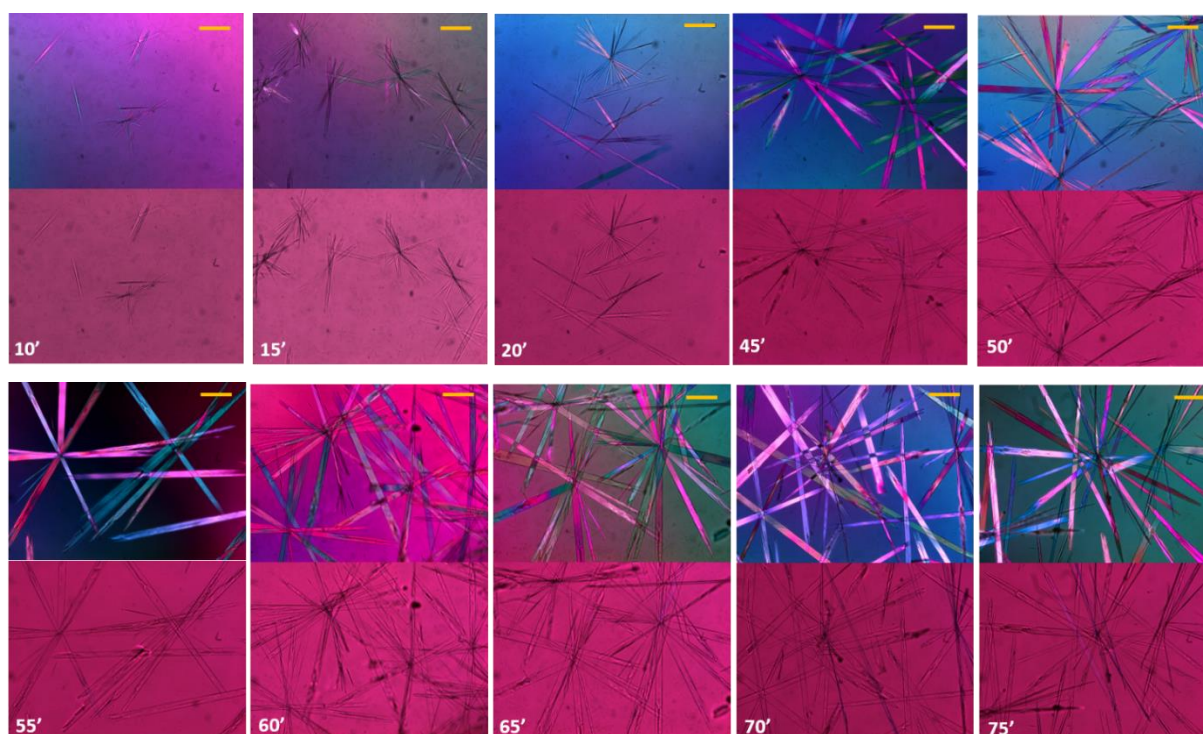


**Figure 5.10** Optical microscope images (polarised light on the top) of sample **AA36(D)** over time. The scale bar represents 300  $\mu\text{m}$ .

Powder X-ray diffraction (pXRD) was performed on the crystals after the growth inside the gels. All crystals were collected directly from their solution. The patterns were compared with the calculated pattern determined from a previously reported crystal structure of 2NapAA<sup>19</sup> as well as a structure collected at room temperature.

The pXRD shows that the underlying crystal structure for AA20, AA36, AA4(D), and AA20(D) can be matched to the predicted pattern from the single crystal data (**Figure 5.11**).

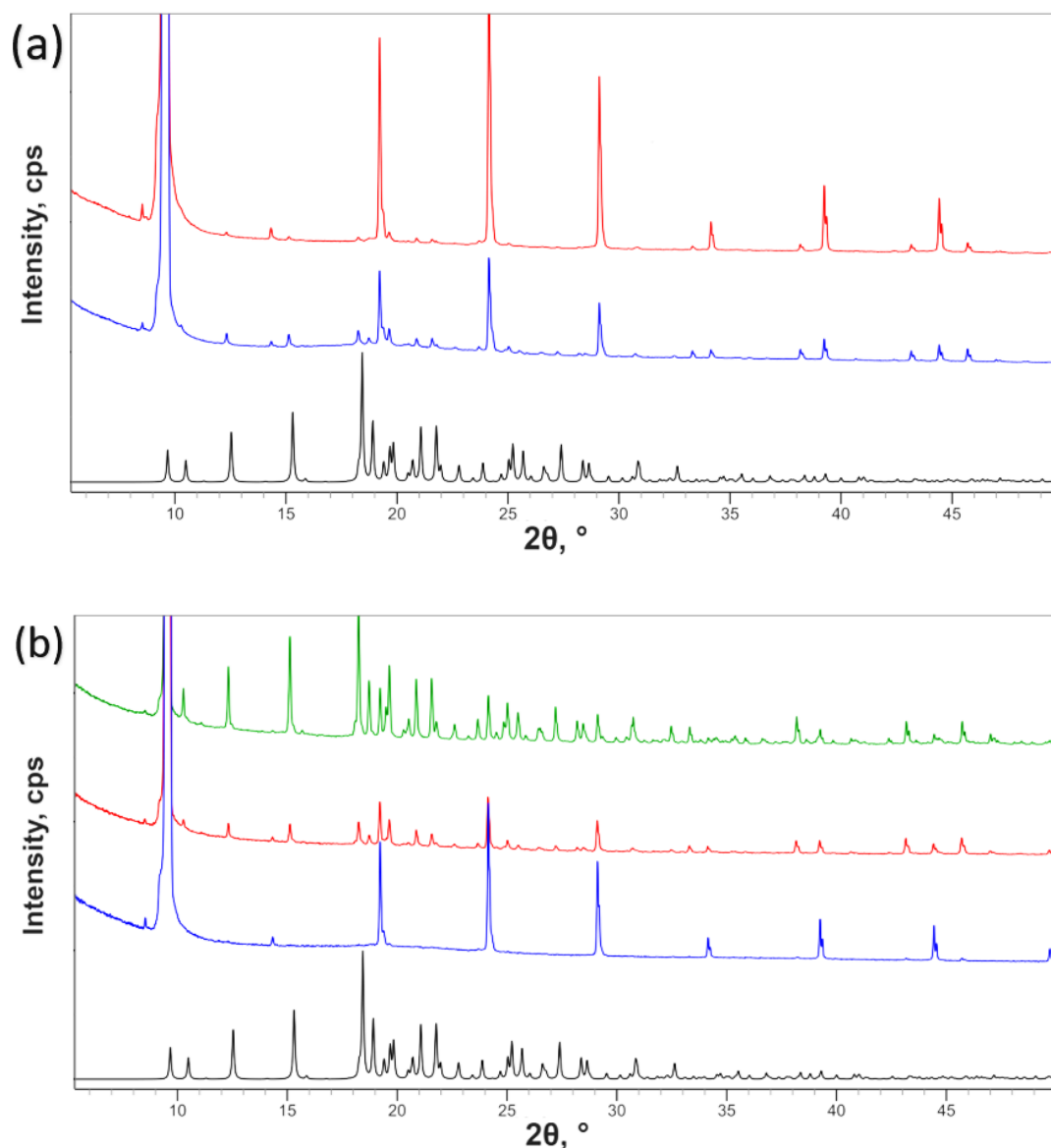


**Figure 5.11** pXRD for the crystals formed in the different systems. (a) shows the data for the samples formed in H<sub>2</sub>O and (b) in D<sub>2</sub>O. In both cases, the black data are calculated from the single crystal structure collected at room temperature. The green data are for the samples with 4 mg of GdL, the red data for 20 mg of GdL and the blue data for the samples at 36 mg of GdL.

These samples suffer from various degrees of preferred orientation effects, due to the crystallite shape (long and thin). This affects the relative intensities of the peaks with some particularly oriented planes being in the correct to diffract far more than others (here, the 001 reflections

are much stronger than expected, especially for the crystals formed at the higher levels of GdL). A hypothesis can be that the higher trigger levels result in quicker growth and more anisotropic crystallites. The patterns for **AA4(D)** and **AA36(D)** were the least and the most affected by preferred orientation, presumably due to the different rate of crystallisation.

The crystal structures do not match the fibre X-ray diffraction data collected from the gel phase previously,<sup>19</sup> again showing that the packing in the gel phase and that in the crystal phases are different.

To understand how the gel phase converts to the crystal phase, confocal microscopy and small angle scattering can be useful. Both of these techniques allow the sample to be monitored without drying artefacts, which are known to be an issue in this class of gels.<sup>230,231</sup> Incorporation of Thioflavin T (ThT) allows imaging of the fibrous structures underpinning the gel network in systems such as these.<sup>14</sup> Incorporating ThT and using confocal microscopy for **AA20**, spherulitic domains with dimensions of about 50  $\mu\text{m}$  are clearly visible in the gel phase 5 minutes after the addition of the GdL (**Figure 5.12 a**). At this point, no crystals are formed and the spherulites are formed from what appear to be fibrous structures. The spherulitic domains seem to become smaller with time, which is presumably because the gel network is converting to a crystal phase. Indeed, after 1 hour, it is possible to image larger, straight crystals in addition to small spherulitic domains (**Figure 5.12 c**).

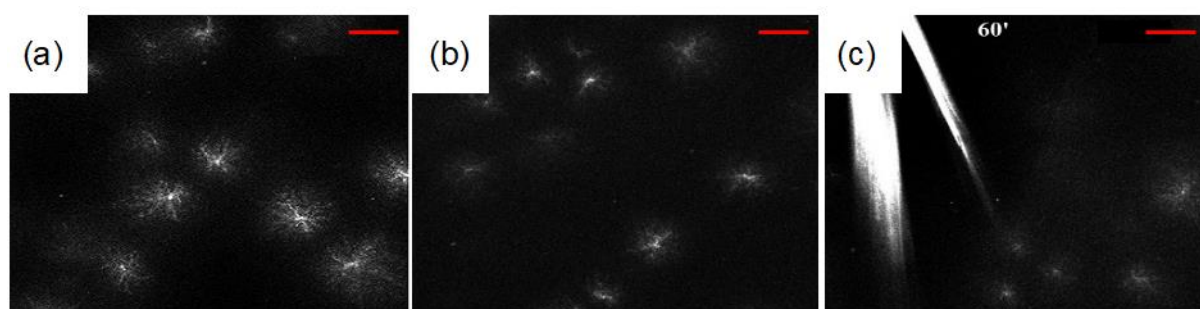


**Figure 5.12** Confocal microscopy images of **AA20** after (a) 5 minutes; (b) 15 minutes; (c) 60 minutes. In all cases, the scale bar shows 50  $\mu\text{m}$ .

In carrying out the above experiments, it became clear that the kinetics of gel and crystal formation are highly dependent on the geometry of the sample holders used. As examples, **Figure 5.13** shows an image of **AA4** and **AA20** in different geometry sample holders. Clear differences were observed, which were dependent only on the geometry of the holder.

The formation of crystals in sample **AA4** started after 30 minutes in the 1 mm path quartz cuvette and after 2 hours in the 2 mm path cuvette, while in the NMR tube and the capillary, gels were formed without crystallisation even after days. For sample **AA20**, crystals formed in all the holders, starting after 10 minutes after addition of the trigger. These observations complicate comparison across techniques which typically use different geometries.

The rheology and pH data in **Figure 5.3** and **Figure 5.4** were collected in the same geometry, but the microscopy for example has to be collected in a different shape holder. Hence, direct comparison of timescales is potentially difficult. Elsewhere, it has been noted that the surface chemistry on which the gel forms can lead to differences in the networks.<sup>283</sup> Here, the two cuvettes and capillary are formed from quartz, whilst the NMR tube is borosilicate glass. As such, there may be some effect, but the differences observed in the degree of crystallisation even within the quartz holders imply that this is not the dominating difference.

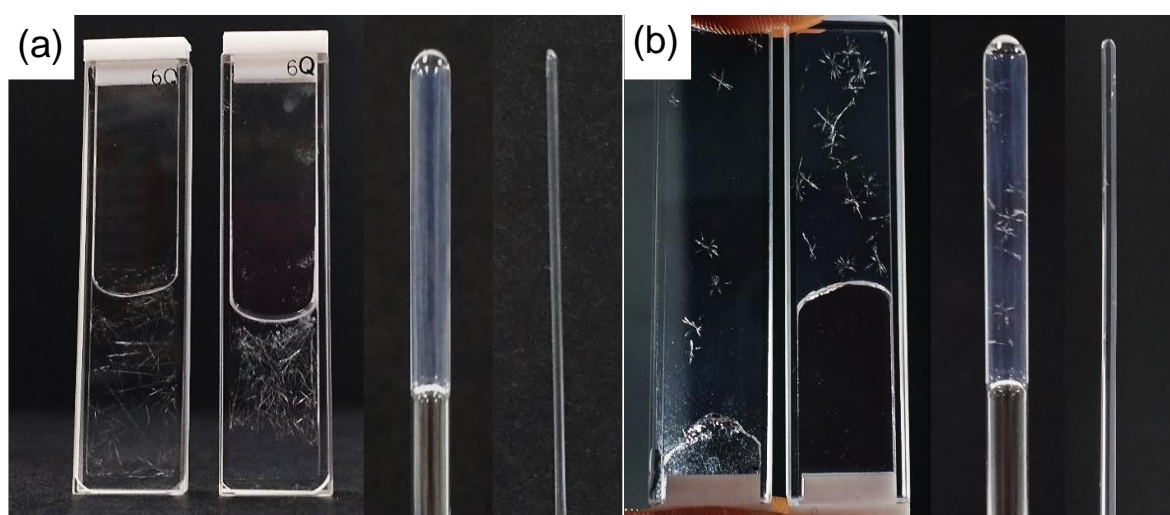


**Figure 5.13** Photographs of samples prepared from (a) **AA4** 19 hours after adding GdL and (b) **AA20** 1 hour after addition of GdL. In both (a) and (b), the same stock solutions were used to prepare all samples. The photographs show from left to right samples in a 1mm thickness cuvette, a 2mm thickness cuvette, a 4 mm diameter NMR tube and a 1.5 mm diameter capillary.

## 5.2 Multicomponent gels

In the vast majority of cases, LMW gels are composed of a single molecule. However, there are a number of examples where two components are necessary to form a gel *in situ*, interacting by noncovalent forces.<sup>284–286</sup> Another interesting situation is the mixture of two LMWGs in which either component can form a gel alone. It has been demonstrated that hybrid supramolecular gels can possess improved or synergistic traits with regard to the mechanical strength of the gel,<sup>287–290</sup> the gelation efficiency and the functionality of the resulting material.<sup>291–293</sup>

Whilst there is conceptually no limit to the number of components that could be mixed, the examples reported so far focus on a mixture of two LMWGs. In this situation, three different scenarios are possible: (i) the LMWG can randomly mix forming fibres that contain a statistical amount of each gelator; (ii) the LMWG can specifically associate such that the fibres formed contain an exact ratio and order of gelators; (iii) the LMWG can self-sort such that fibres contain molecules of only one gelator or the other (**Figure 5.14** (a)–(c)).<sup>294</sup>

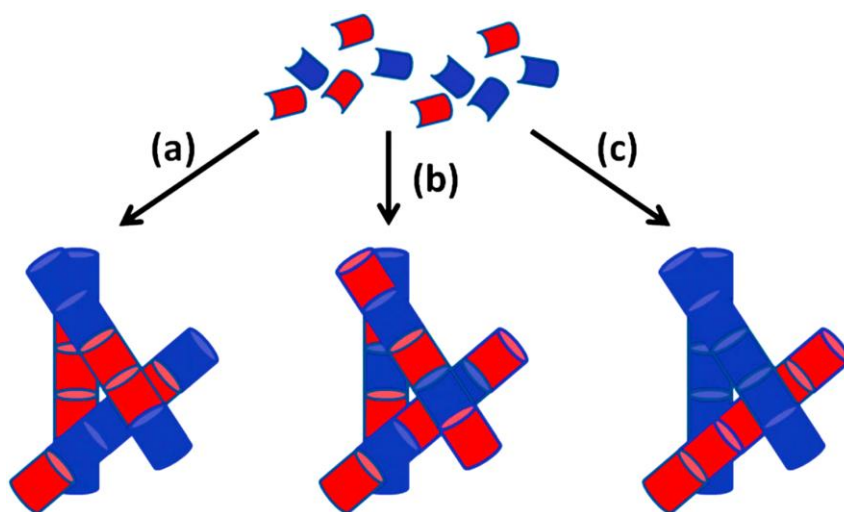


**Figure 5.14** Schematic representation of the possible assembly situation for two LMWG (red and blue): (a) random mixing; (b) specific co-assembly; (c) self-sorting. Adapted from ref.<sup>294</sup>

Assembly of self-sorted fibres could lead to different structures, as shown in **Figure 5.15**: (a) homo-aggregates or (b) hetero-aggregates by lateral association. Different microstructures are conceptually possible, for example (c) and (d), which would both be consistent with a self-sorted system. In many cases, the two-component system is compared to that of the single component and differences are used to infer information about the two-component system.

It is necessary to understand how the system has self-assembled from the molecular level to the multi-micron length-scale.

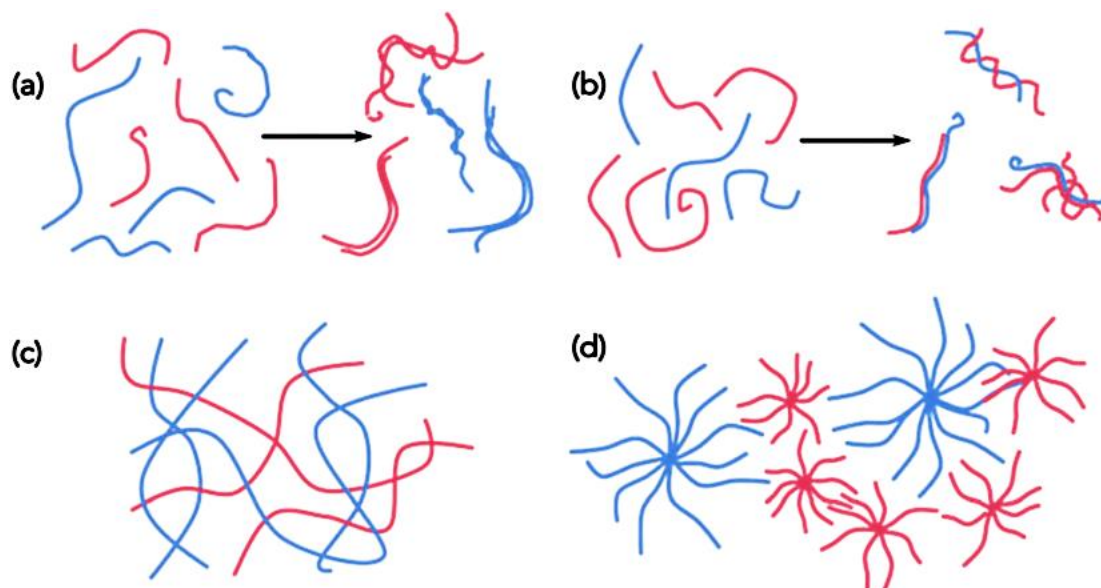


**Figure 5.15** Cartoon representation of the possible structures formed in self-sorted gels. Adapted from ref.<sup>295</sup>

The interactions at the molecular scale will provide information about the assembly in the primary structures. Once the primary fibres have formed, these can interact in different ways on the nanometre scale (for example, lateral associations lead to diameters on the order of 10–100 nm, **Figure 5.15** a and b), with the distribution of fibres in space being homogeneous or heterogeneous on the multi-micron length-scale with potentially different underlying microstructures (**Figure 5.15** c and d). As such, it is necessary to use a range of techniques to access information across these dimensions.<sup>295</sup>

The properties of the final gel will be controlled by the properties of the fibres that give rise to the network as well as how the fibres entangle or cross-link and how the fibres are distributed in space. However, linking the gel properties to the network type is still challenging for even single-component systems.

Multicomponent self-assembled gels offer means to increase the complexity, tune the properties, and possibly add information content into a network.<sup>296–302</sup> These supramolecular systems open up opportunities to build exciting new materials. For example, Zhou *et al.* have shown that random mixing of LMWG into fibres can be used to decorate dipeptide fibres with

a cell adhesive sequence present on a second LMWG.<sup>293</sup> Sugiyasu *et al.* showed that p-n heterojunctions for optoelectronic devices could be prepared from organogels by the self-sorting of two LMWG incorporating suitable aromatic chromophores.<sup>303</sup>

## 5.2.1 Metastable multicomponent gel

The behaviour of 2NapAA in the presence of 2NapFF (**6**) (F=Phenylalanine) (**Figure 5.16**) was examined. First, the behaviour of 2NapFF alone (2.5 mg/mL) was tested.<sup>200</sup>

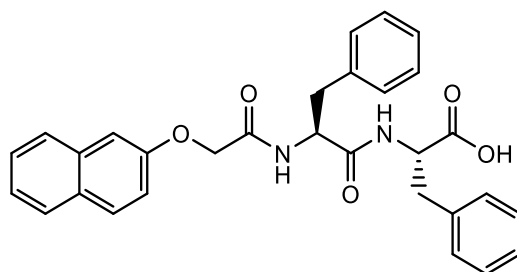


**Figure 5.16** Chemical structure of 2NapFF (**6**).

At the concentration of 2.5 mg/mL, 2NapFF forms a transparent, homogeneous gel when GdL is added. The preparation with 20 mg of GdL in both water (**FF20**) and D<sub>2</sub>O (**FF20(D)**) was chosen for comparison with samples of 2NapAA. Evolution of the gel can be followed by rheology and pH measurements (**Figure 5.17**).

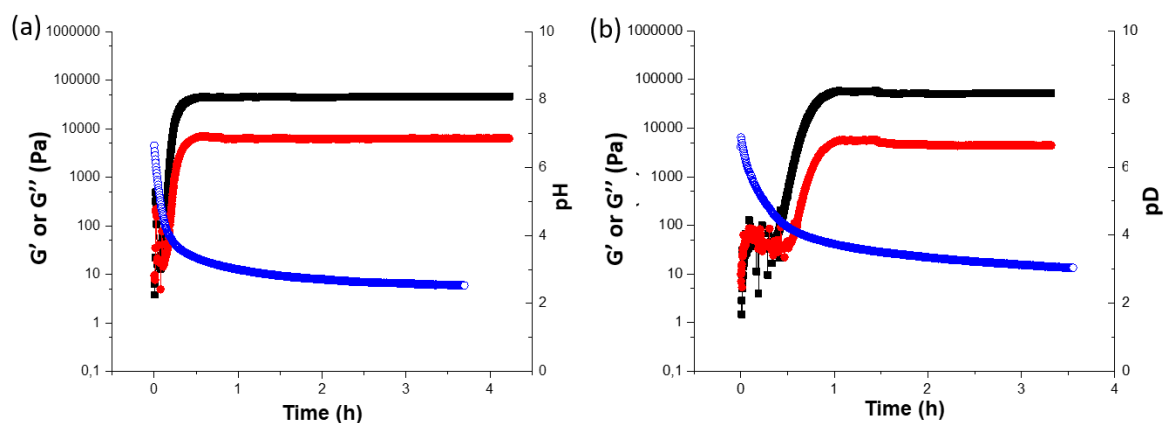


**Figure 5.17** Time sweep rheology and pH change of **FF20** (a) and **FF20(D)** (b). G': black line; G'': red line; pH/pD: blue line.

In both H<sub>2</sub>O and D<sub>2</sub>O, stable gels are formed, with the formation of the gel being slower in D<sub>2</sub>O compared to in H<sub>2</sub>O as previously described.<sup>282</sup> No crystals were observed in the gels, as expected from previous data, and confirmed by the analysis at the optical microscope over time (**Figure 5.18**).

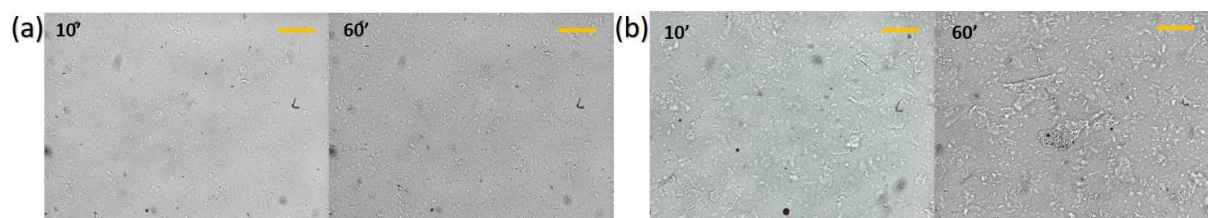


**Figure 5.18** Optical microscope images of **FF20** (a) and **FF20(D)** (b). Over time no crystals were observed. The scale bar represents 300 μm.

Then, 2NapFF (2.5 mg/mL) was used for the preparation of mixed gels with 2NapAA. This concentration of 2NapFF gives relatively non-viscous solutions at high pH, allowing a straightforward mixing. Pre-formed solutions of 2NapAA (at 5 mg/mL) and 2NapFF (at 2.5 mg/mL) were then mixed in 1:1 volumetric ratio at high pH to prepare the multicomponent gels. Increasing amounts of GdL were added (from 1 to 30 mg/mL). The minimum GdL concentration for the formation of crystals inside the mixed gels (**AAFF**) was 6 mg/mL. Increasing the amount of GdL results in the formation of increasing amounts of smaller crystals (**Figure 5.19**).

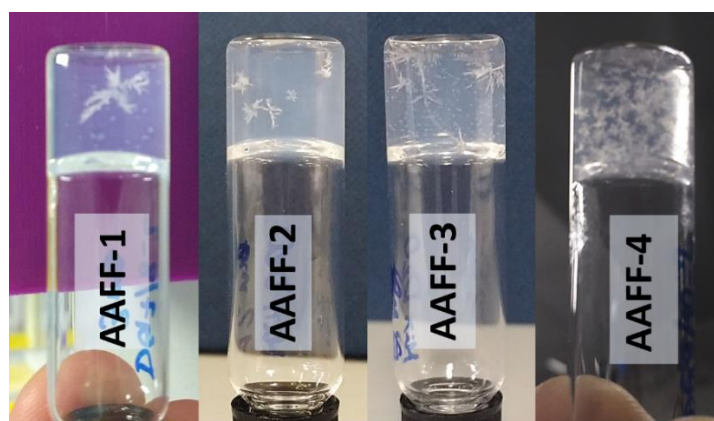


**Figure 5.19** Some mixed gels **AAFF** prepared with increasing amounts of GdL (from left to right). In sample **AAFF-1** (6 mg/mL of GdL) it is possible to see a big single crystal; moving to **AAFF-4** (15 mg/mL GdL) a lot of smaller crystals are visible.

The preparation with 20 mg/mL of GdL was chosen for full characterisation in both H<sub>2</sub>O (denoted **AAFF20**) and D<sub>2</sub>O (denoted **AAFF20(D)**). Time sweep rheology shows the formation of gels which undergo a slow decrease of G' and G'' probably due to the formation of crystals (**Figure 5.20**).

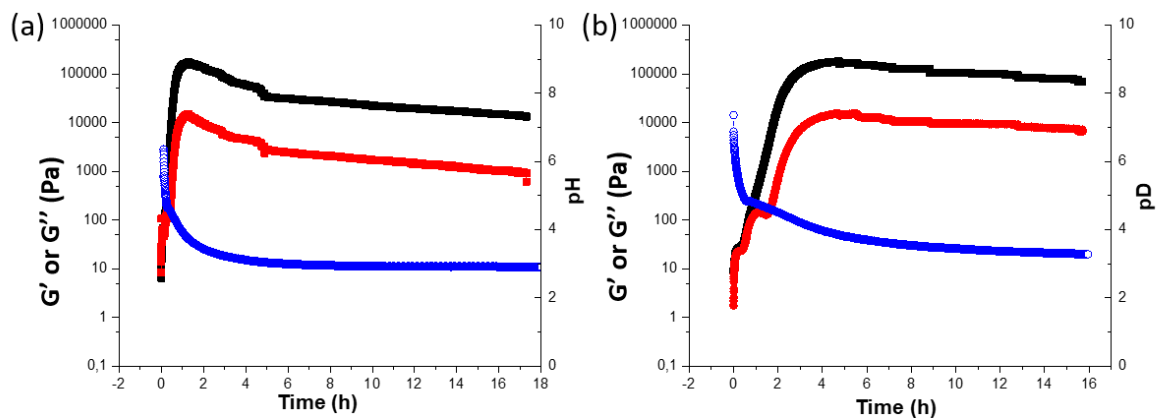


**Figure 5.20** Time sweep rheology and pH change for sample **AAFF20** (a) and **AAFF20(D)** (b).

**Figure 5.21** shows the comparison of the time sweep rheology data for 2NapAA alone, 2NapFF alone, and the mixture of 2NapAA and 2NapFF in H<sub>2</sub>O and in D<sub>2</sub>O. In both H<sub>2</sub>O and D<sub>2</sub>O, gelation is slower in the mixed system as compared to in the case of the 2NapFF alone (**Figure 5.21**). Crystallisation occurs in the single component **AA20** and **AA20(D)** systems as described above.

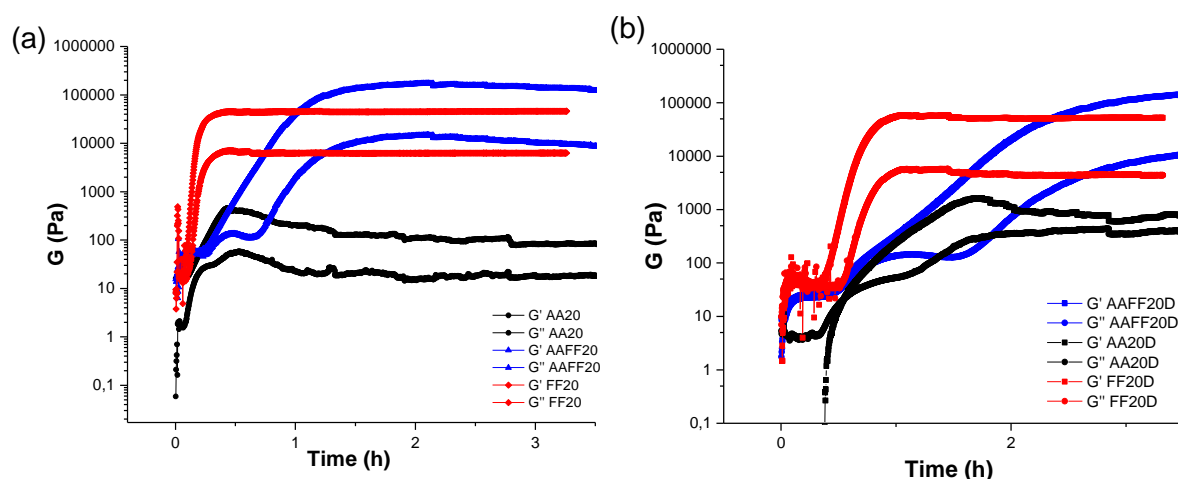


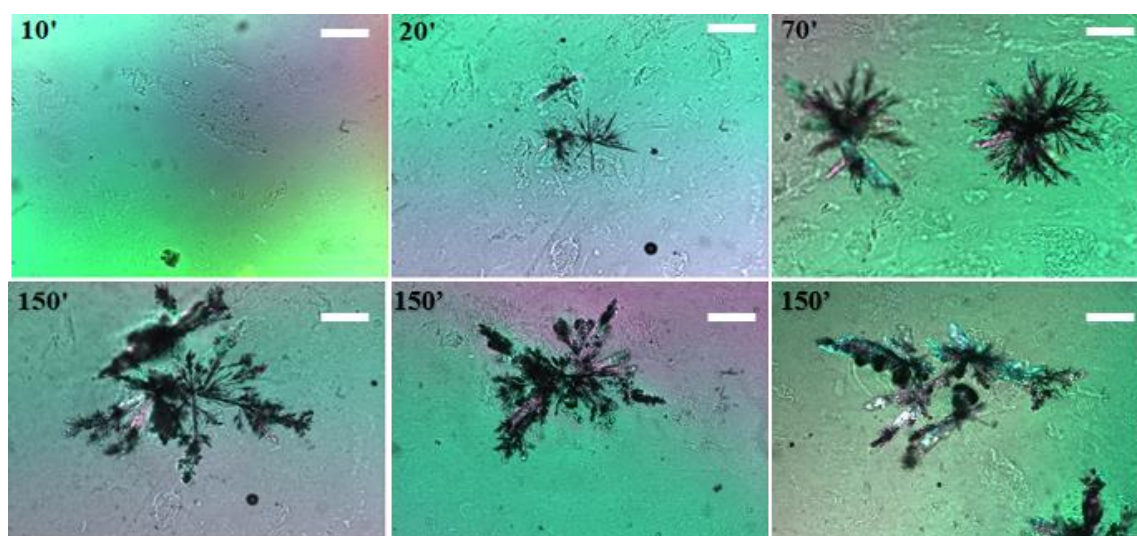
**Figure 5.21** Time sweep rheology comparison of samples in water **AA20**, **FF20**, **AAFF20** and in D<sub>2</sub>O **AA20(D)**, **FF20(D)** and **AAFF20(D)**.

With the formation of the crystals, the multicomponent gel does not convert into solution over time (as in the case of 2NapAA alone). It is a stable gel with crystals inside even after several hours (**Figure 5.22**).



**Figure 5.22** AAFF20(D) after time sweep rheology.

In the mixed gel **AAFF20**, the formation of crystals starts around 20 minutes after the addition of the GdL and after 40 minutes in sample **AAFF20(D)**. This can be seen not only from the time sweep analyses but also from the optical microscope images. The crystals formed in these mixed systems have different shapes at the same time (**Figure 5.23**). The crystals also look different from the crystals formed in **AA20** and **AA20(D)**. In  $D_2O$ , the crystals start growing at later times as compared to in  $H_2O$  but become bigger (**Figure 5.24**). This difference in dimensions can be seen even by eyes looking at the two holders for the optical microscope experiments, since the crystals are big enough to appreciate the comparison (**Figure 5.25**).



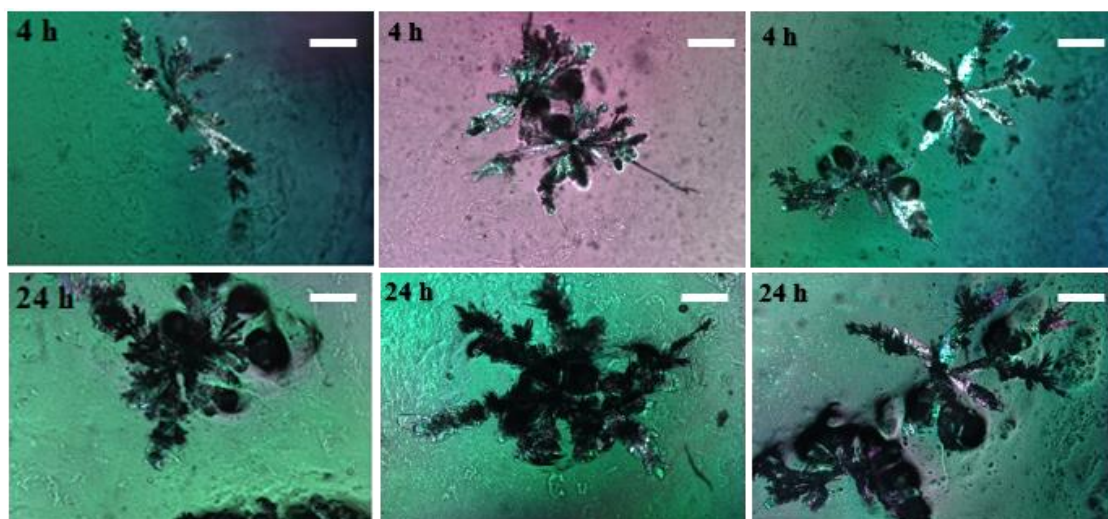


**Figure 5.23** Optical microscope images over time of sample AAF20. Scale bar: 300  $\mu\text{m}$ .

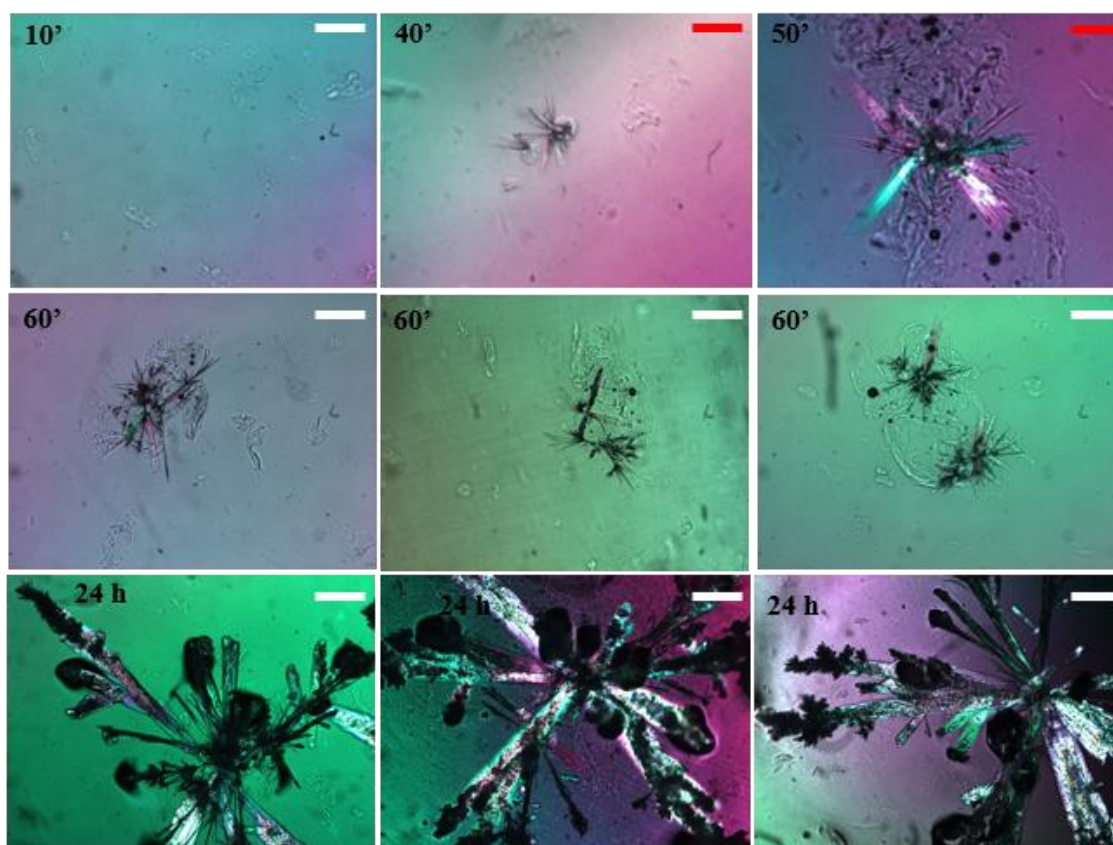


**Figure 5.24** Optical microscope images over time of sample AAF20(D). White scale bar: 300  $\mu\text{m}$ . Red scale bar: 150  $\mu\text{m}$ .



**Figure 5.25** *left*: gel sample of **AAFF20(D)** inside the optical microscope holder after the analysis (24 h). *right*: gel sample of **AAFF20** inside the optical microscope holder after the analysis (24 h). Bigger crystals can be seen inside the D<sub>2</sub>O sample compared to the H<sub>2</sub>O one.

Despite these visual differences, pXRD shows that the crystal structure is the same in all cases in these mixed gels as in the single component systems (**Figure 5.26**).

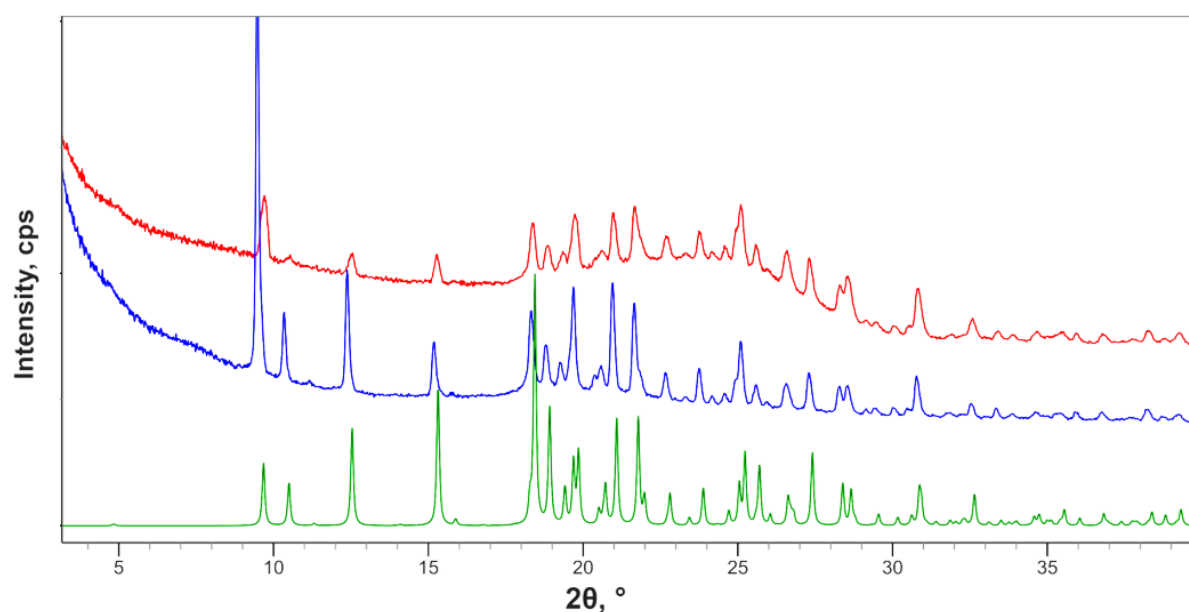


**Figure 5.26** pXRD of the crystals formed in **AAFF20** (red line) and **AAFF20(D)** (blue line). The green data are calculated from the single crystal structure collected at room temperature.

In conclusion, metastable gels undergoing gel-to-crystal transition were prepared using 2NapAA and the pH change method. The crystals formation kinetics can be tuned by changing the amount of GdL. The growth of crystals leads to the slow conversion of the gel network into

solution. In this system the kinetics of gel and crystal formation are highly dependent on the geometry of the sample holders used, which complicates comparisons between different characterisation techniques, requiring different holders. Significant kinetics differences are also noticed when H<sub>2</sub>O is replaced with D<sub>2</sub>O during the gel preparation.

The preparation of multicomponent gels, in combination with 2NapFF, allows the formation of strong gels containing crystals which do not convert into solution over time.

Further characterisation of the multicomponent gels is now taking place. To look at primary fibre structures SAXS and SANS measurements will be performed. Such scattering techniques can be used to determine whether self-sorting or co-assembly has occurred if the two networks scatter significantly differently from each other, or the resulting new network is sufficiently different from than those of the two individual components.<sup>295,304</sup>

## 5.2.2 Materials and Methods

Gelator **5** (2NapAA) and **6** (2NapFF) were synthesised following a literature procedure.<sup>305,306</sup>

**Gelator Solutions.** Stock solutions (20 mL) of 2NapAA (at a concentration of 5 mg/mL) and 2NapFF (at a concentration of 2.5 mg/mL) were prepared by suspending the desired gelator (100 mg for 2NapAA and 50 mg for 2NapFF) in deionized water (17.10 mL for 2NapAA and 19 mL for 2NapFF). An equimolar ratio of NaOH (0.1 M, aq.; 2.90 mL for 2NapAA and 1.00 mL for 2NapFF) was added, and the solutions were gently stirred until a clear solution was formed; the 2NapFF typically takes overnight to fully dissolve.

The pH of the solution was checked and adjusted to 10.5 if needed using NaOH (0.1 M). To form gels, 2 mL aliquots of either solution were placed in a 7 mL volume Sterilin vial containing a pre-weighed amount of GdL. The samples were gently swirled to dissolve the GdL before being left to stand for 24 hours without stirring. After this time, the samples were examined by the vial inversion test to indicate gelation and any measurement was carried out at this point on a fresh sample for each measurement.

The solution of mixed gelators was prepared by dissolving both 2NapAA (such that the final concentration was 5 mg/mL) and 2NapFF (such that the final concentration was 2.5 mg/mL) in

deionized water in the same vial and following the same procedure as for the single component systems.

**Rheology.** All rheological measurements were performed using an Anton Paar Physica MCR101 rheometer. A vane and cup measuring system was used, setting a gap of 1.8 mm. The gels were prepared as described above and tested directly in the Sterilin cup which fits in the rheometer. Time Sweep experiments were performed at 25 °C using a constant angular frequency ( $\omega$ ) of 10 rad/s and a constant shear stress ( $\gamma$ ) of 0.5%.

**pH control.** The pH of the gels was monitored with time after GdL addition, placing the Sterilin vials in a pre-equilibrated water bath to maintain a constant temperature of 25 °C. A FC200 pH probe (HANNA instruments) with a (6 mm x 10 mm) conical tip was employed for the pH measurements with a stated accuracy of  $\pm 0.1$ . pH changes during the gelation process were recorded every 15 seconds for 16 hours.

To log the pH, a custom-built pH and temperature measurement and logging device was used. This is compatible with standard BNC-terminated pH probes and custom-built thermistor-based temperature probes and is capable of recording pH/temperature data over hours to days and then exporting these data as an ASCII file for further processing.

**Optical Microscopy.** All samples were prepared in a CELLstar<sup>®</sup>TC (Greiner Bio-One, Stonehouse, UK) 35/10 mm plastic cell culture dish. 1 mL of the gelator solution was mixed with the desired quantity of GdL, mixed to ensure dissolution of the GdL and placed in the dish. This was covered to prevent drying issues.

**Confocal Microscopy.** All samples were prepared in a CELLview<sup>™</sup> (Greiner Bio-One, Stonehouse, UK) 35/10 mm plastic cell culture dish with a borosilicate glass bottom. Confocal microscope images were taken using a Zeiss LSM710 confocal microscope. Thioflavin T was added as dye (2  $\mu$ L of 0.1% w/w solution for every mL of gelator solution). 1 mL of the gelator solution was mixed with the desired quantity of GdL, mixed to ensure dissolution of the GdL and 0.4 mL of the solution placed in the dish. Fluorescence from Thioflavin T was excited using a 633 nm helium neon laser and emission was detected above 650 nm.

**Single crystal X-ray diffraction.** Single crystal x-ray diffraction data were collected using Bruker D8 Venture equipped with Photon II CPAD detector, dual ImuS 3.0 Cu and Mo sources

and n-Helix low temperature device.

Crystal data.  $C_{18}H_{20}N_2O_5 \cdot H_2O$ ,  $M = 362.37$ , orthorhombic,  $a = 5.8565$  (7),  $b = 8.6565$  (12),  $c = 36.543$  (6) Å,  $U = 1852.6$  (4) Å<sup>3</sup>,  $T = 295$  K, space group  $P2^1_21^1_21^1$  (no.19),  $Z = 4$ , 8786 reflections measured, 3499 unique ( $R_{int} = 0.051$ ), which were used in all calculations. The final  $wR(F^2)$  was 0.099 (all data).

**Powder X-ray diffraction.** PXRD patterns were collected using a Rigaku MiniFlex 6G equipped with a D/teX Ultra detector, a 6-position (ASC-6) sample changer and Cu sealed tube (K $\alpha$ 1 and K $\alpha$ 2 wavelengths - 1.5406 and 1.5444 Å respectively). Patterns were measured as  $q/2q$  scans typically over a range of  $3 > 2q > 60^\circ$ . Data collection and analysis were carried out using Rigaku SmartLab Studio II software (Rigaku Corporation, 2014). All crystal samples were grinded before analyses.

### 5.2.3 Notes

This work has been developed during the period abroad in the in the research group of Prof. Dave J. Adams, at the University of Glasgow.

## Chapter 6

---

### 6. From LMW gelators to LMW adhesives

#### 6.1 Underwater adhesion: a mussel-inspired world

When it comes to underwater adhesion, shellfish are the true experts.<sup>307</sup> The mechanism of adhesion of marine organisms has been largely studied and inspired the production of a huge number of synthetic adhesives for underwater purposes. Over the last few decades, the *Mytilus edulis* (blue mussels) attracted much attention for its ability to secrete the byssus.<sup>308,309</sup> Mussels use the byssus, a protein-based adhesive, for securing themselves to various underwater surfaces, such as sea rocks and ship hulls, and to resist detachments even in marine's harsh and wavy conditions.<sup>310,311</sup> The byssus consists of a bundle of threads composed by three parts: the adhesive plaque, the rigid distal thread and the flexible proximal thread. The byssal thread is deposited by the mussel foot, which is the flexible part responsible for the adhesion on the target surface. So far, roughly 25-30 different mussel foot proteins (mfps) have been identified in byssus, 5 of them (mfp-2 to mfp-6) being unique to the plaque (**Figure 6.1**).<sup>309,310,312</sup>

Mfp-3 and mfp-5 are considered the main proteins responsible for the adhesion of the plaque to the surface. They contain a particularly high amount (up to 30 mol%) of the post-translationally modified tyrosine, L-DOPA.<sup>313</sup> For this reason, it is widely believed that DOPA, and especially its catechol group, has a dominant role in binding to the surface.<sup>308,312,314,315</sup> Moreover, DOPA can efficiently remove the layer of water and ions which generally covers hydrophilic submerged surfaces, while tyrosine, lacking of catechol group, cannot.<sup>309,316</sup>

DOPA is implicated to a variety of different not fully understood adhesion mechanism involving hydrogen bonding, metal-oxide coordination, cation- $\pi$  and hydrophobic interactions, depending upon the surrounding environment: *e.g.* pH, ion concentration, surface material. In the preparation of synthetic adhesives inspired by mussels, the incorporation of DOPA,

catechol groups or other hydrophilic moieties is a common strategy, to overcome the interactions of water with the surface and to provide cohesive forces to the adhesive.<sup>314,317–320</sup>

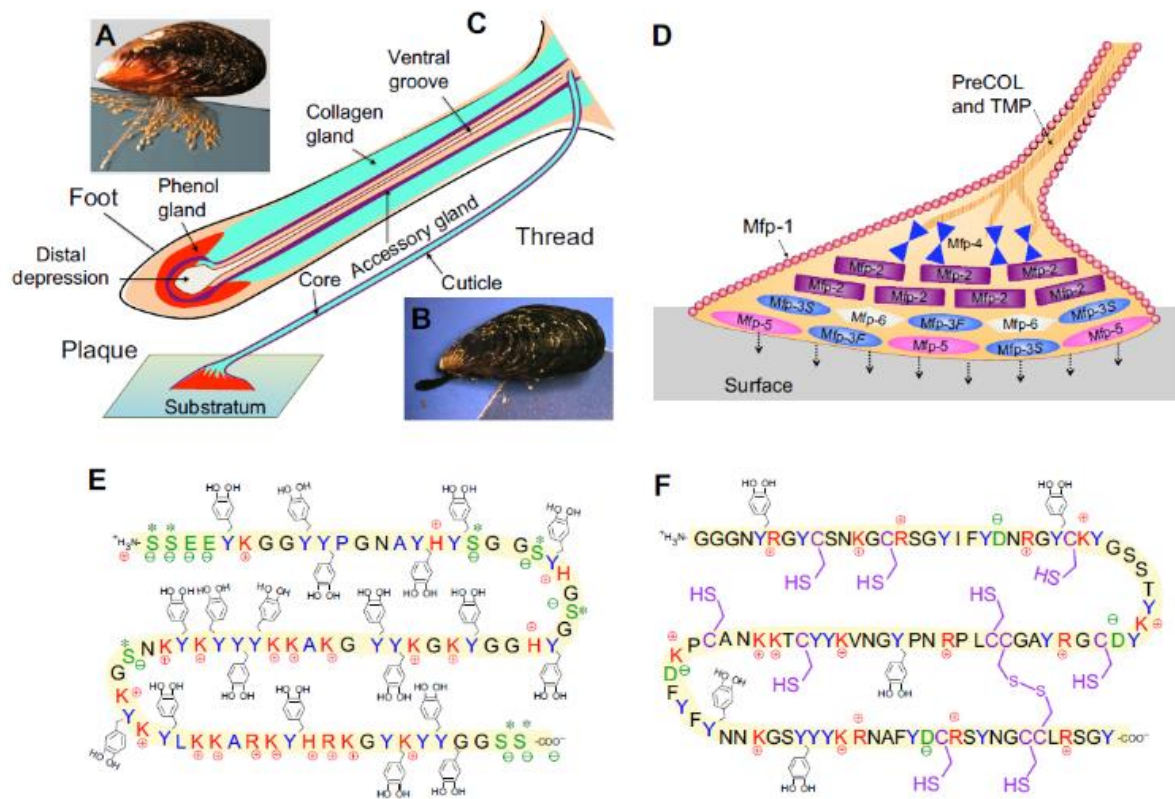


**Figure 6.1** (A) The mussel byssus. (B) To make a new thread, the foot emerges from the living space within the mussel shell and touches a surface. (C) Three gland clusters – phenol, collagen and accessory glands – synthesize and stockpile specific byssal proteins. (D) Schematic representation of the distribution of known proteins in the byssal plaque and distal thread. (E) Sequence of Mfp-5 from *Mytilus edulis*, showing the prominence of DOPA (Y-methyl catechol), Lys (K), Ser (S) and Gly (G). (F) Sequence of Mfp-6 from *M. californianus* with abundant Cys (C), Arg (R) and Lys (K), Gly (G) and Tyr (Y). Color key: Tyr/Dopa (blue), cationic side chains (red), anionic side chains including phosphoSer (green) and thiols (purple). Reproduced from ref.<sup>309</sup>

The role of hydrophobic groups in the removal of water has not been fully exploited in the design of underwater adhesives. It is worth noticing that in water the adhesive forces required to separate two hydrophobic surfaces are very high, even higher than the adhesive forces necessary to separate mfps from model mica surfaces,<sup>321</sup> and it is also much easier to remove water from two hydrophobic than hydrophilic surfaces.<sup>322,323</sup> The design of adhesives which include hydrophobic groups is likely to improve adhesion in wet environments, as recently

reported.<sup>324–328</sup> In sea water DOPA is susceptible to oxidation to DOPA-quinone, which cannot donate hydrogen bonds to surfaces and has lower adhesive properties. In mussels, DOPA oxidation tendency is limited by tautomerization of DOPA-quinone to  $\alpha,\beta$ -dehydro-DOPA (restoring the possibility to form hydrogen bonds) and by the presence of nonpolar amino acids located close to DOPA.<sup>314</sup>

Because of their unique wet adhesive properties, mussel-inspired adhesives have attracted interest for several applications, including biomedical tissue engineering, surgical glues and drug delivery systems.<sup>312,329</sup> Systematic investigation of the behaviour, stability and adhesion mechanisms of these compounds is necessary for their development.

During the synthesis of gelators based on L-DOPA derivatives, the formation of a sticky by-product was observed (Boc<sub>2</sub>-L-DOPA-OMe) and separated by column chromatography from the desired product (Boc-L-DOPA-OMe). Without benzyl ether protecting groups, the catechol moiety of L-DOPA gave sticky compounds which were unable to form gels, illustrating the importance of additional aromatic groups and  $\pi$ - $\pi$  stacking interactions in gel formation.

To study the adhesive properties of such derivatives, a family of Boc<sub>x</sub>-L-(DOPA)<sub>n</sub>-OMe (Me = methyl; x = 1-3; n = 1,2) molecules was synthesised. The number of Boc groups was progressively increased, substituting one or both -OH in the catechol group and compared with the dimer molecule, Boc-(L-DOPA)<sub>2</sub>-OMe, having all the catechol groups free.

Films that were formed with these compounds were examined using the tack test, to study the effects of nonpolar groups on hydrophobicity and adhesive properties. In principle, the production of such biocompatible adhesives may have applications in wound closure materials and delivery systems.<sup>330–332</sup>

### 6.1.1 Synthesis of Boc<sub>x</sub>-L-(DOPA)<sub>n</sub>-OMe adhesives

Four derivatives of the family Boc<sub>x</sub>-L-(DOPA)<sub>n</sub>-OMe were prepared (**Figure 6.2**): three monomers of L-DOPA (n=1) containing an increasing number of Boc protecting groups (x=1-3), from the totally free catechol of Boc-L-DOPA-OMe **6**, to the partially protected Boc<sub>2</sub>-L-DOPA-OMe **7**, to the completely protected Boc<sub>3</sub>-L-DOPA-OMe **8**, and the dimer (n=2) Boc-(L-DOPA)<sub>2</sub>-OMe **9**, whose preparation was suggested by the strong adhesive properties of

oligomers containing more than one catechol group.<sup>333-335</sup> Compound **7** was obtained as a 1:1 inseparable mixture of the *meta*-protected *m-7* and the *para*-protected *p-7* isomer. The synthesis of these compounds started from commercially available L-DOPA.

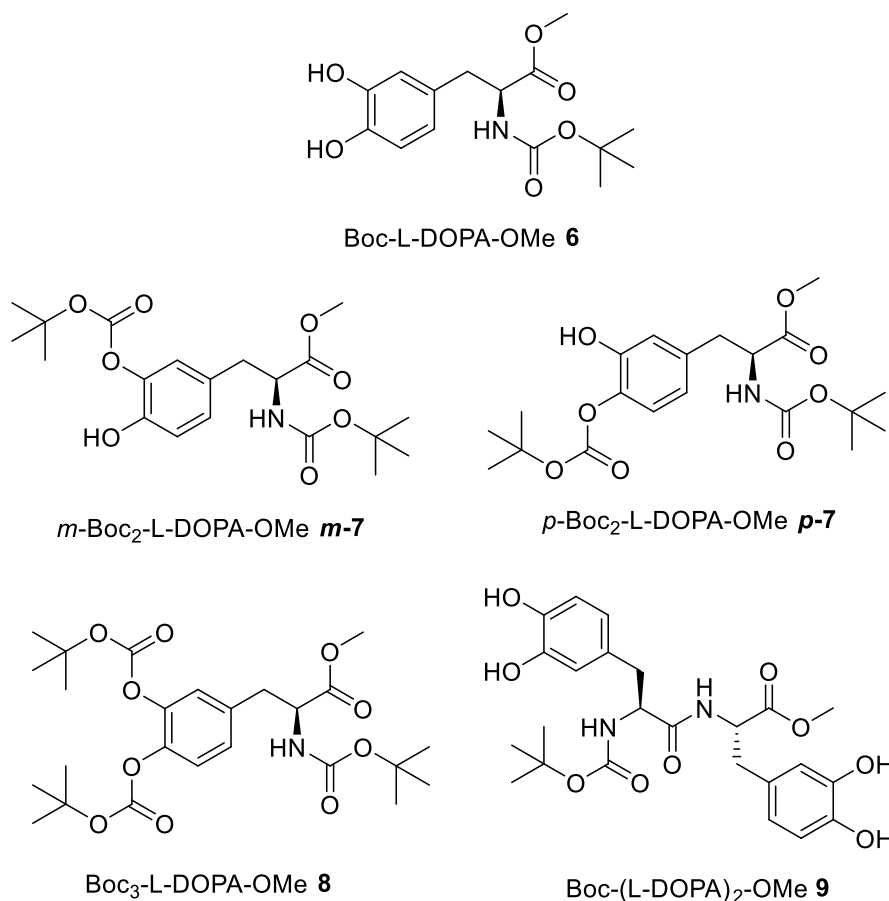


**Figure 6.2** Chemical structure of derivatives **6**, **7**, **8** and **9** synthesised.

The protection of the primary amine is selective, yet also the hydroxyl groups on the catechol are reactive towards this reaction and a mixture of compounds **6**, **7** and **8** is obtained in presence of excess of Boc<sub>2</sub>O. For this reason, selective preparations for these three compounds were investigated. Boc-L-DOPA-OMe **6** is obtained by esterification of commercially available L-DOPA, followed by the selective protection of the nucleophilic primary amine group, according to a reported procedure.<sup>44,102</sup>

The preparation of Boc<sub>2</sub>-L-DOPA-OMe **7** implied several problems, due to the presence of the two hydroxyl groups of the catechol moiety. The selective introduction of a single Boc group on the ring was difficult, even though several different procedures were tested. In any case,

Boc<sub>2</sub>-L-DOPA-OMe was always obtained as an inseparable mixture of *meta* and *para* protected regioisomers *m*-**7** and *p*-**7** (**Figure 6.2**) in about a 1:1 ratio, together with little amounts of Boc-L-DOPA-OMe **6** and/or Boc<sub>3</sub>-L-DOPA-OMe **8** (Materials and methods, **Figure 6.13**). The best result was achieved by reaction of Boc-L-DOPA-OMe **6** with a stoichiometric amount of Boc<sub>2</sub>O and NaHCO<sub>3</sub> in water and THF, with a final yield of about 60% after purification by flash chromatography. Curiously, the direct preparation of Boc<sub>2</sub>-L-DOPA-OMe **7** from L-DOPA-OMe·HCl did not afford the same results. The presence of two regioisomers *m*-**7** and *p*-**7** could be checked only by <sup>1</sup>H NMR (Materials and methods, **Figure 6.14**) as they are inseparable by HPLC-MS (High Performance Liquid Chromatography – Mass Spectrometry) analysis.

In contrast, the preparation of the fully protected Boc<sub>3</sub>-L-DOPA-OMe **8** was selectively obtained in excellent yield by reaction of Boc-L-DOPA-OMe **6** with two equivalents of Boc<sub>2</sub>O, in presence of DMAP (4-(dimethylamino)pyridine) in acetonitrile.<sup>336</sup>

Boc-(L-DOPA)<sub>2</sub>-OMe **9** was prepared in good yield starting from the already described Boc-L-DOPA(Bn)<sub>2</sub>-OMe (Chapter 2 and 4). The preparation of this molecule was suggested by the strong adhesive properties of oligomers containing more than one catechol group.<sup>333–335</sup>

### 6.1.2 Characterisation of L-DOPA based adhesives

The increasing number of Boc groups strongly affects the polarity and hydrophilicity of compounds, as Boc-L-DOPA-OMe **6** is far more hydrophilic than the fully protected Boc<sub>3</sub>-L-DOPA-OMe **8**. The role of hydrophobicity and hydrophilicity in underwater adhesion is controversial. However, some papers recently reported that the introduction of hydrophobic groups in materials for underwater adhesion led to an improvement of the adhesive strength.<sup>324,337</sup> The importance of the presence of hydrophobic functionalities in the processes of surface adhesion and prevention of water penetration prompted us to measure the contact angles of our compounds and check any possible correlation between their hydrophobicity and their adhesive strength values. The hydrophilicity variation was investigated with the analysis of the contact angles between thin layers of molecules **6**, **7**, **8** or **9** and an aqueous medium. Contact angle,  $\theta$ , is a quantitative measure of the wetting of a solid by a liquid. It is defined geometrically as the angle formed by a liquid at the three-phase boundary where a

liquid, gas and solid intersect (**Figure 6.3**). Low contact angle values indicate that the liquid spreads on the surface while high contact angle values show poor spreading. If the contact angle is less than  $90^\circ$  it is said that the liquid wets the surface, zero contact angle representing complete wetting. If the contact angle is greater than  $90^\circ$ , the surface is said to be non-wetting with that liquid. The well-known Young equation describes the balance at the three-phase contact of solid-liquid and gas.<sup>338</sup> The instrument of choice to measure contact angles and dynamic contact angles is an optical tensiometer.

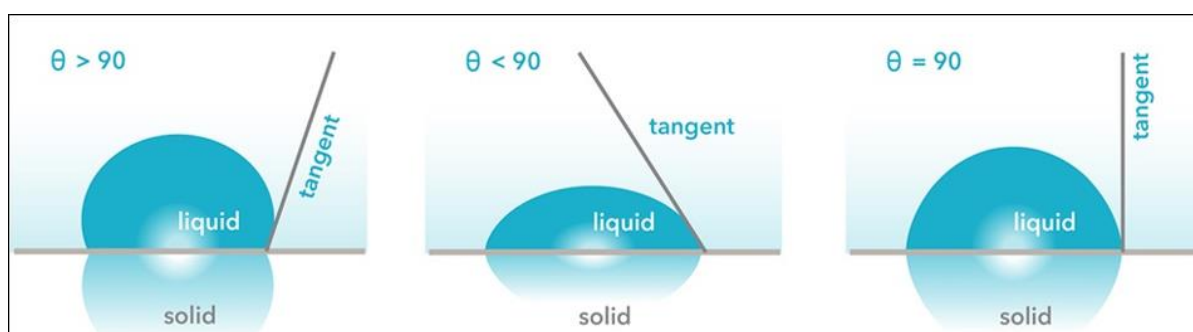


**Figure 6.3** Representation of contact angle measurements and classifications.

To carry out the test, a small amount of the sample is deposited as ethyl acetate solution on a glass slide of an optical tensiometer just enough to cover the entire surface. After solvent evaporation, we measured the contact angles obtained with three media: Milli-Q® water, 1M CaCl<sub>2</sub> aqueous solution and a PBS solution at pH = 7.4.

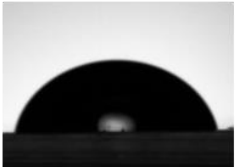
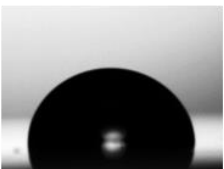
PBS solution is commonly used to imitate the properties of body fluids. The adhesive properties of compounds **6-9** were analysed in presence of this solution to check the possibility to use these adhesives in biomedical application, for example as surgical glue.

The use of CaCl<sub>2</sub> was instead driven by the important interactions between DOPA catechol group and calcium ions. Several examples of formation of three dimensional networks among peptides and Ca<sup>2+</sup> ions have been reported,<sup>45,339-341</sup> and the presence of DOPA enhances this effect, since the catechol group has the ability to chelate Ca<sup>2+</sup> ions.<sup>44,204,342,343</sup>

The values and corresponding photos of the contact angles are reported in **Table 6.1** for the four compounds synthesised and the three aqueous media tested. A continuous increase of the contact angle going from **6** to **8** can be noticed; this effect is more evident in Milli-Q® water.

Sample **9**, having all catechol groups free but also a bigger hydrophobic structure, shows intermediate values between samples **6** and **7**.

**Table 6.1** Contact angles of thin layers of **6**, **7** (m-**7** + p-**7**), **8** and **9** with the three aqueous solutions listed below.

| Sample   | H <sub>2</sub> O  | CaCl <sub>2</sub> 1M  | PBS pH 7.4  |
|----------|---|---|---|
|          | 54.7±3.9°   | 58.0±1.8°   | 49.9±1.0°   |
| <b>6</b> |    |    |    |
|          | 78.2±2.0°   | 63.7±1.0°   | 76.6±5.4°   |
| <b>7</b> |   |   |   |
|          | 94.0±0.5°   | 81.1±1.7°   | 84.0±1.1°   |
| <b>8</b> |  |  |  |
|          | 69.3±2.5°   | 71.2±2.2°   | 67.7±3.9°   |
| <b>9</b> |  |  |  |

Materials that are tacky or sticky are easily identified by touch, however, quantifying tack is not straightforward. The formation of the adhesive bond is not directly measured but assessed by breaking bonds by means of tack tests.<sup>344</sup> To evaluate the ability of films of **6**, **7**, **8** and **9** to adhere to a solid surface when brought into contact by a very light pressure, tack tests were performed using a rheometer.

To prepare the films, 20 mg of each molecule were dissolved in ethyl acetate (1 mL) and poured in a 25 mm glass petri dish (deposition area = 490.6 mm<sup>2</sup>) previously fixed on a disposable aluminium plate for rheometer. After solvent evaporation, 1 mL of aqueous solution was added on the top of the dry layer, covering the whole surface (**Figure 6.4**).

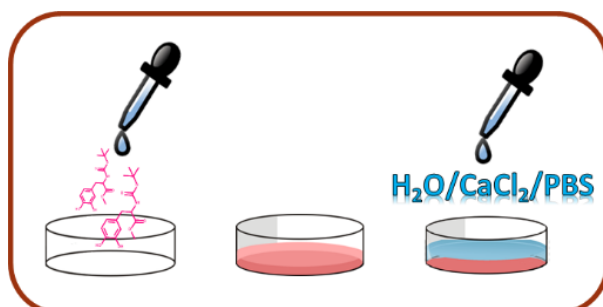


**Figure 6.4** Schematic representation of the procedure used for the preparation of films of **6**, **7**, **8** and **9**.

Films of **6**, **7**, **8** and **9** are not adhesive in the dry phase: the adhesiveness is generally triggered when the dried film is immersed in the aqueous solutions. Adhesion in humid conditions is a fundamental challenge to both natural and synthetic adhesives. Yet some glues from different biological systems appear to enhance their performances with increasing humidity.<sup>345</sup> The tack test experiments were performed using an Anton Paar Rheometer MCR102 with parallel plates geometry (**Figure 6.5**).

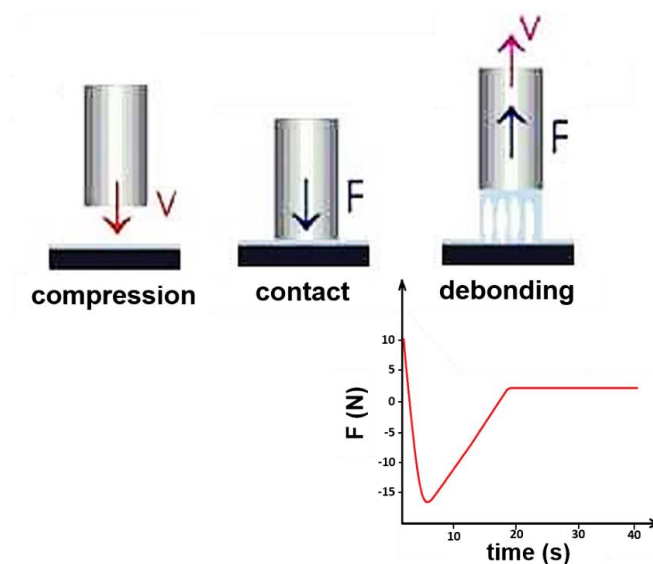


**Figure 6.5** Schematic representation of a generic tack test performed with a rheometer. The shaft moves down on the sample during the compression part, stays in contact for a certain time and then moves up, measuring the necessary force (N) for the debonding. The graph represents an adhesive force of 16 N.

During the test, the shaft moves down on the films immersed in the aqueous solution and, when in contact, applies 25 N force for 5 minutes to allow the adhesive interaction. After this time, the shaft moves up, detaching from the sample at a crosshead speed of 50  $\mu\text{m/s}$  (3 mm/min) and registering the force required for a complete debonding. When the shaft applies a compression force on the sample, the instrument registers a positive force on the graph; when the detachment from the sample takes place, the force registered is negative, but the absolute value should be taken.

All tack measurements were repeated at least three times for all samples and in all aqueous media (**Figure 6.6**).

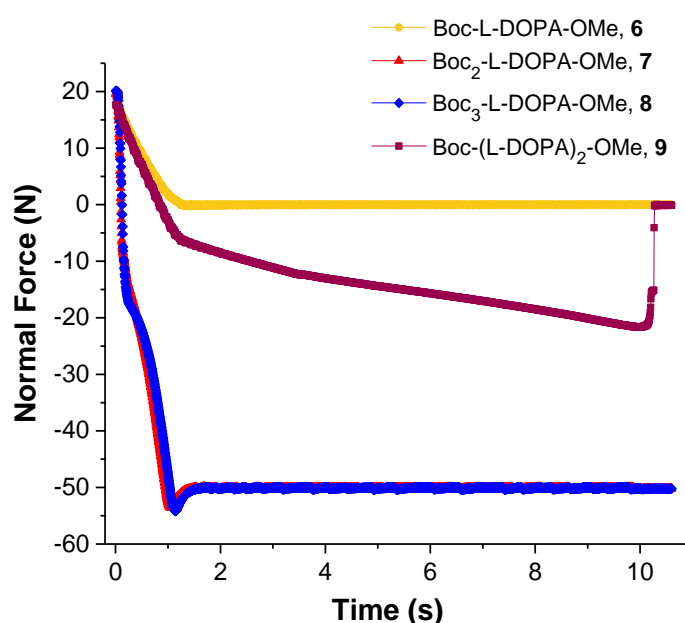


**Figure 6.6** Rheometer tack tests for molecules **6** (yellow), **7** (red), **8** (blue) and **9** (purple) in water.

Both Boc<sub>2</sub>-L-DOPA-OMe **7** and Boc<sub>3</sub>-L-DOPA-OMe **8** behave quite differently from Boc-L-DOPA-OMe **6**. In fact, **7** and **8** reach the maximum scale of the rheometer at 50 N, while **6** shows no adhesion at all. The increased adhesion of compound **9** compared to the monomer **6** may be ascribed to the presence of an additional catechol group.<sup>314</sup>

Unfortunately, the films of **8** completely detach from the petri dish at the end of the experiment and attach to the shaft (**Figure 6.7**). The film on the shaft is brittle in nature and breaks into small pieces by touching. This behaviour prevents the use of these films for multiple adhesion purposes.



**Figure 6.7** Film of **8** after the tack test.

The adhesive properties of the films were also tested in 1M CaCl<sub>2</sub> aqueous solution and in PBS solution at pH = 7.4. Films of compounds **6** and **9** were tested using the rheometer under the same conditions previously reported for the analysis in Milli-Q® water. **6** behaves in the same way in the three media, in agreement with the analysis of the contact angles which range between 50° and 58°. This result is not surprising if compared to the reported adhesive value for Boc-L-DOPA-OMe,<sup>346</sup> measured with AFM (Atomic Force Microscope). The value, measured on TiO<sub>2</sub> surfaces at a pH of 7.2, was 383 ± 21 pN, a very low value of adhesion, not even detectable with a rheometer.

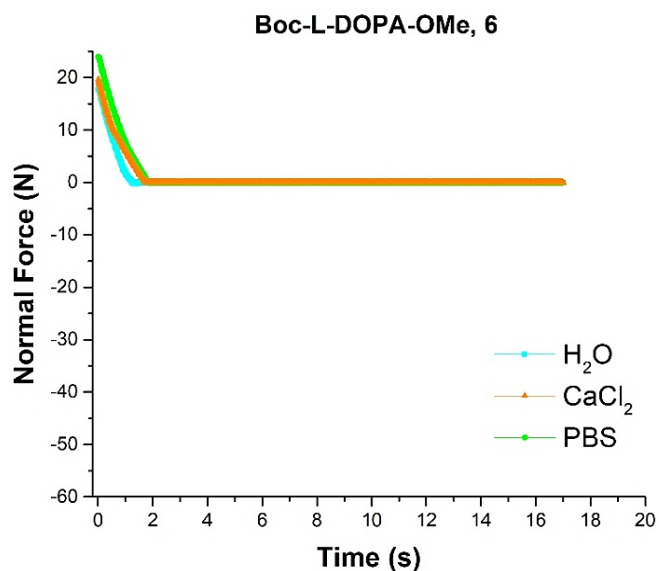


**Figure 6.8** Rheometer tack tests for Boc-L-DOPA-OMe **6** in the three aqueous media.

The behaviour of **9** in the three media (**Figure 6.9**) shows higher adhesion values (**Table 6.2**) compared to **6**, which can possibly be linked to the higher hydrophobicity of the molecule, confirmed by the higher contact angle values (67-71°). It is very clear that the application of CaCl<sub>2</sub> solution has a strong impact on the adhesive property of the molecule, compared with both PBS solution and Milli-Q® water.

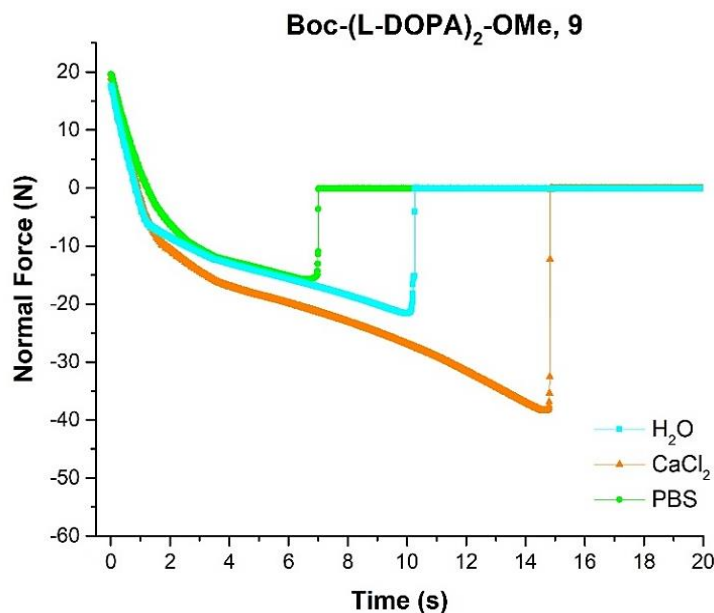


**Figure 6.9** Tack tests for Boc-(L-DOPA)<sub>2</sub>-OMe **9** in the three aqueous media.

**Table 6.2** Rheometer average values and standard deviations for compound **9** in the different aqueous media.

| Solvent              | <b>9</b> , Normal Force (N) |
|----------------------|-----------------------------|
| H <sub>2</sub> O     | 16.4 ± 4.9                  |
| CaCl <sub>2</sub> 1M | 46.7 ± 5.8                  |
| PBS pH 7.4           | 15.4 ± 0.8                  |

The adhesive properties of films of **7** and **8** were analysed with traction tests, because their rheometer tack tests reached the upper limit of the instrument sensitivity (50 N). An Instron 4465 testing system was employed to obtain a wider measuring capacity, up to 5 kN load cells, although with a reduced sensitivity. The tests were carried out with a 100 N load cell. In order to have a good comparison, the behaviour of **7** and **8** was tested once again in the three aqueous media. When the traction test for **7** was performed in a 1M CaCl<sub>2</sub> solution, the instrument could not detach the cell from the sample, meaning that the necessary force was higher than 100 N, the maximum force for that cell. For this reason, this experiment was repeated using a 1 kN load cell and an average value of  $129.7 \pm 16.8$  N was measured (**Figure 6.10**), which is an impressive value for a system not composed by polymers but single molecules. This adhesiveness is remarkable if compared with the tack strength of already reported polymers containing DOPA.<sup>347,348</sup> Moreover, film of **7** shows good resistance to use, not detaching from the petri and not breaking after use. However, this material is obtained by deposition of an inseparable mixture of *m-7* and *p-7*, so the deposition on the glass surface cannot be fully controlled: it is difficult to check the effective ratio and the behaviour of the two components and the exact 1:1 ratio in any sample is not guaranteed.

In contrast, Boc<sub>3</sub>-L-DOPA-OMe **8** is a pure compound and has high adhesiveness as it ranges between 76.3 and 82.3 N in all the media, showing the best results in water. The mechanical analysis of the films of **7** and **8** are summarised in **Figure 6.10**.

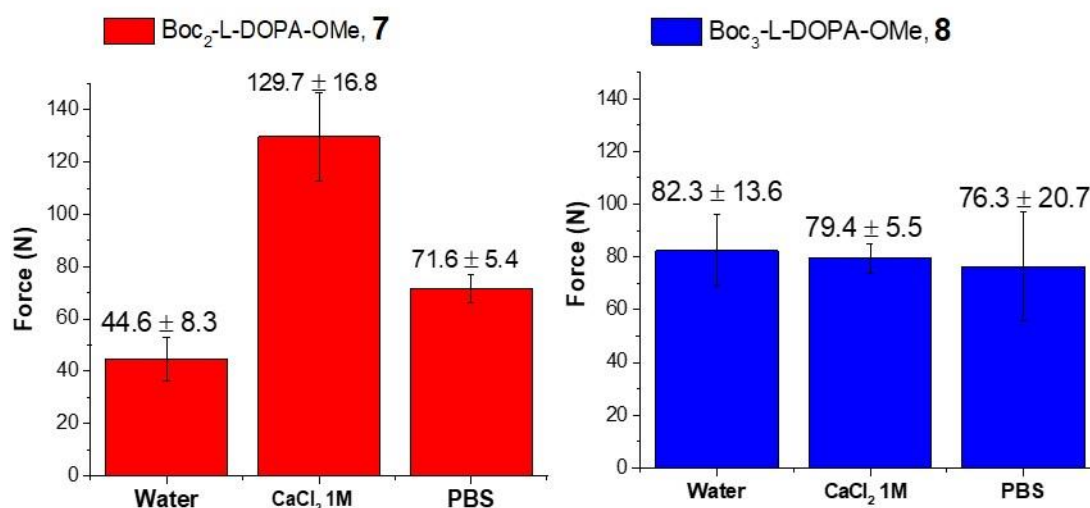


**Figure 6.10** Results for traction tests performed on films of **7** (left) and **8** (right) with an Instron 4465 testing system. Samples were prepared using the same geometry (petri dish with 25 mm of diameter),

deposition method and addition of the triggers used for tack tests. A 1 kN load cell was used for sample **7** in CaCl<sub>2</sub> 1M solution; for all the other measurements a 100 N load cell was used. All experiments were repeated at least three times.

To verify the multiple use properties of films of **9**, the tack test was repeated on the same sample for three times in 1M CaCl<sub>2</sub> aqueous solution, that is the medium where the films showed the most promising properties. These measures were not executed for films of **7**, because it was not possible to use the rheometer which has more reliability than the Instron in terms of sensitivity and reproducibility. Traction tests were not performed on **8**, because after the first tack measurement the film was completely detached from the shaft.

The repeated tests were performed on the same sample with the same parameters, except for the crosshead speed at which the shaft moves up for the test (1000 μm/s or 60 mm/min), to check the behaviour of the material under these conditions. The results reported in **Figure 6.11 a)** clearly show that the film of **9** exhibits repeated adhesiveness even though the adhesive strength is slightly decreased after each trial (**Table 6.3**). This result demonstrates the strong resistance against the destructive effect of water, which often adversely influences the strength of adhesiveness.<sup>316,349–351</sup> Moreover, an increase in the crosshead speed resulted in a faster detachment of the shaft from the adhesive film (from 14 s to 2 s) but did not affect the maximum force required. The tack test was repeated under the same conditions using a 0.1M CaCl<sub>2</sub> aqueous solution, to check the effect of the variation of concentration of Ca<sup>2+</sup> ions (**Figure 6.11 b)**).

**Table 6.3** Rheometer values of the multiple adhesion trials for compound **4** in 1 M and 0.1 M CaCl<sub>2</sub> solutions.

| <b>Trial</b> | <b>Normal Force (N)<br/>1M CaCl<sub>2</sub></b> | <b>Normal Force (N)<br/>0.1M CaCl<sub>2</sub></b> |
|--------------|---|---|
| 1            | 50.0  | 43.8  |
| 2            | 48.4  | 32.0  |
| 3            | 41.4  | 26.1  |

Under these conditions, the adhesive strength decreases in each trial more than in 1M CaCl<sub>2</sub> (Table 6.3), and in general the values are intermediate between the results obtained in water and 1M CaCl<sub>2</sub>. This outcome is in agreement with the previously reported high affinity of the catechol moiety with Ca<sup>2+</sup> ions:<sup>45,204,339–343</sup> when the Ca<sup>2+</sup> ions concentration decreases, the film efficiency for repeated measurements decreases accordingly.

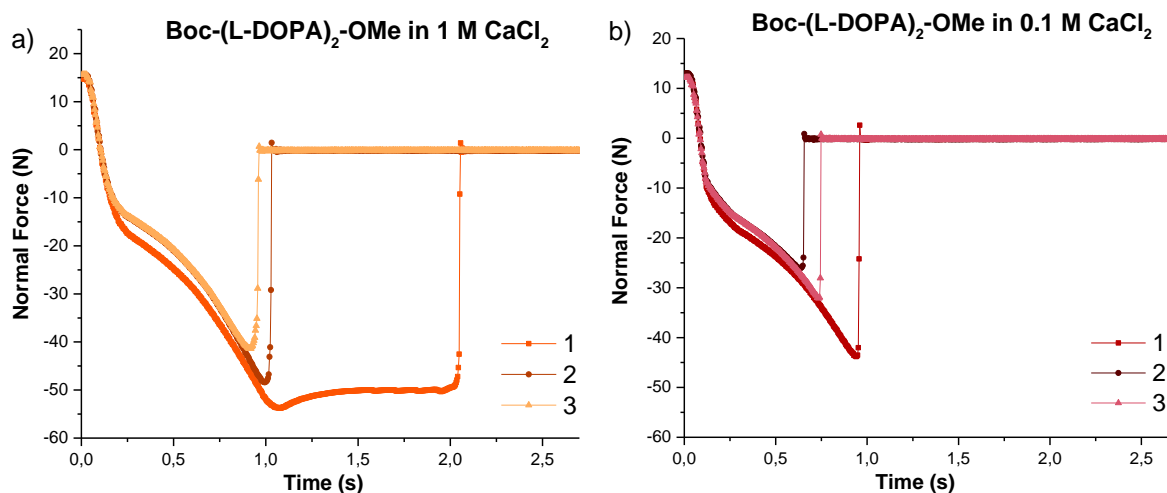


**Figure 6.11** Repeated tack tests for Boc-(L-DOPA)<sub>2</sub>-OMe **9**: **a)** in 1M CaCl<sub>2</sub> aqueous solution; **b)** in 0.1M CaCl<sub>2</sub> aqueous solution. In the legend, 1, 2 and 3 represent with different colours the 1<sup>st</sup>, the 2<sup>nd</sup> and the 3<sup>rd</sup> detachment performed on the same sample, accordingly.

To summarise, four compounds were synthesised through effective synthetic methods and tested as adhesives in three aqueous environments, because they were completely non adhesive in dry conditions.

In contrast to DOPA and catechol functionalised polymeric systems, which require complex preparation and cross-linking methods,<sup>330,347,352,353</sup> films of **6-9** were effectively produced by dissolution of **6-9** in ethyl acetate, deposition and evaporation (film casting). The introduction of protecting Boc groups on the catechol moiety stabilizes the compounds inhibiting the oxidation and increasing the reproducibility of the analyses. It also affects the hydrophobicity of the compounds, measured with the contact angle, which is probably correlated with the increase in the adhesive properties in all the aqueous media tested (Figure 6.12).

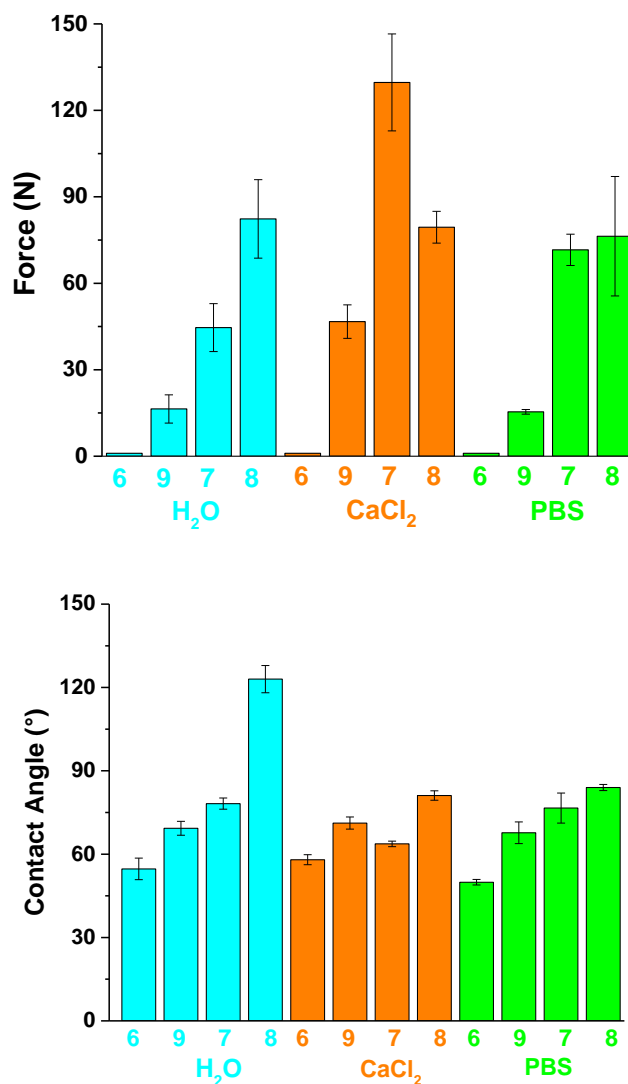


**Figure 6.12** Adhesive forces and contact angles comparison for compounds **6-9** in the three media. Increasing the Boc groups on the catechol (zero for molecules **6** and **9**, one for **7** and two for **8**) increases adhesive forces together with contact angles in all media.

Compound **6** shows no adhesion, in agreement with reported data.<sup>346</sup> Molecules **7**, **8** and **9** have different properties, so they may be all used as adhesives for different purposes.

- Boc<sub>2</sub>-L-DOPA-OMe **7** films show satisfactory performances for all the media tested, mainly in CaCl<sub>2</sub> aqueous solutions, suggesting that the presence of Ca<sup>2+</sup> is crucial for the formation of a complex with higher adhesion capability.

- Boc-(L-DOPA)<sub>2</sub>-OMe **9** has a similar behaviour, showing the highest adhesion value in CaCl<sub>2</sub>, yet appearing less efficient than **7**. It can be also used in multiple adhesion applications.

- Boc<sub>3</sub>-L-DOPA-OMe **8** shows high adhesive values in all the aqueous media tested and the best performance in PBS solution, so it may be used for biomedical purposes.

These functionalisations play a pivotal role in the adhesive behaviour of L-DOPA, yet the process controlling this phenomenon needs further studies, as it is not possible to exclude that the changes in the cohesive strength across compounds may be also due to the introduction of protecting groups and water absorption phenomena.

### 6.1.3 Materials and Methods

**Contact angle** - Each sample is dissolved in ethyl acetate and deposited on a glass slide to cover all the surface. The slide is placed in a vacuum desiccator to allow solvent evaporation and avoid powder contamination. The measurements are performed using a contact angle meter Attension Theta Lite (optical tensiometer), using static contact angle (Young-Laplace) analysis mode. A single drop (5  $\mu$ L) of solvent (Milli-Q® water, 1M CaCl<sub>2</sub> or PBS at pH = 7.4 solutions) at 25 °C is dropped on the sample, recording the contact angle for 10 s.

Each measure was repeated three times for each solvent and molecule. The contact angle value was taken after 3 s, once the droplet reached a stability plateau.

**Tack Test** - Tack tests were performed using an Anton Paar Rheometer MCR 102. All experiments were performed with a plate-system ( $\varnothing=25$  mm, plate-geometry), at a temperature of 23 °C controlled by the integrated Peltier system. Already predefined tack test definitions in the RheoCompass (Rheometer software) with minor changes were used to carry out the tests. Samples were prepared pouring a solution of 20 mg of each molecule in 1 mL ethyl acetate in a 25 mm glass petri dish (deposition area = 490.6 mm<sup>2</sup>) previously fixed on a disposable aluminium plate for rheometer. After solvent evaporation, 1 mL of the trigger solution (Milli-Q® water, CaCl<sub>2</sub> 1M solution or PBS solution) is poured into the petri dish on the dry layer of the deposited molecule, to cover the whole surface. 25 N force is applied from the shaft for 5 mins for the curing of the adhesive material. The experiment was conducted at a crosshead speed of 50  $\mu$ m/s (3 mm/min). All measurements were repeated at least three times.

**Traction Test** - Instron 4465 testing system was used to perform the measurements. Samples were prepared using the same geometry (25 mm petri dish), deposition method and

addition of the triggers used for the Tack Test. A load cell of 100 N was used (1 kN in a specific case) applying 15 N force for 5 mins for the curing of the adhesive material. The experiment was conducted at a crosshead speed of 50  $\mu\text{m/s}$  (3 mm/min). All measurements were repeated at least three times.

### $^1\text{H-NMR}$ characterisation of Boc<sub>2</sub>-L-DOPA-OMe (*p*-7 and *m*-7)

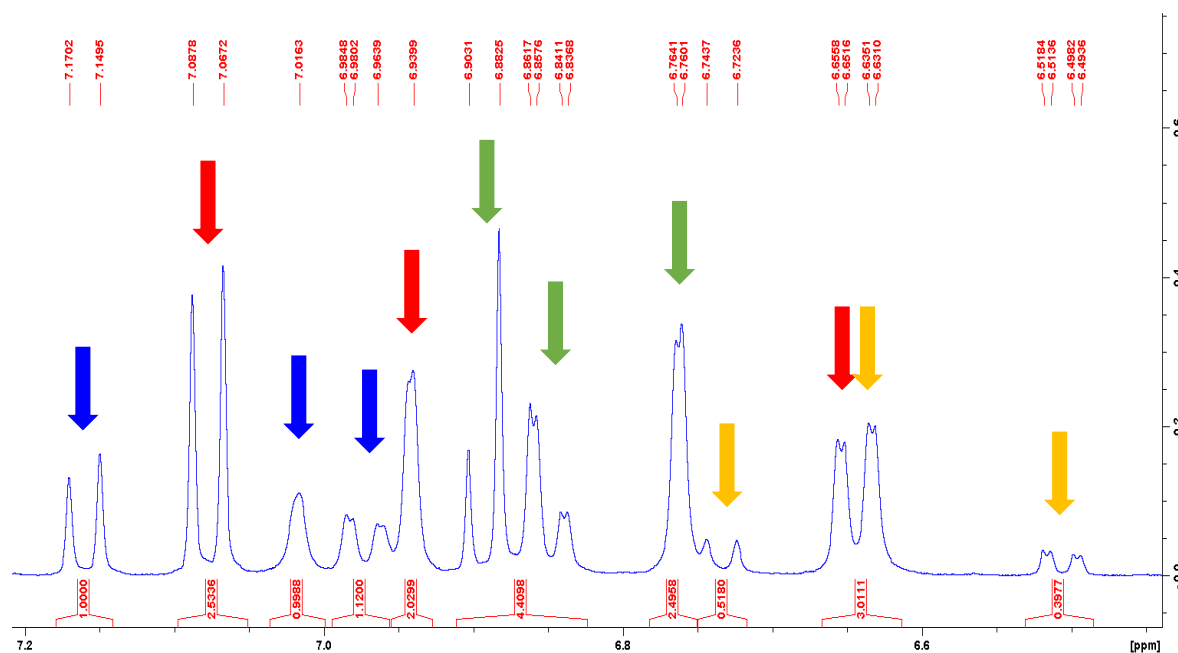


**Figure 6.13** Zoom on the range 6.45 - 7.2 ppm of the  $^1\text{H-NMR}$  spectrum of the crude of the reaction for Boc<sub>2</sub>-L-DOPA-OMe **7** synthesis. Each arrow indicates the shifts of the three H of the aromatic ring for each molecule, divided per colour: blue for **8**, red for *p*-7, green for *m*-7, gold for **6**. It is possible to assign the relative ratio of each molecule in the crude: **8** : *p*-7 : *m*-7 : **6** = 1 : 2.5 : 2.5 : 0.5.

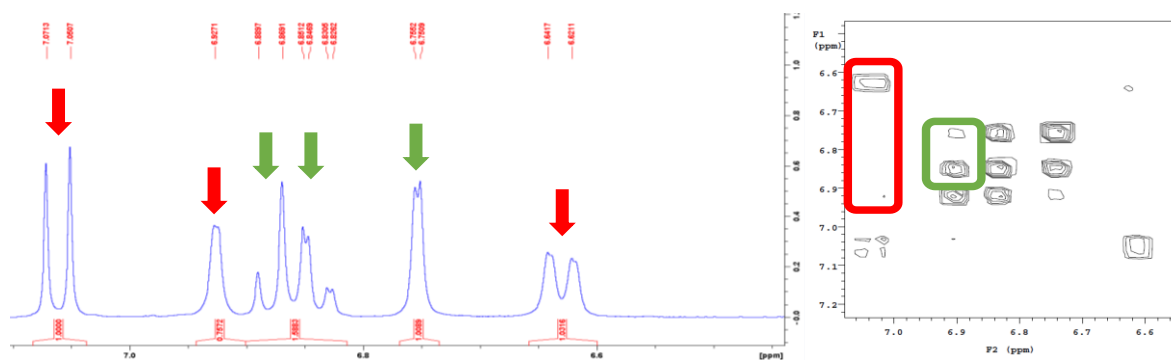


**Figure 6.14** Insets of  $^1\text{H}$  NMR and  $g$ -COSY spectra of an inseparable mixture of  $m$ -7 and  $p$ -7. The signals of the three aromatic hydrogens belonging to the two species are highlighted in red and green.

## Chapter 7

---

### 7. Conclusions

In this thesis, several types of gelators were synthesised, starting from amino acids and long chain fatty acids. The synthesis was performed through multistep procedures in solution and standard reactions of protection, deprotection and coupling. The attention was focused on derivatives of three aromatic amino acids, L-phenylalanine, L-tyrosine and L-DOPA, because the presence of aromatic groups introduces interactions favourable for the formation of supramolecular architectures. These derivatives were further functionalised with long chain fatty acids (azelaic acid or lauric acid), aromatic protecting groups (Fmoc groups or benzyl ethers) or oxazolidin-2-one moieties, to introduce additional hydrophobic interactions,  $\pi$ - $\pi$  stackings or local constraints, because these non-covalent interactions usually favour the formation of the supramolecular material.

After the purification and characterisation of the compounds, the conditions for the formation of self-assembled materials were investigated, varying the combination of gelator concentration, solvent and trigger. All the gelators reported (**1-6**) gave stable self-supporting gels with  $G'$  approximately one order of magnitude higher than  $G''$ . The morphological analyses were performed on the dried samples (xerogels or aerogels) to have a better understanding on the fibres network in terms of arrangement and dimensions. It was observed that the gel morphology is highly affected from the conditions of preparation of the samples. In Chapter 3 and 4, for example, the same gelator is used for the preparation of gels with different triggers, leading to completely different network structures.

Every gel was functionalised for a suitable application depending on its intrinsic features. In Chapter 2, different gelators were studied for application in water remediation. A first study was focused on the synthesis of two gelators, that were compared for the preparation of organogels triggered by sonication. Lau-L-Dopa(Bn)<sub>2</sub>-D-Oxd-OBn is able to gelate several organic solvents at 2% concentration, while Fmoc-L-Dopa(Bn)<sub>2</sub>-D-Oxd-OBn, never formed a gel in any concentration or condition. This result suggests that the saturated long chain of the

lauric acid is crucial for the formation of the three-dimensional network.

Since the ethanol organogel proved to have the best rheological properties among all samples, it was treated with an aqueous solution of Rhodamine B, to perform a preliminary test of its ability to adsorb pollutants from water. After 24 hours, the emission spectrum intensity of the Rhodamine B solution is reduced to the 23% of the original sample, thus confirming that the molecule is trapped into the organogel. Further studies can be performed on similar organogels to improve the efficiency in the removal of pollutant from water and to better investigate the mechanism involved in the absorption process.

The second part of the chapter focused on the preparation of transparent gels in combination with photocatalysts ( $\text{TiO}_2$  or  $\text{TiO}_2$ -graphene combined systems) for pollutant photodegradation. Upon irradiation, the degradation of RhB occurs inside the matrix and its complete for samples containing  $\text{TiO}_2$  nanoparticles. Samples containing the combination of  $\text{TiO}_2$ -graphene showed the presence of aggregates, probably related to the decreased mechanical properties of these samples and the decreased photodegradation efficiency (80%). This result highlights how the addition of a filler should be carefully checked in a supramolecular material, since it may influence the formation of the network and sometimes negatively affect the performances of the material.

In Chapter 3 a further investigation on the addition of graphene inside supramolecular gels was performed. The aim of the study was to use the gelator itself as dispersant for the graphene filler. An already reported robust gelator  $\text{Az}-(\text{L-Phe-D-Oxd-OH})_2$  was chosen, containing aromatic groups of the two phenylalanine that can interact with the aromatic groups of graphene and help the dispersion. The use of this molecule as dispersant for the graphene filler resulted in a library of gels with highly increased mechanical properties, thus suggesting that a positive interaction between the gel network and graphene fillers is possible, using the right gelator and the right preparation method. The hydrogels with a final neutral pH were also tested as biocompatible scaffolds for cell growth. Even though a toxic effect was detected after 24 h in samples containing higher graphene doping, after 48 h cells continued to proliferate, demonstrating that the gel scaffold supports cell growth.

In Chapter 4 composite organic-inorganic materials were prepared, and the interactions between the gel phase and an inorganic mineral phase were investigated. The first part of the chapter was focused on the possibility to grow calcium carbonate crystals inside gels.

The formation of composite materials was confirmed, with the fibrous network of the gel perfectly integrated with the crystal phase. A particular attention was paid to the reversibility of calcium uptake from the gel to the environment and vice versa. Calcium can be removed from the network inducing a modification in the organization of the supramolecular fibres and an improvement in the mechanical properties of the material.

The second part of the chapter continued the investigation on composite materials, using the same gelator and a more complex inorganic matrix, the one used for bone cement scaffolds. Calcium Phosphate Cements were successfully obtained for the first time using LMWGs as fibre reinforcement, thanks to a deep investigation and a fine tuning of the conditions and the method of preparation. The final materials show once again a perfect integration between the mineral phase and the gelator fibres. This study paves the way to a new set of applications in the biomedical field, where LMWGs can form fibres inside biomimetic scaffolds, influencing the mechanical properties and increasing the porosity of the material.

Chapter 5 the formation of crystals of the gelator itself was studied. This gelator forms metastable gels that evolve with time, becoming solution containing crystals. It was noticed that the kinetics of gel and crystal formation are not only affected by the trigger amount but also by the geometry (dimension, thickness, area) of the holder containing the sample. This parameter is rarely reported in literature, even though it can lead to mistakes and complications in the comparison across techniques which typically use different geometries. The metastable gels were also studied in combination with a gelator forming stable gels, for the preparation of multicomponent systems. In this way, it was possible to obtain gels containing crystals, with mechanical properties higher than the two single components.

Finally, in Chapter 6, some molecules based on L-DOPA were studied as underwater adhesives. It was observed that the lack of benzyl ethers as protecting groups of the catechol moiety led to the formation of compounds with a sticky nature and unable to form gels, thus confirming the importance of additional aromatic groups and  $\pi$ - $\pi$  stacking interactions in gel formation. Three out of the four compounds synthesised showed high adhesive properties when immersed in aqueous solutions, even when compared to more complex polymeric systems. The three compounds have different properties and behaviour, so they may be all used as adhesives for different purposes. This result paved the way for new set of applications as biocompatible underwater adhesives.



## Chapter 8

---

### 8. Experimental procedures

#### 8.1 Synthesis and characterisation

All chemicals and solvents were purchased from Sigma-Aldrich, VWR or Iris Biotech and used as received. MilliQ water (Millipore, resistivity = 18.2 m $\Omega$  cm) was used throughout. All reactions were carried out in dried glassware. The melting points of the compounds were determined in open capillaries and are uncorrected. High quality infrared spectra (64 scans) were obtained at 2 cm<sup>-1</sup> resolution with an ATR-FT-IR Bruker Alpha System spectrometer. NMR spectra were recorded with a Varian Inova 400 spectrometer at 400 MHz (<sup>1</sup>H NMR) and at 100 MHz (<sup>13</sup>C NMR). Chemical shifts are reported in  $\delta$  values relative to the solvent peak. HPLC-MS analysis was carried out with an HP1100 liquid chromatograph coupled to an electrospray ionization mass spectrometer (LC-ESI-MS), using a Phenomenex Gemini C18 - 3 $\mu$  - 110 Å column, H<sub>2</sub>O/CH<sub>3</sub>CN as neutral solvent or H<sub>2</sub>O/CH<sub>3</sub>CN with 0.2% formic acid as acid solvent at 40 °C (positive ion mode, m/z = 50-2000, fragmentor 70 V).

**Boc-L-Dopa-OMe (6)** – The compound was synthesized following a multistep procedure in solution as reported in literature.<sup>98</sup>

Thionyl chloride (10 mL, 137 mmol) was added dropwise to MeOH (60 mL) at 0 °C, and the resulting solution was treated portion-wise with 5 g of L-DOPA (25.4 mmol). The ice bath was removed. The reaction mixture warmed to room temperature with stirring for 24 hours. The volatiles were removed under vacuum to afford L-DOPA-OMe·HCl, with a yield of 99%. The ester was dissolved in a solution of NaHCO<sub>3</sub> (4.27 g, 50.8 mmol, 2 eq) in 58 mL of water, treated with a solution of Boc<sub>2</sub>O (5.82 mL, 25.4 mmol, 1 eq) in THF (30 mL), and stirred for 18 hours. The volatiles were removed under reduced pressure. The residue was suspended in H<sub>2</sub>O (10 mL) and extracted with ethyl acetate (150 mL x 3). The combined organic phase was washed with 1M HCl (2 x 20 mL), with a saturated aqueous NaHCO<sub>3</sub> solution (1 x 20 mL) and with H<sub>2</sub>O (1 x 20 mL). The organic phase was dried over Na<sub>2</sub>SO<sub>4</sub> and evaporated. Boc-L-DOPA-OMe was obtained as white solid with 98% yield. M.p. = 137-138 °C; [ $\alpha$ ]<sub>D</sub><sup>25</sup>

+18.0° (c = 0.5 in EtOAc); IR (ATR-IR):  $\nu$  3342, 3297, 1739, 1695, 1606, 1514  $\text{cm}^{-1}$ ;  $^1\text{H}$  NMR ( $\text{CD}_3\text{OD}$ ):  $\delta$  1.38 (9H, s, *t*-Bu), 2.75 (1H, dd,  $J$  = 8.4, 13.6 Hz, PhCHHNH), 2.89 (1H, dd,  $J$  = 5.6, 13.6 Hz, PhCHHNH), 3.66 (3H, s, OCH<sub>3</sub>), 4.25 (1H, dd,  $J$  = 6.0, 7.6 Hz, PhCH<sub>2</sub>CHNH), 6.46 (1H, d,  $J$  = 8.0 Hz, Ar), 6.59 (1H, s, Ar), 6.64 (1H, d,  $J$  = 8.0 Hz, Ar) ppm;  $^{13}\text{C}$  ( $\text{CD}_3\text{OD}$ ):  $\delta$  27.3, 36.8, 51.2, 55.3, 79.3, 114.9, 115.9, 120.3, 128.2, 143.8, 144.8, 156.3, 173.0 ppm. HPLC-MS (API-ES): 4.22 min,  $[\text{M}+\text{Na}]^+=334$ . Anal. Calcd. for  $\text{C}_{15}\text{H}_{21}\text{NO}_6$ : C, 57.87; H, 6.80; N, 4.50. Found: C, 57.84; H, 6.77; N, 4.53

**Boc-L-Dopa(Bn)<sub>2</sub>-OMe** – A solution of 1.5 g (4.82 mmol) of Boc-L-DOPA-OMe in 50 mL of acetone was treated with 1.46 g (10.6 mmol) of  $\text{K}_2\text{CO}_3$ , 144 mg (0.96 mmol) of NaI, 310 mg (0.96 mmol) of TBAB and 1.26 ml (10.6 mmol) of BnBr, heated and stirred at reflux for 4 hours. The volatiles were evaporated under reduced pressure. The residue was dissolved in  $\text{CH}_2\text{Cl}_2$  and washed with water. The organic phase was dried over sodium sulphate and evaporated under reduced pressure. The residue was purified by flash chromatography<sup>354</sup> (cyclohexane:ethyl acetate 8:2) and obtained as a white solid with 95% yield. M.p.=112 °C;  $[\alpha]_{\text{D}}^{25}$  +5.0° (c = 0.5 in EtOAc);  $^1\text{H}$  NMR ( $\text{CDCl}_3$ ):  $\delta$  1.44 (s, 9H,  $\text{CH}_3\text{Boc}$ ), 3.00 (m, poorly resolved ABX system), 2H, ArCH<sub>2</sub>), 3.65 (s, 3H, OCH<sub>3</sub>), 4.54 (m, 1H, CHa), 4.97 (d,  $J$  = 7.9 Hz, 1H, NH), 5.30 (s, 4H, OCH<sub>2</sub>Ph), 6.65 (dd,  $J$  = 8.2 and 1.9 Hz, 1H, ArH) ; 6.74 (d,  $J$  = 1.9 Hz, 1H, ArH); 6.87 (d,  $J$  = 8.1 Hz, 1H, ArH); 7.41 (m, 10H, ArHOBn) ppm.  $^{13}\text{C}$  NMR ( $\text{CDCl}_3$ ):  $\delta$  28.7, 38.2, 52.5, 54.8, 71.7, 71.8, 80.3, 115.6, 116.6, 122.7, 127.7, 128.2, 137.7, 148.5, 149.3, 155.5, 172.7 ppm.

**Boc-L-Dopa(Bn)<sub>2</sub>-OH (4)** - Boc-L-DOPA(Bn)<sub>2</sub>-OH can be obtained by selective deprotection of the C-terminal methyl ester.

A solution of 1.8 g (3.66 mmol) of Boc-L-DOPA(Bn)<sub>2</sub>-OMe in 6 ml of MeOH and 12 ml of THF was cooled to 0 °C and treated with 4.6 ml (4.57 mmol) of NaOH 1M. The ice bath was removed. The mixture warmed to room temperature with stirring for 18 hours. A solution of 5.1 ml of HCl 1M was added to the reaction mixture, which was concentrated in vacuo to remove the volatiles. The reduced volume was then extracted with three portions of  $\text{CH}_2\text{Cl}_2$  (3 x 30 mL). The organic phase was combined, washed with water (60 mL), dried over  $\text{MgSO}_4$ , filtered and evaporated in vacuo, to afford pure Boc-L-DOPA(Bn)<sub>2</sub>-OH (97%) as a white solid. M.p.=120 °C;  $^1\text{H}$  NMR ( $\text{CDCl}_3$ ):  $\delta$  1.42 (s, 9H,  $\text{CH}_3\text{Boc}$ ), 3.04 (m, poorly resolved ABX system), 2H, ArCH<sub>2</sub>), 4.52 (m, 1H, CHa); 4.93 (d (br), 1H, NH), 5.11 (s, 4H, OCH<sub>2</sub>Ph), 6.69

(d,  $J = 7.6$  Hz, 1H, ArH), 6.80 (s, 1H, ArH), 6.85 (d,  $J = 8.0$  Hz, 1H, ArH), 7.37 (m, 10H, ArH OBn), 8.36 (s (br), 1H, COOH) ppm.  $^{13}\text{C}$  NMR ( $\text{CDCl}_3$ ):  $\delta$  28.2, 36.1, 48.6, 70.2, 70.2, 77.9, 114.4, 115.7, 121.8, 127.4, 127.6, 127.7, 127.8, 128.3, 128.4, 131.2, 137.5, 146.8, 148.0, 155.4, 173.9 ppm. HPLC-MS (API-ES): 9.32 min,  $[\text{M}+\text{Na}]^+=500$ .

**Boc-L-Dopa(Bn)<sub>2</sub>-D-Oxd-OMe** - The compound was synthesised according to the previously reported protocol.<sup>355</sup>

To a stirred solution of Boc-L-DOPA(Bn)<sub>2</sub>-OH (466 mg, 0.98 mmol) and HBTU (400 mg, 1.07 mmol) in dry acetonitrile (10 mL) under an inert atmosphere, H-D-Oxd-OBn (229 mg, 0.98 mmol) in dry acetonitrile (5 mL) was added dropwise at room temperature, followed by DIPEA (349  $\mu\text{L}$ , 2.05 mmol). After 4 h the volatiles were removed under reduced pressure. The residue was dissolved in dichloromethane (30 mL), washed with water (30 mL), 1 N aqueous HCl (30 mL) and 5% aqueous  $\text{NaHCO}_3$  (30 mL), dried over anhydrous  $\text{Na}_2\text{SO}_4$ , filtered and concentrated in vacuo. The residue was dissolved in methanol (10 mL), ultrasonicated for 15 min and then filtered through a Gooch funnel. The solid was washed with methanol (1 $\times$ 20 mL), dissolved in dichloromethane to recover it from the filter and concentrated in vacuo to afford Boc-L-DOPA(Bn)<sub>2</sub>-D-Oxd-OBn (576 mg, 0.83 mmol) as a white solid (85% yield). M.p. = 171.6–172.0  $^\circ\text{C}$ ; IR (3 mM in  $\text{CH}_2\text{Cl}_2$ ):  $\nu$  3439, 1791, 1754, 1711, 1508, 1496  $\text{cm}^{-1}$ ;  $^1\text{H}$  NMR ( $\text{CDCl}_3$ ):  $\delta$  1.36 (d,  $J = 6.4$  Hz, 3H,  $\text{CH}_3$  Oxd), 1.40 (s, 9H, t-Bu), 2.81–2.94 (m, 1H,  $\text{CHH}\beta$ -DOPA), 2.96–3.09 (m, 1H,  $\text{CHH}\beta$ -DOPA), 4.25 (d,  $J = 3.9$  Hz, 1H,  $\text{CHN}$  Oxd), 4.43–4.56 (m, 1H,  $\text{CHO}$  Oxd), 5.11 (s, 2H,  $\text{CH}_2\text{Ph}$ ), 5.14 (s, 2H,  $\text{CH}_2\text{Ph}$ ), 5.21 (s, 2H,  $\text{CH}_2\text{Ph}$ ), 5.78 (s, 1H,  $\text{CH}\alpha$ -DOPA), 6.69 (d,  $J = 8.2$  Hz, 1H,  $\text{CH Ar DOPA}$ ), 6.75–6.96 (m, 2H,  $\text{CH Ar DOPA}$ ), 7.14–7.58 (m, 15H, ArH) ppm.  $^{13}\text{C}$  NMR ( $\text{CDCl}_3$ ):  $\delta$  21.1, 28.4, 38.8, 53.9, 61.9, 68.1, 71.3, 71.4, 73.6, 79.9, 115.1, 116.4, 122.5, 127.3, 127.6, 127.8, 127.9, 128.4, 128.5, 128.8, 129.1, 134.7, 137.3, 137.4, 148.2, 149.0, 151.2, 154.7, 167.5, 172.7 ppm. Anal. Calcd. for  $\text{C}_{50}\text{H}_{44}\text{N}_2\text{O}_9$ : C, 73.52; H, 5.43; N, 3.43. Found: C, 73.48; H, 5.41; N, 3.39.

**Lau-L-Dopa(Bn)<sub>2</sub>-D-Oxd-OBn (1)** - Trifluoroacetic acid (1.14 mL, 14.40 mmol) was added under an nitrogen atmosphere to a solution of Boc-L-DOPA(Bn)<sub>2</sub>-D-Oxd-OBn (558 mg, 0.80 mmol) in dry dichloromethane (5 mL). After 4 h, the reaction was complete, the volatiles were removed under reduced pressure, and H-L-DOPA(Bn)<sub>2</sub>-D-Oxd-OBn $\cdot\text{CF}_3\text{CO}_2\text{H}$  was obtained in quantitative yield.

The resulting compound (1 eq.) was dissolved in a solution of dry ACN and DIPEA (2.2 eq.) and added dropwise to a stirred solution of lauric acid (1 eq.) and HBTU (1.1 eq.) in dry ACN.

After 2 h at r.t., the solution was evaporated under reduced pressure. The residue was dissolved in DCM and extracted with H<sub>2</sub>O, HCl 1M, saturated NaHCO<sub>3</sub>, H<sub>2</sub>O. The organic layer was dried over sodium sulphate, filtered, and concentrated under reduced pressure. The residue was washed with MeOH, sonicated and filtered. The product (Lau-L-Dopa(Bn)<sub>2</sub>-D-Oxd-OBn) was obtained as a white solid with a yield of 85%. M.p. = 172-175 °C; IR: 3324, 1792, 1739, 1711, 1645 cm<sup>-1</sup>; <sup>1</sup>H NMR (CDCl<sub>3</sub>): δ 0.9 (t, 3H, CH<sub>3</sub> Lau), 1.25 (m, 18H, CH<sub>2</sub> Lau), 1.36 (d, J = 6.4 Hz, 3H, CH<sub>3</sub> Oxd), 2.1 (m, 2H, CH<sub>2</sub>CO Lau), 2.93 (dd, J = 6.8, 13.6 Hz, 1H, CHHβ-Dopa), 3.04 (dd, J = 6.0, 13.6 Hz, 1H, CHHβ-Dopa), 4.23 (d, J = 3.9 Hz, 1H, CHN Oxd), 4.49 (dq, J = 3.9, 6.4 Hz, 1H, CHO Oxd), 5.09 (s, 2H, CH<sub>2</sub>Ph), 5.11 (s, 2H, CH<sub>2</sub>Ph), 5.18 (s, 2H, CH<sub>2</sub>Ph), 5.92 (d, J = 7.6 Hz, 1H, NH), 6.00 (dt, J = 6.8, 7.6 Hz, 1H, CHα-Dopa), 6.69 (d, J = 8.0 Hz, 1H, CH Ar Dopa), 6.79 (s, 1H, CH Ar Dopa), 6.81 (d, J = 8.0 Hz, 1H, CH Ar Dopa), 7.24–7.45 (m, 15H, ArH) ppm. <sup>13</sup>C NMR (CDCl<sub>3</sub>): δ 14.1, 21.1, 22.7, 25.5, 29.2, 29.3, 29.4, 29.5, 29.6, 29.6, 31.9, 36.4, 38.1, 52.5, 61.8, 68.0, 71.3, 73.6, 115.0, 116.3, 122.3, 127.2, 127.4, 127.7, 127.8, 128.4, 128.5, 128.7, 128.8, 128.9, 134.6, 137.2, 137.3, 148.2, 148.9, 151.0, 167.3, 172.2 ppm.

**Fmoc-L-Tyr-D-Oxd-OBn** - The compound was synthesized from Fmoc-L-Tyr(*t*-Bu)-OH and D-Thr following a multistep procedure in solution, reported in ref.<sup>95</sup>.

To a stirred solution of Fmoc-Tyr(O-*tert*-Bu)-OH (0.64 mmol, 294 mg) and HATU (0.70 mmol, 267 mg), in dry acetonitrile (15 mL), under inert atmosphere, D-Oxd-OBn (0.64 mmol, 150 mg) in dry acetonitrile (7 mL) was added at room temperature, followed by a solution of N,N-diisopropylethylamine (1.6 mmol, 272 μL). The solution was stirred for 2 hours under inert atmosphere. The volatiles were removed under reduced pressure. The residue was dissolved in dichloromethane (30 mL). The mixture was washed with brine (30 mL), 1 N aqueous HCl (30 mL) and with saturated aqueous NaHCO<sub>3</sub> (30 mL), dried over sodium sulphate and concentrated in vacuo. The product was obtained pure after silica gel chromatography (dichloromethane → dichloromethane/ethyl acetate 98:2). Evaporation of the collected fractions gave the solid product in 90% of yield (0.576 mmol, 389 mg). M.p. = 89-90 °C; [α]<sub>D</sub><sup>20</sup> 31.5 (c = 0.20 in CH<sub>2</sub>Cl<sub>2</sub>); IR (CH<sub>2</sub>Cl<sub>2</sub> 3 mM) ν = 3429, 1793, 1755, 1712, 1608, 1506 cm<sup>-1</sup>; <sup>1</sup>H NMR (CDCl<sub>3</sub>): δ 1.29 (s, 9H, CH<sub>3</sub> *tert*-Bu), 1.47 (d, J = 6.2 Hz, 3H, CH<sub>3</sub> Oxd), 2.95 (dd, J = 7.5, J = 13.3 Hz, 1H, CH<sub>2</sub>β-Tyr), 3.15 (dd, J = 5.4 Hz, J = 13.7 Hz, 1H, CH<sub>2</sub>β-Tyr), 4.15-4.21 (m, 1H, O-CH-CH<sub>2</sub>-Fluorene), 4.23-4.29 (m, 1H, O-CH-CH<sub>2</sub><sup>2</sup>-Fluorene), 4.38 (s, 2H, CHN Oxd + O-CH-CH<sub>2</sub>-Fluorene), 4.52-4.58 (m, 1H, CHO Oxd), 5.19 (s, 2H, O-CH<sub>2</sub>-Ph), 5.42 (d, J = 8.4 Hz, 1H, NH Tyr), 5.82-5.89 (m, 1H, CHα-Tyr), 6.89 (d, J = 7.4 Hz, 2H, CH Ar Tyr), 7.08 (d, J = 7.4

Hz, 2H, CH Ar Tyr), 7.28-7.34 (m, 7H, 2 CH Fluorene + 5 CH Ph), 7.40 (t,  $J=7.4$  Hz, 2H, CH Fluorene), 7.56 (d,  $J=7.1$  Hz, 2H, CH Fluorene), 7.76 (d,  $J=7.1$  Hz, 2H, CH Fluorene) ppm.  $^{13}\text{C}$  NMR ( $\text{CDCl}_3$ ):  $\delta$  21.3, 28.9, 38.4, 47.2, 54.5, 62.0, 67.1, 68.2, 73.8, 78.5, 120.0, 124.2, 125.2, 125.3, 127.2, 127.8, 128.4, 128.8, 130.0, 130.2, 134.6, 141.4, 144.0, 151.2, 154.7, 155.3, 167.4, 172.3 ppm.

**Fmoc-L-Tyr-D-Oxd-OH (2)** - To a stirred solution of Fmoc-L-Tyr(O-*tert*-Bu)-D-Oxd-OBn (0.576 mmol, 389 mg) in dry dichloromethane (6 mL), under inert atmosphere, trifluoroacetic acid (10.4 mmol, 800  $\mu\text{L}$ ) was added at room temperature. The solution was stirred for 4 hours under inert atmosphere, then the mixture was washed with water (3 x 5 mL), dried over sodium sulphate and concentrated in vacuo. The white solid obtained (356 mg) was dissolved in methanol (10 mL) and treated with Pd/C (10% w/w, 39 mg) under inert atmosphere. Vacuum was created inside the flask using the vacuum line. The flask was then filled with hydrogen using a balloon (1 atm). The solution was stirred for 4 hours under a hydrogen atmosphere. After filtration through Celite<sup>TM</sup> filter and concentration in vacuo, the acid was obtained as a solid (0.563 mmol, 299 mg, 98%). M.p. = 192-195 °C;  $[\alpha]_{\text{D}}^{20}$  9.5 (c = 0.13 in  $\text{CH}_3\text{OH}$ ); ATR-IR  $\nu$  = 3326, 1781, 1691, 1535, 1513  $\text{cm}^{-1}$ ;  $^1\text{H}$  NMR ( $\text{CD}_3\text{OD}$ ):  $\delta$  = 1.45 (d,  $J$  = 6.3 Hz, 3H,  $\text{CH}_3$  Oxd), 2.76 (dd,  $J=9.6$  Hz,  $J=13.5$  Hz 1H,  $\text{CH}_2\beta$ -Tyr.), 3.07 (dd,  $J=4.7$  Hz,  $J=13.7$  Hz, 1H,  $\text{CH}_2\beta$ -Tyr), 4.12-4.20 (m, 2H, O-CH- $\text{CH}_2$ -Fluorene), 4.25-4.29 (m, 1H, O-CH- $\text{CH}_2$ -Fluorene), 4.40 (d,  $J=3.6$  Hz 1H, CHN Oxd.), 4.65-4.73 (m, 1H, CHO Oxd), 5.73 (dd,  $J=4.8$  Hz,  $J=9.6$  Hz, 1H,  $\text{CH}\alpha$ -Tyr), 6.70 (d,  $J=8.3$  Hz, 2H, CH Ar Tyr), 7.14 (d,  $J=8.5$  Hz, 2H, CH Ar Tyr), 7.29 (q,  $J=7.8$  Hz, 2H, CH Fluorene), 7.38 (t,  $J=7.4$  Hz, 2H, CH Fluorene), 7.52-7.57 (m, 1H, NH Tyr), 7.60 (d,  $J=7.5$  Hz, 2H, CH Fluorene), 7.78 (d,  $J=7.4$  Hz, 2H, CH Fluorene) ppm.  $^{13}\text{C}$  NMR ( $\text{CD}_3\text{OD}$ ):  $\delta$  = 21.2, 38.6, 48.2, 56.3, 68.0, 76.1, 116.2, 120.8, 126.2, 126.3, 128.1, 128.7, 131.2, 131.6, 142.4, 145.1, 145.2, 153.8, 157.3, 158.0, 174.1 ppm.

**Boc-L-Phe-D-Oxd-OBn** - To a stirred solution of Boc-L-Phe-OH (0.66 g, 2.5 mmol) in acetonitrile (20 mL), HBTU (0.98 g, 2.6 mmol), then D-Oxd-OBn (0.59 g, 2.5 mmol) and lastly triethylamine (0.75 mL, 5 mmol) were added. The mixture was stirred over 1 hour, then acetonitrile was removed under reduced pressure and replaced by ethyl acetate. The mixture was washed with brine, 1 N aqueous HCl (1 x 30 mL), and 5% aqueous  $\text{NaHCO}_3$  (1 x 30 mL), dried over sodium sulphate and concentrated in vacuo. The product was obtained pure in 88% yield (0.89 g) as a solid after silica gel chromatography (cyclohexane/ethyl acetate 8:2  $\rightarrow$  1:1 as eluant). M.p. = 118-120 °C.  $[\alpha]_{\text{D}} = +36.7$  (c 1.0,  $\text{CH}_2\text{Cl}_2$ ). IR ( $\text{CH}_2\text{Cl}_2$ , 3 mM):  $\nu$  = 3433,

1793, 1756, 1710  $\text{cm}^{-1}$ .  $^1\text{H}$  NMR ( $\text{CDCl}_3$ , 300 MHz):  $\delta$  1.20-1.60 (m, 12 H, Me + t-Bu), 2.80-3.18 (m, 2H, CHN- $\text{CH}_2$ -Ph), 4.40 (d, 1H,  $J = 3.9$  Hz, CHN), 4.51 (dq, 1H,  $J = 3.9, 6.3$  Hz, CHO), 4.90 (bs, 1H, NH) 5.12-5.31 (m, 2H,  $\text{OCH}_2\text{Ph}$ ), 5.85 (bs, 1H, CHN- $\text{CH}_2\text{Ph}$ ), 7.20-7.45 (m, 10H, 2 x Ph) ppm.  $^{13}\text{C}$  NMR ( $\text{CDCl}_3$ , 75 MHz):  $\delta$  21.0, 28.2, 39.1, 53.7, 61.8, 68.0, 73.5, 79.8, 127.0, 128.3, 128.4, 128.7, 129.5, 134.6, 135.7, 151.1, 154.6, 167.4, 172.6 ppm.  $\text{C}_{26}\text{H}_{30}\text{N}_2\text{O}_7$  (482.53): Anal. Calcd. C 64.72, H 6.27, N 5.81. Found: C 64.81, H 6.34, N 5.72

**$\text{H}_2\text{C}[(\text{CH}_2)_3\text{CO-L-Phe-D-Oxd-OBn}]_2$**  - The compound was synthesized following a multistep procedure in solution, reported in ref.<sup>54,72</sup>

A solution of Boc-L-Phe-D-Oxd-OBn (2 mmol, 0.96 g) and TFA (36 mmol, 2.78 mL) in dry dichloromethane (20 mL) was stirred at room temperature for 4 h, then the volatile compounds were removed under reduced pressure and the corresponding amine salt was obtained pure in quantitative yield without further purification. A solution of azelaic acid (0.98 g, 0.52 mmol) and HBTU (0.4 g, 1.04 mmol) in dry acetonitrile (22 mL) was stirred under nitrogen atmosphere for 10 min at room temperature. Then, a mixture of the previously obtained amine salt (1.04 mmol) and TEA (3.2 mmol, 0.47 mL) in dry acetonitrile (15 mL) was added dropwise at room temperature. The solution was stirred for 40 min under a nitrogen atmosphere then acetonitrile was removed under reduced pressure and replaced with ethyl acetate. The mixture was washed with brine, 1 N aqueous HCl ( $3 \times 30$  mL), and 5 % (w/v) aqueous  $\text{NaHCO}_3$  ( $1 \times 30$  mL), dried with sodium sulphate and concentrated in vacuo. The pure product was obtained after silica gel chromatography [ $\text{CH}_2\text{Cl}_2$  100 %  $\rightarrow$   $\text{CH}_2\text{Cl}_2$ /ethyl acetate (80:20) as eluent] in 64 % (1.17 g) overall yield; m.p. 207  $^\circ\text{C}$ .  $[\alpha]_{\text{D}}^{20} = 45.0$  (c 0.1,  $\text{CHCl}_3$ ). IR ( $\text{CH}_2\text{Cl}_2$ , 3 mM):  $\nu$  3428, 1789, 1754, 1707, 1672  $\text{cm}^{-1}$ . IR (1 % in dry KBr):  $\nu$  3309, 1793, 1765, 1736, 1708, 1650  $\text{cm}^{-1}$ .  $^1\text{H}$  NMR (DMSO, 300 MHz):  $\delta$  0.95-1.18 [m, 10 H,  $\text{CH}_2(\text{CH}_2)_5\text{CH}_2$ ], 1.20-1.40 [m, 4 H,  $\text{CH}_2(\text{CH}_2)_5\text{CH}_2$ ], 1.50 (d,  $J = 6.3$  Hz, 6 H,  $\text{OCHCH}_3$ ), 2.00 (m, 4 H,  $\text{CH}_2\text{CO}$ ), 2.70 (dd,  $J = 10.8, 13.5$  Hz, 2 H, CHN- $\text{CHH}$ -Ph), 3.10-3.20 (dd,  $J = 3.3, 13.5$  Hz, 2 H, CHN- $\text{CHH}$ -Ph), 4.65 (d,  $J = 4.2$  Hz, 2 H, CHN), 4.80-4.90 (m, 2 H, OCH), 5.18 (d,  $J = 12.3$  Hz, 2 H,  $\text{OCHHPh}$ ), 5.25 (d,  $J = 12.6$  Hz, 2 H,  $\text{OCHHPh}$ ), 5.8 (m, 2 H, CHN- $\text{CH}_2\text{Ph}$ ), 7.20-7.40 (m, 20 H, 4  $\times$  Ph), 8.25 (d,  $J = 8.7$  Hz, 2 H, NH) ppm.  $^{13}\text{C}$  NMR (DMSO, 75 MHz):  $\delta$  14.8, 15.3, 21.1, 25.9, 29.0, 35.7, 37.7, 38.5, 51.0, 53.1, 55.4, 62.0, 67.7, 74.3, 127.2, 128.6, 128.8, 128.9, 129.2, 129.8, 136.0, 138.0, 152.5, 168.6, 172.7, 173.2 ppm.  $\text{C}_{51}\text{H}_{56}\text{N}_4\text{O}_{12}$  (916.4): Anal. Calcd. C 66.80, H 6.16, N 6.11; found C 66.75, H 6.19, N 6.07.

**H<sub>2</sub>C[(CH<sub>2</sub>)<sub>3</sub>CO-L-Phe-D-Oxd-OH]<sub>2</sub> (3)** - The previously synthesised compound (1 mmol, 0.92 g) was dissolved in MeOH (35 mL) under nitrogen. Pd/C (50 mg, 10 % w/w) was added under nitrogen. Vacuum was created inside the flask by using the vacuum line. The flask was then filled with hydrogen by using a balloon (1 atm). The solution was stirred for 2 h under a hydrogen atmosphere. The pure product was obtained in quantitative yield (0.73 g) after the solution was filtered through a Celite pad using ethyl acetate and concentrated in vacuo. M.p. 201 °C.  $[\alpha]_D^{20} = -36.0$  (c 1.2, MeOH). <sup>1</sup>H NMR (CD<sub>3</sub>OD): δ 1.06-1.47 [m, 10 H, CH<sub>2</sub>(CH<sub>2</sub>)<sub>5</sub>CH<sub>2</sub>], 1.58 (d, *J* = 6.4 Hz, 6 H, OCHCH<sub>3</sub>), 2.03-2.15 [m, 4 H, CH<sub>2</sub>(CH<sub>2</sub>)<sub>5</sub>CH<sub>2</sub>], 2.91 (dd, *J* = 9.6, 13.6 Hz, 2 H, CHN-CHHPh), 3.14 (dd, *J* = 5.2, 13.6 Hz, 2 H, CHN-CHHPh), 4.00 (d, *J* = 5.6 Hz, 2 H, CHN-CHHPh), 4.62-4.87 (m, 2 H, OCH), 5.80 (m, 2 H, CHN-CH<sub>2</sub>Ph), 7.20-7.40 (m, 20 H, 4 × Ph) ppm. <sup>13</sup>C NMR (CD<sub>3</sub>OD): δ 19.8, 25.3, 28.3, 28.5, 35.2, 37.6, 52.7, 61.7, 74.4, 126.5, 128.0, 129.1, 136.6, 151.1, 153.3, 169.7, 172.7, 174.4 ppm. C<sub>37</sub>H<sub>44</sub>N<sub>4</sub>O<sub>12</sub> (736.3): Anal. Calcd. C 60.32, H 6.02, N 7.60; found C 60.36, H 6.04, N 7.55.

**2NapAA-OH (5)** - The compound was collected as a white solid with 87% yield, following a literature procedure.<sup>305,306</sup>

The C-methyl-protected alanine was coupled to 2-(naphthalen-2-yloxy)acetic acid using standard coupling methodologies. To a stirred solution of 2-(naphthalen-2-yloxy)acetic acid (1.00 g, 3.56 mmol) in chloroform (20 mL) N-methylmorpholine (NMM) (0.40 mL, 3.60 mmol), and isobutylchloroformate (IBCF) (0.49 mL, 3.60 mmol) were added at 0 °C. The solution was stirred at 0 °C for 5 minutes. A solution of alanine methyl ester (0.35 g, 2.5 mmol) and NMM (0.40 mL, 3.60 mmol) in chloroform (20 mL) was added. The solution was allowed to warm to room temperature and stirring continued overnight. The solution was washed with distilled water (2x100 mL), hydrochloric acid (2x100 mL, 0.1 M), aqueous potassium carbonate solution (100 mL, 0.1 M), and distilled water again (4x100 mL) and dried over magnesium sulphate, and the solvent was removed under reduced pressure. The solid was then washed with petroleum ether (10 mL) and dried under vacuum to give methyl 2-(2-(naphthalen-2-yloxy)acetamido)propanoate (2NapA-OMe) in a 73% yield. <sup>1</sup>H NMR (CDCl<sub>3</sub>): δ 1.29 ppm (t, OCH<sub>2</sub>CH<sub>3</sub>, 3H, *J*=7.0 Hz), 1.49 (d, NHCH(CH<sub>3</sub>), 3H, *J*=6.6Hz), 4.23 (m, OCH<sub>2</sub>CH<sub>3</sub>, 2H, *J* = 7.0 Hz), 4.62 (s, OCH<sub>2</sub>CdO, 2H), 4.71 (m, CH<sub>3</sub>CHCdO, 1H), 7.12 (s, ArH, 1H), 7.26 (m, ArH, 2H, *J* = 8.3 Hz), 7.53 (d, ArH, 1H, *J*= 8.3 Hz), 7.62 (d, ArH, 1H, *J*=8.3 Hz), 7.70 (d, ArH, 1H, *J*=8.8 Hz), 7.94 (s, ArH, 1H) ppm.

$^{13}\text{C}$  NMR ( $\text{CDCl}_3$ ):  $\delta$  14.5, 18.9, 48.2, 62.1, 67.7, 108.0, 118.3, 119.7, 129.0, 130.1, 130.4, 130.9, 133.1, 155.7, 167.8, 172.9, ppm.

To deprotect the C-terminus, lithium hydroxide (0.2 g) was added to a solution of 2NapA-OMe (0.5 g) in a THF:water solution (3:1 mixture, 25 mL), and the solution was stirred for 18 h. After this time, distilled water (ca. 100 mL) was added, and then hydrochloric acid (1.0 M) was added dropwise until the pH was lowered to pH 3. The resulting white precipitate was collected by filtration and washed well with water and petroleum ether before being dried *in vacuo* to give 2-(2-(naphthalen-2-yloxy)acetamido) propanoic acid (2Nap-OH) as a white powder in 89% yield.  $^1\text{H}$  NMR(DMSO):  $\delta$  1.33 (d,  $(\text{CH}_3)\text{CHC}=\text{O}$ , 3H,  $3\text{JHH} = 7.2$  Hz), 3.42 (s, OH), 4.30 (m,  $(\text{CH}_3)\text{CHCdO}$ , 1H), 4.65 (m,  $\text{OCH}_2\text{-CdO}$ , 2H), 7.31 (dd, ArH, 1H,  $3\text{JHH} = 2.4$  Hz), 7.34 (m, NH, 1H), 7.58 (dd, ArH, 1H,  $3\text{JHH} = 1.9$  Hz), 7.75 (d, ArH, 1H,  $3\text{JHH} = 8.8$  Hz), 7.86 (d, ArH, 1H,  $3\text{JHH} = 8.8$  Hz), 8.13 (d, ArH, 1H,  $3\text{JHH} = 1.6$  Hz), 8.44 (d, ArH, 1H,  $3\text{JHH} = 7.5$  Hz) ppm.  $^{13}\text{C}$  (DMSO):  $\delta$  17.6, 47.8, 67.1, 107.8, 116.9, 120.2, 129.0, 129.3, 129.7, 130.3, 133.0, 156.4, 167.5, 174.3, ppm.

The same coupling and deprotection procedures were followed for the addition of the second alanine and the final C-terminus deprotection. 2NapAA-OH was collected as a white solid in a 87% yield.  $^1\text{H}$  NMR (DMSO):  $\delta$  1.28 (d,  $\text{CHCH}_3$ , 3H,  $J = 7.9$  Hz) 1.30 (d,  $\text{CHCH}_3$ , 3H,  $J = 7.3$  Hz), 4.23 (m, CHNH, 1H), 4.47 (m, CHNH, 1H), 4.67 (s,  $\text{OCH}_2$ , 2H), 7.26 (d, ArH, 1H,  $J = 8.7$  Hz,  $J = 2.3$  Hz), 7.36 (t, ArH, 1H,  $J = 7.1$  Hz), 7.47 (t, ArH, 1H,  $J = 7.1$  Hz), 7.84 (m, ArH, 3H), 8.22 (d, NH, 1H,  $J = 7.9$  Hz), 8.30 (d, NH, 1H,  $J = 7.2$  Hz) ppm.  $^{13}\text{C}$  NMR (DMSO):  $\delta$  17.0, 18.4, 47.4, 47.5, 66.8, 107.3, 118.5, 123.8, 126.4, 126.7, 127.5, 128.7, 129.3, 134.0, 155.5, 167.0, 171.7, 173.9 ppm. MS (ES) = 343 ( $[\text{M-H}]^-$ ). Anal. Calcd. for  $\text{C}_{18}\text{H}_{20}\text{N}_2\text{O}_5$ : C, 62.78%; H, 5.85%; N, 8.13%. Found: C, 62.72%; H, 5.80%; N, 7.97%.

**2NapFF-OH (6)** - The compound was collected following the same literature procedure and synthetic steps already reported for 2NapAA. The product was collected as a white solid with 90% yield.<sup>305,306</sup>  $^1\text{H}$  NMR (DMSO)  $\delta = 2.84 - 3.11$  (m,  $\text{CH}_2\text{Ph}$ , 4H), 4.46 (m, CHNH, 1H), 4.53 (s,  $\text{OCH}_2$ , 2H), 4.64 (m, CHNH, 1H), 7.15 - 7.24 (m, ArH, 12H), 7.37 (t, ArH, 1H,  $J = 7.2$  Hz), 7.45 (t, ArH, 1H,  $J = 8.0$  Hz), 7.73 (d, ArH, 1H,  $J = 8.0$  Hz), 7.84 (d, ArH, 2H,  $J = 7.2$  Hz), 8.12 (d, NH, 1H,  $J = 8.5$  Hz), 8.41 (d, NH, 1H,  $J = 7.8$  Hz), ppm.  $^{13}\text{C}$  NMR (DMSO):  $\delta$  36.7, 37.4, 53.2, 53.5, 66.6, 107.3, 117.4, 123.8, 126.2, 126.4, 126.8, 127.5, 127.9, 128.7, 129.0, 129.1,

129.3, 133.9, 137.4, 137.5, 155.4, 167.2, 170.7, 172.6 ppm. MS (ES<sup>+</sup>) = 519 ([M+Na]<sup>+</sup>). Anal. Calcd. for C<sub>30</sub>H<sub>28</sub>N<sub>2</sub>O<sub>5</sub>: C, 72.56; H, 5.68; N, 5.64. Found: C, 72.34; H, 5.69; N, 5.60

***m*-(Boc)<sub>2</sub>-L-DOPA-OMe (*m*-7) + *p*-(Boc)<sub>2</sub>-L-DOPA-OMe (*p*-7) - Boc-L-DOPA-OMe **6**** (0.60 g, 1.93 mmol) is dissolved in 4.4 mL of saturated NaHCO<sub>3</sub> solution, then Boc<sub>2</sub>O (0.89 mL, 3.86 mmol) in THF (4.56 mL) is added. The solution is stirred for 18 hours at room temperature. The THF is removed under vacuum, the residue is suspended in 4 mL HCl 1M and extracted with ethyl acetate (15 mL x 3). The combined organic phase is washed twice with 2.5 mL of 1M HCl, once with 2 mL of a saturated aqueous NaHCO<sub>3</sub> solution and with 2 mL of H<sub>2</sub>O. The organic phase is then dried over Na<sub>2</sub>SO<sub>4</sub> and the solvent is evaporated. Products ***m*-7** and ***p*-7** were obtained as an inseparable mixture in 1:1 ratio after flash chromatography (cyclohexane:ethyl acetate 4:1) with 50% yield as a transparent solid. IR (ATR-IR):  $\nu$  3367, 1756, 1742, 1717, 1685, 1607, 1510 cm<sup>-1</sup>; <sup>1</sup>H NMR (CDCl<sub>3</sub>):  $\delta$  1.40 (9H, s, *t*-Bu), 1.53 (9H, s, *t*-Bu), 2.89-3.08 (2H, m, PhCH<sub>2</sub>NH), 3.69 (3H, s, OCH<sub>3</sub>), 4.47-4.57 (1H, m, PhCH<sub>2</sub>CHNH), 4.99 (1H, d, *J* = 6.4 Hz, NH), 5.87 (0.5H, bs, OH), 5.87 (0.5H, bs, OH), 6.63 (0.5H, d, *J* = 8.0 Hz, Ar), 6.75 (0.5H, s, Ar), 6.86 (2 x 0.5H, AB, *J* = 8.0 Hz), 6.93 (0.5H, s, Ar), 7.02 (0.5H, d, *J* = 8.0 Hz, Ar) ppm. <sup>13</sup>C NMR (CDCl<sub>3</sub>):  $\delta$  27.6, 28.2, 37.4, 37.7, 52.2, 54.3, 54.4, 60.4, 80.1, 84.3, 117.4, 118.2, 121.4, 122.1, 122.9, 127.5, 128.4, 134.9, 137.9, 146.2, 147.1, 151.2, 151.3, 155.1, 171.2, 172.2 ppm. HPLC-MS (API-ES): 8.93 min, [M+Na]<sup>+</sup>=434. Anal. Calcd. for C<sub>20</sub>H<sub>29</sub>NO<sub>8</sub>: C, 58.38; H, 7.10; N, 3.40. Found: C, 58.40; H, 7.12; N, 3.37.

**Boc<sub>3</sub>-L-DOPA-OMe (**8**) - Boc-L-DOPA-OMe **6**** (1 g, 3.2 mmol) is dissolved in 40 mL of CH<sub>3</sub>CN, then 195 mg of DMAP (1.6 mmol) and 1.475 mL of Boc<sub>2</sub>O (6.4 mmol) are added. The solution is stirred for 40 minutes at room temperature. The solvent is removed under vacuum, then the residue is suspended in 2 mL of HCl 1M, extracted with ethyl acetate (50 mL x 3) and washed with H<sub>2</sub>O (1 x 20 mL). The organic layer is then dried over Na<sub>2</sub>SO<sub>4</sub> and concentrated under *vacuum*. The product is eventually purified through flash chromatography (cyclohexane:ethyl acetate 4:1). The pure product is obtained with a 93% yield as a transparent, sticky liquid that becomes a white solid after about 24 hours. M.p. = 95-98 °C; [ $\alpha$ ]<sub>D</sub><sup>25</sup> +33.0 ° (c = 0.5 in CH<sub>2</sub>Cl<sub>2</sub>); IR (ATR-IR):  $\nu$  3334, 1737, 1690, 1659, 1587, 1516 cm<sup>-1</sup>; <sup>1</sup>H NMR (CDCl<sub>3</sub>):  $\delta$  1.40 (9H, s, *t*-Bu), 1.52 (18H, s, 2 x *t*-Bu), 3.01-3.10 (2H, m, PhCH<sub>2</sub>NH), 3.68 (3H, s, OCH<sub>3</sub>), 4.55 (1H, q, *J* = 6.8 Hz, PhCH<sub>2</sub>CHNH), 4.99 (1H, d, *J* = 8.0 Hz, NH), 6.97 (1H, dd, *J* = 1.7, 8.4 Hz, Ar), 7.02 (1H, d, *J* = 1.7 Hz, Ar), 7.16 (1H, d, *J* = 8.4 Hz, Ar) ppm. <sup>13</sup>C NMR (CDCl<sub>3</sub>):  $\delta$  26.9, 27.6, 28.2, 37.5, 52.3, 54.2, 80.0, 83.7, 113.0, 124.0, 127.1, 134.7, 141.5,

142.3, 150.6, 150.7, 171.9 ppm. HPLC-MS (API-ES): 11.30 min,  $[M+Na]^+=534$ . Anal. Calcd. for  $C_{25}H_{37}NO_{10}$ : C, 58.70; H, 7.29; N, 2.74. Found: C, 58.75; H, 7.32; N, 2.75

**Boc-(L-DOPA)<sub>2</sub>-OMe (9)** - 1.8 g (3.67 mmol) of Boc-L-DOPA(Bn)<sub>2</sub>-OMe is deprotected to obtain Boc-L-DOPA(Bn)<sub>2</sub>-OH (previously described).

An equal amount of Boc-L-DOPA(Bn)<sub>2</sub>-OMe (1.8 g, 3.67 mmol) is dissolved in 25 mL of  $CH_2Cl_2$ , then 5.1 mL of TFA (64.8 mmol) are added. The solution is stirred at room temperature for 4 hours. The solvent is removed under reduced pressure and the whole residue, composed of the desired intermediate  $[F_3CCOO^- \ ^+H_3N-L-DOPA(Bn)_2-OMe]$  **9i** and the remaining TFA, is used for the next step of the reaction, considering a quantitative yield for this one.

1.75 g of Boc-L-DOPA(Bn)<sub>2</sub>-OH (3.67 mmol) is dissolved in 40 mL of  $CH_3CN$  together with 1.53 g of HBTU (4.0 mmol) and left under stirring at room temperature while a mixture of the previous residue containing **9i**, DIPEA (1.8 mL, 10.3 mmol) (the amount of DIPEA is calculated considering 2.2 equivalents plus 1 equivalent per equivalent of TFA remained in the residue after the solvent removal) and 10 mL of  $CH_3CN$  is added dropwise. After two hours the solvent is evaporated under vacuum, the residue is suspended in 10 mL of water, extracted with  $CH_2Cl_2$  (50 mL x 3) and washed with 20 mL of water, HCl, saturated solution of  $NaHCO_3$  and water again. The organic layer is dried over  $Na_2SO_4$  and the solvent removed under vacuum. Boc-(L-DOPA(Bn)<sub>2</sub>)<sub>2</sub>-OMe is obtained as a white solid with a 94% yield.

0.70 g of Boc-(L-DOPA(Bn)<sub>2</sub>)<sub>2</sub>-OMe (0.82 mmol) is dissolved in 50 mL of  $CH_3OH$  and 70 mg of Pd/C 10% w/w are added to the solution, then the reaction is left under vigorous stirring for 4 h under  $H_2$  atmosphere. The solution is filtered over Celite, then the solvent is evaporated under vacuum. The product is further purified by washing with n-hexane (2 mL x 3) to obtain a sticky liquid that becomes a white solid in 48 h hours (96% yield).  $[\alpha]_D^{25} -3.0^\circ$  (c = 0.5 in  $CH_3OH$ ); IR (ATR-IR):  $\nu$  3310, 1732, 1658, 1608, 1515  $cm^{-1}$ ;  $^1H$  NMR ( $CD_3OD$ ):  $\delta$  1.4 (s, 9H, *t*-Bu), 2.61 (dd, 1H,  $J = 3.2, 12.4$  Hz, ArCHHNH), 2.81 – 2.97 (m, 3H, ArCHHNH + ArCH<sub>2</sub>NH), 3.63 (s, 3H, OCH<sub>3</sub>), 4.18 (t, 1H,  $J = 5.6$  Hz, CH<sub>2</sub>CHNH), 4.56 (t, 1H,  $J = 6.0$  Hz, CHNH<sub>2</sub>Boc), 6.44 (d, 1H,  $J = 7.6$  Hz, CHNHCO), 6.49 (d, 1H,  $J = 8.4$  Hz, CHNHCO), 6.58 – 6.65 (m, 4H, Ar) ppm.  $^{13}C$  NMR ( $CD_3OD$ ):  $\delta$  26.5, 27.3, 36.6, 37.2, 51.2, 53.8, 56.1, 79.3, 82.7, 89.7, 114.8, 115.9, 116.3, 117.4, 120.3, 122.0, 123.1, 127.2, 127.6, 128.4, 143.9, 144.8, 152.0, 156.1, 171.8, 172.8 ppm. HPLC-MS (API-ES): 8.00 min,  $[M+H]^+=491$ . Anal. Calcd. for  $C_{24}H_{30}N_2O_9$ : C, 58.77; H, 6.17; N, 5.71. Found: C, 58.76; H, 6.19; N, 5.70.



## References

---

- 1 D. Haldar, D. Podder, S. Roy Chowdhury and S. K. Nandi, *New J. Chem.*, 2019, **43**, 3743–3749.
- 2 L. Latxague, M. A. Ramin, A. Appavoo, P. Berto, M. Maisani, C. Ehret, O. Chassande and P. Barthélémy, *Angew. Chemie - Int. Ed.*, 2015, **54**, 4517–4521.
- 3 C. Tomasini, N. Castellucci, V. C. Caputo, L. Milli, G. Battistelli, S. Fermani and G. Falini, *CrystEngComm*, 2015, **17**, 116–123.
- 4 B. D. Wall and J. D. Tovar, *Pure Appl. Chem.*, 2012, **84**, 1039–1045.
- 5 T. Park and S. C. Zimmerman, *J. Am. Chem. Soc.*, 2006, **128**, 11582–11590.
- 6 A. Harada, R. Kobayashi, Y. Takashima, A. Hashidzume and H. Yamaguchi, *Nat. Chem.*, 2011, **3**, 34–37.
- 7 K. L. Morris, L. Chen, A. Rodger, D. J. Adams and L. C. Serpell, *Soft Matter*, 2015, **11**, 1174–1181.
- 8 B. Y. P. J. Flory, *Lancet*, 1855, **66**, 309–313.
- 9 R. Vegners, I. Shestakova, I. Kalvinsh, M. Ezzell, Robert and P. A. Janmey, *J. Pept. Sci.*, 1995, **1**, 371–378.
- 10 G. Cravotto and P. Cintas, *Chem. Soc. Rev.*, 2009, **38**, 2684–2697.
- 11 E. Gazit, A. Mahler, M. Reches, M. Rechter and S. Cohen, *Adv. Mater.*, 2006, **18**, 1365–1370.
- 12 L. Chen, G. Pont, K. Morris, G. Lotze, A. Squires, L. C. Serpell and D. J. Adams, *Chem. Commun.*, 2011, **47**, 12071–12073.
- 13 C. Tang, R. V. Ulijn and A. Saiani, *Eur. Phys. J. E*, 2011, **36**, 111.

- 14 E. R. Draper and D. J. Adams, *Langmuir*, 2019, **35**, 6506–6521.
- 15 J. Raeburn, A. Z. Cardoso and D. J. Adams, *Chem. Soc. Rev.*, 2013, **42**, 5143–5156.
- 16 R. G. Weiss, *J. Am. Chem. Soc.*, 2014, **136**, 7519–7530.
- 17 V. Jayawarna, M. Ali, T. A. Jowitt, A. F. Miller, A. Saiani, J. E. Gough and R. V. Ulijn, *Adv. Mater.*, 2006, **18**, 611–614.
- 18 L. Chen, K. Morris, A. Laybourn, D. Elias, M. R. Hicks, A. Rodger, L. Serpell and D. J. Adams, *Langmuir*, 2010, **26**, 5232–5242.
- 19 K. A. Houton, K. L. Morris, L. Chen, M. Schmidtman, J. T. A. Jones, L. C. Serpell, G. O. Lloyd and D. J. Adams, *Langmuir*, 2012, **28**, 9797–9806.
- 20 D. J. Adams, K. Morris, L. Chen, L. C. Serpell, J. Bacsá and G. M. Day, *Soft Matter*, 2010, **6**, 4144–4156.
- 21 S. Fleming and R. V. Ulijn, *Chem. Soc. Rev.*, 2014, **43**, 8150–8177.
- 22 A. Grauer and B. König, *European J. Org. Chem.*, 2009, **2009**, 5099–5111.
- 23 C. Tomasini and N. Castellucci, *Chem. Soc. Rev.*, 2013, **42**, 156–172.
- 24 Y. Zhang, H. Gu, Z. Yang and B. Xu, *J. Am. Chem. Soc.*, 2003, **125**, 13680–13681.
- 25 Z. Yang, G. Liang, M. Ma, Y. Gao and B. Xu, *J. Mater. Chem.*, 2007, **17**, 850–854.
- 26 Y. Zhang, Z. Yang, F. Yuan, H. Gu, P. Gao and B. Xu, *J. Am. Chem. Soc.*, 2004, **126**, 15028–15029.
- 27 Z. Qiu, H. Yu, J. Li, Y. Wang and Y. Zhang, *Chem. Commun.*, 2009, 3342–3344.
- 28 D. M. Ryan, S. B. Anderson, F. T. Senguen, R. E. Youngman and B. L. Nilsson, *Soft Matter*, 2010, **6**, 475–479.
- 29 M. Reches and E. Gazit, *Nat. Nanotechnol.*, 2006, **1**, 195–200.
- 30 A. M. Smith, R. J. Williams, C. Tang, P. Coppo, R. F. Collins, M. L. Turner, A. Saiani and R. V. Ulijn, *Adv. Mater.*, 2008, **20**, 37–41.

- 31 H. Xu, A. K. Das, M. Horie, M. S. Shaik, A. M. Smith, Y. Luo, X. Lu, R. Collins, S. Y. Liem, A. Song, P. L. A. Popelier, M. L. Turner, P. Xiao, I. A. Kinloch and R. V Ulijn, *Nanoscale*, 2010, **2**, 960–966.
- 32 G. Cheng, V. Castelletto, C. M. Moulton, G. E. Newby and I. W. Hamley, *Langmuir*, 2010, **26**, 4990–4998.
- 33 D. J. Adams, L. M. Mullen, M. Berta, L. Chen and W. J. Frith, *Soft Matter*, 2010, **6**, 1971–1980.
- 34 S. Awhida, E. R. Draper, T. O. McDonald and D. J. Adams, *J. Colloid Interface Sci.*, 2015, **455**, 24–31.
- 35 S. Ray, A. K. Das and A. Banerjee, *Chem. Mater.*, 2007, **19**, 1633–1639.
- 36 N. Zanna, A. Merlettoni and C. Tomasini, *Org. Chem. Front.*, 2016, **3**, 1699–1704.
- 37 J. Raeburn, C. Mendoza-Cuenca, B. N. Cattoz, M. a. Little, A. E. Terry, A. Zamith Cardoso, P. C. Griffiths and D. J. Adams, *Soft Matter*, 2015, **11**, 927–935.
- 38 S. Sutton, N. L. Campbell, A. I. Cooper, M. Kirkland, W. J. Frith and D. J. Adams, *Langmuir*, 2009, **25**, 10285–10291.
- 39 T. Das, M. Häring, D. Haldar and D. Díaz Díaz, *Biomater. Sci.*, 2018, **6**, 38–59.
- 40 R. Martí-Centelles and B. Escuder, *ChemNanoMat*, 2018, **4**, 796–800.
- 41 G. Bastiat, F. Plourde, A. Motulsky, A. Furtos, Y. Dumont, R. Quirion, G. Fuhrmann and J. C. Leroux, *Biomaterials*, 2010, **31**, 6031–6038.
- 42 L. Majumder, M. Chatterjee, K. Bera, N. C. Maiti and B. Banerji, *ACS omega*, 2019, **4**, 14411–14419.
- 43 G. Aykent, C. Zeytun, A. Marion and S. Özçubukçu, *Sci. Rep.*, 2019, **9**, 4893.
- 44 N. Zanna, D. Iaculli and C. Tomasini, *Org. Biomol. Chem.*, 2017, **15**, 5797–5804.
- 45 N. Zanna, S. Focaroli, A. Merlettoni, L. Gentilucci, G. Teti, M. Falconi and C. Tomasini, *ACS Omega*, 2017, **2**, 2374–2381.

- 46 G. Fichman, L. Adler-Abramovich, S. Manohar, I. Mironi-Harpaz, T. Guterman, D. Seliktar, P. B. Messersmith and E. Gazit, *ACS Nano*, 2014, **8**, 7220–7228.
- 47 G. Fichman, T. Guterman, L. Adler-Abramovich and E. Gazit, *Nanomaterials*, 2014, **4**, 726–740.
- 48 H. Ceylan, M. Urel, T. S. Erkal, A. B. Tekinay, A. Dana and M. O. Guler, *Adv. Funct. Mater.*, 2013, **23**, 2081–2090.
- 49 A. Saha, S. Bolisetty, S. Handschin and R. Mezzenga, *Soft Matter*, 2013, **9**, 10239.
- 50 E. Faure, C. Falentin-Daudré, C. Jérôme, J. Lyskawa, D. Fournier, P. Woisel and C. Detrembleur, *Prog. Polym. Sci.*, 2013, **38**, 236–270.
- 51 J. Sedó, J. Saiz-Poseu, F. Busqué and D. Ruiz-Molina, *Adv. Mater.*, 2013, **25**, 653–701.
- 52 S. Ray, A. K. Das and A. Banerjee, *Chem. Mater.*, 2007, **19**, 1633–1639.
- 53 A. Meister, M. Bastrop, S. Koschoreck, V. M. Garamus, T. Sinemus, G. Hempel, S. Drescher, B. Dobner, W. Richtering, K. Huber and A. Blume, *Langmuir*, 2007, **23**, 7715–7723.
- 54 N. Castellucci, G. Angelici, G. Falini, M. Monari and C. Tomasini, *European J. Org. Chem.*, 2011, **2011**, 3082–3088.
- 55 N. Castellucci, G. Sartor, N. Calonghi, C. Parolin, G. Falini and C. Tomasini, *Beilstein J. Org. Chem.*, 2013, **9**, 417–424.
- 56 S. Lucarini and C. Tomasini, *J. Org. Chem.*, 2001, **66**, 727–732.
- 57 C. Tomasini, V. Trigari, S. Lucarini, F. Bernardi, M. Garavelli, C. Peggion, F. Formaggio and C. Toniolo, *European J. Org. Chem.*, 2003, **4**, 259–267.
- 58 G. Angelici, G. Luppi, B. Kaptein, Q. B. Broxterman, H. J. Hofmann and C. Tomasini, *European J. Org. Chem.*, 2007, 2713–2721.
- 59 L. Garbuio, B. Lewandowski, P. Wilhelm, L. Ziegler, M. Yulikov, H. Wennemers and G. Jeschke, *Chem. - A Eur. J.*, 2015, **21**, 10747–10753.

- 60 N. Zanna, L. Milli, B. Del Secco and C. Tomasini, *Org. Lett.*, 2016, **18**, 1662–1665.
- 61 N. D. Bansode, M. V Sonar and K. N. Ganesh, *Chem. Commun.*, 2016, **52**, 4884–4887.
- 62 R. W. Newberry and R. T. Raines, *Acc. Chem. Res.*, 2017, **50**, 1838–1846.
- 63 C. Tomasini and N. Zanna, *Biopolymers*, 2017, **108**, 1–14.
- 64 D. J. Adams, M. F. Butler, W. J. Frith, M. Kirkland, L. Mullen and P. Sanderson, *Soft Matter*, 2009, **5**, 1856–1862.
- 65 C. Tang, A. M. Smith, R. F. Collins, R. V Ulijn and A. Saiani, *Langmuir*, 2009, **25**, 9447–9453.
- 66 J. Raeburn, G. Pont, L. Chen, Y. Cesbron, R. Lévy and D. J. Adams, *Soft Matter*, 2012, **8**, 1168–1174.
- 67 P. A. Korevaar, C. J. Newcomb, E. W. Meijer and S. I. Stupp, *J. Am. Chem. Soc.*, 2014, **136**, 8540–8543.
- 68 K. Isozaki, H. Takaya and T. Naota, *Angew. Chemie - Int. Ed.*, 2007, **46**, 2855–2857.
- 69 D. Bardelang, F. Camerel, J. C. Margeson, D. M. Leek, M. Schmutz, M. B. Zaman, K. Yu, D. V. Soldatov, R. Ziessel, C. I. Ratcliffe and J. A. Ripmeester, *J. Am. Chem. Soc.*, 2008, **130**, 3313–3315.
- 70 N. Castellucci, G. Falini, G. Angelici and C. Tomasini, *Amino Acids*, 2011, **41**, 609–620.
- 71 I. Fraeye, T. Duvetter, E. Dounghla, A. Van Loey and M. Hendrickx, *Trends Food Sci. Technol.*, 2010, **21**, 219–228.
- 72 N. Zanna, A. Merlettini and C. Tomasini, *Org. Chem. Front.*, 2016, **3**, 1699–1704.
- 73 S. R. Raghavan and B. H. Cipriano, in *Molecular Gels*, eds. R. G. Weiss and P. Terech, Springer Netherlands, 2005, pp. 233–234.
- 74 P. Terech and R. G. Weiss, *Chem. Rev.*, 1997, **97**, 3133–3160.
- 75 M. A. Rogers and J. H. J. Kim, *Food Res. Int.*, 2011, **44**, 1447–1451.

- 76 S. Lin-Gibson, H. J. Walls, S. B. Kennedy and E. R. Welsh, *Carbohydr. Polym.*, 2003, **54**, 193–199.
- 77 F. Chambon, Z. S. Petrovic, W. J. MacKnight and H. H. Winter, *Macromolecules*, 1986, **19**, 2146–2149.
- 78 A. Mishra and J. Clark, *RSC Green Chem.*, 2013, 1–10.
- 79 S. Babel and T. A. Kurniawan, *J. Hazard. Mater.*, 2003, **97**, 219–243.
- 80 V. K. Gupta and Suhas, *J. Environ. Manage.*, 2009, **90**, 2313–2342.
- 81 B. O. Okesola and D. K. Smith, *Chem. Soc. Rev.*, 2016, **45**, 4226–4251.
- 82 F. Rodríguez-Llansola, B. Escuder, J. F. Miravet, D. Hermida-Merino, I. W. Hamley, C. J. Cardin and W. Hayes, *Chem. Commun.*, 2010, **46**, 7960–7962.
- 83 D. M. Wood, B. W. Greenland, A. L. Acton, F. Rodríguez-Llansola, C. A. Murray, C. J. Cardin, J. F. Miravet, B. Escuder, I. W. Hamley and W. Hayes, *Chem. – A Eur. J.*, 2012, **18**, 2692–2699.
- 84 S. Song, L. Feng, A. Song and J. Hao, *J. Phys. Chem. B*, 2012, **116**, 12850–12856.
- 85 P. K. Sukul and S. Malik, *RSC Adv.*, 2013, **3**, 1902–1915.
- 86 J. Lu, Y. Gao, J. Wu and Y. Ju, *RSC Adv.*, 2013, **3**, 23548–23552.
- 87 L. Milli, N. Zanna, A. Merlettini, M. Di Giosia, M. Calvaresi, M. L. Focarete and C. Tomasini, *Chem. - A Eur. J.*, 2016, **22**, 12106–12112.
- 88 C. Tomasini and M. Villa, *Tetrahedron Lett.*, 2001, **42**, 5211–5214.
- 89 S. Lucarini and C. Tomasini, *J. Org. Chem.*, 2001, **66**, 727–732.
- 90 L. Milli, M. Larocca, M. Tedesco, N. Castellucci, E. Ghibaudi, A. Cornia, M. Calvaresi, F. Zerbetto and C. Tomasini, *J. Org. Chem.*, 2014, **79**, 5958–5969.
- 91 N. Castellucci, G. Falini, L. Milli, M. Monari, S. Abbate, G. Longhi, E. Castiglioni, G. Mazzeo and C. Tomasini, *Chempluschem*, 2014, **79**, 114–121.

- 92 G. Longhi, S. Abbate, F. Lebon, N. Castellucci, P. Sabatino and C. Tomasini, *J. Org. Chem.*, 2012, **77**, 6033–6042.
- 93 G. Angelici, G. Falini, H. J. Hofmann, D. Huster, M. Monari and C. Tomasini, *Chem. - A Eur. J.*, 2009, **15**, 8037–8048.
- 94 G. Angelici, G. Falini, H.-J. Hofmann, D. Huster, M. Monari and C. Tomasini, *Angew. Chemie Int. Ed.*, 2008, **47**, 8075–8078.
- 95 N. Zanna, A. Merlettini, G. Tatulli, L. Milli, M. L. Focarete and C. Tomasini, *Langmuir*, 2015, **31**, 12240–12250.
- 96 L. Milli, N. Castellucci and C. Tomasini, *European J. Org. Chem.*, 2014, **2014**, 5954–5961.
- 97 G. Angelici, N. Castellucci, G. Falini, D. Huster, M. Monari and C. Tomasini, *Cryst. Growth Des.*, 2010, **10**, 923–929.
- 98 N. Zanna, D. Iaculli and C. Tomasini, *Org. Biomol. Chem.*, 2017, **15**, 5797–5804.
- 99 F. A. Maulvi, A. R. Desai, H. H. Choksi, R. J. Patil, K. M. Ranch, B. A. Vyas and D. O. Shah, *Int. J. Pharm.*, 2017, **524**, 193–204.
- 100 J. Galindo-Alvarez, V. Sadtler, P. Marchal, P. Perrin, C. Tribet, E. Marie and A. Durand, *Colloids Surfaces A Physicochem. Eng. Asp.*, 2012, **396**, 115–121.
- 101 L. Streck, A. L. P. F. Caroni and J. L. C. Fonseca, *Colloids Surfaces A Physicochem. Eng. Asp.*, 2018, **538**, 720–728.
- 102 A. Gaucher, L. Dutot, O. Barbeau, W. Hamchaoui, M. Wakselman and J. P. Mazaleyrat, *Tetrahedron Asymmetry*, 2005, **16**, 857–864.
- 103 G. E. Magoulas, A. Rigopoulos, Z. Piperigkou, C. Gialeli, N. K. Karamanos, P. G. Takis, A. N. Troganis, A. Chrissanthopoulos, G. Maroulis and D. Papaioannou, *Bioorg. Chem.*, 2016, **66**, 132–144.
- 104 L. Marton, J. W. McBain and R. D. Vold, *J. Am. Chem. Soc.*, 1941, **63**, 1990–1993.

- 105 D. Wang and J. Hao, *Langmuir*, 2011, **27**, 1713–1717.
- 106 F. O. Akong, A. Pasc, M. Emo and C. Gérardin-Charbonnier, *New J. Chem.*, 2013, **37**, 559–562.
- 107 D. Giuri, N. Zanna and C. Tomasini, *Gels*, 2019, **5**, 27.
- 108 J. Bonnet, G. Suissa, M. Raynal and L. Bouteiller, *Soft Matter*, 2015, **11**, 2308–2312.
- 109 S. Dai, S. Wang, Z. Wu, L. Miao and M. Wang, *Colloids Surfaces A Physicochem. Eng. Asp.*, 2020, **602**, 125096.
- 110 A. R. Hirst and D. K. Smith, *Langmuir*, 2004, **20**, 10851–10857.
- 111 I. M. Smallwood, *Oppor. Emerg. Mark.*, 2015, 1–326.
- 112 Z. Gong, Y. Yang, Q. Ren, X. Chen and Z. Shao, *Soft Matter*, 2012, **8**, 2875.
- 113 Y. Liu, S. Ling, S. Wang, X. Chen and Z. Shao, *Biomater. Sci.*, 2014, **2**, 1338–1342.
- 114 Y. S. Pek, A. C. A. Wan and J. Y. Ying, *Biomaterials*, 2010, **31**, 385–391.
- 115 Y. Li, F. Zhou, Y. Wen, K. Liu, L. Chen, Y. Mao, S. Yang and T. Yi, *Soft Matter*, 2014, **10**, 3077–3085.
- 116 S. Basak, J. Nanda and A. Banerjee, *Chem. Commun.*, 2014, **50**, 2356–2359.
- 117 C. K. Karan and M. Bhattacharjee, *ACS Appl. Mater. Interfaces*, 2016, **8**, 5526–5535.
- 118 S. Roy, A. Baral and A. Banerjee, *Chem. Eur. J.*, 2013, **19**, 14950–14957.
- 119 Y. Liu, S. Ling, S. Wang, X. Chen and Z. Shao, *Biomater. Sci.*, 2014, **2**, 1338–1342.
- 120 Y. S. Jeon, J. Lei and J. H. Kim, *J. Ind. Eng. Chem.*, 2008, **14**, 726–731.
- 121 J. Naskar, G. Palui and A. Banerjee, *J. Phys. Chem. B*, 2009, **113**, 11787–11792.
- 122 W. Wang, X. Chen, C. Hong, F. Zhu, Y. Yao and Z. Xue, *Int. J. Photoenergy*, 2012, **2012**, 1–5.

- 123 M. Montalti, A. Credi, L. Prodi and M. T. Gandolfi, *Handbook of Photochemistry, Third Edition*, CRC Press, 2006.
- 124 D. Genovese, S. Bonacchi, R. Juris, M. Montalti, L. Prodi, E. Rampazzo and N. Zaccheroni, *Angew. Chemie Int. Ed.*, 2013, **52**, 5965–5968.
- 125 Y. Nosaka and A. Y. Nosaka, *Chem. Rev.*, 2017, **117**, 11302–11336.
- 126 G. Guidetti, D. Giuri, N. Zanna, M. Calvaresi, M. Montalti and C. Tomasini, *ACS Omega*, 2018, **3**, 8122–8128.
- 127 Y. Lai, J. Huang, Z. Cui, M. Ge, K. Q. Zhang, Z. Chen and L. Chi, *Small*, 2016, **12**, 2203–2224.
- 128 S. Nishimoto and B. Bhushan, *Rsc Adv.*, 2013, **3**, 671–690.
- 129 A. H. Mamaghani, F. Haghighat and C.-S. Lee, *Appl. Catal. B Environ.*, 2017, **203**, 247–269.
- 130 C. Yu, W. Zhou, H. Liu, Y. Liu and D. D. Dionysiou, *Chem. Eng. J.*, 2016, **287**, 117–129.
- 131 T. Xia, M. Kovoichich, J. Brant, M. Hotze, J. Sempf, T. Oberley, C. Sioutas, J. I. Yeh, M. R. Wiesner and A. E. Nel, *Nano Lett.*, 2006, **6**, 1794–1807.
- 132 M. R. Hoffmann, S. T. Martin, W. Choi and D. W. Bahnemann, *Chem. Rev.*, 1995, **95**, 69–96.
- 133 G. Vale, K. Mehennaoui, S. Cambier, G. Libralato, S. Jomini and R. F. Domingos, *Aquat. Toxicol.*, 2016, **170**, 162–174.
- 134 A. B. Djurišić, Y. H. Leung, A. M. C. Ng, X. Y. Xu, P. K. H. Lee, N. Degger and R. S. S. Wu, *Small*, 2015, **11**, 26–44.
- 135 N. Zanna, A. Merlettini, G. Tatulli, L. Milli, M. L. Focarete and C. Tomasini, *Langmuir*, 2015, **31**, 12240–12250.
- 136 K. Tao, A. Levin, L. Adler-Abramovich and E. Gazit, *Chem. Soc. Rev.*, 2016, **45**, 3935–

- 3953.
- 137 R. Orbach, I. Mironi-Harpaz, L. Adler-Abramovich, E. Mossou, E. P. Mitchell, V. T. Forsyth, E. Gazit and D. Seliktar, *Langmuir*, 2012, **28**, 2015–2022.
- 138 A. L. Linsebigler, G. Lu and J. T. Yates Jr, *Chem. Rev.*, 1995, **95**, 735–758.
- 139 A. Ciesielski and P. Samori, *Chem. Soc. Rev.*, 2014, **43**, 381–398.
- 140 K. Dai, T. Peng, D. Ke and B. Wei, *Nanotechnology*, 2009, **20**, 125603.
- 141 M. Sun, X. Ma, X. Chen, Y. Sun, X. Cui and Y. Lin, *Rsc Adv.*, 2014, **4**, 1120–1127.
- 142 K. R. Reddy, M. Hassan and V. G. Gomes, *Appl. Catal. A Gen.*, 2015, **489**, 1–16.
- 143 L. Han, P. Wang and S. Dong, *Nanoscale*, 2012, **4**, 5814–5825.
- 144 N. Serpone, D. Lawless and R. Khairutdinov, *J. Phys. Chem.*, 1995, **99**, 16646–16654.
- 145 A. Kathiravan and R. Renganathan, *J. Colloid Interface Sci.*, 2009, **331**, 401–407.
- 146 A. Folli, U. H. Jakobsen, G. L. Guerrini and D. E. Macphee, *J. Adv. Oxid. Technol.*, 2009, **12**, 126–133.
- 147 A. Folli, C. Pade, T. B. Hansen, T. De Marco and D. E. Macphee, *Cem. Concr. Res.*, 2012, **42**, 539–548.
- 148 S. N. Zailan, N. Mahmed, M. M. A. Abdullah, A. Victor Sandu and N. F. Shahedan, *Engineering Technology International Conference 2016*, eds. M. A. B. Abdullah, S. Z. AbdRahim, M. E. M. Suandi, M. N. M. Saad and M. F. Ghazali, 2017, **97**.
- 149 W. Haiss, N. T. K. Thanh, J. Aveyard and D. G. Fernig, *Anal. Chem.*, 2007, **79**, 4215–4221.
- 150 A. Trapalis, N. Todorova, T. Giannakopoulou, N. Boukos, T. Speliotis, D. Dimotikali and J. Yu, *Appl. Catal. B Environ.*, 2016, **180**, 637–647.
- 151 R. Zondervan, F. Kulzer, M. A. Kol'chenk and M. Orrit, *J. Phys. Chem. A*, 2004, **108**, 1657–1665.

- 152 P. Wilhelm and D. Stephan, *J. Photochem. Photobiol. A Chem.*, 2007, **185**, 19–25.
- 153 M. Dahl, Y. Liu and Y. Yin, *Chem. Rev.*, 2014, **114**, 9853–9889.
- 154 G. Baldi, M. Bitossi and A. Barzanti, *Method for the Preparation of Aqueous Dispersions of TiO<sub>2</sub> in the Form of Nanoparticles, and Dispersions Obtainable with This Method*, Google Patents, US8431621B2, April 2013.
- 155 L. Guardia, M. J. Fernández-Merino, J. I. Paredes, P. Solís-Fernández, S. Villar-Rodil, A. Martínez-Alonso and J. M. D. Tascón, *Carbon N. Y.*, 2011, **49**, 1653–1662.
- 156 T. R. Hoare and D. S. Kohane, *Polymer (Guildf.)*, 2008, **49**, 1993–2007.
- 157 J. M. Saul and D. F. Williams, *Handb. Polym. Appl. Med. Med. Devices*, 2013, 279–302.
- 158 S. Van Vlierberghe, P. Dubruel and E. Schacht, *Biomacromolecules*, 2011, **12**, 1387–1408.
- 159 P. Chakraborty and E. Gazit, *ChemNanoMat*, 2018, **4**, 730–740.
- 160 M. W. Tibbitt and K. S. Anseth, *Biotechnol. Bioeng.*, 2009, **103**, 655–663.
- 161 D. Seliktar, *Science*, 2012, **336**, 1124–1128.
- 162 N. Wang, M. Ma, Y. Luo, T. Liu, P. Zhou, S. Qi, Y. Xu and H. Chen, *ChemNanoMat*, 2018, **4**, 631–641.
- 163 M. Barbalinardo, M. Di Giosia, I. Polishchuk, G. Magnabosco, S. Fermani, F. Biscarini, M. Calvaresi, F. Zerbetto, G. Pellegrini, G. Falini, B. Pokroy and F. Valle, *J. Mater. Chem. B*, 2019, **7**, 5808–5813.
- 164 N. M. Sangeetha and U. Maitra, *Chem. Soc. Rev.*, 2005, **34**, 821.
- 165 J. W. Steed, *Chem. Commun.*, 2011, **47**, 1379–1383.
- 166 E. A. Appel, J. Del Barrio, X. J. Loh and O. A. Scherman, *Chem. Soc. Rev.*, 2012, **41**, 6195–6214.
- 167 A. M. Jonker, D. W. P. M. Löwik and J. C. M. Van Hest, *Chem. Mater.*, 2012, **24**, 759–

- 773.
- 168 D. Das, T. Kar and P. K. Das, *Soft Matter*, 2012, **8**, 2348–2365.
- 169 A. Memic, H. A. Alhadrami, M. A. Hussain, M. Aldhahri, F. Al Nowaiser, F. Al-Hazmi, R. Oklu and A. Khademhosseini, *Biomed. Mater.*, 2015, **11**, 014104.
- 170 A. K. Gaharwar, N. A. Peppas and A. Khademhosseini, *Biotechnol. Bioeng.*, 2014, **111**, 441–453.
- 171 D. Iglesias, S. Bosi, M. Melchionna, T. Da Ros and S. Marchesan, *Curr. Top. Med. Chem.*, 2016, **16**, 1976–1989.
- 172 S. R. Shin, H. Bae, J. M. Cha, J. Y. Mun, Y.-C. Chen, H. Tekin, H. Shin, S. Farshchi, M. R. Dokmeci, S. Tang and A. Khademhosseini, *ACS Nano*, 2012, **6**, 362–72.
- 173 H. Komatsu, M. Ikeda and I. Hamachi, *Chem. Lett.*, 2011, **40**, 198–200.
- 174 K. Sugikawa, Y. Inoue, K. Kozawa and A. Ikeda, *ChemNanoMat*, 2018, **4**, 682–687.
- 175 S. Paul, K. Basu, K. S. Das and A. Banerjee, *ChemNanoMat*, 2018, **4**, 882–887.
- 176 S. R. Shin, S. M. Jung, M. Zalabany, K. Kim, P. Zorlutuna, S. B. Kim, M. Nikkhah, M. Khabiry, M. Azize, J. Kong, K. T. Wan, T. Palacios, M. R. Dokmeci, H. Bae, X. Tang and A. Khademhosseini, *ACS Nano*, 2013, **7**, 2369–2380.
- 177 D. Iglesias, M. Melle-Franco, M. Kurbasic, M. Melchionna, M. Abrami, M. Grassi, M. Prato and S. Marchesan, *ACS Nano*, 2018, **12**, 5530–5538.
- 178 H. Wang, Q. Chen and S. Zhou, *Chem. Soc. Rev.*, 2018, **47**, 4198–4232.
- 179 B. Adhikari and A. Banerjee, *Soft Matter*, 2011, **7**, 9259–9266.
- 180 J. M. González-Domínguez, C. Martín, Ó. J. Durá, S. Merino and E. Vázquez, *ACS Appl. Mater. Interfaces*, 2018, **10**, 1987–1995.
- 181 J. K. Wychowaniec, M. Iliut, M. Zhou, J. Moffat, M. A. Elsayy, W. A. Pinheiro, J. A. Hoyland, A. F. Miller, A. Vijayaraghavan and A. Saiani, *Biomacromolecules*, 2018, **19**, 2731–2741.

- 182 R. Das Mahapatra, J. Dey and R. G. Weiss, *Soft Matter*, 2019, **15**, 433–441.
- 183 Kenry, W. C. Lee, K. P. Loh and C. T. Lim, *Biomaterials*, 2018, **155**, 236–250.
- 184 Y. Yang, A. M. Asiri, Z. Tang, D. Du and Y. Lin, *Mater. Today*, 2013, **16**, 365–373.
- 185 S. Kumar and K. Chatterjee, *ACS Appl. Mater. Interfaces*, 2016, **8**, 26431–26457.
- 186 C. Chung, Y. K. Kim, D. Shin, S. R. Ryoo, B. H. Hong and D. H. Min, *Acc. Chem. Res.*, 2013, **46**, 2211–2224.
- 187 J. Wu, A. Chen, M. Qin, R. Huang, G. Zhang, B. Xue, J. Wei, Y. Li, Y. Cao and W. Wang, *Nanoscale*, 2015, **7**, 1655–1660.
- 188 H. Bai, C. Li, X. Wang and G. Shi, *Chem. Commun.*, 2010, **46**, 2376–2378.
- 189 S.-Z. Zu and B.-H. Han, *J. Phys. Chem. C*, 2009, **113**, 13651–13657.
- 190 H. Gao, Y. Sun, J. Zhou, R. Xu and H. Duan, *ACS Appl. Mater. Interfaces*, 2013, **5**, 425–432.
- 191 H. P. Cong, P. Wang and S. H. Yu, *Chem. Mater.*, 2013, **25**, 3357–3362.
- 192 H. Guo, T. Jiao, Q. Zhang, W. Guo, Q. Peng and X. Yan, *Nanoscale Res. Lett.*, 2015, **10**, 272.
- 193 M. Calvaresi and F. Zerbetto, *Acc. Chem. Res.*, 2013, **46**, 2454–2463 .
- 194 S. Marchesan and M. Prato, *Chem. Commun.*, 2015, **51**, 4347–4359.
- 195 A. W. N. Sloan, A. L. R. Santana-Pereira, J. Goswami, M. R. Liles and V. A. Davis, *ACS Macro Lett.*, 2017, **6**, 1228–1231.
- 196 M. Di Giosia, F. Valle, A. Cantelli, A. Bottoni, F. Zerbetto, E. Fasoli and M. Calvaresi, *Carbon N. Y.*, 2019, **147**, 70–82.
- 197 C. A. Angulo-Pachón, S. Díaz-Oltra, J. J. Ojeda-Flores, E. Falomir, F. Galindo and J. F. Miravet, *ChemNanoMat*, 2018, **4**, 769–771.
- 198 D. Giuri, M. Barbalinardo, N. Zanna, P. Paci, M. Montalti, M. Cavallini, F. Valle, M.

- Calvaresi and C. Tomasini, *Molecules*, 2019, **24**, 1–12.
- 199 E. R. Draper and D. J. Adams, *Chem*, 2017, **3**, 390–410.
- 200 C. Colquhoun, E. R. Draper, R. Schweins, M. Marcello, D. Vadukul, L. C. Serpell and D. J. Adams, *Soft Matter*, 2017, **13**, 1914–1919.
- 201 F. Beckert, S. Trenkle, R. Thomann and R. Mülhaupt, *Macromol. Mater. Eng.*, 2014, **299**, 1513–1520.
- 202 S. Weiner and L. Addadi, *Annu. Rev. mater.*, 2011, **41**, 21–40.
- 203 H. A. Lowenstam and S. Weiner, *On biomineralization*, Oxford University Press, 1989.
- 204 A. E. S. Van Driessche, M. Kellermeier, L. G. Benning and D. Gebauer, *New Perspectives and Growth Nucleation on Mineral. From Solutions Precursors to Solid Materials*, 2017.
- 205 J. Gómez-Morales, G. Falini and J. M. García-Ruiz, in *Handbook of Crystal Growth*, Elsevier, 2015, **1**, 873–913.
- 206 E. Asenath-Smith, H. Li, E. C. Keene, Z. W. Seh and L. A. Estroff, *Adv. Funct. Mater.*, 2012, **22**, 2891–2914.
- 207 S. Weiner and L. Addadi, *J. Mater. Chem.*, 1997, **7**, 689–702.
- 208 S. Weiner, *Am. Zool.*, 2015, **24**, 945–951.
- 209 H. Zheng, C. Y. Neo, X. Mei, J. Qiu and J. Ouyang, *J. Mater. Chem.*, 2012, **22**, 14465.
- 210 L. Y. Zhang, T. Wang, H. Y. Wang, Y. Meng, W. T. Yu and L. Y. Chai, *Chem. Commun.*, 2013, **49**, 9974–9976.
- 211 R. S. Jacob, D. Ghosh, P. K. Singh, S. K. Basu, N. N. Jha, S. Das, P. K. Sukul, S. Patil, S. Sathaye, A. Kumar, A. Chowdhury, S. Malik, S. Sen and S. K. Maji, *Biomaterials*, 2015, **54**, 97–105.
- 212 H. Wang, A. Han, Y. Cai, Y. Xie, H. Zhou, J. Long and Z. Yang, *Chem. Commun. (Camb)*, 2013, **49**, 7448–50.

- 213 G. Perale, C. Giordano, F. Bianco, F. Rossi, M. Tunesi, F. Daniele, F. Crivelli, M. Matteoli and M. Masi, *Int. J. Artif. Organs*, 2011, **34**, 295–303.
- 214 A. S. Weingarten, R. V. Kazantsev, L. C. Palmer, D. J. Fairfield, A. R. Koltonow and S. I. Stupp, *J. Am. Chem. Soc.*, 2015, **137**, 15241–15246.
- 215 E. Schön, C. Saldías, D. Haldar and D. Díaz, *Macromol. Symp.*, 2019, **385**, 1800193.
- 216 A. P. Jackson, J. F. V Vincent, R. M. Turner and R. M. Alexander, *Proc. R. Soc. London. Ser. B. Biol. Sci.*, 1988, **234**, 415–440.
- 217 J. Aizenberg, A. Tkachenko, S. Weiner, L. Addadi and G. Hendler, *Nature*, 2001, **412**, 819–822.
- 218 Y. Ma, S. R. Cohen, L. Addadi and S. Weiner, *Adv. Mater.*, 2008, **20**, 1555–1559.
- 219 Y. Ma and Q. Feng, *J. Solid State Chem.*, 2011, **184**, 1008–1015.
- 220 S.-T. Tomás, S. Fermani, M. A. Durándurán-Olivencia, F. Otaíora, J. Gómezgómez-Morales, G. Falini and J. M. García-Ruiz, *Cryst. Growth Des.*, 2013, **13**, 3884–3891.
- 221 G. Falini, S. Fermani, M. Gazzano and A. Ripamonti, *Chem. – A Eur. J.*, 1997, **3**, 1807–1814.
- 222 C. Kosanović, S. Fermani, G. Falini, D. Kralj, C. Kosanović, S. Fermani, G. Falini and D. Kralj, *Crystals*, 2017, **7**, 355.
- 223 T. Mass, A. J. Giuffre, C.-Y. Sun, C. A. Stiffler, M. J. Frazier, M. Neder, N. Tamura, C. V Stan, M. A. Marcus and P. U. P. A. Gilbert, *Proc. Natl. Acad. Sci. U. S. A.*, 2017, **114**, E7670–E7678.
- 224 L. A. Estroff, L. Addadi, S. Weiner and A. D. Hamilton, *Org. Biomol. Chem.*, 2004, **2**, 137–141.
- 225 L. A. Estroff, L. Leiserowitz, L. Addadi, S. Weiner and A. D. Hamilton, *Adv. Mater.*, 2003, **15**, 38–42.
- 226 E. R. Draper and D. J. Adams, *Chem*, 2017, **3**, 390–410.

- 227 L. Chen, T. O. McDonald and D. J. Adams, *RSC Adv.*, 2013, **3**, 8714.
- 228 H. Mcewen, E. Y. Du, J. P. Mata, P. Thordarson and A. D. Martin, *J. Mater. Chem. B*, 2017, **5**, 9412–9417.
- 229 G. Yu, X. Yan, C. Han and F. Huang, *Chem. Soc. Rev.*, 2013, **42**, 6697–6722.
- 230 D. Adams, *Gels*, 2018, **4**, 32.
- 231 L. L. E. Mears, E. R. Draper, A. M. Castilla, H. Su, Zhuola, B. Dietrich, M. C. Nolan, G. N. Smith, J. Douth, S. Rogers, R. Akhtar, H. Cui and D. J. Adams, *Biomacromolecules*, 2017, **18**, 3531–3540.
- 232 B. S. Yandell, *Practical Data Analysis for Designed Experiments*, Routledge, 2017.
- 233 *PDF-4+ 2019 (Database)*, Ed. by Dr. Soorya Kabekkodu, *Int. Cent. Diffraction Data, Newtown Square, PA, USA*.
- 234 A. P. Hammersley, *J. Appl. Crystallogr.*, 2016, **49**, 646–652.
- 235 Q. Chen and G. A. Thouas, *Mater. Sci. Eng. R Reports*, 2015, **87**, 1–57.
- 236 B. D. Boyan, M. I. Baker, C. S. D. Lee, A. L. Raines, A. S. Greenwald, R. Olivares-Navarrete and Z. Schwartz, ed. P. B. T.-C. B. Ducheyne, Elsevier, Oxford, 2011, 237–255.
- 237 F. Baino, eds. P. Palmero, F. Cambier and E. B. T.-A. in C. B. De Barra, Woodhead Publishing, 2017, 249–278.
- 238 S. Samavedi, A. R. Whittington and A. S. Goldstein, *Acta Biomater.*, 2013, **9**, 8037–8045.
- 239 C. Drouet, A. Leriche, S. Hampshire, M. Kashani, A. Stamboulis, M. Iafisco and A. Tampieri, eds. P. Palmero, F. Cambier and E. B. T.-A. in C. B. De Barra, Woodhead Publishing, 2017, 21–82.
- 240 K. L. Low, S. H. Tan, S. H. S. Zein, J. A. Roether, V. Mouriño and A. R. Boccaccini, *J. Biomed. Mater. Res. Part B Appl. Biomater.*, 2010, **94B**, 273–286.

- 241 W. Habraken, P. Habibovic, M. Epple and M. Bohner, *Mater. Today*, 2016, **19**, 69–87.
- 242 J. Zhang, W. Liu, V. Schnitzler, F. Tancret and J.-M. Bouler, *Acta Biomater.*, 2014, **10**, 1035–1049.
- 243 K. Ishikawa, ed. P. B. T.-C. B. I. I. Ducheyne, Elsevier, Oxford, 2017, 368–391.
- 244 H. H. K. Xu, P. Wang, L. Wang, C. Bao, Q. Chen, M. D. Weir, L. C. Chow, L. Zhao, X. Zhou and M. A. Reynolds, *Bone Res.*, 2017, **5**, 17056.
- 245 H. Jiang, Y. Zuo, Q. Zou, H. Wang, J. Du, Y. Li and X. Yang, *ACS Appl. Mater. Interfaces*, 2013, **5**, 12036–12044.
- 246 G. Lewis, *J. Biomed. Mater. Res. Part B Appl. Biomater.*, 2017, **105**, 1260–1284.
- 247 A. Sugawara, K. Asaoka and S.-J. Ding, *J. Mater. Chem. B*, 2013, **1**, 1081–1089.
- 248 R. Z. LeGeros, *Chem. Rev.*, 2008, **108**, 4742–4753.
- 249 M. P. Ginebra, T. Traykova and J. A. Planell, *J. Control. Release*, 2006, **113**, 102–110.
- 250 U. Gbureck, J. E. Barralet, L. Radu, H. G. Klinger and R. Thull, *J. Am. Ceram. Soc.*, 2004, **87**, 1126–1132.
- 251 A. Bigi, B. Bracci and S. Panzavolta, *Biomaterials*, 2004, **25**, 2893–2899.
- 252 S. Larsson and G. Hannink, *Injury*, 2011, **42 Suppl 2**, S30-4.
- 253 S. V Dorozhkin, *Materials (Basel)*, 2009, **2**, 221–291.
- 254 M. Bohner, U. Gbureck and J. E. Barralet, *Biomaterials*, 2005, **26**, 6423–6429.
- 255 J. W. Callister and D. Rethwisch, *Materials science and engineering: an introduction*, John Wiley Sons Inc., Hoboken, 2009.
- 256 B. L. Karihaloo and J. Wang, *Comput. Mech.*, 1997, **19**, 453–462.
- 257 C. Canal and M. P. Ginebra, *J. Mech. Behav. Biomed. Mater.*, 2011, **4**, 1658–1671.
- 258 Y. Zuo, F. Yang, J. G. C. Wolke, Y. Li and J. A. Jansen, *Acta Biomater.*, 2010, **6**, 1238–

- 1247.
- 259 M. F. Di Filippo, L. S. Dolci, B. Albertini, N. Passerini, P. Torricelli, A. Parrilli, M. Fini, F. Bonvicini, G. A. Gentilomi, S. Panzavolta and A. Bigi, *Ceram. Int.*, 2020, **46**, 10048–10057.
- 260 S. Panzavolta, P. Torricelli, B. Bracci, M. Fini and A. Bigi, *J. Inorg. Biochem.*, 2009, **103**, 101–106.
- 261 S. Panzavolta, P. Torricelli, B. Bracci, M. Fini and A. Bigi, *J. Inorg. Biochem.*, 2010, **104**, 1099–1106.
- 262 Y. Xu, C. Kang, Y. Chen, Z. Bian, X. Qiu, L. Gao and Q. Meng, *Chem. - A Eur. J.*, 2012, **18**, 16955–16961.
- 263 J. Wang, Y. J.; Tang, L. M.; Yu, *Cryst. Growth Des.*, 2008, **8**, 884–889.
- 264 J. Liu, F. Xu, Z. Sun, Y. Pan, J. Tian, H. C. Lin and X. Li, *Soft Matter*, 2015, **12**, 141–148.
- 265 G. O. Jones, C. D.; Tan, J. C.; Lloyd, *Chem. Commun.*, 2012, **48**, 2110.
- 266 J. W. A. Lloyd, G. O.; Steed, *Soft Matter*, 2011, **7**, 75–84.
- 267 K. M. . Byrne, P.; Lloyd, G. O.; Applegarth, L.; Anderson and J. W. Clarke, N.; Steed, *New J. Chem.*, 2010, **34**, 2261–2274.
- 268 F. Braga, D.; d’Agostino, S.; D’Amen, E.; Grepioni, *Chem. Commun.*, 2011, **47**, 5154–5156.
- 269 S. Saito, S.; Nakakura, K.; Yamaguchi, *Angew. Chemie - Int. Ed.*, 2012, **51**, 714–717.
- 270 A. K. Roy, B.; Bairi, P.; Nandi, *Soft Matter*, 2012, **8**, 2366–2369.
- 271 L. Chen, K. Morris, A. Laybourn, D. Elias, M. R. Hicks, A. Rodger, L. Serpell and D. J. Adams, *Langmuir*, 2010, **26**, 5232–5242.
- 272 L. Chen, S. Revel, K. Morris, L. C. Serpell and D. J. Adams, *Langmuir*, 2010, **26**, 13466–13471.

- 273 A. Z. Cardoso, A. E. Alvarez Alvarez, B. N. Cattoz, P. C. Griffiths, S. M. King, W. J. Frith and D. J. Adams, *Faraday Discuss.*, 2013, **166**, 101–116.
- 274 L. A. Estroff and A. D. Hamilton, *Chem. Rev.*, 2004, **104**, 1201–1217.
- 275 A. Barth, *Biochim. Biophys. Acta - Bioenerg.*, 2007, **1767**, 1073–1101.
- 276 P. I. Haris and D. Chapman, *Biopolymers*, 1995, **37**, 251–263.
- 277 J.-B. Guilbaud and A. Saiani, *Chem. Soc. Rev.*, 2011, **40**, 1200–1210.
- 278 M. J. Hollamby, *Phys. Chem. Chem. Phys.*, 2013, **15**, 10566–10579.
- 279 G. Némethy and H. A. Scheraga, *J. Chem. Phys.*, 1964, **41**, 680–689.
- 280 L. Dougan, A. S. R. Koti, G. Genchev, H. Lu and J. M. Fernandez, *ChemPhysChem*, 2008, **9**, 2836–2847.
- 281 Y. Pocker and E. Green, *J. Am. Chem. Soc.*, 1973, **95**, 113–119.
- 282 K. McAulay, H. Wang, A. M. Fuentes-Caparrós, L. Thomson, N. Khunti, N. Cowieson, H. Cui, A. Seddon and D. J. Adams, *Langmuir*, 2020, **36**, 8626–8631.
- 283 M. G. F. Angelero, A. Sabri, R. Creasey, P. Angelero, M. Marlow and M. Zelzer, *Chem. Commun.*, 2016, **52**, 4298–4300.
- 284 A. R. Hirst, J. F. Miravet, B. Escuder, L. Noirez, V. Castelletto, I. W. Hamley and D. K. Smith, *Chem. – A Eur. J.*, 2009, **15**, 372–379.
- 285 L. E. Buerkle and S. J. Rowan, *Chem. Soc. Rev.*, 2012, **41**, 6089–6102.
- 286 W. Edwards and D. K. Smith, *J. Am. Chem. Soc.*, 2014, **136**, 1116–1124.
- 287 S. Boothroyd, A. Saiani and A. F. Miller, *Biopolymers*, 2014, **101**, 669–680.
- 288 D. Li, Y. Shi and L. Wang, *Chinese J. Chem.*, 2014, **32**, 123–127.
- 289 C. Colquhoun, E. R. Draper, E. G. B. Eden, B. N. Cattoz, K. L. Morris, L. Chen, T. O. McDonald, A. E. Terry, P. C. Griffiths, L. C. Serpell and D. J. Adams, *Nanoscale*, 2014, **6**, 13719–13725.

- 290 D. G. Velázquez and R. Luque, *Chem. – A Eur. J.*, 2011, **17**, 3847–3849.
- 291 Z. Džolić, K. Wolsperger and M. Žinić, *New J. Chem.*, 2006, **30**, 1411–1419.
- 292 R. K. Das, R. Kandaneli, J. Linnanto, K. Bose and U. Maitra, *Langmuir*, 2010, **26**, 16141–16149.
- 293 M. Zhou, A. M. Smith, A. K. Das, N. W. Hodson, R. F. Collins, R. V Ulijn and J. E. Gough, *Biomaterials*, 2009, **30**, 2523–2530.
- 294 J. Raeburn and D. J. Adams, *Chem. Commun.*, 2015, **51**, 5170–5180.
- 295 E. R. Draper and D. J. Adams, *Chem. Soc. Rev.*, 2018, **47**, 3395–3405.
- 296 M. M. Safont-Sempere, G. Fernández and F. Würthner, *Chem. Rev.*, 2011, **111**, 5784–5814.
- 297 C. C. Horgan, A. L. Rodriguez, R. Li, K. F. Bruggeman, N. Stupka, J. K. Raynes, L. Day, J. W. White, R. J. Williams and D. R. Nisbet, *Acta Biomater.*, 2016, **38**, 11–22.
- 298 K. Medini, B. West, D. E. Williams, M. A. Brimble and J. A. Gerrard, *Chem. Commun. (Camb)*, 2017, **53**, 1715–1718.
- 299 A. Sandeep, V. K. Praveen, K. K. Kartha, V. Karunakaran and A. Ajayaghosh, *Chem. Sci.*, 2016, **7**, 4460–4467.
- 300 H. A. M. Ardoña and J. D. Tovar, *Chem. Sci.*, 2015, **6**, 1474–1484.
- 301 K. Fan, H. Kong, X. Wang, X. Yang and J. Song, *RSC Adv.*, 2016, **6**, 80934–80938.
- 302 N. Singh, K. Zhang, C. A. Angulo-Pachón, E. Mendes, J. H. van Esch and B. Escuder, *Chem. Sci.*, 2016, **7**, 5568–5572.
- 303 K. Sugiyasu, S. Kawano, N. Fujita and S. Shinkai, *Chem. Mater.*, 2008, **20**, 2863–2865.
- 304 A. M. Castilla, E. R. Draper, M. C. Nolan, C. Brasnett, A. Seddon, L. L. E. Mears, N. Cowieson and D. J. Adams, *Sci. Rep.*, 2017, **7**, 1–10.
- 305 L. Chen, K. Morris, A. Laybourn, D. Elias, M. R. Hicks, A. Rodger, L. Serpell and D. J.

- Adams, *Langmuir*, 2010, **26**, 5232–5242.
- 306 D. J. Chen, L.; Revel, S.; Morris, K.; Serpell, L. C.; Adams, *Langmuir*, 2010, **26**, 13466–13471.
- 307 J. H. Waite, *Int. J. Adhes. Adhes.*, 1987, **7**, 9–14.
- 308 S. A. Mian and Y. Khan, *J. Chem.*, 2017, **2017**, 1–6.
- 309 J. H. Waite, *J. Exp. Biol.*, 2017, **220**, 517–530.
- 310 J. H. Waite, *Biochemistry*, 2002, **1180**, 1172–1180.
- 311 J. H. Waite and M. L. Tanzer, *Biochem. Biophys. Res. Commun.*, 1980, **96**, 1554–1561.
- 312 B. P. Lee, P. B. Messersmith, J. N. Israelachvili and J. H. Waite, *Annu. Rev. Mater. Res.*, 2011, **41**, 99–132.
- 313 H. Zhao, C. Sun, R. J. Stewart and J. H. Waite, *J. Biol. Chem.*, 2005, **280**, 42938–42944.
- 314 A. H. Hofman, I. A. van Hees, J. Yang and M. Kamperman, *Adv. Mater.*, 2018, **30**, 1704640.
- 315 M. Shin, J. Y. Shin, K. Kim, B. Yang, J. W. Han, N. K. Kim and H. J. Cha, *J. Colloid Interface Sci.*, 2020, **563**, 168–176.
- 316 J. H. Waite, W. Wei, L. Petrone, Y. Tan, H. Cai, J. N. Israelachvili and A. Miserez, *Adv. Funct. Mater.*, 2016, **26**, 3496–3507.
- 317 S. A. Burke, M. Ritter-Jones, B. P. Lee and P. B. Messersmith, *Biomed. Mater.*, 2007, **2**, 203–210.
- 318 B. P. Lee, C. Y. Chao, F. Nelson Nunalee, E. Motan, K. R. Shull and P. B. Messersmith, *Macromolecules*, 2006, **39**, 1740–1748.
- 319 L. Ninan, J. Monahan, R. L. Stroshine, J. J. Wilker and R. Shi, *Biomaterials*, 2003, **24**, 4091–4099.
- 320 G. Westwood, T. N. Horton and J. J. Wilker, *Macromolecules*, 2007, **40**, 3960–3964.

- 321 K. Kristiansen, S. H. Donaldson, Z. J. Berkson, J. Scott, R. Su, X. Banquy, D. W. Lee, H. B. De Aguiar, J. D. McGraw, G. D. Degen and J. N. Israelachvili, *Langmuir*, 2019, **35**, 15500–15514.
- 322 A. P. Defante, T. N. Burai, M. L. Becker and A. Dhinojwala, *Langmuir*, 2015, **31**, 2398–2406.
- 323 N. Dhopatkar, A. P. Defante and A. Dhinojwala, *Sci. Adv.*, 2016, **2**, 1–10.
- 324 Y. Xu, Q. Liu, A. Narayanan, D. Jain, A. Dhinojwala and A. Joy, *Adv. Mater. Interfaces*, 2017, **4**, 1–6.
- 325 M. Tavafoghi, A. Sheikhi, R. Tutar, J. Jahangiry, A. Baidya, R. Haghniaz and A. Khademhosseini, *Adv. Healthc. Mater.*, 2020, 1901722.
- 326 M. A. North, C. A. Del Grosso and J. J. Wilker, *ACS Appl. Mater. Interfaces*, 2017, **9**, 7866–7872.
- 327 C. W. Peak, J. J. Wilker and G. Schmidt, *Colloid Polym. Sci.*, 2013, **291**, 2031–2047.
- 328 B. D. B. Tiu, P. Delparastan, M. R. Ney, M. Gerst and P. B. Messersmith, *ACS Appl. Mater. Interfaces*, 2019, **11**, 28296–28306.
- 329 M. Mehdizadeh, H. Weng, D. Gyawali, L. Tang and J. Yang, *Biomaterials*, 2012, **33**, 7972–7983.
- 330 N. K. Kaushik, N. Kaushik, S. Pardeshi, J. G. Sharma, S. H. Lee and E. H. Choi, *Mar. Drugs*, 2015, **13**, 6792–6817.
- 331 G. M. Glenn, D. N. Taylor, X. Li, S. Frankel, A. Montemarano and C. R. Alving, *Nat. Med.*, 2000, **6**, 1403–1406.
- 332 M. Mehdizadeh and J. Yang, *Macromol. Biosci.*, 2013, **13**, 271–288.
- 333 Y. Ai, J. Nie, G. Wu and D. Yang, *J. Appl. Polym. Sci.*, 2014, **131**, 31–35.
- 334 Q. Ye, F. Zhou and W. Liu, *Chem. Soc. Rev.*, 2011, **40**, 4244–4258.
- 335 H. J. Lee, A. N. Koo, S. W. Lee, M. H. Lee and S. C. Lee, *J. Control. Release*, 2013,

- 170**, 198–208.
- 336 S. V. Chankeshwara, R. Chebolu and A. K. Chakraborti, *J. Org. Chem.*, 2008, **73**, 8615–8618.
- 337 B. Soltannia and D. Sameoto, *ACS Appl. Mater. Interfaces*, 2014, **6**, 21995–22003.
- 338 T. Young, in *Philos. Trans. R. Soc. London*, 1805, **95**, 65–87.
- 339 M. A. Greenfield, J. R. Hoffman, M. O. De La Cruz and S. I. Stupp, *Langmuir*, 2010, **26**, 3641–3647.
- 340 M. Suzuki, Y. Hayakawa and K. Hanabusa, *Gels*, 2015, **1**, 81–93.
- 341 A. Z. Cardoso, L. L. E. Mears, B. N. Cattoz, P. C. Griffiths, R. Schweins and D. J. Adams, *Soft Matter*, 2016, **12**, 3612–3621.
- 342 J. Li, H. Ejima and N. Yoshie, *ACS Appl. Mater. Interfaces*, 2016, **8**, 19047–19053.
- 343 H. Ejima, A. Oba and N. Yoshie, *J. Photopolym. Sci. Technol.*, 2018, **31**, 75–80.
- 344 C. L. Rohn, *TA Instruments USA*.
- 345 G. Amarpuri, C. Zhang, C. Diaz, B. D. Opell, T. A. Blackledge and A. Dhinojwala, *ACS Nano*, 2015, **9**, 11472–11478.
- 346 P. Das and M. Reches, *Nanoscale*, 2016, **8**, 15309–15316.
- 347 S. K. Clancy, A. Sodano, D. J. Cunningham, S. S. Huang, P. J. Zalicki, S. Shin and B. K. Ahn, *Biomacromolecules*, 2016, **17**, 1869–1874.
- 348 J. Shin, J. S. Lee, C. Lee, H.-J. Park, K. Yang, Y. Jin, J. H. Ryu, K. S. Hong, S.-H. Moon, H.-M. Chung, H. S. Yang, S. H. Um, J.-W. Oh, D.-I. Kim, H. Lee and S.-W. Cho, *Adv. Funct. Mater.*, 2015, **25**, 3814–3824.
- 349 J. Comyn, in *Adhesion 6*, London, 19th Annua., 1982, 159–171.
- 350 K. W. Allen, *Adhesion 6*, London, 19th Annua., 1982.
- 351 R. A. Gledhill and A. J. Kinloch, *J. Adhes.*, 1974, **6**, 315–330.

- 352 M. Rahimnejad and W. Zhong, *RSC Adv.*, 2017, **7**, 47380–47396.
- 353 J. H. Ryu, S. Hong and H. Lee, *Acta Biomater.*, 2015, **27**, 101–115.
- 354 W. C. Still, M. Kahn and A. Mitra, *J. Org. Chem.*, 1978, **43**, 2923–2925.
- 355 E. Falb, A. Nudelman and A. Hassner, *Synth. Commun.*, 1993, **23**, 2839–2844.



## ACKNOWLEDGEMENTS

Innanzitutto, vorrei ringraziare l'Università di Bologna per le innumerevoli opportunità che mi ha offerto durante gli ultimi otto anni. Ho iniziato il mio percorso in questa Alma Mater con tante preoccupazioni e incertezze, e lei ha saputo farmi innamorare della Chimica, in tutte le sue sfaccettature, insegnamento dopo insegnamento, guidandomi con mano ferma ma gentile durante questo lungo percorso.

Un grandissimo ringraziamento va poi alla Prof.ssa Tomasini, la Supervisor di questo dottorato. Per tre anni ha creduto in me e mi ha spronata a fare del mio meglio, lanciandomi nuove sfide e affidandomi delle responsabilità; mi ha lasciata libera di fare le mie scelte sui progetti e mi ha sempre fatta sentire apprezzata, a livello lavorativo e umano. Questo percorso sarebbe sicuramente stato più faticoso se non ci fosse stata lei a guidarmi.

Un enorme grazie va sicuramente alla mia famiglia. La più grande forza me l'avete data voi. Grazie mamma e papà perché nessuno mi amerà mai quanto voi. Mi avete dato la forza di non arrendermi mai, nonché la positività e il coraggio nell'affrontare gli ostacoli. Mi avete supportata in ogni mia scelta e avete sempre creduto in me in maniera incondizionata. Voi non avete mai dubitato, e questo è stato essenziale per dissolvere le mie insicurezze e spingermi a fare sempre del mio meglio. Essere lontani è sicuramente difficile e mi mancate da morire, ma nel momento stesso in cui torno a casa passa tutto, e sembra che siamo sempre stati insieme. Lo stesso si può dire di mia sorella, la leonessa che mi ha insegato a difendermi e a buttarmi con grinta e passione nelle cose che amo. La nostra complicità e la capacità di capirci al volo sono gli ingredienti segreti che ci terranno sempre unite. Ti auguro di raggiungere tutti gli obiettivi che ti sei prefissata, pur restando sempre la mia sorellona. Hai una forza incredibile: credi in te stessa come hai sempre creduto in me.

Un grande ringraziamento va anche alla famiglia allargata, zii e zie, cugini e cugine, che hanno sempre avuto un pensiero nei miei confronti per ogni traguardo raggiunto e ostacolo superato, hanno rallegrato le occasioni in cui ci siamo riuniti e hanno sempre regalato sorrisi, oltre che leccornie di ogni tipo. Tra tutti, un pensiero speciale va sicuramente a Laura e Simona. Laura, sei sempre stata un punto di riferimento, la donna di successo impeccabile che un po' aspiro a diventare. Simo, sei proprio la più pazza delle mie cugine e sei sempre stata presente nonostante i tantissimi km a separarci. C'eri per farmi sfogare, c'eri per gioire dei miei successi, c'eri per farmi visitare la tua città stupenda (e quante ne abbiamo combinate in

quell'occasione!), c'eri per fare Zumba in quarantena...Anche a te auguro di avverare tutti i tuoi sogni e non lasciarti fermare da nulla. Di coraggio ne hai sicuramente da vendere.

Ringrazio Cecilia e Giada, le amiche con cui ho condiviso tanto durante gli anni di studio, e con cui ho continuato a condividere tanto durante il dottorato. Rincontrarci e raccontarci le novità sulle nostre vite è proprio una necessità e troviamo sempre il modo per farlo senza perderci di vista.

Lo stesso posso dire di Fil e Nya, compagni di tante avventure (reali e immaginarie), a cui ho aperto il mio cuore su tutto. Siete semplicemente due persone su cui so di poter contare qualunque cosa succeda. Due amici che non giudicano, ma consigliano, che hanno sempre voluto il mio bene e mi hanno sempre incoraggiata. Grazie di esserci e di esserci sempre stati. Non possono mancare i ringraziamenti ai “compagni di giochi” e non solo, Emanuele, Gaia e Davide. Con voi ho condiviso davvero tante esperienze, che sono servite per scaricare lo stress di questi anni, oltre che a divertirci un sacco. Grazie anche a Riccardo. Abbiamo condiviso davvero tanto e aldilà di come è andata, sei stato fondamentale per la mia crescita come persona.

Un enorme grazie va poi agli amici del laboratorio, e qui la lista si fa davvero molto lunga. Grazie a Lucia, Dario e Giulia, ferma tripletta del Lab. Tolomelli, i veri compagni di lunghe giornate di risate, scleri, ansie, canti, congressi, festeggiamenti e reazioni, tante reazioni, accompagnate dal ritmo incessante della musica del lab. (nonché della pompa).

E grazie a tutti i tirocinanti che sono passati negli anni, che mi hanno insegnato la pazienza e l'entusiasmo, nonché ai “nuovi acquisti”, Paolo, Davide e Tommaso, che hanno reso ancora più divertente l'ultimo anno. Grazie davvero a tutti, perché l'ambiente del laboratorio non sarebbe potuto essere più bello di così.

Grazie a Giulia e Ada. Mi avete sempre saputo ascoltare e consigliare sulle questioni più delicate, capendo tante cose di me prima che io stessa ne fossi consapevole. Siete due amiche con cui non ci si può annoiare. Mi avete insegnato a divertirmi veramente e a dare più ascolto a quella parte spensierata e incosciente di me che tante volte tendo a reprimere. Ringrazio anche Costanza e Martina, perché quando siamo tutte assieme il gruppetto è davvero completo e non ce n'è per nessuno.

Grazie a tutti gli altri ragazzi di Organica (e non solo), Ciccio, Simone P., Lello, Biondo, Giacomo, Michele, Paolo, Ruben, Federica, Franca, Simone B., Pedro, Iacopo, Jhon, Juzeng, Young, Alexia, Assunta, Edoardo, Mattia...Siete tantissimi e avete reso il Ciamician un posto

dove è proprio bello andare a lavorare. Fra i pranzi assieme e le uscite squinternate ne abbiamo passate davvero tante, ma siete un gruppo talmente variopinto e ben assortito che non ci si stanca mai di stare insieme. Un enorme ringraziamento è sicuramente dovuto, tra il personale tecnico, ad Andrea e Stefano, per la pazienza che avete sempre dimostrato nell'ascoltare le mie richieste e nel soddisfarle. Siete sinceramente fantastici nel mandare avanti tutto, e mi avete insegnato davvero tanto. Grazie.

Grazie all'Università di Glasgow per avermi permesso di trascorrere il periodo all'estero, ma soprattutto al Prof. Dave Adams per avermi accolta nel suo gruppo di ricerca. Mi ha messa a mio agio fin da subito, premurandosi che non mi mancasse nulla e mi piacesse il progetto. Grazie a tutti i ragazzi del lab di Glasgow, Ana Maria, Sam, Lisa, Dan, Maria Laura, Jacky, Becky, Tom, Santanu, Emily ma soprattutto a Bart, *leader* e compagno di cappa a cui sapevo di potermi rivolgere per fugare ogni dubbio, e a Courteney, Valentina e Libby, il trio che mi ha davvero accolta a braccia aperte, con cui ho condiviso tanti pranzi, cene e uscite. Mi avete davvero fatta sentire una di voi, tra balli popolari, birre e pancakes. Grazie anche ad Alex e Vassilios, compagni d'appartamento, pizze, viaggi e presunte malattie. È stata un'esperienza stupenda e mi è dispiaciuto tanto andare via prima del tempo. Sono sicura che troveremo il modo per riabbracciarci presto.

Il ringraziamento più profondo, infine, lo faccio a te Paolo. Non è facile esprimere a parole quanto tu mi abbia stravolto la vita nell'ultimo anno. Senza di te sarebbe stato tutto un po' più sbiadito, un po' più difficile, a volte probabilmente insormontabile. Mi hai fatto superare tanti momenti difficili (il periodo all'estero, la quarantena, un trasloco che altrimenti mi avrebbe spezzato il cuore) e hai reso indelebili i momenti belli. Le tue parole gentili mi hanno infuso coraggio, cancellando paure e insicurezze. Hai messo in luce aspetti del mio carattere che non conoscevo, sei stato paziente quando andavo di fretta e mi hai saputa aspettare quando rimanevo indietro. Spero di poter continuare a crescere insieme e supportarci a vicenda, raggiungendo insieme tanti altri traguardi, miei e tuoi, mano nella mano.